

Politechnika Śląska

Wydział Inżynierii Materiałowej



ROZPRAWA DOKTORSKA

Effect of the chemical composition and processing parameters on the
microstructure and mechanical properties of the bars subjected to
innovative XTP process

mgr inż. Radosław Rozmus

PROMOTOR

dr hab. inż. Krzysztof Radwański

PROMOTOR POMOCNICZY

dr inż. Radosław Swadźba

GLIWICE 2023

*Pracę dedykuję mojej Rodzinie,
w szczególności Żonie Patrycji,
za wsparcie oraz cierpliwość*

*Serdecznie dziękuję
Promotorowi dr hab. inż. Krzysztofowi Radwańskiemu
oraz Panu dr inż. Radosławowi Swadźbie
za pomoc w realizacji pracy doktorskiej, opiekę naukową,
za cenne uwagi i wskazówki udzielone w czasie
wykonywania badań i redakcji pracy,
jak również wszystkim Koleżankom i Kolegom
Grupy Badawczej Badania Właściwości i Struktury Materiałów
Sieci Badawczej Łukasiewicz – Górnośląski Instytut Technologiczny
za wsparcie i pomoc w realizacji pracy*

Radosław Rozmus

List of key abbreviations

A	Austenite
AED	Average Equivalent Diameter
DBTT	Ductile Brittle Transition Temperature
DLB	Degenerate Lower Bainite
DP	Dual Phase
DUB	Degenerate Upper Bainite
EBSD	Electron Backscatter Diffraction
FC	Fast Cooling
GB	Granular Bainite
HAGB	High Angle Grain Boundaries
LAGB	Low Angle Grain Boundaries
LB	Lower Bainite
LOM	Light Optical Microscope
M	Martensite
M/A	Martensite/Austenite
PAG	Prior Austenite Grain
PAGS	Prior Austenite Grain Size
RA	Retained Austenite
RT	Room Temperature
SC	Slow Cooling
SEM	Scanning Electron Microscope
TEM	Transmission Electron Microscope
TM	Tempered Martensite
UB	Upper Bainite

Contents

1.	Introduction	6
2.	Review of the literature	8
2.1.	Development of rolling processes and bars production.....	8
2.2.	Strengthening and softening of austenite during forming	18
2.3.	The role of alloying elements in steel.....	26
2.4.	Influence of alloying elements on austenite grain size.....	29
2.5.	Phase transformation of austenite during cooling	31
2.6.	Precipitation hardening of ferrite.....	34
2.7.	Summary.....	38
3.	The aim of the study	40
3.1.	The scope of the study	41
3.2.	Thesis.....	43
4.	Research methodology	45
4.1.	Dilatometry tests.....	45
4.2.	Design and production of steels with modified chemical composition.....	48
4.3.	Structural investigations	50
4.4.	Mechanical properties.....	56
5.	Results	58
5.1.	Process simulations.....	58
5.1.1.	The grain growth kinetics	59
5.1.2.	Process simulation with various parameters based on 7MnB8 steel	61
5.1.3.	Thermodynamic calculations.....	74
5.2.	Industrial trials with the developed process parameters for 7MnB8 steel.....	75
5.2.1.	Tensile tests.....	76
5.2.2.	Hardness measurements.....	77
5.2.3.	Charpy tests.....	78

5.2.4.	Light optical microscopy	78
5.2.5.	Scanning electron microscopy	82
5.2.6.	X-ray diffraction - retained austenite.....	88
5.2.7.	Scanning-Transmission electron microscopy	88
5.3.	New steels with selected chemical composition.....	94
5.3.1.	Justification of the chemical composition of experimental steels	94
5.4.	Investigation of the rods structure in the forged state	101
5.4.1.	Tensile tests.....	101
5.4.2.	Hardness measurements.....	102
5.4.3.	Charpy tests.....	102
5.4.4.	Light optical microscopy	103
5.4.5.	Scanning electron microscopy	106
5.4.6.	X-ray diffraction - retained austenite.....	111
5.4.7.	Scanning-Transmission electron microscopy	112
5.5.	The new steels after rolling with optimized production parameters	119
5.5.1.	Rolling conditions.....	119
5.5.2.	Tensile test	120
5.5.3.	Hardness measurements.....	121
5.5.4.	Charpy tests.....	122
5.5.5.	Light optical microscopy	123
5.5.6.	Scanning electron microscopy	125
5.5.7.	X-ray diffraction - retained austenite.....	131
5.5.8.	Scanning-Transmission electron microscopy	132
6.	Discussion.....	140
7.	Summary.....	154
8.	Conclusions	156
9.	Literature	159

1. Introduction

Due to possibilities of obtaining various mechanical properties by different types of treatments, steel found application in many branches of industry. For many years, formation and development of new technologies resulted in a constant rise of demand and production of steel in comparison to other metals. Fig. 1a shows a diagram of total crude steel production since 1967, while a comparison of steel to the other commonly used metals like aluminum, copper and chromium is presented in Fig. 1b. Those diagrams show the importance of steel in the world and indirectly indicate superiority of steel above other metals in terms of production volume.

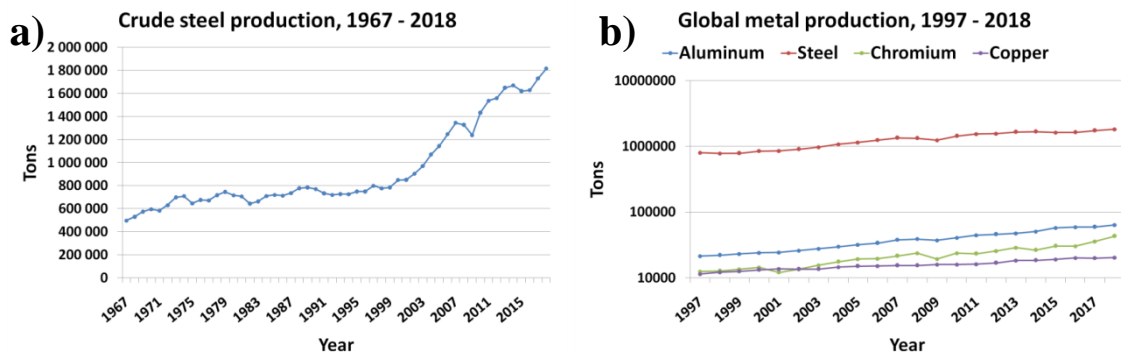


Fig. 1. Charts of: a) crude steel production in the world [1], b) comparison of chosen metal production in the world [1,2].

The phenomenon of steel is strictly connected with the ability to shape its mechanical properties and it is due to the possibility of obtaining different microstructures in the volume of the final product. That leads to different mechanical properties required in chosen application. For years many researches have led to the development of the technology and have provided the knowledge of dependence and influence of different factors like carbon content, microalloying elements, temperature of the process or degree of deformation on the final structure of steel. Nowadays, the term "steel" is no longer so obvious due to the division of steel depending on its use, chemical composition, microstructure and others. However, technological development sets new, more stringent requirements for steel, which means that it is justified to conduct research aimed at ensuring the required properties, improving production technology and seeking for new steel grades to replace those used so far. It is an indisputable fact that steel, due to its availability and wide range of applications, makes it a timeless material whose growing demand and production indicate that it is difficult to replace it in the growing industry.

History of bainite began in 1930, when Davenport and Bain published the article "Transformation of Austenite at Constant Subcritical Temperatures" [3]. However, in their nomenclature it was "dark etching acicular aggregate somewhat similar to martensite" and the "bainite" word, was first cited 12 years later [4]. Nowadays, it is well known that bainite is the most complicated microstructure found in steel and difficult to interpret quantitatively [5]. Despite that, the complex structure of described bainite morphologies, obtained depending on the transformation temperature, provides good combination of various mechanical properties, compared to other types of steels (Fig. 2).

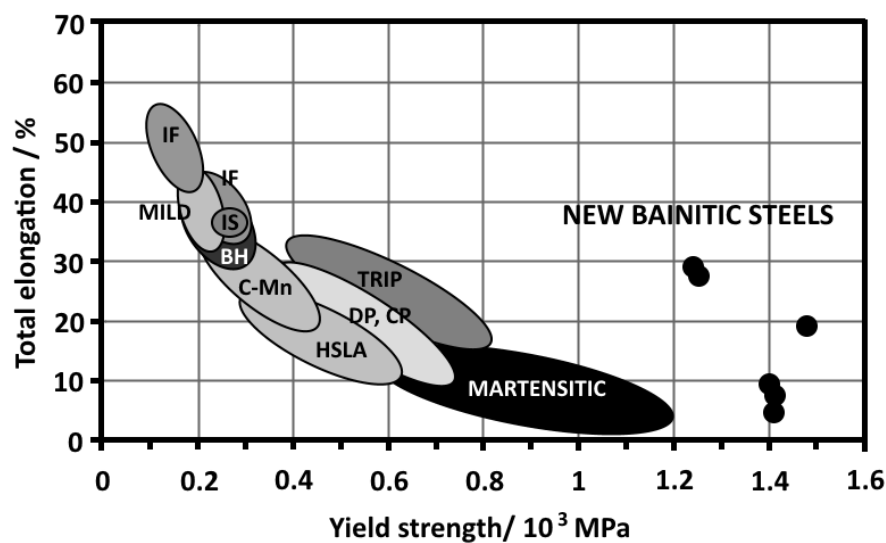


Fig. 2. Comparison of strength versus total elongation of conventional steels and new bainitic steels. IF, interstitial free; CMn, carbon Mn; BH, bake hardenable; IS, isotropic; DP - dual phase; CP, complex phase [6,7].

Slender plates of bainitic ferrite in conjunction with high dislocation density in ferrite, are the main strengthening mechanism operating in bainitic steels, while their ductility and fracture toughness are controlled by the amount of the softer phase, retained austenite (RA), present in the microstructures [8–13]. Due to this, novel bainitic steels are in an advantageous position for an increasing number of applications ranging from rails to formula one gear boxes [7,11,14,15].

2. Review of the literature

The literature review addresses issues related to thermomechanical processing methods, depending on the temperature at which the deformation is carried out. In addition, literature data on radial-displacement rolling is presented to determine the state of current knowledge related to both the process itself and the workpiece materials. The following section focuses on the phenomena occurring in the structure of the deformed austenite, the role alloying additives play in steels and their influence on austenite grain size during material reheating. This is followed by a characterisation of the transformation of the steel during cooling and a description of the differences in the solubility of alloying agents in austenite and ferrite, which, among other things, influence precipitation processes during cooling.

2.1. Development of rolling processes and bars production

The thermomechanical process is a method that combines the operations of deformation, heating and cooling, performed in different cycles during a single process, where the microstructure of the final product is shaped in the last stage during accelerated cooling. The ability to shape the microstructure of alloys is due to the presence of structural imperfections, mainly linear defects, i.e. dislocations [16]. Structural changes during the thermomechanical process result in the formation of new defects and redistribution of existing defects. During the deformation process, defects, mainly dislocations, are generated and annihilated and their distribution in the material changes. Depending on the temperature at which the plastic deformation of the material takes place, different effects on the structure are obtained. Hot working of metals takes place above the recrystallisation temperature, conventionally 0.5 of the melting point for alloys, where softening processes occur due to polygonisation and recrystallisation of the deformed structure. The dislocation density decreases and the material is characterized by low yield strength, hardness and high ductility [17].

Thermo-plastic processing is a process of deforming a material at an elevated temperature, which can involve several stages. Finishing deformation, on the other hand, is followed by accelerated cooling. A distinction can be made between thermo-plastic processing, where deformation of the material occurs at different temperatures (Fig. 3). The structural phenomena that accompany processing are heat-activated, as described in

Section 2.2. Depending on the process used, recovery and recrystallization can occur in the deformed material. This is mainly dependent on the temperature of the process, the amount and rate of deformation.

The chemical composition of the material to be treated also plays a crucial role, affecting, among other things, the onset temperature of the ferritic transformation. Some alloying elements (e.g. Nb) cause a decrease in the A_{c3} temperature [18], while others, such as S, influence its increase. Therefore, bearing in mind the alloying additives present in the steel, the nomenclature of the A_{r3} temperature was adopted which, for undeformed steels with large grain size, can be determined from the following formula [19]:

$$A_{r3} (^{\circ}C) = 868 - 189\%C - 75.8\%Mn + 1086\%S - 3799\%N_{free} - 1767\%Nb - 0.0933CRt \quad (1)$$

where CRt is the cooling rate in K/min.

However, in the process where the workpiece is deformed, the grain size also affects the change in A_{r3} temperature. A coarse-grained structure causes a delay in the phase transformation, due to the smaller number of favored nucleation sites of the new phase. Therefore, it is necessary to take the grain size into account in the formula, which for the steel set studied by B. Mintz takes the form of [19]:

$$A_{r3} (^{\circ}C) = 833.6 - 190.6\%C - 67.4\%Mn + 1522\%S - 2296\%N_{free} - 1532\%Nb + 7.91d^{-1/2} - 0.117CRt \quad (2)$$

where d is the diameter of the austenite grain.

Moreover, during the process of thermomechanical processing, it is necessary to characterize the T_{nr} temperature, below which strain is accumulated, which leads to an increase in mean flow stress and is given by the Boratto equation [20,21]:

$$T_{NR} = 464C - (644\sqrt{Nb} - 6445Nb) - (230\sqrt{V} - 732V) + 363Al + 890Ti - 357Si + 887 \quad (3)$$

where Nb, V, Ti, Al, C, and Si are the elements in wt% of steel.

By determining these characteristic temperatures for a given chemical composition, it is possible to control the thermo-mechanical treatment processes in such a way that the selected processes of structure reconstruction after deformation take place. Given the characteristic temperatures of the material being treated, it is possible to carry out the process in various combinations, as shown in Fig. 3.

Conventional high-temperature rolling (Fig. 3 - 2)

The first conventional rolling processes with recrystallization control involve deformation above the T_{nr} temperature. As a result of high temperature and deformation, static recrystallization of the structure occurs between successive passes of the material through the rolls and intensive cooling. As a result, refinement of the structure takes place,

however, this strategy has its limitations regarding the obtained grain size. In addition, in the case of static recrystallization, the time of accommodation plays an important role, since the reconstruction process does not begin immediately after the material passes through the rollers [22–25].

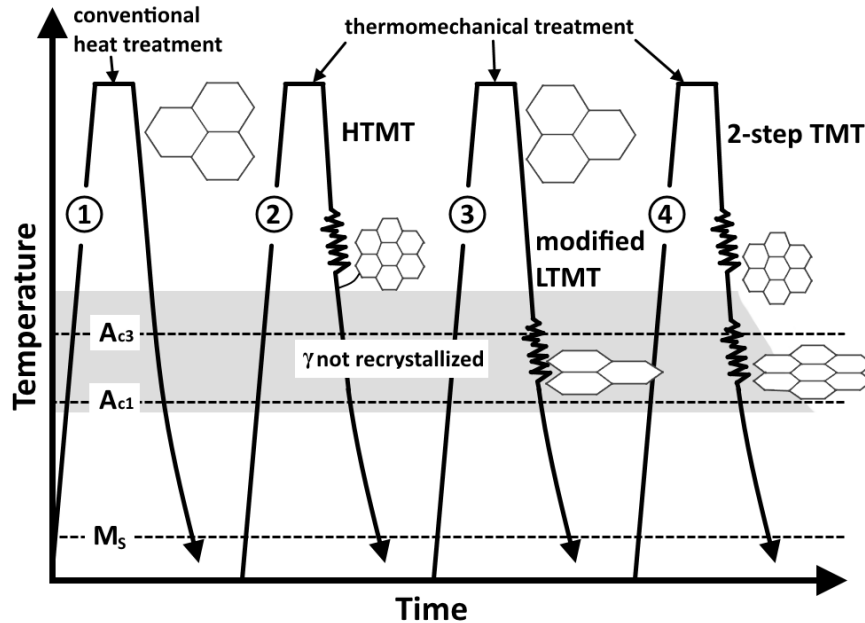


Fig. 3. Different rolling strategies [22].

Recrystallization-controlled rolling (Fig. 3 – 3)

The development of rolling processes resulted in the addition of so-called final rolling, which, unlike the previous methods, takes place at a lower temperature. The application of a final strain below T_{nr} , results in deformation of the austenite structure. The grains become elongated and flattened. While combined with the structure defects (dislocations, misalignments) inside the grains created by deformation, the surface area of the privileged nucleation sites during the phase transformations that occur during the cooling of the processed material increases. As a result, the introduction of final rolling results in additional refinement of the final structure [22–24].

Thermomechanically-controlled rolling (TMCP) (Fig. 3 – 4)

The next step in the development of thermo-mechanical processes is the documentation of dynamic structure restoration processes, which, unlike static processes, occur during the infliction of strain. No incubation time is required between stages. A sufficiently large strain inflicted in a single pass or accumulated in several runs is the most important factor for the occurrence of recovery and/or dynamic recrystallization processes. Lower process temperature and fewer rolling stages are the advantages of this

type of solution, which finds economic justification by reducing production costs [22–24]. However, in this case, the structure of the material has a substructure in which the strain energy is still stored. Thus, static processes can occur in the material if it is subjected to further isothermal reheating or slow cooling. For this reason, accelerated cooling is generally used to ensure that the desired phase transformations occur, which leads to a refined final structure. Fig. 4 illustrates the differences between α -phase nucleation sites for conventional and TMCP rolling.





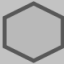

	Conventional hot rolling	TMCP
γ grain structure		
Nucleation of α grain		
α grain structure		

Fig. 4. Differences between α nucleation sites when for conventional rolling and TMCP [24].

In recent years, additional modifications to rolling processes have emerged involving the addition of further stages immediately after accelerated cooling. An example of such a process compared to the conventional process is shown in Fig. 5. In this case, intensive induction heating is used, which introduces online heat treatment (HOP - online heat-treatment process) followed by slow air cooling. This treatment causes diffusion of C into austenite and tempering of bainite in the structure. After slow cooling, the material is mainly characterized by a bainitic structure with islands of martensite [26].

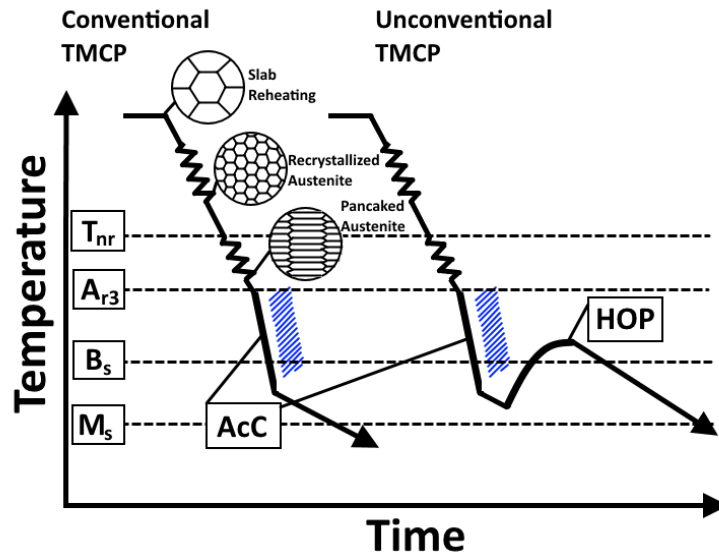


Fig. 5 Schematic illustration of TMCP diagram for ‘conventional’ vs. ‘unconventional’ processing [26].

Bars can be produced by two types of rolling: conventional and thermomechanical. Conventional rolling of bars relies on sequential reduction of the cross-sectional area to obtain required dimensions. During the process, the material subjected to rolling is usually plastically deformed by the compressive force, applied by a set of rolls and it depends on calibration. Multiple stages are involved during the production of bars, mainly: initial heating, roughing, intermediate rolling, finishing, quenching and self-tempering. On the whole, the bars are cooled in still air. Schematic stepwise reduction during rolling is shown in Fig. 6 [27].

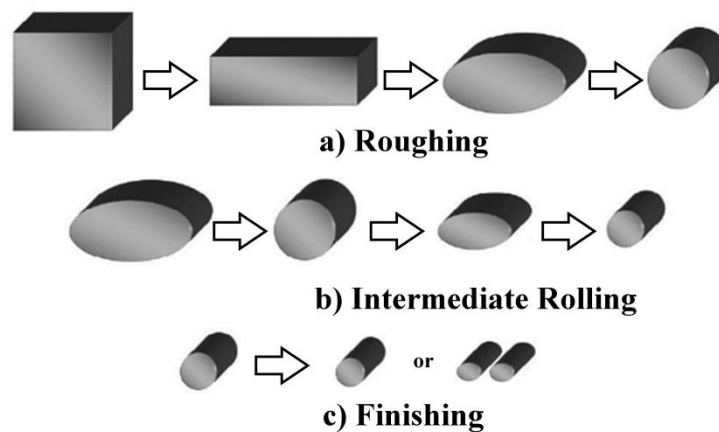


Fig. 6. Systematic stepwise reduction of the treated material during rolling; a) Roughing, b) Intermediate rolling and c) Finishing [27].

Bar rolling is mostly achieved by two rolls for each step, until the required diameter of the bar is obtained. An arrangement of rolls is schematically illustrated in Fig. 7 [28]. As it can be seen, the rolls at every subsequent step of the rolling process are rotated by a 90° angle, therefore vertical and horizontal rolls can be distinguished. Due to the reduction of the cross-section area of the bar, its velocity after passing through the rolls is higher than before the rolling. It is presented in Fig. 8 [29]. Therefore, two types of strain path in reference to bar rolling can be distinguished, which is described in Fig. 9 [30].

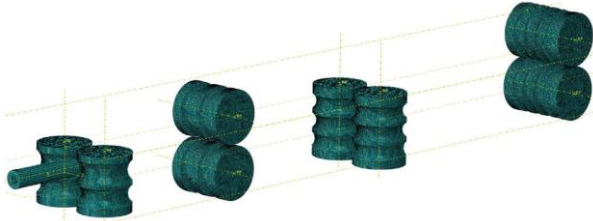


Fig. 7. Scheme of round bar hot rolling process [28].

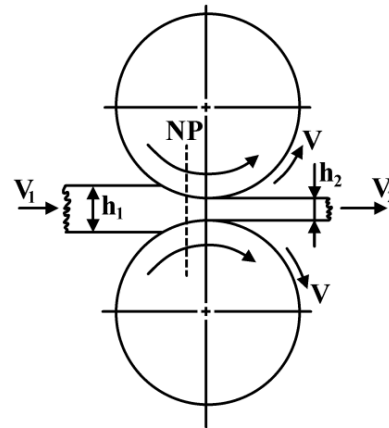


Fig. 8. Schematic representation of the rolling gap in hot rolling of a bar, in which h_1 is the entry thickness and h_2 the exit thickness of the bar. Due to cross-section area reduction, the bar exit velocity V_2 is higher than the entry velocity V_1 . The line NP represents the neutral plane, at which the contact pressure between roll and bar reaches a maximum and the roll and bar surfaces have the same velocity V [29].

Unlike in rolling of flat products, the deformation inflicted during bar rolling changes with the alignment of the rollers. During sheet rolling, the strain is inflicted in one direction (X) due to the use of horizontal rollers in each pass of the workpiece material. The difference in the geometry of the manufactured products results in the use of a sequence of vertical rollers and horizontal rollers in the bar rolling process. For this reason, deformation takes place in 2 axes: X and Y (Fig. 9).

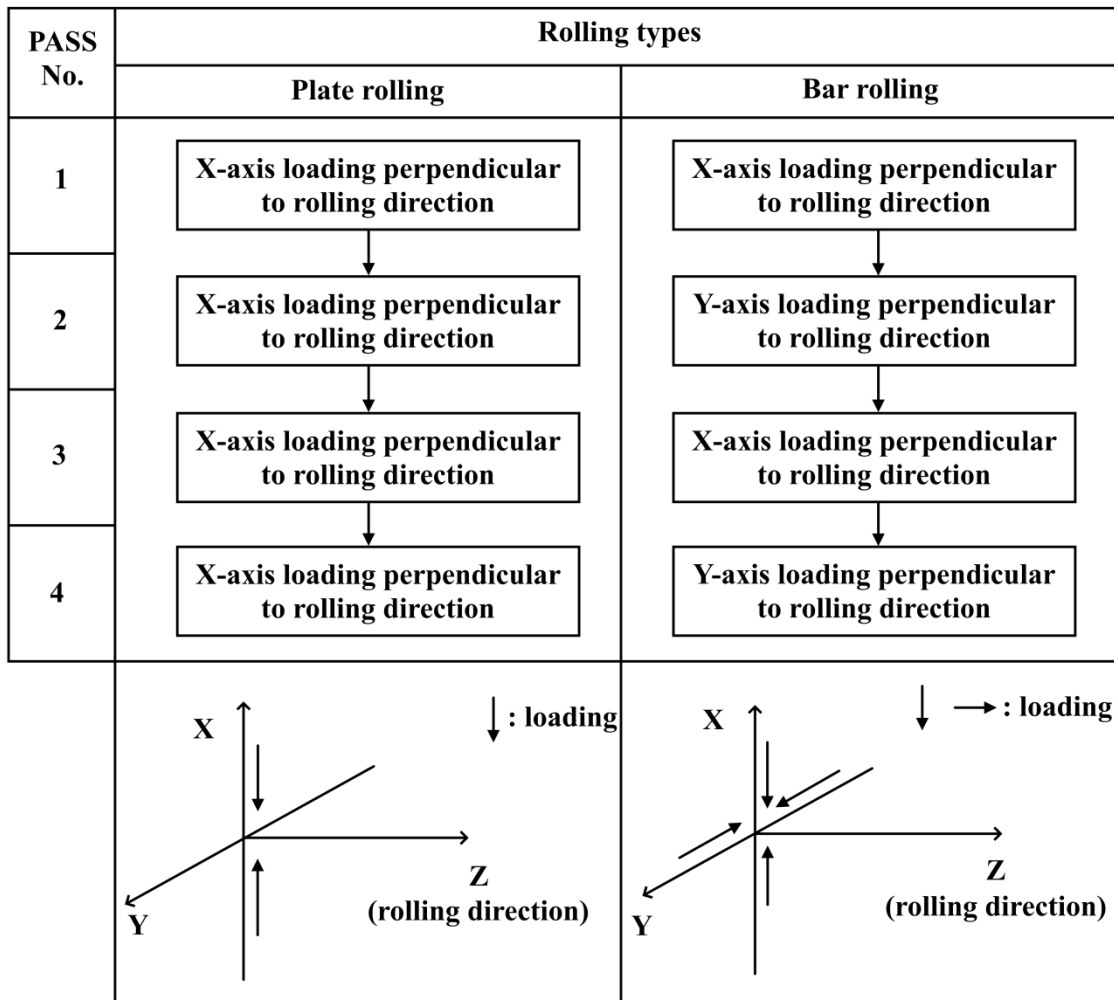


Fig. 9. Schematic diagram for the change of strain path in the rolling types [30].

Cross rolling, particularly one of this kind which is defined by its authors as a separate way called radial-displacement rolling (RDR) is another method to receive long products with significant changes in microstructure and mechanical properties that should be noted [31]. In the process, heating is realized by induction heating. The deformation in the radial-displacement rolling stand to a predefined final diameter is realized with 3 cone-shaped rolls that are offset by 120° . The specific feature of that combination of rolls is that the deformation takes place over very small contact surfaces between roll and rolling blank. High Deformation Radial-Displacement Cross Rolling (HDCR) stand, in the process rolling forces in the deformed area are at a low level and simultaneously high reductions are obtained. The deformation value increases continuously because the space between the rolls decreases when the material goes through the rolls, a high reduction rate is obtained in one pass. Furthermore, the rolls can be axially adjusted, so it is possible to roll different diameters within a wide dimensional range. Less than 0.5 % tolerances for the produced diameters tolerances and ovalities over the bar length can be obtained by

the HDCR. The final diameter of the produced bars is defined before the process starts, when the spacing of the rolls is set. The grain size and structure are controlled by recrystallization induced by the deformation rate and the temperature in this one pass of the material. After the deformation, the steel bar passes through the accelerate cooling section [32–37]. Similarly to the conventional rolling systems, the structure of the long products can be subsequently tempered.

Due to the specific arrangement of the rolls, three trajectory-oriented elements and the kind of metal structure processing can be determined during radial-displacement rolling (Fig. 10).

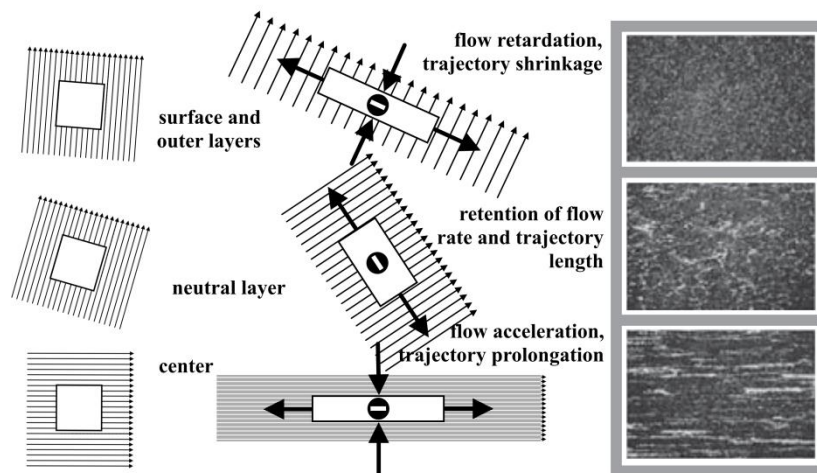


Fig. 10. Forming of trajectory-oriented elements during radial-displacement rolling and the kind of metal structure processing [31].

Accordingly, the trajectory-velocity result of rolling varies as well, acquiring the character of the specific non-uniformity [31]. The outer layers undergo metal flow slowdown and the central layers do acceleration. Every small trajectory-oriented element of the outer layer is subject to compression deformation along the billet radius, compression deformation in the line of movement (along the helical trajectory), and consequently tensile deformation across the helical trajectory. In case of stationary flow of incompressible material, the decrease of the outer layer particle movement velocity is necessitated with the formation of expandable metal flow tubes (diffusers). The elements of metal structure, which are subject to expandable flow with two-sided upset (along the trajectory and the radius), assume the shape of isolated isotropic particles with high dispersion ability [31]. Particle velocity in the axial fiber and its length increases proportionally to the reduction in a similar manner to lengthwise rolling. The section of central flow tubes decreases. Treatment of the metal structure is carried out by

longitudinal groove rolling with multilateral reduction or pressing. The elements of metal structure are stretched and thinned with formation of structurally banded orientation. Thus, the method allows to produce rolled products with an isotropic outer layer and a fibrous inner layer finely dispersed down to a submicro-crystalline level. Such a structural state can be classified as naturally composite layered one [31,38,39]. Furthermore, with the HDQT (High Deformation Quenching and Tempering) process, different mechanisms for grain refinement may be used (Fig. 11). The first one is made possible by the activation of a dynamic recrystallization processes in the range above the recrystallization temperature (1) after surpassing a critical deformation. After exiting the stand, an equiaxial fine-grained dynamically recrystallized structure is obtained in this case. A deformation below the recrystallization temperature (2), but still above A_{c3} , leads to the formation of deformed austenite grains that transform into a fine acicular martensite or austempered structure. Due to this, grain refinement is achieved by the formation of a refined substructure of the material [31].

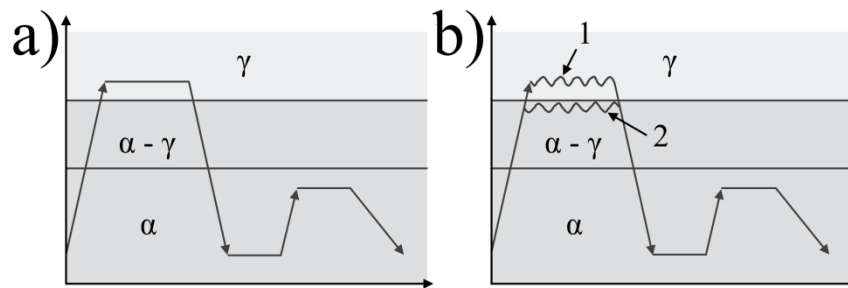


Fig. 11. Scheme of a) conventional and b) HDQT heat treatment [31].

An additional beneficial effect is based on the torsional, partially compressive and tensile forming pattern of radial-displacement rolling, which results in a spiral crystalline structure (texture) or structure weave as a result of the molding process, and thus the rolled products exhibit special properties during torsional loading. Furthermore, the development of a very fine-grained structure can be observed particularly near the surface [31,38,39].

Xtreme Performance Technology (XTP) is a one-step high strain bar rolling technology. The process allows to produce bars with a diameter of 18 - 40 mm. A diagram of such a line, located at Steeltec, is shown in Fig. 12. Heating up to the austenitizing temperature is done inductively. The number of induction coils in the heating section can be changed, so the austenitizing temperature (T_A) can be controlled. However, the process has some limitations in this regard, namely a low austenitizing temperature possible to achieve and a short heating time. The rolling temperature (T_R) can be controlled by slow

cooling in air while the material is being transported on the line, or cooling can be accelerated with an air jet. Thus, despite the continuity of the process, T_R can be independent of T_A . Deformation is inflicted using three rollers in a $3 \times 120^\circ$ arrangement (Fig. 13). The degree of deformation is controlled by changing the distance between them, which ensures the reciprocating motion of each roller. At the same time, the diameter of the bars produced is adjusted by means of roller settings. After rolling, the temperature is measured (T_1), and then there is a cooling section with 4 places for cooling boxes. Depending on the number of boxes and water output, the cooling rate can be controlled and the temperature after cooling (T_2) can be controlled. Further cooling from T_2 is done in air. Therefore, depending on T_2 , which may be within the tempering range, self-tempering can occur in the bar volume. The process parameters can be controlled separately, but the velocity of the line affects the temperature achieved in all stages of the process simultaneously. Therefore, although the temperature can be adjusted at each stage, calibration of the line to the required values is a complicated process.

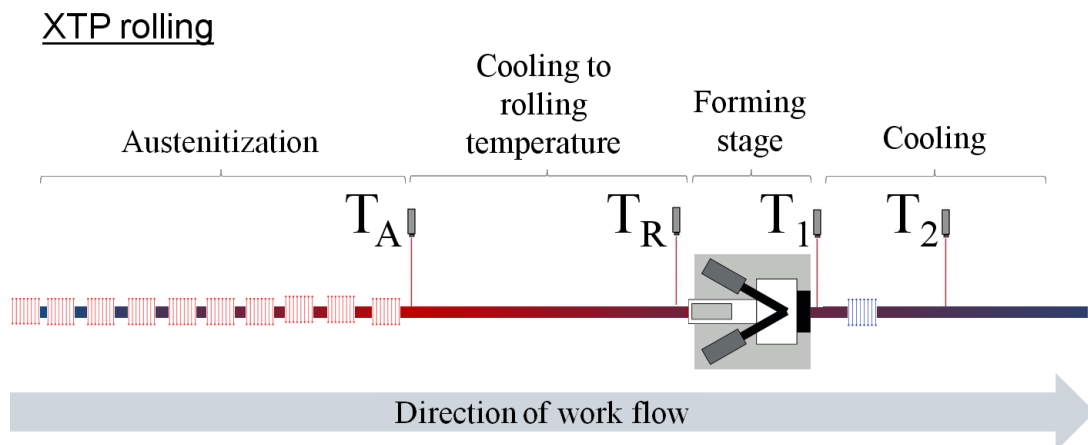


Fig. 12. Scheme of the XTP line with characteristic temperatures [37].

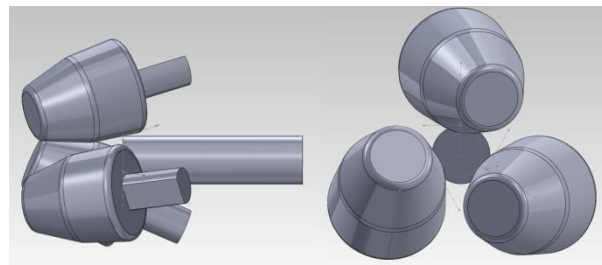


Fig. 13. Scheme of the $3 \times 120^\circ$ system of the rolls.

Three-roll bar rolling technology is a well-known technology and is encountered in the literature under various names, e.g. radial-displacement rolling or cross-helical rolling. The principle of bar production is similar to the XTP process carried out at the Swiss Steel company. Despite common knowledge of this type of material processing,

there is little knowledge in the literature on the rolling of steel with bainitic structure. Some of the first works were carried out as a result of cooperation between Steeltec and Swiss Steel while using 7MnB8 steel [14]. Earlier studies by P. Galkin et al. mainly presented the assumptions and characteristics of the process taking into account the structural changes occurring in the workpiece materials such as ferritic-pearlitic steel and 54SiCr6 spring steel [31]. Subsequent work has focused on steels with higher chromium content, such as 40X and AISI-321 steel or copper [38,39], as well as D16 or 6005 aluminum alloy [40,41] A common feature of the works conducted by the teams of researchers was to conduct deformation in several passes through the rollers. All research results focused on the phenomenon of cumulative deformation on the surface of the fabricated rods, leading to a large grain size (~ 300 - 900 nm) in this region of the rod, which provides an increase in the strength of the components manufactured.

2.2. Strengthening and softening of austenite during forming

During thermomechanical treatment, the workpiece is affected by two factors: deformation and temperature. The nature of the process and the phenomena associated with it depend on the temperature. During deformation, material strengthening occurs through mechanisms related to structural features, which we can include mechanisms such as [42–45]:

- solid solution strengthening (σ_{ss})
- dislocation strengthening (σ_d)
- precipitation strengthening (σ_p)
- grains size strengthening (σ_{gs})
- strengthening by second phase (σ_{sp})

Therefore, the strength of the material is a result of all obtained strengthening mechanisms, where σ_0 is intrinsic strength of ferritic iron:

$$\sigma = \sigma_0 + \Delta\sigma_{ss} + \Delta\sigma_d + \Delta\sigma_p + \Delta\sigma_{gs} + \Delta\sigma_{sp} \quad (4)$$

Solid solution strengthening is caused by the presence of alloy additives in the crystal lattice of the matrix, which causes strengthening. The basic formula for determination of σ_{ss} includes the strengthening factor A_i for 1.0 wt. % of the element [43]:

$$\Delta\sigma_{ss} = \sum A_i \cdot wt.\% \quad (5)$$

With regard to dislocations, a significant role is played by the so-called dislocation density. As it increases, the strength of the material also increases due to impeded

movement and the formation of new dislocations. The relationship of strength increase and dislocation density is described by [43,46,47]:

$$\Delta\sigma_d = \beta Gb(\rho)^{1/2} \quad (6)$$

where $\Delta\sigma$ = the increase in yield strength, β = constant, b = Burgers vector, G = shear modulus and ρ = dislocation strengthening.

Precipitation strengthening mechanism relies on the interaction of moving dislocation with precipitations, located in a relatively soft matrix. Depending on crystallographic correlation of matrix and precipitation, two types of particles can be characterized: coherent and incoherent. As it was shown in Fig. 14 and Fig. 15, crystallographic planes of coherent precipitation form a definite relationship between its planes, and the planes of the matrix (Fig. 14a and 15a). However, incoherent precipitations have no relationship with the crystallographic structure of the matrix (Fig. 14b and 15b). Fig. 16. presents the TEM investigations of some example coherent and incoherent precipitations, where the electron diffraction pattern from the coherent precipitation contains visible spots belonging to the precipitation and to the matrix, whereas from incoherent precipitation, only the precipitation's spots are visible.



Fig. 14. Two types of particles depending on crystallographic correlation of matrix and precipitation: a) coherent - with relationship between the crystallographic planes, b) incoherent - no relationship with the crystallographic planes.

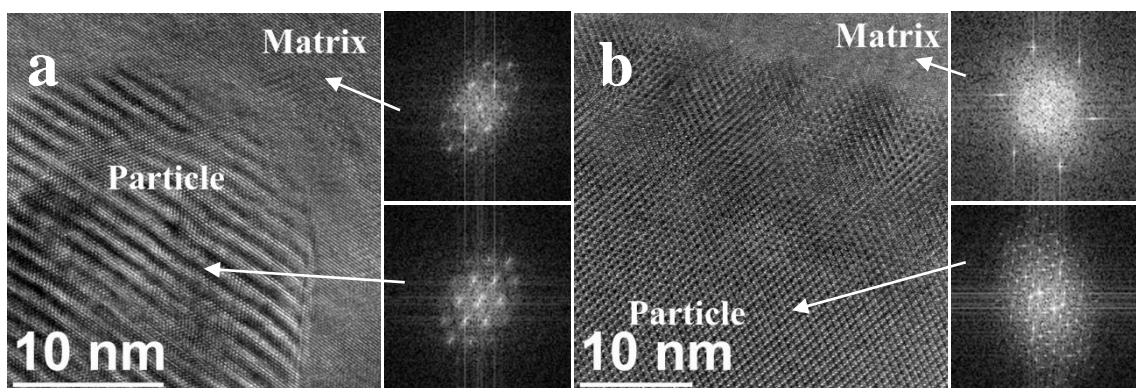


Fig. 15. HRTEM of the: a) coherent precipitation, b) incoherent precipitation, with FFT from matrix and particle areas, P92 steel, own research within [48].

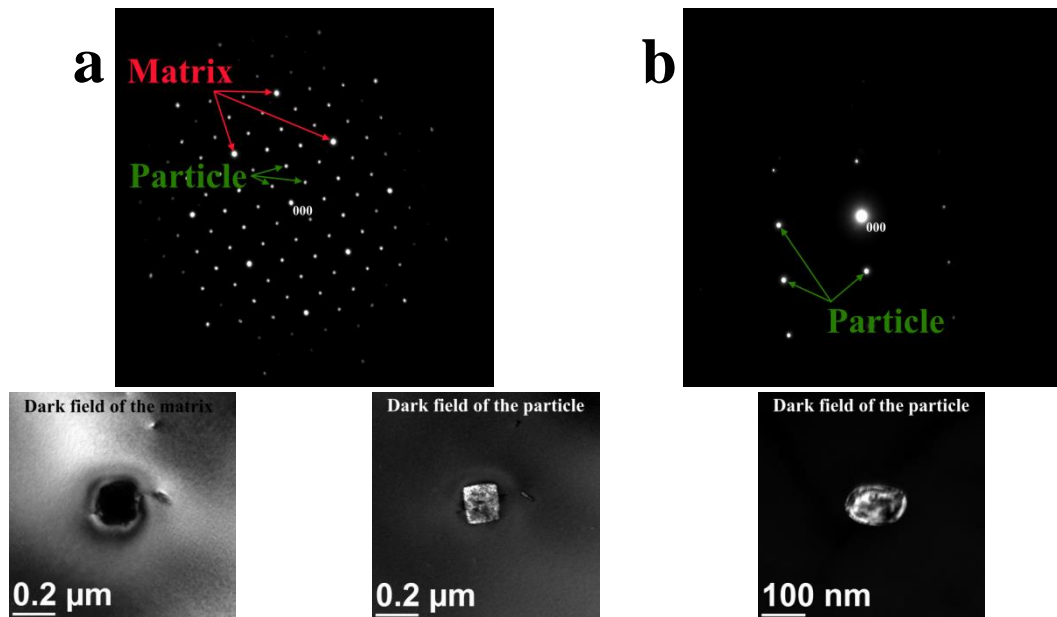


Fig. 16. Electron diffraction patterns from: a) coherent, b) incoherent particles with dark field images, HR3C steel, own research within [49].

Depending on the crystallographic precipitation/matrix relation, different strengthening mechanisms occur. When a moving dislocation encounters a coherent particle on its way, it cuts through the particle, i.e. the dislocation passes through the precipitation on the same slip plane as in the matrix. This is shown schematically in Fig. 17. However, with increasing particle size, shearing of the coherent precipitation becomes more difficult. For this reason, there is a critical particle size beyond which a second amplification mechanism occurs [50,51]. The dependence on the particle size and strength increment is shown in Fig. 18. As it can be seen, after the coherent precipitation size reaches specific value, a critical radius above which the particle loses coherence with the matrix, the second operative mechanism occurs, which is the Orowan mechanism.

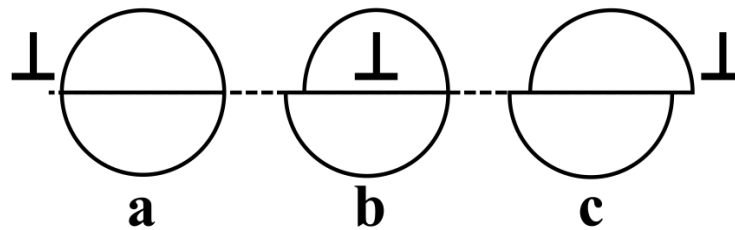


Fig. 17. Schematic illustration of subsequent phases of the strengthening mechanism due to shearing [52].

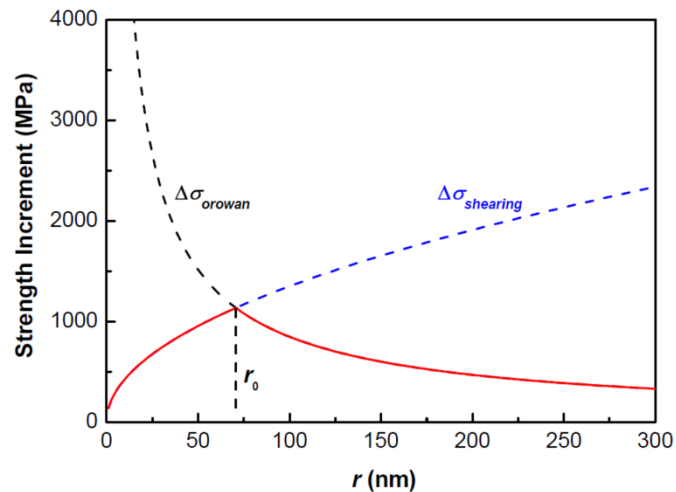


Fig. 18. The variation tendency of yield strength increment with the particle size [50,53], in which the strength increments caused by dislocation shearing mechanism ($\Delta\sigma_{\text{shearing}}$) and Orowan mechanism ($\Delta\sigma_{\text{Orowan}}$) are shown, and the maximum increment reaches at a critical particle size r_0 .

The same mechanism occurs when incoherent particles are present in the matrix. It was discovered in 1934 and is explained by impenetrable precipitates in the matrix that interrupt dislocation migration and thus cause plastic deformation via interaction with dislocations, which results in an increase in the matrix strength [54,55]. Fig. 19 shows a schematic illustration of the Orowan mechanism. At the first stage, moving dislocation meets a hard phase (precipitation) and starts interacting with it. The dislocation line bends between the precipitations, entwines the particle with a continued movement, and after passing behind it a loop is left around each particle. Due to the dislocation loop on the precipitation, the movement and passing through the obstacle of the next dislocation is hindered. In Fig. 20, TEM bright field images of materials with different structure are shown. Fig. 20a is a material where dislocation can readily move, while in Fig. 20b the obstacles as precipitations initialize the Orowan mechanism.

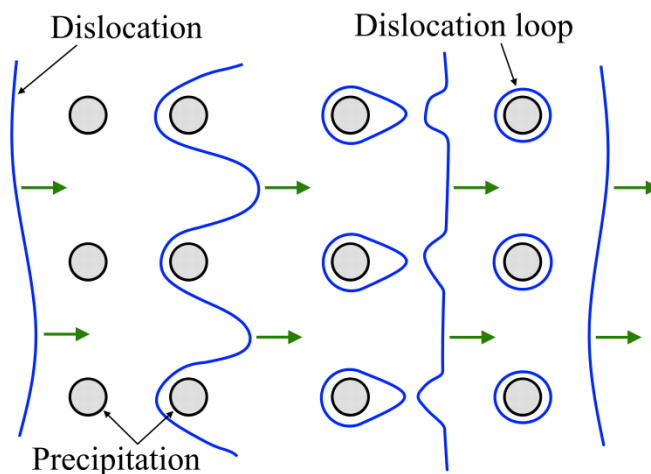


Fig. 19. Scheme of the Orowan mechanism [53,54].

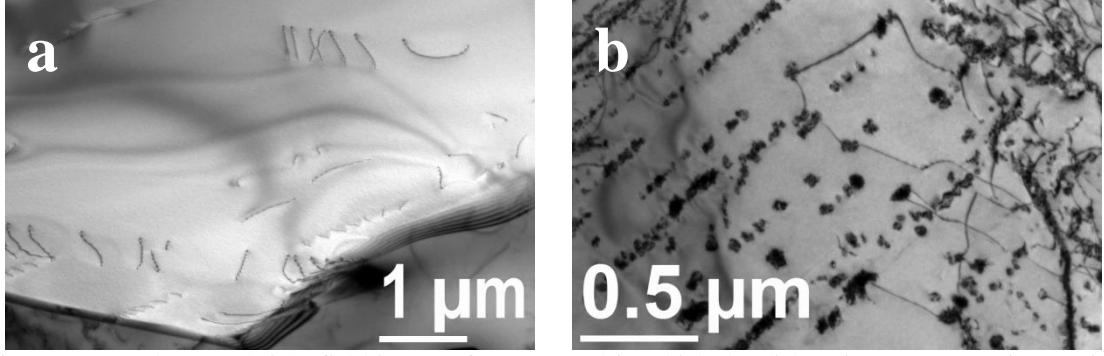


Fig. 20. Example TEM bright field image of HR3C steel in which the dislocation movement is: a) with freely dislocation movement, b) dislocation movement limited by precipitations, own research within [49].

Thus, the mechanism of strengthening caused by the presence of fine precipitations involves their interaction with dislocations. The lattice of precipitates present in the material acts as obstacles for the dislocations to move. There are two types of precipitation/dislocation interactions. Therefore, the mathematical equations specifying the increase of yield strength based on the shearing ($\sigma_{Shearing}$) and Orowan (σ_{Orowan}) mechanisms were developed. Preparation of new chemical compositions of the steels, complemented by the ability to predict the mechanical properties of a material, allows to provide the continuously increasing utility requirements from the new materials [56,57]:

$$\sigma_{Shearing} = \frac{2 \times 1.1}{\sqrt{2AG}} \times \frac{y^2}{b^2} \times d^{\frac{3}{2}} f^{\frac{1}{2}} \quad (7)$$

$$\sigma_{Orowan} = \frac{0.3728Gb}{K} \frac{f^{\frac{1}{2}}}{d} \ln\left(\frac{1.2d}{2b}\right) \quad (8)$$

where:

G - the shear modulus; $A = \frac{1}{2\pi K} \ln\left(\frac{d}{2b}\right)$ - the dislocation line tension function;

K - related to the type of dislocation and Poisson's ratio ν of the material, while: $K = 1$

for screw dislocation, $K = (1-\nu)$ for edge type dislocation, and $\frac{1}{K} = \frac{1}{2} \left(1 + \frac{1}{1-\nu}\right)$ for

mixed type dislocation; b - the absolute value of the Burgess vector for dislocation; d - the second-phase particle diameter in μm ; f - the volume percentage.

Grain refinement is a widely understood mechanism for strengthening steels and alloys. It is the only mechanism for which an improvement in material strength is observed without significant loss of properties such as toughness and ductility [42,58–62]. The effect of grain size on yield strength is described by the Hall-Petch equation (9).

$$\sigma_y = \sigma_0 + k\sqrt{d} \quad (9)$$

where σ_y is the yield stress, σ_0 is the lattice friction stress, which includes contributions from solutes and particles but not from dislocations, i.e. σ_0 is the flow stress of an undeformed single crystal oriented for multiple slip or approximately the yield stress of a very coarse-grained, untextured polycrystal [63]. k is a quantity that characterizes the transfer of slips through the grain boundaries and d is the mean grain size [58].

In the case of the dual-phase ferritic-martensitic steel, the strengthening of the material is also affected by the contribution of the strengthening component, in this case the M/A islands in the structure, whose contribution to the strengthening of the material can be determined from the formula [44,64]:

$$\Delta\sigma_{MA} = 900 f_{MA} \quad (10)$$

where f_{MA} is the volume fraction of M/A islands.

During thermomechanical processing, which is achieved through hot deformation, the processes involved in the recovery and recrystallization of the material result in the restoration of the deformed structure state. During rolling, each pass of the material through the rollers is characterized by a series of variable process parameters such as temperature, set strain, strain rate, strain history and time between operations. These parameters, combined with the characteristics of the material being machined, i.e. the chemical composition and initial grain size, determine the final grain size and shape obtained in the structure reconstruction processes. During steel processing in thermomechanical processes, deformation is carried out at an elevated temperature, in the austenite region, which, depending on the temperature used, can be in a stable or unstable state. Austenite can strengthen through straining, undergo dynamic recovery and dynamic recrystallization during its deformation. When considering austenite in terms of the microstructure obtained during thermomechanical processing, variables such as the following should be taken into account: strain (ε), strain rate ($\dot{\varepsilon}$), grain size in the initial state, flow stress or Zener-Holomon parameter (Z). The last Z -parameter depends on the temperature and the strain rate and is expressed by the formula [25]:

$$Z = \dot{\varepsilon} \exp(Q/RT) \quad (11)$$

where $\dot{\varepsilon}$ - strain rate [s^{-1}], Q – activation energy [$J \cdot mol^{-1}$] for plastic deformation, R - gas constant ($R = 8.314 J \cdot mol^{-1} K^{-1}$) and T - temperature [$^{\circ}C$]. In addition, the following formula is used to determine flow stress [25]:

$$\sigma = \frac{1}{\alpha} \ln \left\{ \left(\frac{Z}{A} \right)^{1/n} + \left[\left(\frac{Z}{A} \right)^{2/n} + 1 \right]^{1/2} \right\} \quad (12)$$

σ is the flow stress (MPa), A , n_1 , α , n , and β ($\beta = \alpha n_1$) are the material constants.

Hardening-softening behavior of the material can be divided into three stages, which are applied depending on the strain (Fig. 21). In the initial phase of hot deformation, the processes occurring in the deformed material are dominated by work hardening of the material, until the deformation ε_c is reached. This happens due to an increase in the density of dislocations, their spreading and interaction in the material. In such conditions, between rolling stages, static recrystallization can occur in unstable austenite, which has a regime of strain rate, elevated temperature and adequate incubation time for it to occur. However, when, for example, the degree of strain is too small, then only recovery processes can occur in such a material. Thus, this type of deformation course is dominated by work hardening over the softening mechanisms, and the true stress grows linearly. Further deformation causes the accumulated energy in the material to increase. Work hardening, is an option that manifests itself during cold deformation. The other two are typical of hot deformation. In combination with thermal activation energy, the hardening-softening ratio is changed. Hardening is initially compensated for by the recovery processes. The dynamic recovery is enhanced by the combination and recombination of dislocations. As a result, the true stress curve flattens out. If the strengthening of the material is below the required level, when the critical stress σ_c is reached, the driving force for nucleation in the dynamic recrystallization process may be insufficient. In this case, only dynamic recovery occurs, and the true stress remains unchanged after reaching its maximum value at the point of σ_p . Otherwise, when the dislocation density is at the right level, nucleation of new grains with initially low dislocation density in the process of dynamic recrystallization becomes possible. Moreover, with favorable conditions, the dynamic recrystallization can predominate the effect of work hardening [23,25,65–67]. Therefore, after reaching the maximum point σ_p , the true stress decreases and the curve waveform has the characteristics of the red line in Fig. 21.

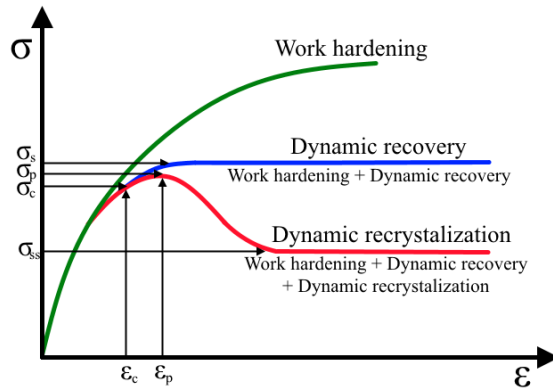


Fig. 21. Dynamic recovery and dynamic recrystallization type stress-strain curves [25].

An example of the recrystallization process during hot rolling is shown on Fig. 22. The microstructure before rolling is characterized by large austenite grains (2). Further on, the deformed grains become elongated into a pancaked structure, due to the passage of the material through the rollers. Thus, there is a change in the dimensions of the grains, and the structure becomes pancaked. In addition, deformation bands are induced in the grain structure and the dislocation density increases (3). In the example shown, the first pass through the rollers is followed by work hardening of the material. After an appropriate incubation time, static recrystallization occurs in the structure (4). During hot rolling, this period is very short. At the next point (5), the structure is recrystallized and grain growth occurs (6). The material then passes through the next roller system, where dynamic recrystallization is initiated due to the operating parameters in the material. At this stage of the process, recrystallization of the structure takes place at the same time as the deformation, dynamic processes take place (7). The final microstructure is characterized by an even finer grain size when compared to the previous state (8) [65].

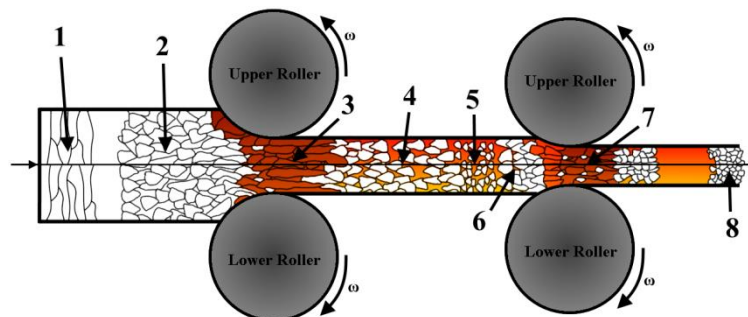


Fig. 22. Recrystallization during the hot rolling process: (1) Ingot with non-uniform grains, (2) Coarse equiaxed grains, (3) pancaking (grains elongated), (4) Static recrystallization, (5) Complete recrystallization, (6) Grain growth, (7) Dynamic recrystallization, (8) Complete recrystallization with finer grains [65].

Changes in the proportion of recrystallized structure over time can be determined using the equation [20]:

$$X_d = 1 - \left[-k \left(\frac{\varepsilon - a\varepsilon_p}{\varepsilon_p} \right)^{m'} \right] \quad (13)$$

$\varepsilon > a\varepsilon_p$

where X_d - the recrystallized fraction, k and m' are coefficients with values between $0 < k < 1$ and $1 < m' < 2$, $a\varepsilon_p$ - strain above the strain at which dynamic recrystallization begins. The grain size of recrystallized austenite is determined by the following equation [20]:

$$D_d = 38.26 \left(\frac{Z}{A} \right)^{-0.08} \quad (14)$$

where Z is Zener-Hollomon parameter and A is chemical composition of the austenite.

2.3. The role of alloying elements in steel

In the industry, there are many types of steels, depending on chemical composition and microstructure, which strictly condition mechanical properties and application possibilities. Moreover, alloying elements, as well as impurities, may form new phases in the material and can be incorporated into the crystal structure of basic phases like austenite (A), ferrite or cementite. If the additional element atom is similar in size to the iron atom, its incorporation to the crystal structure is easier. It is done by replacement of the iron atoms in the crystal lattice. However, sometimes the atoms go into interstitial sites if they are significantly smaller than iron, as for example nitrogen. Effects of individual alloying elements on the microstructure are different, which provides the possibility of shaping the microstructure already at the casting stage of producing. Basic division is made according to the stabilized phase by the introduced element. Some of the elements present in steels are A stabilizers like, for instance, Mn and Ni [68–70], and some are ferrite stabilizers like Si and Cr. Other elements, like Ti, Nb, Mo, and V are strong carbide formers, if present in sufficient quantity [71–75].

Considerations about alloying elements ensuring grain refinement have to be started from their solubility in the solid solution. The concept of solubility of elements was well known and described as early as in 1963 by E. Hornbogen, among others [76]. Based on this, binary systems where precipitations inhibiting grain growth can be predicted, where the solubility decreases with decreasing temperature. Basically, the ability to dissolve the

alloying elements in alpha iron is based on the atomic size ratio of the solute and solvent and also on chemical similarity. Furthermore, the atomic size ratio determines the place in the crystallographic structure, which the addition atom assumes. According to it, the atoms having smaller atomic size than iron, will occupy octahedral and tetrahedral gaps in solid solution. B, C and N can be included in that type. When atomic sizes are similar, the substitutional solid solution is obtained and the addition atoms replace iron in the crystallographic lattice. Elements with greater atomic size are the last group. This group of elements shows no measurable solubility in alpha iron. The character of the elements in reference to their solubility is presented in Fig. 23. Here, only the elements which could precipitate from substitutional solid solutions will be considered (marked as 2 in Fig. 23). The chosen group can be additionally limited, because of decreasing solubility of the elements with decreasing temperature. In principle, this phenomenon forces creating new phases in the structure, based on the elements the content of which exceeds the level of their solubility at a given temperature. In Fig. 24, the elements with decreasing solubility as the temperature decreases are marked as "A".

H 1																		He 3
Li 3	Be 2											B 1	C 1	N 1	O 3	F 3	Ne 3	
Na 3	Mg 3											Al 2	Si 2	P 2	Se 3	Cl 3	Ar 3	
K 3	Ca 3	Sc ?	Ti 2	V 2	Cr 2	Mn 2	Fe 2	Co 2	Ni 2	Cu 2	Zn 2	Ga 2	Ge 2	As 2	Se 3	Br 3	Kr 3	
Rb 3	Sr 3	Y 3	Zr 2	Nb 2	Mo 2	Tc 2	Ru 2	Rh 2	Pd 2	Ag 3	Cd 3	In 3	Sn 2	Sb 2	Te 3	I 3	Xe 3	
Cs 3	Ba 3	La 3	Hf ?	Ta 2	W 2	Re 2	Os 2	Ir 2	Pt 2	Au 2	Hg 3	Tl 3	Pb 3	Bi 3	Po 3	At 3	Rn 3	

Fig. 23. Solid solution behavior of the elements in alpha iron: 1 - interstitial solid solution, 2 - substitutional solid solution, 3 - no solubility in solid solution [76].

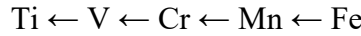
In Fig. 24, the elements of interest are marked because of their precipitation processes, which will be discussed in the next part. Despite the influence of the atomic size ratio, another feature allowing the creation of carbides by elements has to be mentioned. Wesołowski writes in his work that in steel, carbides can precipitate while accompanied by those elements which on every energy level have d sublayers, with fewer electrons than iron [77].

										Al A/C	Si A/C	P A
Ti A	V A	Cr A	Mn B	Fe	Co B/C	Ni B	Cu A	Zn A	Ga A/C	Ge A	As A	
Zr A	Nb A	Mo A	Tc B	Ru B/C	Rh B/C	Pd B/C						

Fig. 24. Selected substitutional solid solubility in alpha iron: A - decreasing solubility with decreasing temperature, B - complete sequence of alpha and/or gamma solid solutions, C - ordering [76].

Moreover, the lower the number of electrons an element has on the d sublayer, the greater its ability to form carbides and the more stable its carbides are. In Fig. 25, the energy state and the size of the atomic radius of chosen elements is given. According to the rule, the stability of the elements carbides increases in the following directions:

from iron to Ti



and from Mo to zirconium



Ti $3d^24s^2$ 1.47 Å	V $3d^34s^2$ 1.35 Å	Cr $3d^54s^1$ 1.29 Å	Mn $3d^54s^2$ 1.27 Å	Fe $3d^64s^2$ 1.26 Å
Zr $4d^25s^2$ 1.58 Å	Nb $4d^45s^2$ 1.47 Å	Mo $4d^55s^1$ 1.41 Å		

Fig. 25. The energy state and the size of the atomic radius of the most important carbide formers [77].

If more than one element forming carbides is present in the alloy, carbon always has stronger affinity to the element with higher carbides forming ability. For example, if the steel has additions of Cr and Ti, the presence of the Ti carbides should be primarily expected, with Cr carbides following later. However, with higher amounts of those elements, iron carbides may not precipitate at all. Simultaneously, when comparing V with Nb, the first one has a higher energy state, thus its carbides should be expected first. However, as it can be noticed in Fig. 26, the thermal stability of V carbides is less than Nb carbides. Thus, reheating can cause dissolution of the V precipitations, so after the next steps of the process, all V can be dissolved in alpha iron. The relationship between the content of a given alloying element (wt. %) and the dissolution temperature of the precipitates occurring in 16MnNi4 steel is shown in Fig. 26. It can be seen that the

precipitation dissolution temperature depends on the concentration of elements forming the precipitations [78]. It can be seen in Fig. 27 that the stability of nitrides is usually higher than in carbides, thus the second ones are dissolved earlier and at lower temperature during reheating, with the exception of niobium which tends to form carbonitrides, Nb(C, N). The stability of the precipitates at elevated temperature has an impact on their influence on changes in the steel microstructure during subsequent process stages. However, the influence of each of the alloying elements is individual.

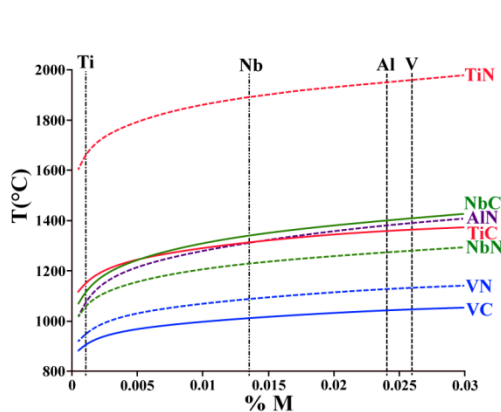


Fig. 26. The relationship between the content of the alloying element (wt. %) and the precipitation dissolution temperature in 16MnNi4 steel [78].

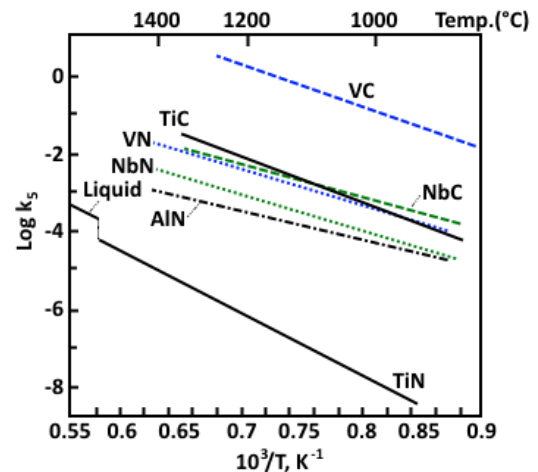


Fig. 27. Solubility products for important carbides and nitrides in A at different temperatures [79].

2.4. Influence of alloying elements on austenite grain size

During thermo-plastic processing of a material, both temperature (T_A) and holding time play an important role. Both components affect the size of the A grain, which undergoes deformation or phase transformations during cooling in subsequent process steps. In addition, the grain size is also affected by the deformation history of the workpiece, as well as its chemical composition. The research by Kvackaj et al. on the dependence of A grain size on temperature and holding time showed a very low increase in grain size when reheating at temperatures below 1000 °C. Subsequently, there was an increase between 1000 °C and 1150 °C, and an abnormal increase in grain size was observed when the temperature exceeded 1150 °C. The chemical composition of the tested steel included V and Nb additives, whose precipitates inhibit grain growth through the mechanism of the so-called pinning effect [80–85]. Carbides and temperature-stable nitrides effectively inhibit grain growth, however, above the temperature of their thermal

stability they dissolve, and the effect associated with inhibition of grain growth is lost [86–88]. In this case, Kvackaj points to the ascendancy of three temperature ranges, where the alloying additive precipitates, V and Nb, present in the steel, act simultaneously up to 1000 °C, where dissolution of the V precipitates occurs. In the 1000 - 1150 °C range, where a small increase in grain size was observed, the pinning effect is still provided in the material structure by Nb precipitates, which show stability up to 1050 - 1200 °C. When the reheating temperature was raised, the Nb precipitates also dissolve, with abnormal grain growth as a consequence [89]. The described observations are well represented by a plot of the dependence of average A grain size on temperature and reheating time, as shown in Fig. 28.

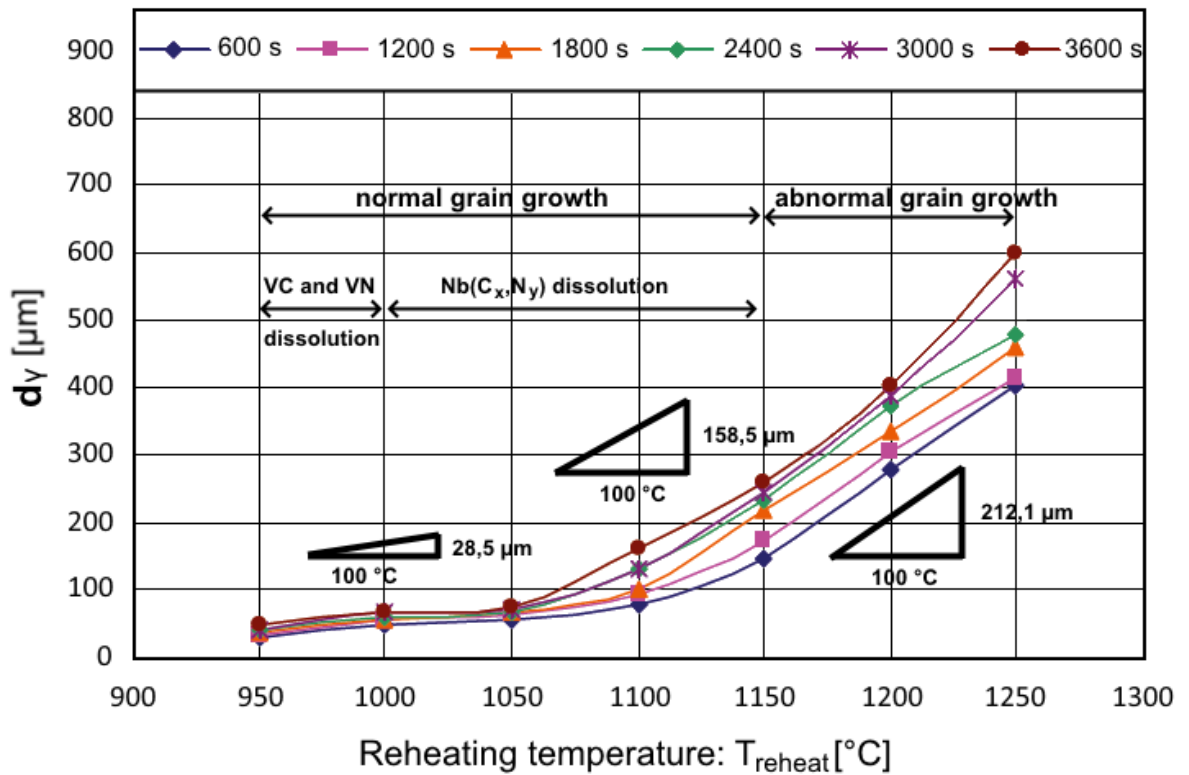


Fig. 28. Dependence of the average AGS growth on the reheating temperature and holding time [89].

It can be noted that inhibition of the A grain growth during reheating can be achieved by carbides and nitrides of alloying elements [86,90–92]. Depending on the temperature stability, the precipitates will remain undissolved in the material, leading to boundary anchoring. Thus, the higher thermal stability of the precipitates makes the use of an element to inhibit grain growth justifiable when the reheating temperature is high.

Once the recrystallization processes are complete, growth of the recrystallized grain occurs due to the increased temperature in the rolling process. The grain growth will proceed, depending on the transition time of the material to the next rolling phases,

i.e. to the next deformation. Thus, it is possible to control the interval of individual deformation operations to control grain growth, depending on the intended end result. The equation used to calculate austenite grain size changes under isothermal conditions is as follows [65]:

$$D^n = D_{rex}^n + B \cdot t_q \cdot \exp\left(-\frac{Q_{gg}}{RT}\right) \quad (15)$$

where: D_{rex} - recrystallized grain size, t_q - time, when recrystallization has completed (usually take as 95% of recrystallized grains fraction), Q_{gg} - activation energy for grain growth, n and B - material constants.

During further isothermal reheating, the recrystallized structure strives for the state with the lowest internal energy. Therefore, the grain growth of the recrystallized structure occurs, the average grain size increases, with the disappearance of small grains. As a result, the surface area of grain boundaries decreases, which at the same time lowers the value of free energy. When grain growth leads to a structure with uniform grain size, this process is called normal grain growth. On the other hand, when there is selective growth of grains that reach a significant size compared to the rest, there is also abnormal grain growth. Due to the inhomogeneity of the structure as a result of this type of grain growth, this process is undesirable, as it leads to a deterioration of the mechanical properties of a component with an inhomogeneous structure. The cause of abnormal grain growth can be a short reheating time, the presence of phases at grain boundaries that inhibit grain mobility, or the presence of texture in the structure of the material.

2.5. Phase transformation of austenite during cooling

During the cooling of steel from the re-austenitization temperature, depending on the chemical composition of the steel and the cooling rate, austenite phase transformations are possible:

- pearlitic - a transformation of a diffusive nature that occurs after a slight cooling of austenite to A_{r1} temperature. Nucleation of perlite takes place at the austenite grain boundary. There is an increase in the cementite plate, which causes a decrease in the carbon content of austenite, so that a ferrite plate is formed. Due to the limited solubility of C in ferrite, enrichment of austenite with carbon takes place at the site of the formed ferrite plate, allowing the formation of another

cementite plate. At the same time, the growth of the formed cementite plates occurs by diffusion of carbon from austenite to the face of the plates.

- martensitic - non-diffusion transformation, which occurs at a high, higher than the so-called critical, cooling rate. The beginning of the transformation begins at the M_s temperature, which happens during continuous cooling until the temperature of the end of the M_f transformation. The values of M_s and M_f are affected by the carbon content of the steel and alloying additives which, like carbon, reduce the temperature of the beginning and end of the transformation as a rule.
- bainitic - this transformation combines features of diffusion and non-diffusion transformations. It occurs in the temperature range of 500 – 250 °C, in which the diffusion of alloying elements is limited, so the content of alloying elements in bainitic ferrite corresponds to that in austenite. The difference between ferrite and bainitic ferrite lies in the concentration of carbon, the diffusion of which is possible in that temperature range. The formation of bainite begins the nucleation of ferrite with a para-equilibrium concentration. Precipitation of secondary phases between or within the grains of bainitic ferrite occurs at the expense of an increased carbon content. Depending on the structural components and their distribution in the structure, 5 characteristic morphologies of bainite can be distinguished, as shown in Fig. 29.

Ferritic, pearlitic and bainitic transformations are transformations that occur after a specific incubation time. In contrast to the martensitic transformation, which occurs at a specific overcooling state of austenite.

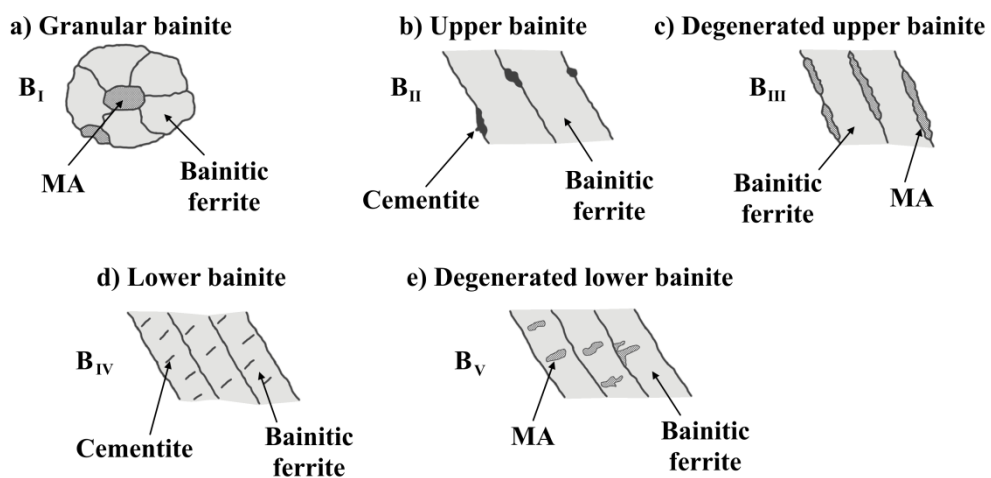


Fig. 29. Classification of morphological types of bainite in low-carbon steels [93].

The different types of bainite are transformation temperature dependent. Cooling influence on the bainite morphology described below is presented in Fig. 30.

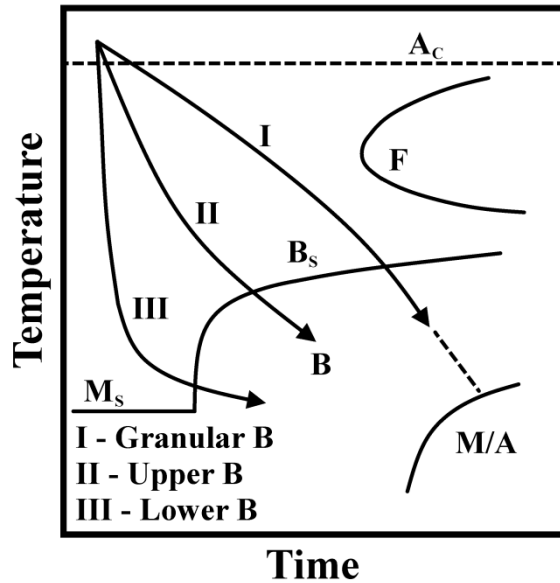


Fig. 30. Formation of various bainite morphologies [5,94–96]

- Granular bainite (GB)

The morphology of this type of bainite is characterized by irregular grain ferrite with second phases that are distributed between the grains of ferrite. Carbon from the bainitic ferrite stabilizes the retained austenite, so the phases between the ferrite grains can be any products of the transformation of carbon-rich austenite. In addition, no carbide precipitates are observed in the structure that are present in upper or lower bainite.

- Upper bainite (UB)

It has a lath-like ferrite morphology because it is the product of transformation at a lower temperature compared to GB. In the case of UB, the second phase is cementite, which is formed from carbon-enriched retained austenite. In the case of steels with micro alloying additives, the ferrite laths may contain finely dispersed carbides that provide the precipitate strengthening.

- Degenerate upper bainite (DUB)

This type of bainite is formed through alloying additives, such as Si, through inhibition of cementite precipitation. As a result, the structure contains lath ferrite and carbon-enriched retained austenite and/or martensite between the laths.

- Lower bainite (LB)

LB forms mainly in low-carbon steels and, like UB, has a lath-like ferrite morphology. As the carbon content of the steel increases, the ferrite morphology changes to lamellar.

Characteristic of this type of bainite are the precipitates of cementite, which emanate from within the laths of ferrite. The elongated cementite precipitates are inclined at an angle of $\sim 60^\circ$ to the direction of growth of the laths.

- Degenerate lower bainite (DLB)

In DLB, unlike LB, cementite precipitates are replaced by martensite/austenite (M/A) islands. It is suggested that, at high transformation rates in austenite, a carbon concentration gradient is formed causing high carbon supersaturation at the α/γ phase separation boundary. As a result, cementite precipitates at the boundary during the process of growth of transformation products, which occurs in UB. If the transformation rate decreases, then the area of the carbon gradient in austenite increases, while the supersaturation at the phase separation boundary decreases, so that the precipitation of cementite is reduced or even inhibited, in which case the remaining M/A islands present in DLB are favored.

2.6. Precipitation hardening of ferrite

Solubility of alloying additives that form carbide and/or nitride precipitates is temperature-dependent, as shown in Fig. 27. Due to the different crystal lattice structure of austenite (FCC) and ferrite (BCC), the solubility of elements in their structure differs [97]. Considering the limited solubility of alloying additives in Fe, some of the alloying additives take part in the precipitation processes, forming carbides, nitrides or carbide-nitrides in the structure of the material. The volume fraction of the precipitated particles of a given element depends on the solubility of that particle in a given phase and on the temperature of the. Fig. 32 shows the solubility of nitrides and carbides in liquid steel, austenite and ferrite. As it can be seen, the greatest thermal stability is featured by titanium nitride, the presence of which in steel is commonly used in metallurgical processes to control the austenite grain size. Due to the fact that TiN precipitates are already formed in the liquid steel, during reheating of the steel at an elevated austenitizing temperature, their presence prevents excessive austenite grain growth [98]. As the temperature is lowered, the solubility of elements in the ferrite decreases, thus promoting precipitation processes. At the same time, during reheating of the steel as part of heat or thermo-mechanical treatment processes, the limited solubility of the precipitates present in the steel and their stability temperature allow to control the structure in order to achieve the desired mechanical properties. In the first stage, reheating at the austenitizing temperature

can be guided so that the V and Nb additives bound in the carbides are dissolved. The size of the primary austenite grain will be controlled by the undissolved TiN precipitates. The dissolved Nb in the austenite during its deformation, inhibits dynamic recrystallization processes, so that in the deformation-reinforced austenite the accumulated lattice defects increases the surface area of privileged sites for phase transformation [23,24]. Accelerated cooling after deformation results in a phase transformation, and due to the increased number of crystallization nuclei of the new phase, the post-transformation structure is further refined. Moreover, the addition of V in hardened and tempered steels improves their hardenability and mechanical properties after tempering [99]. V additions present in solid solution retard the bainite transformation to lower temperatures with cooling rates in the range of 1 - 50 °C/s [100]. As a result, the refinement of the lath structure and an increase of the dislocation density caused by the addition of V is obtained in comparison to the steel without that element. Similar observations were done during the tempering process of the steel with low and increased V content. The investigations of hardness after tempering at temperature of 500 °C and 650 °C showed higher hardness values after tempering for steels with higher V content. It was noticed that by increasing V, higher dislocation densities and higher MX volume fractions were obtained after the process. Simultaneously, it was found that the majority of the strengthening was due to the higher dislocation density and increased MX precipitation strengthening in the steels with an increased V content after tempering at 500 °C and 650 °C, respectively [101].

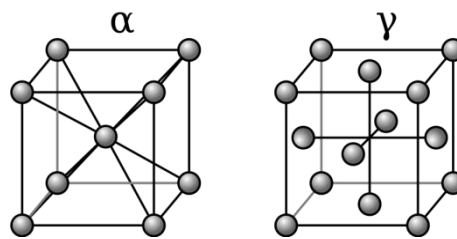


Fig. 31. Allotropes of iron; alpha iron and gamma iron [102].

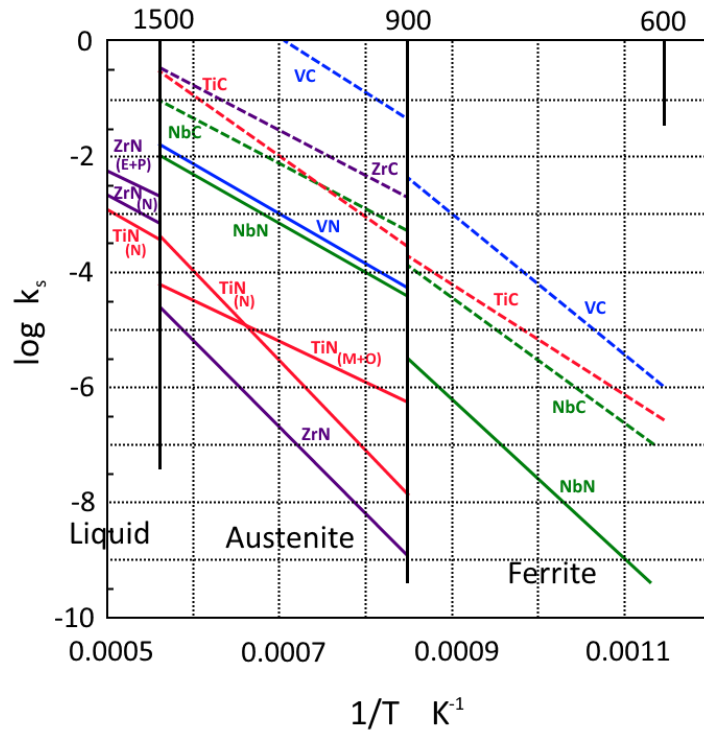


Fig. 32. Comparison of solubility products of transition metal carbides and nitrides found in micro-alloyed steel [98,103–105]

The precipitation processes occurring during the austenite-ferrite phase transformation, at the interfacial boundary, lead to the formation of a dense network of regularly spaced bands of fine precipitates in the structure of the material. This allows to improve the mechanical properties of ferritic steels with appropriate alloying additives. The basic precipitates that form such a system are carbides of elements such as Nb, Ti and V, i.e. strongly carbide-forming elements. Depending on the morphology of the precipitates or the arrangement of the carbide rows in the structure, several mechanisms can be distinguished that take place during the austenite-ferrite phase transformation, leading to the formation of this characteristic structure (Table 1).

Table 1. Models of interfacial precipitation [106,107].

Model	Mechanism
Gray Model	Carbides separate at the interfacial boundary when its movement slows down due to increased carbon concentration at the austenite-ferrite boundary. The carbide bands are parallel to the moving interfacial boundary.
Ledge Mechanism	The carbides separate at the edge plane of the ferrite-austenite interfacial boundary. The direction of movement of the boundary is parallel to the rows of carbides arranged in a straight line.
Bowling Mechanism & Quasi-ledge Mechanism	In the case of bowling mechanism, dispersive carbide precipitations are randomly generated at the interfacial boundary, characterized by high energy. At the same time, these precipitations anchor the movement of the boundary, causing it to be stressed. Quasi-ledge mechanism is a combination of bowling and ledge mechanisms which explains the cases in which carbide bands are undulated.
Eutectoid Mechanism	The mechanism of carbide release is similar to that observed during pearlite transformation.
Solute-Drag Nucleation Model	This mechanism explains the elongated morphology of the carbides observed in the bands. The longer edge of the precipitates is perpendicular to the direction of motion of the austenite-ferrite interfacial boundary, while the rows of precipitates are parallel to it.
Solute-Depletion Model	Carbides precipitate at the austenite-ferrite interfacial boundary. However, their growth takes place in slowly cooled ferrite as the interfacial boundary moves further away. An area of depletion in carbide-forming elements is formed in the ferrite, in the vicinity of the present precipitates. The direction of precipitate distribution lines is parallel to the direction of movement of the interfacial boundary.

2.7. Summary

The conducted literature review allows to define the state of the art and the possibilities of obtaining the mechanical properties directly controlled by chemical composition of the material and/or process parameters applied in the manufacturing technology. A thorough characterization of the role and influence of alloying elements commonly used in the steelmaking industry will ensure an informed selection of their type and quantity during the development of new steels in this study. In the context of grain size, elements have been defined that can form separate phases that contribute to grain refinement during heat treatment, indirectly improving mechanical properties and directly acting through strengthening mechanisms in the structure of the final material. At the same time, the dangers of impurities in steel showing a tendency to segregate were discussed, and the possibility of inhibiting this tendency by other alloying elements was pointed out. In addition, the influence of microstructure on mechanical properties was characterized on many levels. Particular focus was placed on bainite, due to its properties such as high strength with equally good ductility. The types of its morphology and the role of the structure's components present were analyzed, as well as their size, volume proportion and distribution throughout the material. From a technological point of view, the conventional bar rolling process and HDCR, their fundamentals and advantages were presented. Additionally, the parameters controlling the thermomechanical process were determined and their effect on the structure of steel was defined.

The analysis of the state of technology conducted on many levels allowed to characterize the most important variables from the point of view of obtaining a specific structure to ensure the required mechanical properties. In order to reduce the grain size of final microstructure, the deformation should be applied in the stable or just below the stable region of A. Thus, the recrystallization processes reduce the grain size which, with further cooling and transformation processes, produces very fine bainite. Furthermore, the morphology of bainite should be granular, as it results in the best combination of strength and toughness. On the other hand, the optimization of process parameters should include changes in the deformation temperature. Decreasing the temperature increases the material work hardening, so the recrystallization kinetics changes. Thus, the recrystallized volume fraction of the material can be increased, which can allow to lower the grain size after the transformation and because of this, the mechanical properties improve. Furthermore, the austenitization temperature has to be controlled to dissolve

elements in the matrix, which influences the precipitation processes. Thus, the formation of fine precipitations intensifies, leading to grain refinement. However, on the other hand, the austenitization temperature cannot be too high, because the abnormal grain growth during reheating has to be avoided. In terms to the chemical composition, a few promising selections can be specified: Mo addition to avoid the impurities segregation on the grain boundaries, Mn for hardenability increase and combining the sulfur with MnS precipitations, so Ti should not be present as Ti_2CS precipitations. Finally, selection of precipitation-forming elements like Ti, Nb and V, for grain refinement due to pinning.

The expectations from the XTP technology include additional grain fineness compared to conventional thermomechanical rolling technology, to a grain size of less than 5 μm , in addition to obtaining a favorable combination and morphology of structural components as a result of the use of accelerated cooling.

3. The aim of the study

The three-roll bar rolling technology described in chapter 2.1 is well-established and encountered in the literature under various names, e.g. radial-displacement rolling or cross-helical rolling [38–40,108,109]. The principle of bar production is similar to the XTP process carried out at the Swiss Steel company. Despite common knowledge of this type of material processing, there is little knowledge in the literature on the rolling of steel with bainitic structure. Earlier studies by P. Galkin et al. mainly presented the assumptions and characteristics of the process taking into account the structural changes occurring in the workpiece materials such as ferritic-pearlitic steel and 54SiCr6 spring steel [31]. Subsequent work has focused on steels with higher chromium content, such as 40X and AISI-321 steel or copper [38,39], as well as D16 or 6005 aluminum alloy [40,41]. In the field of single-step XTP rolling of bainitic steels, knowledge is insufficient and limited only to the first works that were carried out as a result of cooperation between Steeltec and Swiss Steel using 7MnB8 steel [14,37]. First results of bainitic steel 7MnB8 XTP are promising and show the potential of this new class of steel products [14]. As a result of research and process tests, the DBTT of -100 °C was obtained for 7MnB8 steel, with YS in the range of 425 - 644 MPa and UTS of 700 - 809 MPa, depending on the variant of the rolling process [14,37]. All the work carried out so far has focused on the phenomenon of cumulative deformation on the surface of the produced bars, leading to a large grain size (~ 300 - 900 nm) in that area of the bar, and indicates an increase in the strength of the produced parts [31,38–41]. The issues related to the effect of refinement of the bainitic structure on impact strength have not been addressed in any of the publications. In addition, these have usually been attempts to tailor the process to the steel being machined, and the process involved rolling in several passes of material through the rolls, which generates additional cost. In the single-step XTP process, the economic factor is minimized by limiting the process to a single pass where, after the bar has passed through the production line, a finished product with a gradient structure is obtained at the end, without the need for additional heat treatment or surface finishing operations on the bar.

The aim of the study assumed two steps which focused on obtaining steel with improved toughness at low temperature in comparison to conventional steels produced by the industrial partner, Swiss Steel company. The first part of the study was to determine

the process parameters to achieve the best results of toughness. The study was performed with the use of 7MnB8 industrial steel. Conducted research allows to optimize the rolling process in terms of obtaining an improvement in ductile brittle transition temperature (DBTT) at low temperatures up to $-100\text{ }^{\circ}\text{C}$, while preserving the strength properties obtained in preliminary work for 7MnB8 steel [14,37].

The second assumption was to produce new steels, which allows to maximize the effect obtained for 7MnB8 steel, in toughness context. That stage of the research comprised a selection of the chemical composition based on 7MnB8 to increase the obtained effect, achieved in the first stage of the research. For this, mainly changes in the contribution of such elements as Mn, Mo, Nb, V and Ti were assumed. The previous investigations showed the specific two-zone bars produced by the XTP process with severe cooling [14]. The first selection included an increase in the Mn content to 2.9 wt. % in comparison to 7MnB8 steel in order to increase hardenability. Thus, a more homogeneously structure should be obtained on the cross-section of the bar, so the properties will be comparable in the volume of the produced bar. Mo addition will be increased to prevent segregation of impurities like P on the grain boundaries. The positive effect of this element should be observed due to the fact, that 7MnB8 steel contains low Mo level of 0.02%. The three elements: Ti, Nb and V are strong carbide formers. The purpose of those additions to the steel is to produce very fine precipitations which, by pinning effect, will provide structure refinement. By increasing the total area of grain boundaries, it is expected to decrease in concentration of impurities on grain boundaries, so its negative influence, which causes brittle fracture, should be reduced. Moreover, by increasing the volume fraction of high angle grain boundaries (HAGB), which prevent cracking propagation, the effect should be intensified.

It is expected that the development of new steels will allow to produce new fine-grained steels with improved embrittlement resistance below $-150\text{ }^{\circ}\text{C}$.

3.1. The scope of the study

The base material for the investigations was 7MnB8 steel. The steel was developed in 2011 by the Swiss Steel company. As proven, the composition of this bainitic steel presented in Table 2 is optimally qualified for cold forging of high strength parts without the heat treatment [95]. However, to enrich the offer for customers, a new, different process called XTP was introduced [110]. The implementation and optimization

of the process started with use of 7MnB8 steel and first dependencies resulting from the process were investigated. Steeltec's new long bar manufacturing process achieves a considerable ~ 2,5 times, reduction in the grain size in comparison to the material before rolling and thus enables the material properties produced by conventional processes, e.g. hot rolling, to acquire previously unobtainable values [111,112]. The high degrees of deformation allowed to obtain a very small average grain size < 5 μm (Fig. 33) and the impact ductile-brittle transition temperature was shifted from 20 °C to -100 °C [37]. It is known that the required properties like strength or toughness of the same material can be different and can be improved depending on the used production process or additionally steps such as heat treatment conducted after thermomechanical processing.

Therefore, due to the complexity of the process and the material development, a cooperation with an industrial partner was initiated to create a new product based on the chemical composition of 7MnB8 steel, directly intended for the XTP process with emphasis to obtain improvement in the mechanical properties and lowering ductile-to-brittle transition temperature.

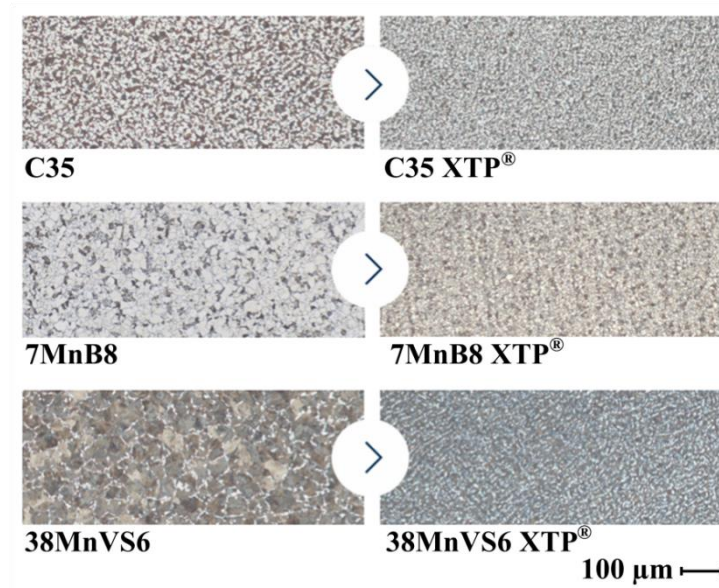


Fig. 33. Microstructure of 7MnB8 after conventional rolling and after the high deformation process (XTP), degree of deformation of 0.6 and air cooling [37,113].

Table 2. The chemical analysis corresponds to 7MnB8 [114].

Elements [wt. %]													
C	Mn	Si	P	S	Cr	Mo	Ni	V	Nb	Ti	Al	B	N
0.070	1.90	0.19	0.013	0.009	0.08	0.02	0.100	0.035	0.005	0.0880	0.028	0.0028	0.0101

In order to achieve the assumed aims described in Chapter 3, mainly lowering the DBTT, the research program was developed. This program is divided into three main blocks which are presented in Fig. 34. The first block included preliminary investigation of the 7MnB8 industrial steel state. The characterization of the grain growth kinetics during the reheating was used to propose the austenitization temperature. Then, different process parameters were simulated using 7MnB8 steel in order to characterize the structural dependence on the parameters. The investigation aimed at identifying the type of the structure, its constituents and the state of grain boundaries. Block two was based on the obtained results, four groups of the process parameters were proposed and performed industrial tests with use of 7MnB8 steel. Then, the structure and mechanical properties of the produced bars were characterized. The conclusions from the investigations were taken in to account in developing new chemical compositions with modified Mn, Mo, Ti, Nb and V content, which were produced as part of one of the tasks in the third block of the study. The wider explanation of the elements used and their purposes are described in section 2.3. Five labcasts manufactured and a 100 kg ingot was produced for each type of steel. Subsequently, bars were made from the new steels, as charge for the XTP process and the industrial trials were performed with the process parameters for which the lowest DBTT was obtained for 7MnB8 steel. After rolling, the structure and mechanical properties of bars with modified chemical composition were studied. The obtained results were analyzed and based on that, the final conclusions were formulated.

3.2. Thesis

The selection of alloying additive content of bainitic steel, in conjunction with the development of parameters for an innovative one-step XTP thermomechanical rolling process, makes it possible to obtain a gradient structure leading to a reduction in the transition temperature of the material into the brittle state with no significant changes in the values of other basic mechanical properties of the bars, relative to conventional 7MnB8 steel.

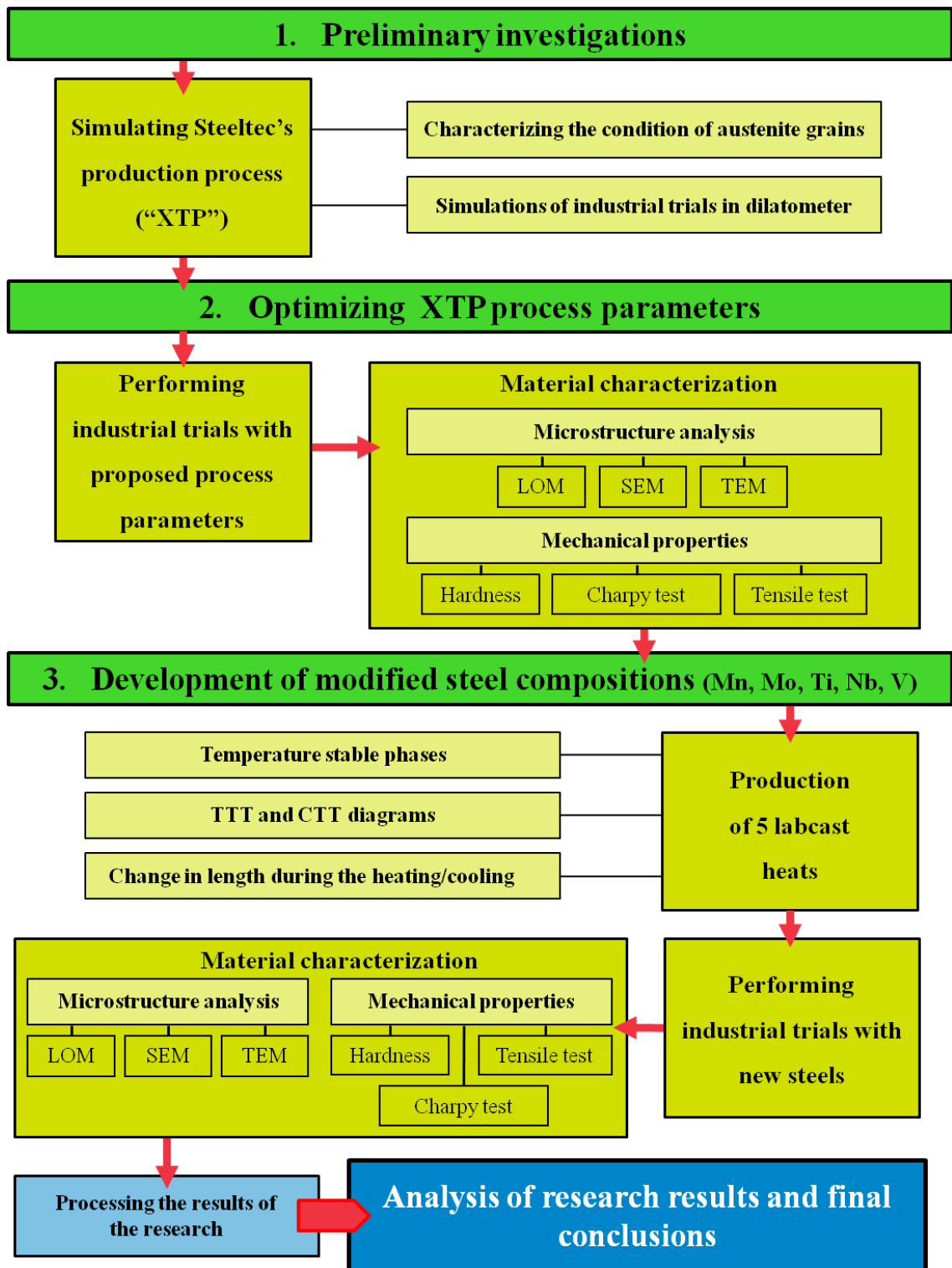


Fig. 34. The research program of the study.

4. Research methodology

4.1. Dilatometry tests

Dilatometric samples were cut from 7MnB8 steel after hot rolling at 1000 °C (initial state). The steel in this state is an input for the industrial trials of XTP process. Dimensions of the machined samples are presented in Fig. 35. Those samples were used in dilatometric simulations of the production process and to estimate grain growth kinetics necessary for the proposal of real industrial production parameters.

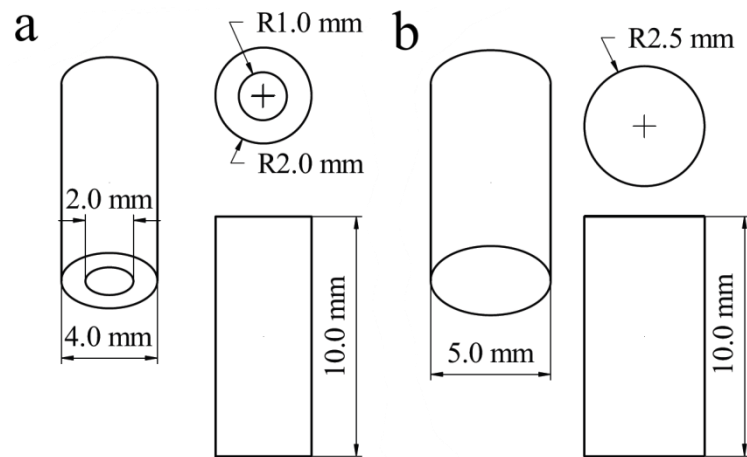


Fig. 35. Dilatometric samples: a) standard Ø4 / 2 x 10 mm b) Ø5 x 10 mm, allowing deformation.

Experiments were performed using the DIL805A/D/T dilatometer. The first set of experiments was conducted to characterize the grain growth kinetics depending on the austenitizing temperature. The tests were carried out on samples from 7MnB8 steel in the initial state from which samples for dilatometric tests were made. The scheme of the experiment is shown in Fig. 36a. The heat treatment was carried out at temperatures of 940 °C and 1000 °C, so between the austenitization temperature of 960 °C currently used in the process. The samples were heated to the set temperature, then intensively cooled, immediately after reaching the temperature and after a 60 s hold-up.

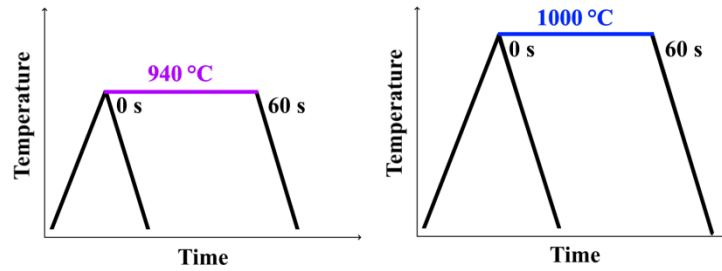


Fig. 36. Scheme of the dilatometric experiments of grain growth kinetics.

Subsequently, using the DIL805A/D/T dilatometer, simulations of the oblique rolling process were performed, according to the diagram presented in Fig. 37. The simulations were carried out with the samples made of 7MnB8 steel heated from room temperature (RT) to the austenitizing temperature of 915 °C and 980 °C, so the temperature below and above the temperature commonly used for the process (940 °C or 960 °C). At the same time, having lowered the temperature by 20 °C, it was assumed to obtain a finer grain before deformation, which would directly increase the proportion of wide-angle grain boundaries, providing effective barriers to cleavage fracture [115].

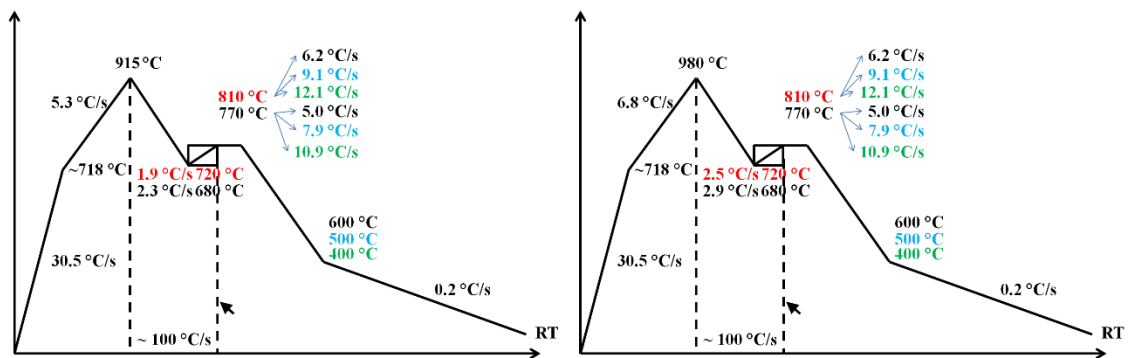


Fig. 37. Simulations of the technological process with DIL805A/D/T dilatometer. Black arrows mark the samples with applied deformation.

After reaching the austenitizing temperature, two samples were intensively cooled to ambient temperature. Subsequently, samples were cooled to rolling temperature, one set of samples was deformed at this stage (marked by the arrows), while the rest was not processed. Based on the results of continuous temperature measurement in the production line during rolling, the temperature after deformation was increased by about 90 °C, to 770 °C and 810 °C, respectively. In the next stage, the material was cooled to three final temperatures: 600 °C, 500 °C and 400 °C, while deformed samples were intensively cooled to ambient temperature to freeze the structure. During the final cooling of the samples without deformation, a slow cooling (SC) rate of 0.2 °C/s was used, which corresponds to the cooling of the bars in air.

Based on the results obtained in the dilatometric investigations supplemented with the characteristic temperature stable phases, 4 different combinations of proposed process parameters were developed (Table 3), which consist of austenitization temperature (T_A), rolling temperature (T_R) and cooling rate. The last parameter, associated with cooling section, combines three values, which describes water flow through one of three cooling boxes, measured in liters per minute. For example, the notation "120;0;25" indicates an arrangement of three cooling stations, where the first station has a water flow rate of 120 liters per minute, the second station remains switched off, while the water flow rate at the last station is set to 25 liters per minute.

Table 3. Proposed rolling parameters for real industrial production, used in trials.

Variant	Austenitization temperature [°C]	Rolling temperature [°C]	Cooling [l/min]	Cooling [°C/s]
1	915	720	120;0;25	~ 7.6
2	915	720	25;0;0	~ 2.3
3	915	680	120;0;25	~ 7.6
4	980	700	120;0;25	~ 7.6

Temperatures of 915 °C and 980 °C were used as austenitizing temperatures. Maintaining a lower austenitizing temperature will, by design, produce a finer grain, but may not be sufficient to dissolve the carbides. Therefore, using a higher temperature was assumed to ensure the dissolution of thermally stable precipitates while maintaining a fine grain. This will reduce the negative impact on the properties of large hard precipitates, at the expense of a small increase in grain size. In order to increase work hardening of the material, it was assumed to conduct rolling at a temperature of (T_R) 720 °C and at a temperature reduced to 680 °C. The possibility to increase energy accumulation in the material due to a higher degree of deformation is limited by the required diameter of the finished product. Therefore, it was impossible to change the alignment of the rollers. As a result of this limitation, it was decided to use a lower temperature in one of the rolling runs. The assumption was that the increase in strain would mean lower recrystallization temperature, resulting in a finer rolled bar structure. The last parameter changed as part of the process proposals was the cooling rate, the control of which is provided by swapping the layout of the cooling boxes and the water output for each of them. For the

most part, a 120;0;25 arrangement was used, that is, an arrangement of 2 boxes. The first one with a water output of 120 L/min, the second of the boxes was idle, while the last one had a water output of 25 L/min. One of the rolling runs was modified in terms of the configuration of the cooling section, where a 25;0;0 arrangement was used, that is, one box with a water output of 25 L/min. Reducing the cooling rate should result in a higher final temperature after rolling (T_2) which, according to the results obtained from the process simulation, will result in a different structure.

4.2. Design and production of steels with modified chemical composition

The reference chemical composition for selections was that of 7MnB8 steel. The main reason to produce new steel grades was to decrease their DBTT. The selections were focused on element content like Mn, Mo, V, Nb, Ti, Al and B. Adjustment of the chemical composition of experimental steels was performed with the aid of thermodynamic calculations, which were made using Thermo-Calc and JMatPro software. Depending on temperature, stable phases were determined for the proposed steels compositions, focusing on precipitation processes. TTT (Time Temperature Transformation) and CCT (Continuous Cooling Transformation) charts were generated. Furthermore, samples were prepared from the new steels according to the Fig. 35a and investigations of the change in length during the heating/cooling were performed to estimate and confirm the transition temperatures obtained in thermodynamics calculations when compared to the real values.

Five experimental heats were produced, the chemical compositions of which are shown in Table 4. Mo improves temper embrittlement by avoiding impurity segregation like P, S, Sb, Sn and As on the grain boundaries. The analysis of P and S, which are specified in the chemical composition of industrial steel demonstrated the content of these elements at the level of ~ 0.004 wt. % in case of P and ~ 0.006 wt. % for S. These values are comparable for all new steels produced in laboratory conditions. Moreover, Mo dissolved in the matrix has beneficial influence on strength of the material by solid solution strengthening. Furthermore, as a carbide former, Mo can replace other elements like Ti in precipitation processes, therefore its content was increased to 0.2% in all new steels. In S657 steel the Mo content was increased to 0.49%. Another assumption was to increase the hardenability of one steel by increasing the Mn content, which would allow to obtain a homogenous structure on the cross-section of the produced bars. In S658 steel

the Mn content was changed from 1.9% to 2.9% to increase hardenability of the steel. The rest of the selections were performed to interfere in precipitation processes by changing carbide formers like V, Nb and Ti. In S654 steel Ti was increased to 0.11%. On the other hand, two steels: S659 and S660 with decreased Ti content were produced, in which Nb and V were added. The results of 7MnB8 steel showed that the Ti content has to be decreased in steels to avoid coarse TiN precipitations, but it has to be kept on an adequate level to achieve grain refinement by the pinning effect. The Nb additions dissolved in the matrix retard dynamic recrystallization. The grain refinement phenomenon increases the volume of regions for nucleation and leads to structure refinement after the phase transformation. Moreover, in terms to V, F. Fazeli et al. found that V atoms in solution delay the bainite reaction to lower transformation temperatures, which results in a refined bainite structure [100]. Therefore, the improvement of toughness can be obtained.

Table 4. Modified chemical composition of new steels.

Steel	Elements [wt. %]													
	C	Mn	Si	P	S	Cr	Mo	Ni	V	Nb	Ti	Al	B	N
S654	0.080	1.93	0.21	0.004	0.008	0.10	0.19	0.110	0.042	0.00	0.110	0.030	0.0024	0.0070
S657	0.071	1.89	0.21	0.003	0.006	0.10	0.49	0.100	0.040	0.00	0.092	0.027	0.0023	0.0060
S658	0.076	2.90	0.21	0.005	0.006	0.10	0.21	0.100	0.040	0.00	0.036	0.017	0.0027	0.0080
S659	0.064	1.89	0.22	0.004	0.006	0.10	0.20	0.095	-	0.037	0.023	0.026	-	0.0097
S660	0.068	1.90	0.21	0.004	0.006	0.09	0.20	0.098	0.150	0.021	0.019	0.005	-	0.0088

One 100 kg ingot was made for each grade, which was then forged into square bars with a side of about 35 mm. In the next stage, bars with a diameter of Ø30 mm were made by machining (Fig. 38a). Four rods 600 mm and one 1000 mm long were made from each heat. The ends of the bars were milled, drilled in the axis and an M10 thread was made.



Fig. 38. The next steps of machining steel with a modified chemical composition: a) machining process of material after forging on a rod with a diameter of Ø30 mm, b) connected rods made of experimental melts, consisting of 5 different materials.

Then, using pins with a thread about 50 mm long, one of each grade was screwed together, and then in place of the previously made cutter, a MIG weld was made. The finished rods, 3.4 m long, contained sections from each experimental heat (Fig. 38.b). The material prepared in this way was then subjected to an oblique industrial rolling process at the Steeltec company.

4.3. Structural investigations

All the cross-section samples from raw materials and after the XTP process, were embedded in a resin, grounded and polished using standard metallographic techniques. The grinding procedure involved the application of sandpaper up to #1000 grit, while polishing was performed up to 1 μm finish using Struers Nap cloths. After process simulations, the samples were prepared according to the same procedure. For light optical microscope (LOM) and scanning electron microscope (SEM) observations, 1% solution of nitric acid was used to reveal the microstructure. Furthermore, samples were electropolished by a Struers TenuPol-5 electrolytic polishing machine for the SEM investigations. A8 electrolyte containing perchloric acid, acetic acid and methanol were used in the process. The polishing voltage at the range of 30 - 35V was applied, depending on the steel. Polishing time was 50 sec. After the process, etching in a 1% solution of nitric acid was used to reveal the microstructure.

Microstructure investigations of the steel were conducted with LOM OLYMPUS DSX500i equipped with an integrated optical and digital head. Observations were carried out in the bright field mode. Macrostructures of cross-sections of the bars were taken and investigated in the core and at the surface. Furthermore, LOM was used for the observation of the prior austenite grains (PAG) from the samples after simulations. Microstructures were recorded and analyzed using MetIlo software for quantitative investigations. The investigations were performed with the use of various magnifications, depending on the grains size, with average 500 grains per sample. Etching to reveal the PAG was performed using a mixture of chromium oxide (VI), sodium hydroxide and distilled water. The solution was heated up to 120 °C. Etching with this reagent was an hour of slow boiling for each sample which could not be mounted in resin.

SEM JEOL JSM7200F equipped with electron backscatter diffraction (EBSD) detector Hikari Plus, was used for microstructural investigations. For observations, a SE (Secondary Electrons) detector providing topographic contrast was used. EBSD maps

were made for cores and at the surface areas. Details of the analysis during the SEM investigations are summarized in Table 5. The obtained results from EBSD were analyzed by OIM software from EDAX. In the cleanup procedure "Grain CI Standardization" and "Grain Dilation" were used to define "Grain Tolerance Angle" and "Minimum Grain Size" of 5° and 2 pixels, respectively. The grain boundaries marked on the EBSD maps were divided to low angle and HAGB with ranges 2° - 15° and 15° - 62°, respectively.

EBSD samples were cut out from the bars after the rolling process and from raw materials. Cross-section specimens were prepared. Next step was to grind the samples with sandpaper from gradation 80 to 1000. In the next steps, samples were ground using sandpaper with 50, 15 and 5 µm grain and polished with colloidal silica for one hour. The final stage was carried out using a Fischione ion polishing machine Model 1061 SEM Mill for an hour, with voltage 2 kV and 2° angle. The sample was rotating with 3 rpm during the process. Furthermore, after process simulations, samples underwent the EBSD tests to characterize the content of RA.

For the purpose of determining the fineness of the structure, the D_{ef} parameter was used, established on the basis of the obtained EBSD results, which were analyzed using a "Grain Tolerance Angle" of 15° and a "Minimum Grain Size" of 2 pixels. This is the critical grain size, which refers to the limiting grain size at 80 percent area fraction in the grain size distribution histogram [62,116]. Cumulative grain size distributions were made for each sample, and the D_{ef} parameter size was read at the intersection of the graph with the 80 percent value on the Y axis.

Table 5. JEOL JSM7200 F settings during the investigations.

Type of research	Detector	Accelerating voltage [kV]	Spot size	Working distance [mm]	Step size [µm]	Area [µm ²]	Sample
Microstructure	SE	15	16	6	-	-	Etched specimens
Crystallographic characterization	EBSD	15	18	15	0,1	10000	Ion polished sample

Phase Quick Maps were generated to determine the distribution and content of RA in microareas of steels in the initial state and after rolling. Moreover, based on the distribution of the misorientation angles the structural constituents of the investigated materials were identified. Commonly used misorientation values are results of the possible FCC (Face Centered Cubic) - BCC (Body Centered Cubic) or BCT (Body Centered Tetragonal) orientation relationship, during the transformation. Well-known

orientation relationships (OR) were described by Nishiyama–Wasserman and Kurdjumov–Sachs in the 1930s. Accounting those OR, two characteristic misorientation angles (MA) between RA and ferrite were designated and amount to 45.99° and 42.85°, respectively. These characteristic MA values are based on the correspondence of certain crystallographic planes and directions in the FCC and the BCC lattices. Moreover, each orientation can be expressed by rotating the site around a parallel direction to the $\langle uvw \rangle$ (crystal direction) direction in one of the crystals by a certain angle. This leads to a superposition of the coordinate systems of both crystals, thereby more correlation variants occur, 12 and 24 for N-W and K-S orientation relationships, respectively [117–121]. In the Table 6, OR between FCC and BCC phases are shown in more detail, with included crystal planes and directions parallelisms. An example of this correlation is shown in the Fig. 40, where it could be seen, that misorientation of RA and ferrite is close to those values and is located in their range.

Table 6. Orientation relationship between FCC and BCC phases [119].

Orientation relationship	Parallel planes	Parallel directions	Misorientation angle [°]	Axis	No. of variants
Nishiyama-Wasserman (N-W)	$\{111\}_{\gamma} // \{110\}_{\alpha}$	$\langle 112 \rangle_{\gamma} // \langle 110 \rangle_{\alpha}$	45.98	0.976 0.083 0.201	12
Kurdjumov-Sachs (K-S)	$\{111\}_{\gamma} // \{110\}_{\alpha}$	$\langle 110 \rangle_{\gamma} // \langle 111 \rangle_{\alpha}$	42.85	0.968 0.178 0.178	24

For martensite (M), as a result of its crystal structure (BCT or slightly distorted BCC) and parent A (FCC), only a limited number of variants of M are possible in a given PAG and the number of variants depends on the OR followed in a particular steel. Further, M variants can have a limited range of misorientation angles within a single PAG. Specifically, assuming a Kurdjumov–Sachs orientation relationship, the misorientation associated with M boundaries is $\sim 10^{\circ}$ in the case of sub-blocks, varies from $\sim 10^{\circ}$ to 21° and 47° to 57° in the case of packets, and varies from $\sim 49^{\circ}$ to 60° in the case of blocks (Fig. 39) [122–124]. This dependence can be seen in many works, where linear analysis shown changes in the misorientation varies between 50° - 60° along the line led by M [93]. Similar analysis is shown as an example in Fig. 41.

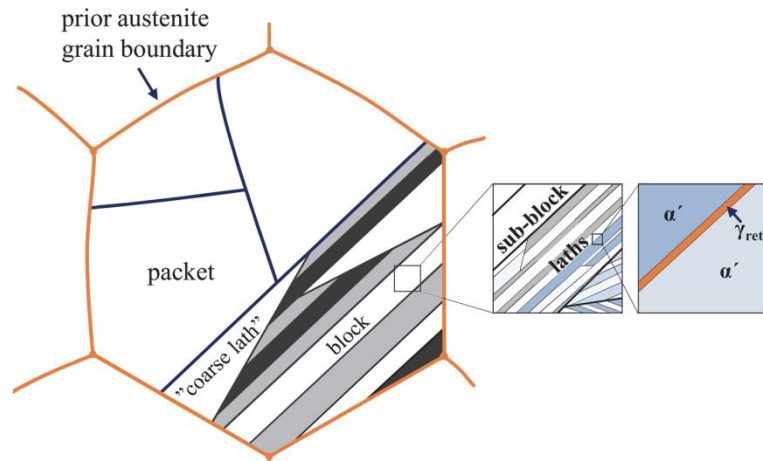


Fig. 39. The schematic structure of as-quenched lath M [125,126].

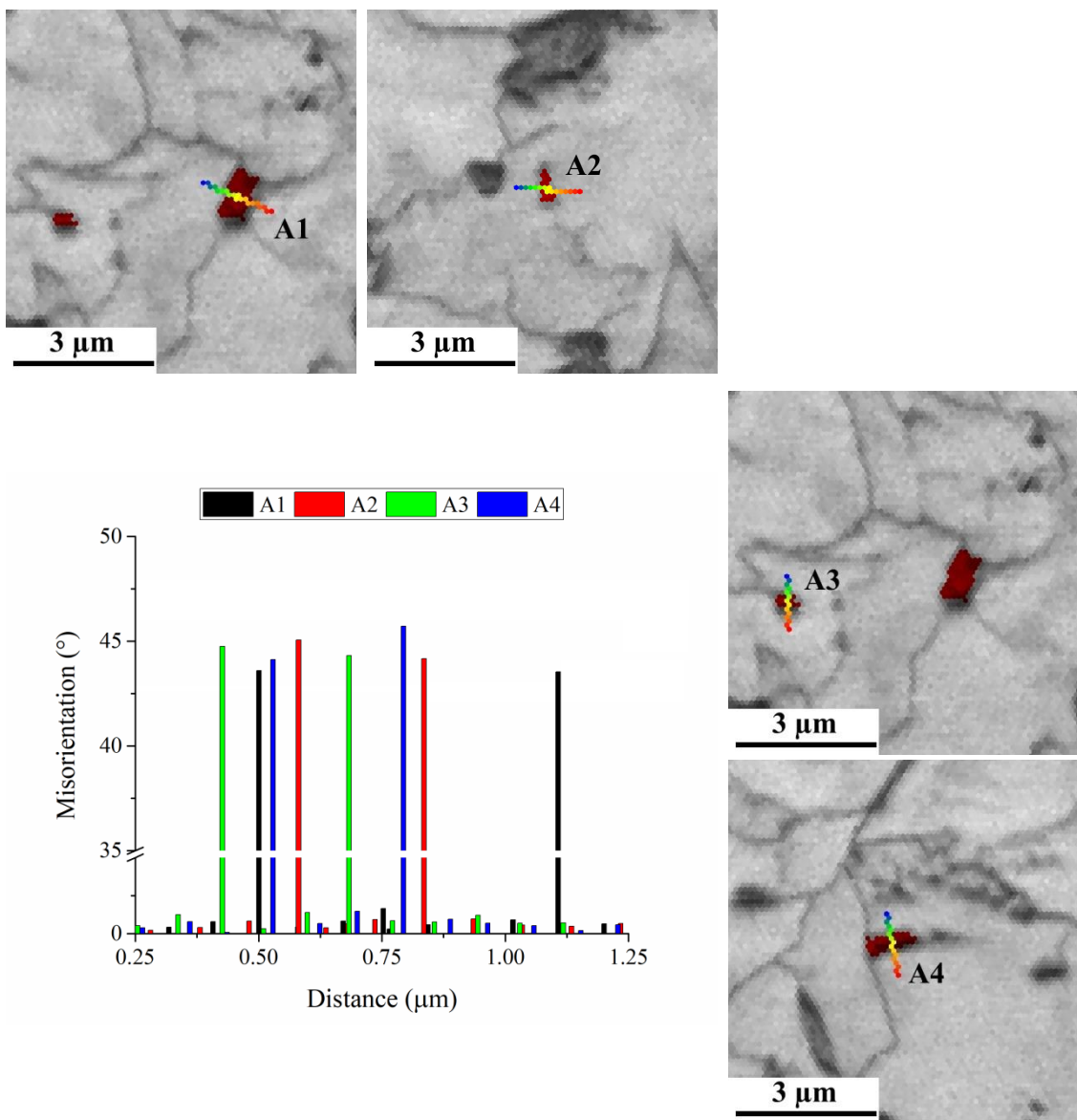


Fig. 40. Point-to-Point misorientation along lines marked on the grains of RA.

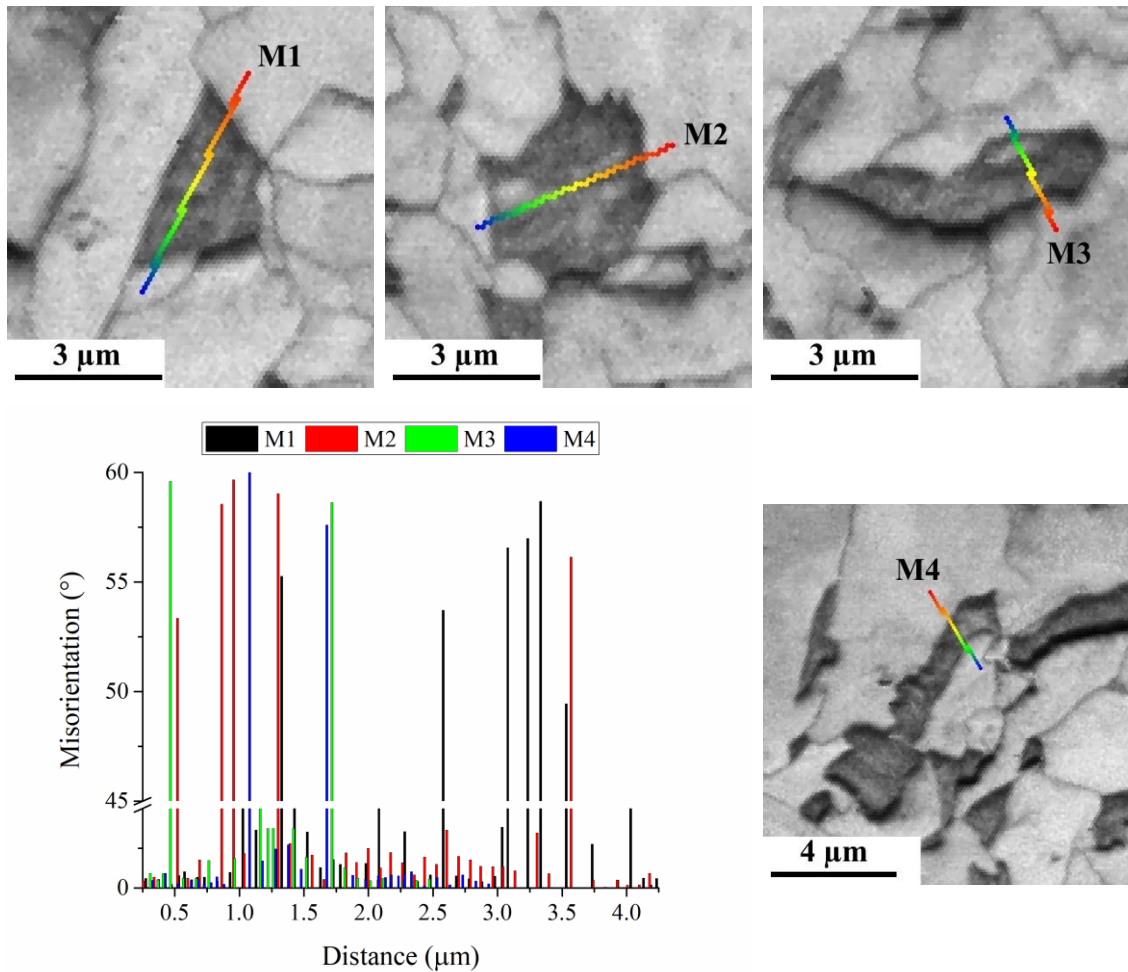


Fig. 41. Point-to-Point misorientation along lines marked on M.

Interpretation of the misorientation angles regarding bainite is more complicated. Due to its complex structure, which is a mixture of ferrite and second phases of cementite, M and/or RA. Depending on a type of bainite, the different misorientation angles can be observed on the distribution graphs. LB has a high proportion of boundaries with misorientation in the range of $50^\circ - 60^\circ$ and very few boundaries with low misorientations ($< 20^\circ$) [5]. UB has a high proportion of low angle boundaries with low misorientations, $< 20^\circ$ and fewer high angle boundaries $> 50^\circ$ [5]. In GB (with irregular ferrite) the distribution of grain boundaries is more random with a broad peak at about 45° . The existence of substructure produces a minor peak below 20° [5]. These dependencies are presented in visual form in Fig. 42. Some sources give more narrowed ranges characteristic for bainite, separating the high-angle $55^\circ - 60^\circ$ and $55^\circ - 60^\circ$ boundaries characteristic for lower and upper bainite, respectively [127]. However, the EBSD results clearly indicate that the distribution of boundary misorientations provides a means of

reliably distinguishing between the different forms of bainite. An approach that is proposed in Fig. 42 is based on the relationship between the number density of high and low angle boundaries and refers to the features of the specific type of bainite, as described above [5].

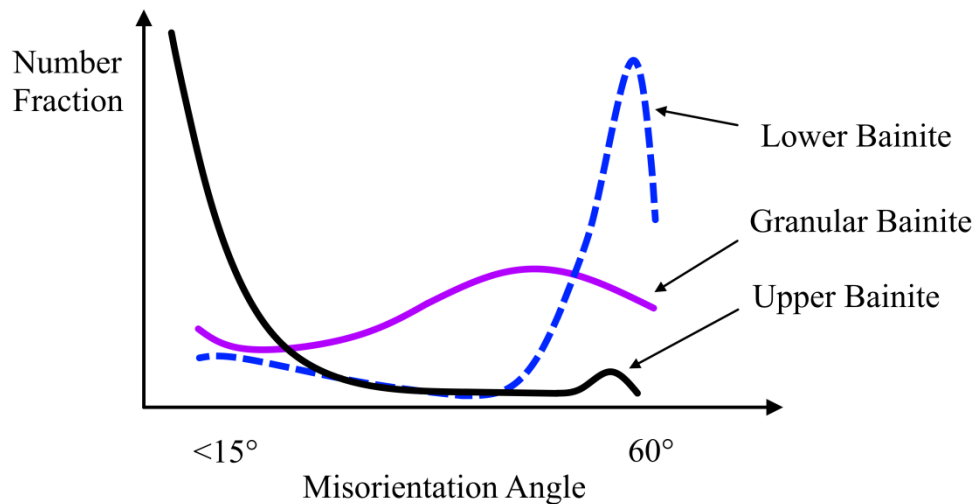


Fig. 42. Definition of bainite based on distribution of misorientation angles between grains/laths [5].

The μ -X360s analyzer from Pulstec equipped with a high-sensitivity flat-panel detector was used to study the proportion of retained austenite. The operating conditions of the X-ray tube were 30 kV and 1 mA. A lamp with a chromium anode was used ($\lambda = 2,291 \text{ \AA}$). The wavelength $K\alpha$, plane family $\{211\}$, Bragg's angle $2\theta = 156,396^\circ$ and $K\beta$ filter were used. The depth of X-ray penetration was about 10 microns. The Pulstec analyzer was positioned at an angle of $\psi 0^\circ$, the distance from the sample was 27 mm, and the measurement time was 30 seconds. A collimator with a diameter of 2 mm was used. The resulting deflected X-rays from 0° to 360° around the beam were recorded with a two-dimensional detector at 125 points and formed a Debye-Scherrer ring. The proportion of retained austenite was the average value of the measurement from 0° to 360° (the Debye - Scherrer ring). The tests were carried out in the core areas of the bars in their initial state, as well as after the rolling process.

The precipitation effects in the steels were examined using the ultra-high-resolution scanning transmission electron microscope (TEM) TITAN 80-300. The microscope was equipped with an energy dispersive spectrometer (EDS) for chemical composition microanalysis and a HAADF (High-angle annular dark-field) detector for observations with chemical contrast in the scanning mode. The accelerating voltage during the investigations was 300 keV. For phase identification, selected area diffraction (SAD) or convergent beam electron diffraction (CBED) were performed. For very fine

precipitations, investigation of high-resolution transmission electron microscopy (HRTEM) mode allowing for direct imaging of the atomic structure of samples was used. Further analysis was performed using Fast Fourier Transform (FFT) that computes the discrete Fourier transform of a sequence, or its inverse. In TEM investigations it allows for phase identification. 3 mm diameter thin foils from each material were prepared with an electropolishing process, performed by a Struers TenuPol-5 electrolytic polishing machine. First, 2 mm thick, cross-section slices were cut out from the cores of the bars. Next step was thinning of the material by grinding with a precision grinding handle and then cutting the 3 mm diameter discs by using a disc punch. The final thinning was carried out with a 1000 gradation paper to the thickness of around 100 μm . In the polishing process, A8 electrolyte was used and the current range of 30 - 35V, depending on the steel. After the process ended, samples were removed immediately from the holder and rinsed with methanol. Mounted on a TEM holder before investigation, samples were cleaned in a plasma cleaner for 10 s.

The quantitative analysis of the precipitations in the steels were performed using MetIlo software. For the analysis images obtained in SEM and TEM investigations were used. During the analysis the limited number of the investigated objects was assumed as no less than 100 per sample. For the estimation of the precipitation density factor [precipitation/ μm^3], the volume of investigated areas was calculated separately by multiplication of the surface area by maximum precipitation diameter of the area. After that, the results from volume calculations and number of the precipitation for the investigated steel were added up. The last mathematical operation comprised dividing the number of the precipitations and volumes.

4.4. Mechanical properties

Mechanical properties of rods made of 7MnB8 conventional steel and the new steel grades were investigated. Hardness measurements were performed on as-polished state of the samples with the use of a microhardness tester Future-Tech FM-700 with a load of 1000 g (HV_1), according to PN-EN ISO 6507-1. Linear cross-section hardness distribution and hardness measurements in the core and at the surfaces were made. The mean hardness and standard deviation of the steel in the initial state were determined from 99 measurements. For the determined values for the steel after rolling, the average of 20 and 28 measurements were taken for the near-surface region and the core, respectively.

Static tensile tests at 20 °C and Charpy V-notch investigations were carried out with a Zwick/Roell Z250 strength testing device and a Zwick/Roell RKP 450 hammer for the impact test, respectively.

Tensile tests were performed according to the PN-EN ISO 6892-1 standard. M16 ϕ 10 samples were prepared from the core areas in the axes of the bars. Fig. 43 and Fig. 44 present a sketch of the sample and its location in the bar, respectively.

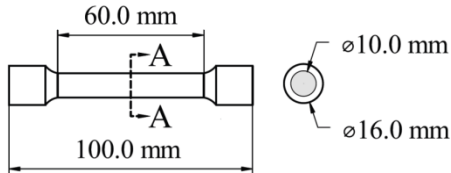


Fig. 43. Sketch of the prepared samples for tensile tests.

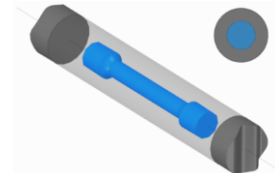


Fig. 44. Sampling scheme of the tensile test samples.

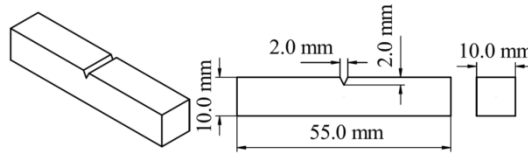


Fig. 45. Dimensions of the Charpy impact samples.

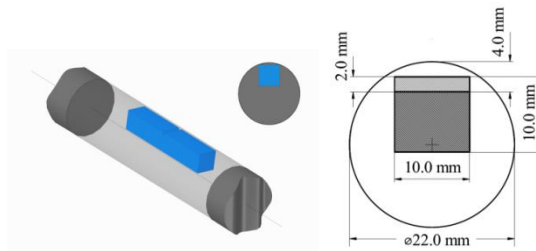


Fig. 46. Sampling scheme for Charpy impact tests.

Charpy impact tests were performed according to the PN-EN ISO 148-1: 2017 standard. Samples were prepared according to the presented sketch (Fig. 45), also their location in the bar is presented (Fig. 46). Tests were performed at temperatures: -100 °C, -60 °C, -40 °C, -20 °C and 22 °C. The DBTT of the investigated steels was determined as the temperature with fracture energy in a Charpy impact test of 27 J (T_{27J}). Depending on the values obtained at a given temperature, tests were continued by lowering the temperature. Because fracture energies of less than 27 J were obtained for most of the steels in the initial state, additional tests were carried out at elevated temperatures up to 100 °C to determine the DBTT.

5. Results

The results of the research are presented in blocks due to the specificity of the work strategy adopted, which was divided into three main stages (Fig. 28). The implementation of each stage allowed to formulate partial conclusions, which had a direct impact on the further implementation of the research. Therefore, in the first part, the results of the research include studies aimed at simulating the process and characterizing the structural changes in the process. Based on the results of the research, four groups of process parameters were proposed and process tests were carried out using bars of 7MnB8 steel, which at the same time served to calibrate the process parameters. After the rolling process, the structure and mechanical properties were characterized for all four groups of process parameters. The results of the research showed the group of process parameters for which the best results were achieved to ensure the DBTT reduction for the 7MnB8 steel bar. The third stage consisted of selecting the chemical composition based on conventional steel. Therefore, in the first part of the study, thermodynamic calculations were performed for the proposed new steels. Then the structure and mechanical properties of the new steels were characterized in the initial state, i.e. after forging at ~ 1200 °C. The results of the tests were a reference for the obtained material changes as a result of XTP rolling. The model for the presentation of test results, the pattern of which has a recurrent character, is therefore a cause-and-effect result, leading to the achievement of the stated purpose of this study.

5.1. Process simulations

To determine the effect of temperature and austenitizing time on the grain size of the primary austenite using 7MnB8 steel, thermodynamic calculations of ferrite and A mass fractions were performed and heat treatment was carried out to simulate the first stage of the process (austenitizing). In addition, in order to characterize the structure at each stage of the rolling process and determine the effect of the final temperature on the structural components after accelerated cooling, process simulations were carried out under laboratory conditions. Intense cooling with He was used to "freeze" the structure.

5.1.1. The grain growth kinetics

The preliminary investigations of grain growth kinetics of 7MnB8 steel using dilatometric experiments at different temperatures and with two holding times made it possible to determine the grain size and structure of 7MnB8 steel due to the austenitizing temperature used. Examples of LOM structures are shown in Fig. 47. The results presented in Fig. 48 and 49 show the distribution of the prior austenite grain size (PAGS) after the experiments. Moreover, the average equivalent diameter (AED) of the PAG is marked in the graphs. As it can be seen, the grain size increases with increasing holding time for both temperatures. The same dependence was observed for the same holding time at different temperatures, the higher the temperature the higher grain size was obtained. Moreover, the proportion of grains with the largest size is increasing.

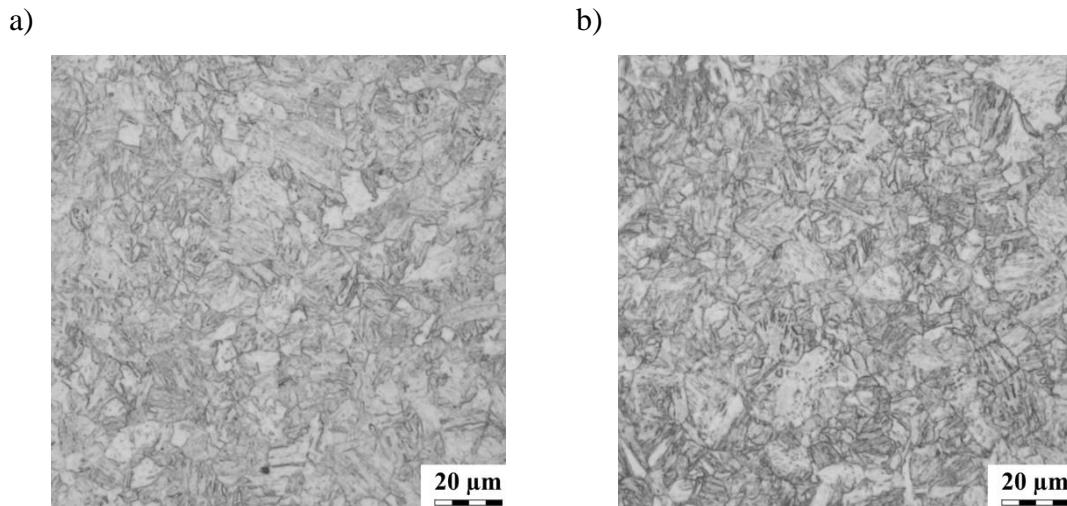


Fig. 47. Examples of LOM images used for grain size analysis of former austenite: a) 940 °C 60 s, b) 1000 °C 60 s.

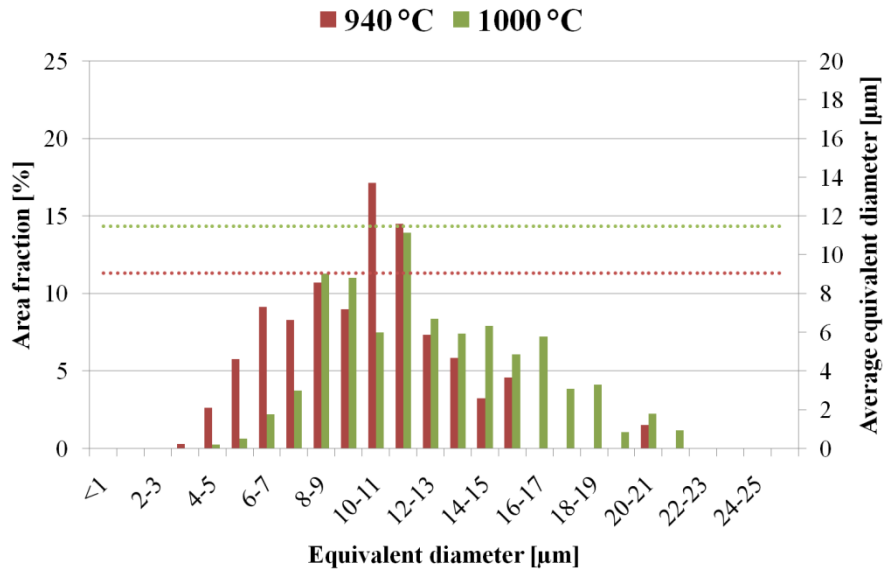


Fig. 48. Grain size distribution of former austenite as a function of austenitizing temperature. Holding time at 0 s. The lines represent the average values for all measurements.

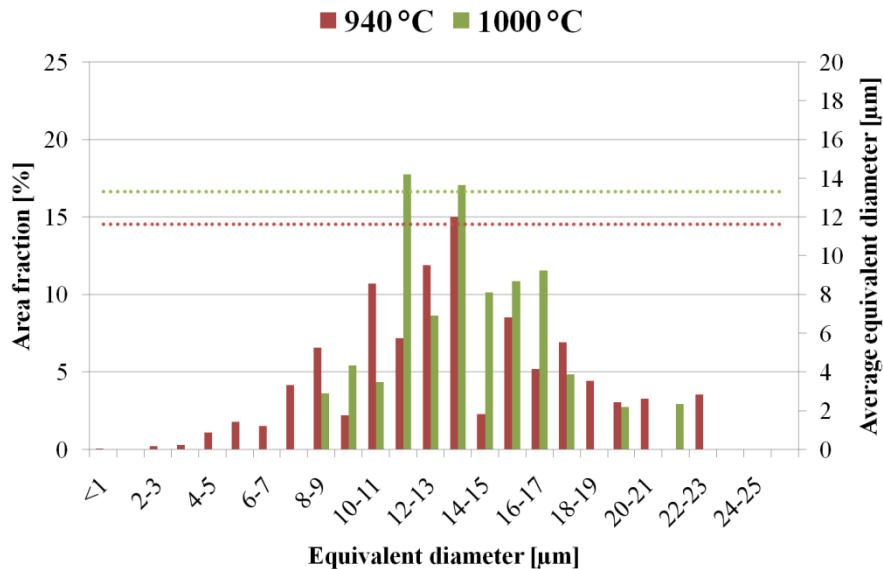


Fig. 49. Grain size distribution of former austenite as a function of austenitizing temperature. Holding time at 60 s. The lines represent the average values for all measurements.

However, it has to be noticed that comparing the same tests conditions, holding time or temperature, the differences of the grain sizes are very small and amount to about 2 μm , in relation to an equivalent diameter (Fig. 48 and 49). Furthermore, the graphs of distributions of the PAGS indicate an approximate normal distribution shape, so it can be assumed that abnormal grain growth does not take place in the material during reheating, due to the TiN precipitations pinning the grain boundaries.

5.1.2. Process simulation with various parameters based on 7MnB8 steel

The results of the simulation studies are presented in Fig. 50 - 80. In the initial phase thermodynamic calculations of ferrite and A mass fractions were made (Fig. 50), in order to confirm T_A which can provide a fully austenitic structure for 7MnB8 steel. Experiments were performed according to the scheme presented in Fig. 37. The structure after experiments observed using LOM and SEM are presented in Fig. 51, 52 for frozen structures after austenitization and Fig. 56, 57 and 60, 61, for deformed samples. The results for samples cooled to different final temperatures (400 °C, 500 °C and 600 °C) from four different temperature passes are presented in Fig. 64 and 65 for 915 °C →680 °C →770 °C, Fig. 68 and 69 for 980 °C →680 °C →770 °C, Fig. 72 and 73 for 915 °C →720 °C →810 °C, and Fig. 76 and 77 for 980 °C →720 °C →810 °C. Moreover, the results of EBSD investigations defining the grain boundaries total length and distribution of misorientations angles are presented in the same sequence: after austenitization (Fig. 53, 54), after deformation at different temperatures: 680 °C and 720 °C in Fig. 58, 59 and 62, 63, respectively. Fig. 66, 67, 70, 71, 74, 75 and Fig. 78 -79 present the results for samples after cooling to the different final temperature. Furthermore, in Fig. 80 the area fraction and average diameter of RA for all samples after process simulations are compared.

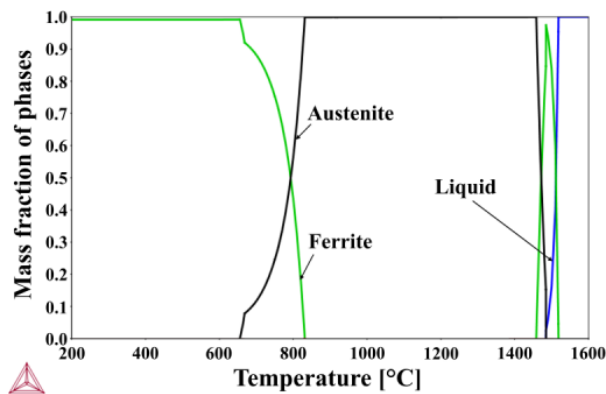


Fig. 50. Mass fraction of phases dependence on temperature for 7MnB8 steel.

The results for samples heated to the austenitization temperature with fast cooling rates are presented in Fig. 51 - 54. For both temperatures, 915 and 980 °C, the structures are similar and consist of UB and LB mixture, as can be seen in Fig. 51 and 52. The distributions of disorientation angles are characteristic for the occurrence of the listed components of the structure (Fig. 54). The higher temperature does not cause essential growth of grain sizes, which can be seen in Fig. 53, where the distribution of low angle grain boundaries (LAGB) and HAGB (for all components of the structure) for both

samples are similar. The total length of HAGB is similar for both samples. However, in the sample austenitized at 980 °C, more LAGB occur (Fig. 55). It is because cooling starts from higher temperature, so the cooling curve is shifted to the right of the UB region for which the LAGB are the characteristic ones (Fig. 42).

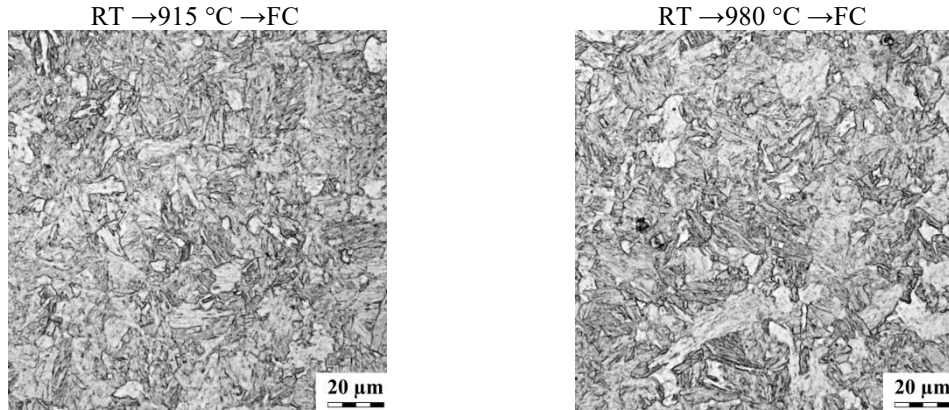


Fig. 51. LOM structure of the samples after heating to the austenitization temperature with fast cooling (FC).

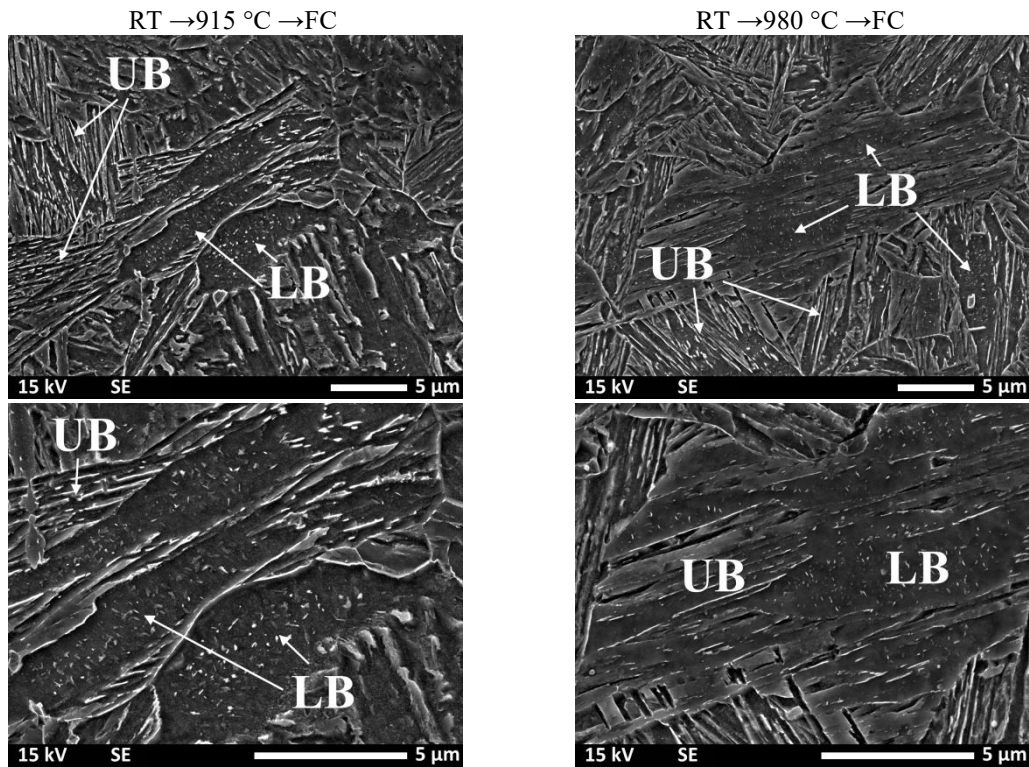


Fig. 52. Upper and LB mixture structure of the samples after heating to the austenitization temperature with fast cooling (FC).

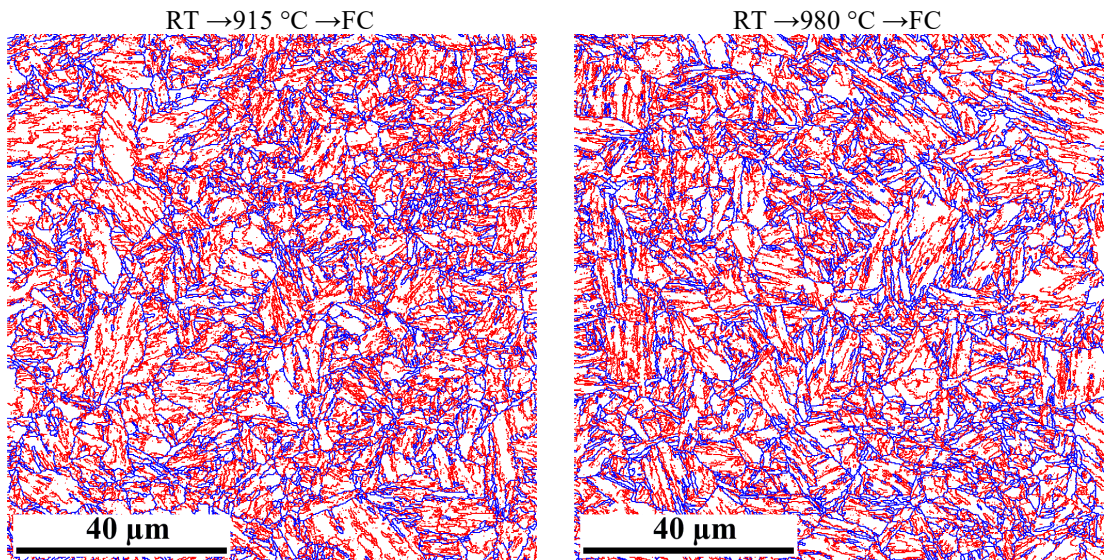


Fig. 53. Distribution of the LAGB (red) and HAGB (blue) for the samples after heating to the austenitization temperature with fast cooling (FC).

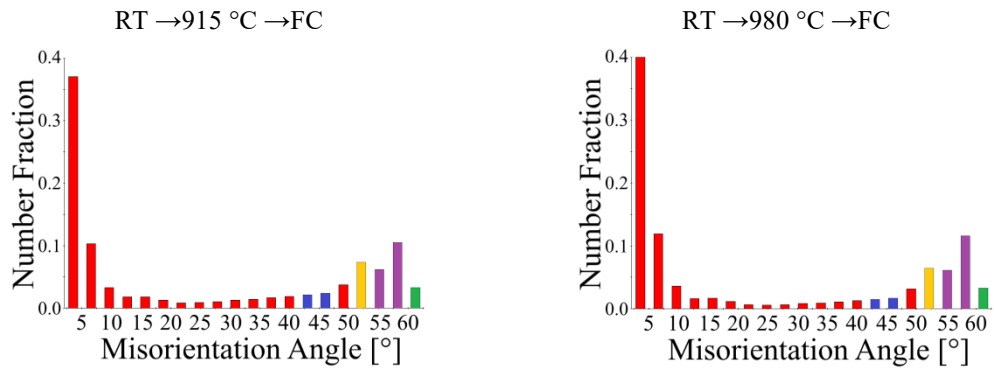


Fig. 54. Misorientation angles for the samples after heating to the austenitization temperature with fast cooling (FC).

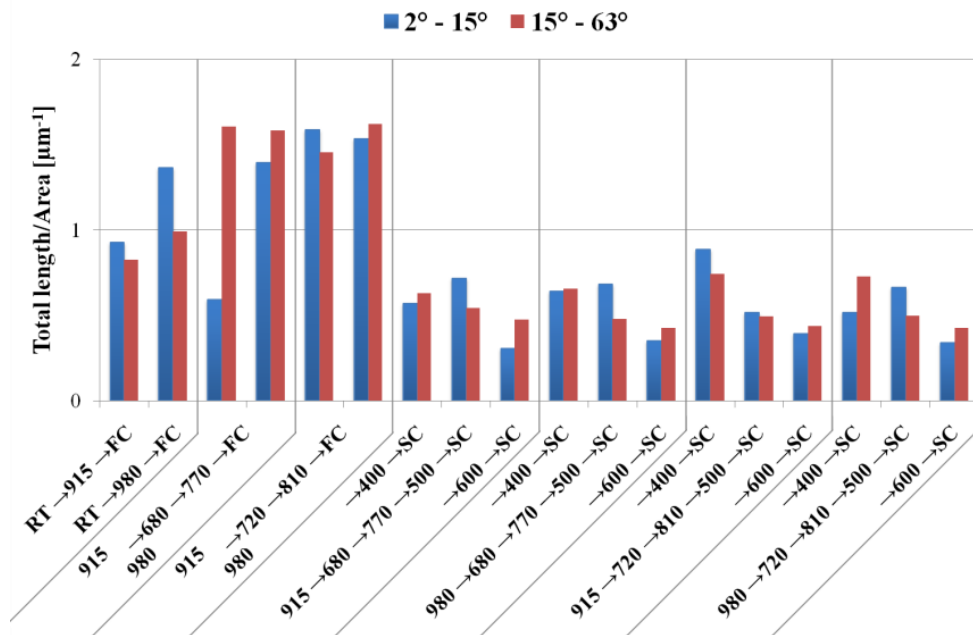


Fig. 55. Grain boundaries density for all samples after process simulations.

Then, Fig. 56 - 59 and Fig. 60 - 63 present the results for the austenitized samples at the same temperature (915 °C and 980 °C), which were cooled to 680 °C and 720 °C, and deformed. Samples deformed at 680 °C, have mostly GB structure with UB areas (Fig. 56 and 57). Increased austenitizing temperature to 980 °C resulted in a higher proportion of UB, however, GB is still predominant (Fig. 57). Those differences can be seen in the EBSD results. In Fig. 59 more fraction of LAGB, characteristic for UB can be observed for sample austenitized at 980 °C. It has to be noticed, that the distribution of the UB regions in both samples is non-uniform (Fig. 58). Simultaneously, in Fig. 59, for sample austenitized at 915 °C, the distribution of misorientation angles has lower number fraction for low angles and mild curve at the end, which is characteristic for GB (Fig. 42). Structure of samples deformed at 720 °C consists of GB and UB (Fig. 60 and 61). Increasing the temperature at which the samples were deformed to 720 °C increased the proportion of LAGB in the structures as well. High LAGB total length/area can be seen in Fig. 55, which is also visible in Fig. 62 and 63. This is due to the mixture of GB and UB observed in the structure of the samples. In addition, unlike samples deformed at 680 °C, the distribution of boundaries in the structure of samples deformed at higher temperatures is homogeneous (Fig. 62). The proportion of HAGB in all deformed samples is comparable (Fig. 55). The increase in austenitization temperature and strain temperature did not cause significant differences in the total HAGB length/area.

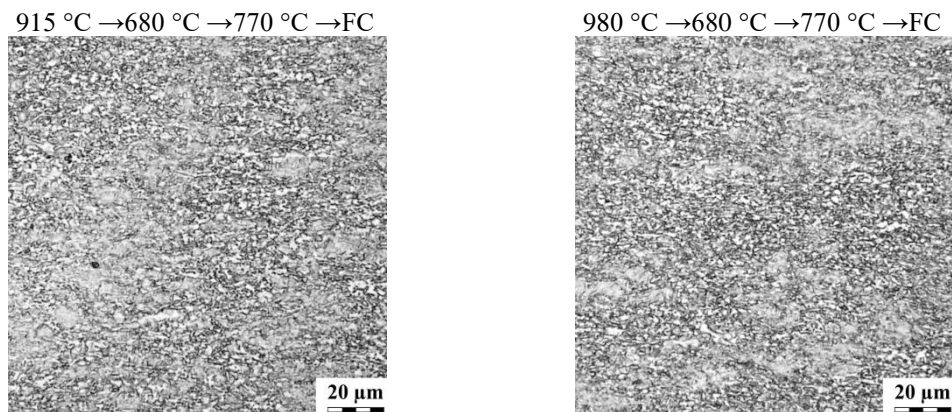


Fig. 56. LOM structure of the samples after heating to the austenitization, deformation at 680 °C with increased temperature and fast cooling (FC).

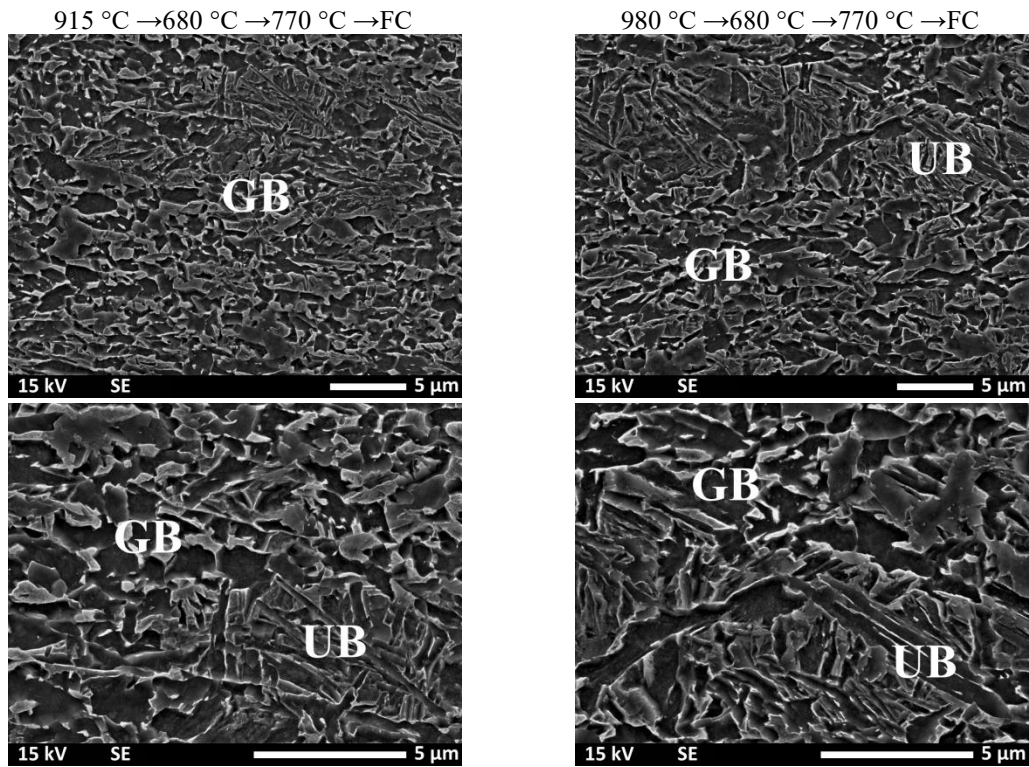


Fig. 57. GB with some UB regions in the samples after heating to the austenitization, deformation at 680 °C with increased temperature and fast cooling (FC).

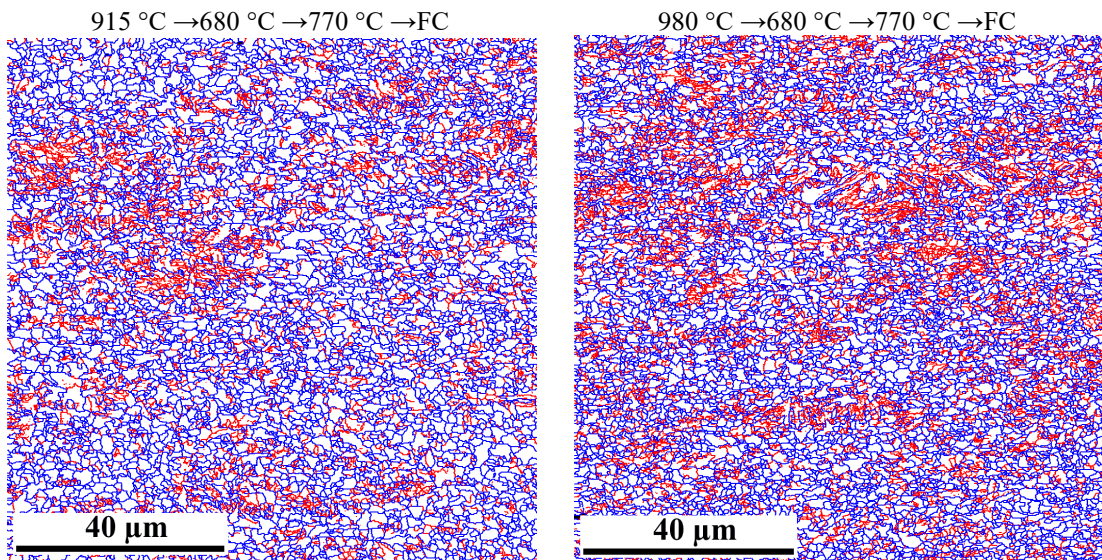


Fig. 58. Distribution of the LAGB (red) and HAGB (blue) for the samples after heating to the austenitization, deformation at 680 °C with increased temperature and fast cooling (FC).

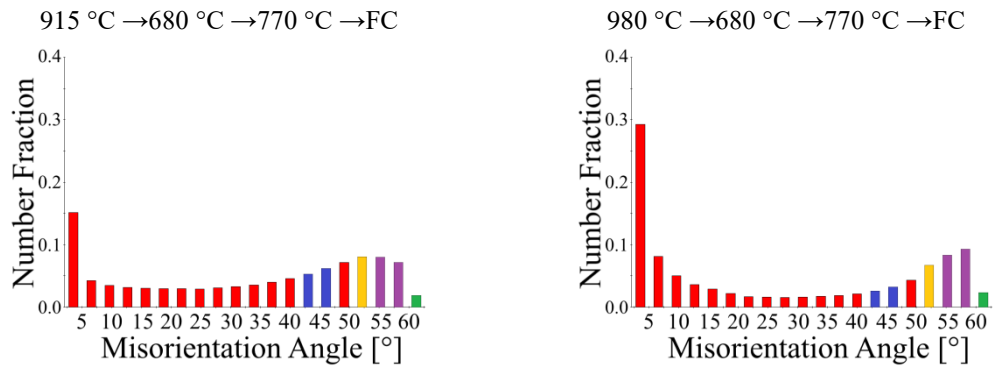


Fig. 59. Misorientation angles for the samples after heating to the austenitization, deformation at 680 °C with increased temperature and fast cooling (FC).

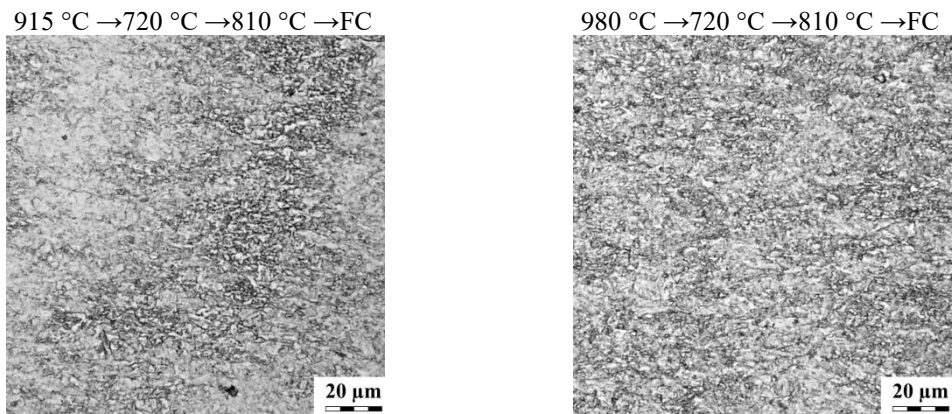


Fig. 60 LOM structure of the samples after heating to the austenitization, deformation at 720 °C with increased temperature and fast cooling (FC).

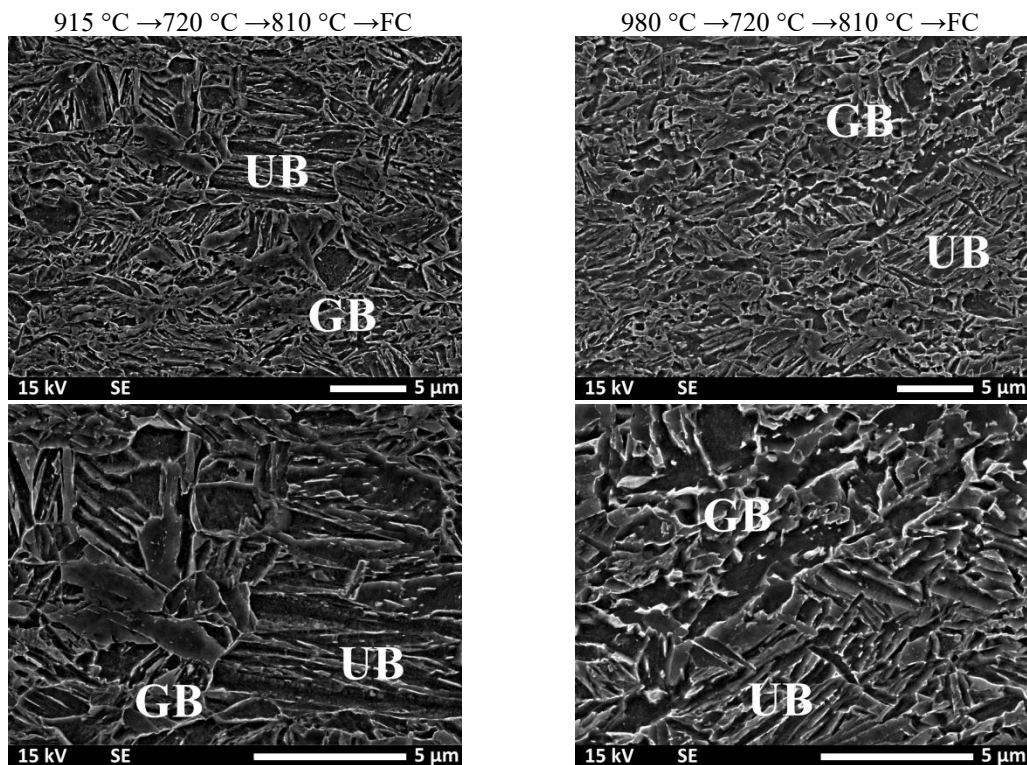


Fig. 61. Mixture of upper and GB in the samples after heating to the austenitization, deformation at 720 °C with increased temperature and fast cooling (FC).

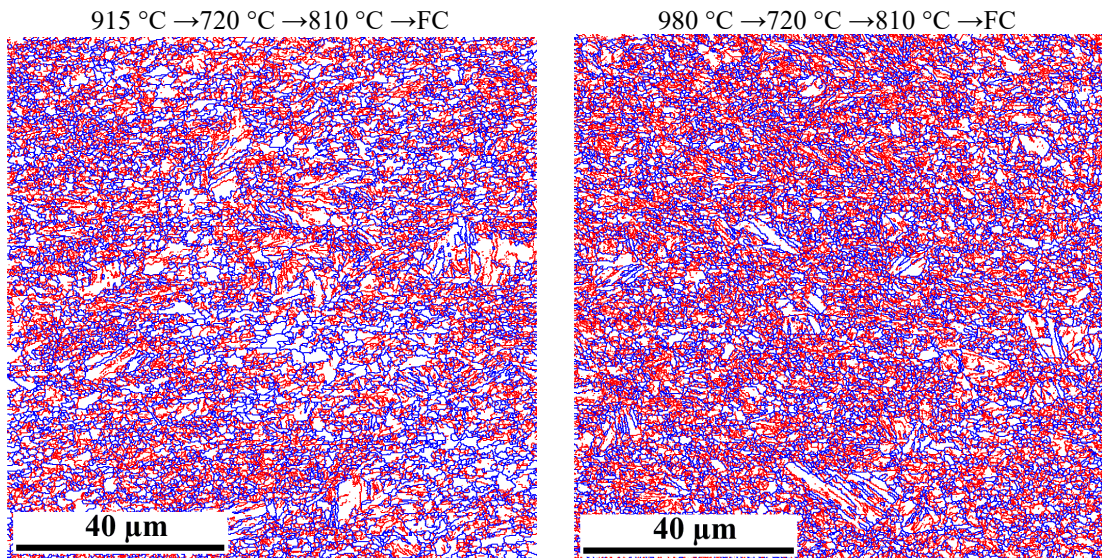


Fig. 62. Distribution of the LAGB (red) and HAGB (blue) for the samples after heating to the austenitization, deformation at 720 °C with increased temperature and fast cooling (FC).

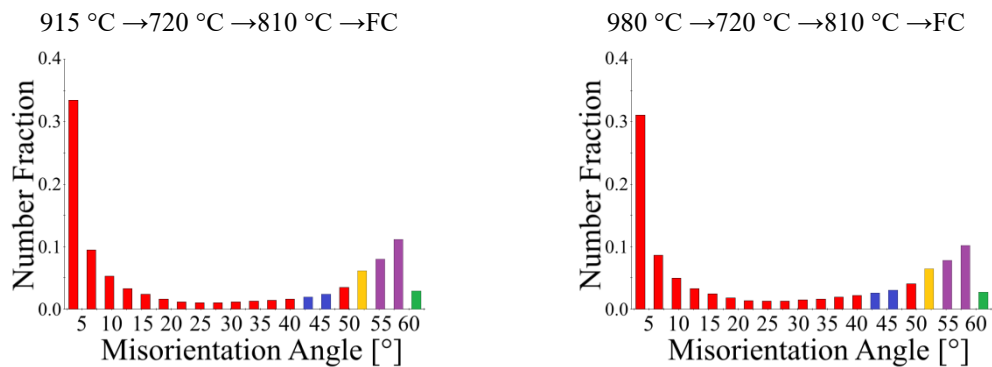


Fig. 63. Misorientation angles for the samples after heating to the austenitization, deformation at 720 °C with increased temperature and fast cooling (FC).

The last part of the process simulation was performed without deformation. Samples were heated to the austenitization temperature, then cooled to the rolling temperature. In this case, the samples were not deformed, only cooled to three final temperatures (T_2) and then cooled in air. The results for samples groups are presented in Fig. 64 - 67, 68 - 71, 72 - 75 and 76 - 79 for the same initial temperature sets "915 °C → 680 °C → 770 °C", "980 °C → 680 °C → 770 °C", "915 °C → 720 °C → 810 °C" and "980 °C → 720 °C → 810 °C", respectively. For samples cooled down to 400 °C mostly LB was obtained (Fig. 65, 69, 73 and 77), according to the lowest temperature of formation of this type of bainite. The cooling to 500 °C and 600 °C allows to obtain the GB structure with allotrimorphic ferrite characterized by varying proportion and size (Fig. 65, 69, 73 and 77). However, the higher final temperature causes coarser GB due to a higher transformation temperature (Fig. 66, 70, 74 and 78). In HAGB terms, it can be seen that the total length of these boundaries decreases as the final temperature increases

(Fig. 55). This is related to the morphology of the resulting bainitic structure. Samples cooled to 400 °C contain LB, which is characterized by a low proportion of LAGB and an elevated proportion for HAGB, especially from 55° to 60°, as can be seen in the distributions of MA (Fig. 67, 71, 75 and 79). On the other hand, the difference observed for samples where GB was obtained is due to the final temperature for these samples (500 °C and 600 °C). For 600 °C temperature, coarser packets of bainite in comparison to 500 °C were observed, so the HAGB total length/area is lower (Fig. 66, 70, 74 and 78).

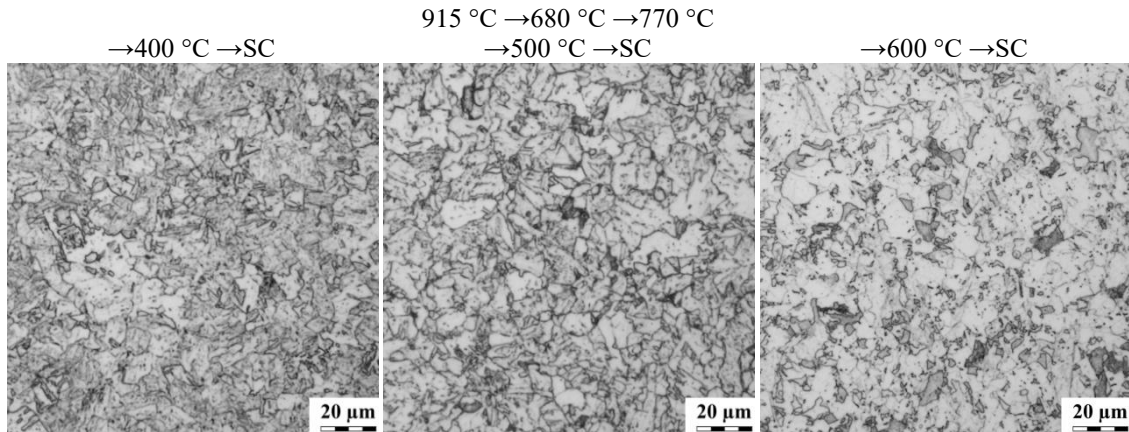


Fig. 64. LOM structure of the samples after heating to the austenitization temperature 915 °C, cooling to 680 °C with increased temperature to 770 °C, fast cooling to the different temperature and slow cooling (SC).

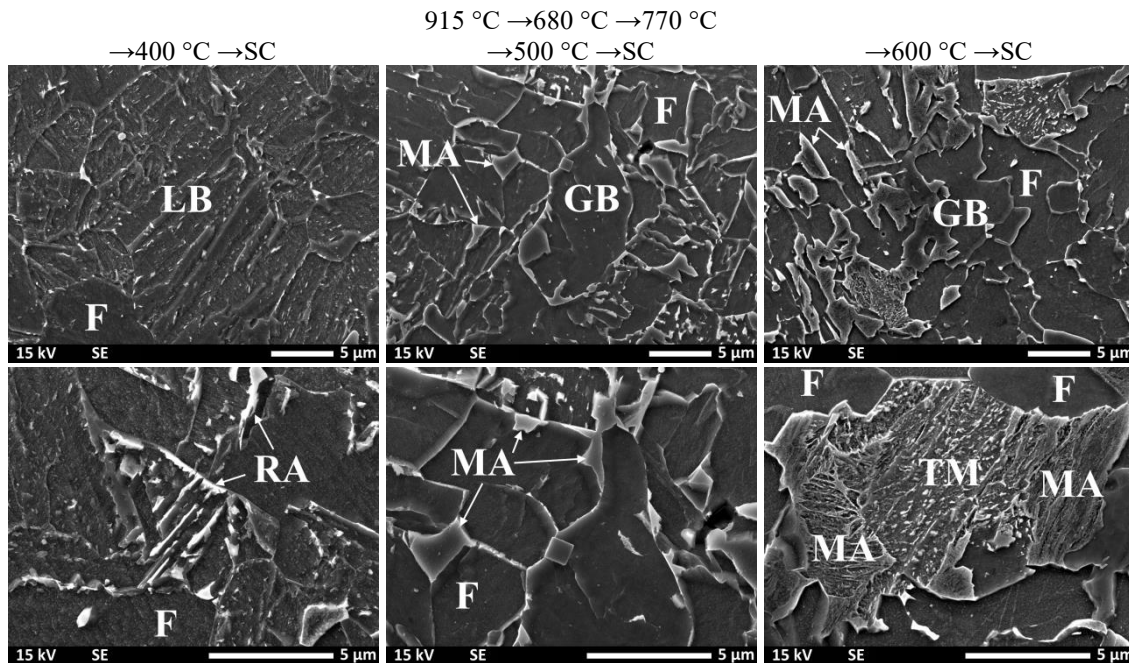


Fig. 65. SEM structure of the samples after heating to the austenitization temperature 915 °C, cooling to 680 °C with increased temperature to 770 °C, fast cooling to the different temperature and slow cooling (SC).

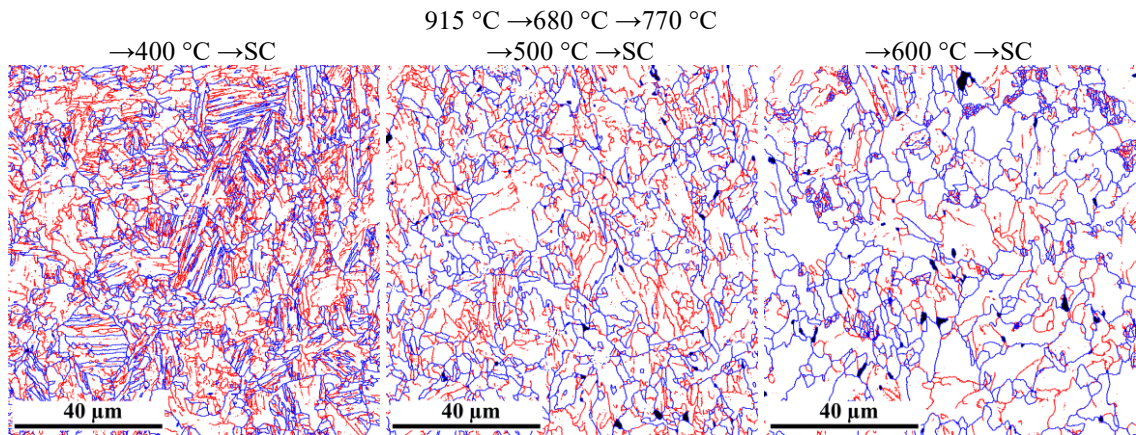


Fig. 66. Distribution of the LAGB (red) and HAGB (blue) on the phase map with A (black) for the samples after heating to the austenitization temperature 915 °C, cooling to 680 °C with increased temperature to 770 °C, fast cooling to the different temperature and slow cooling (SC).

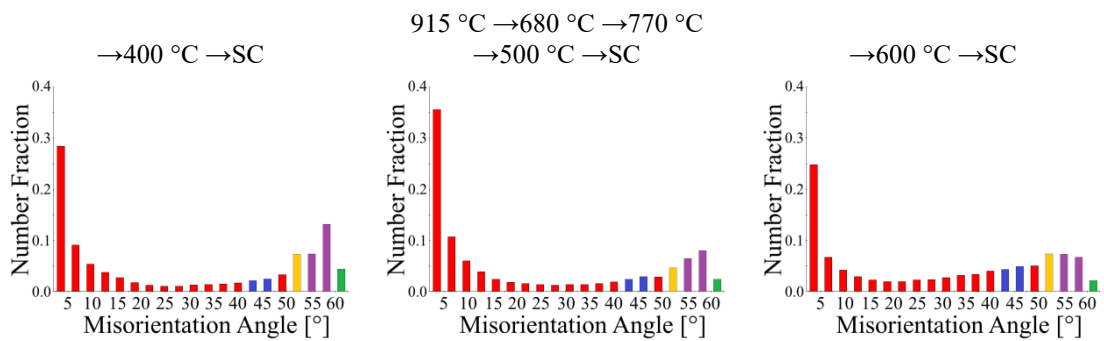


Fig. 67. Misorientation angles for the samples after heating to the austenitization temperature 915 °C, cooling to 680 °C with increased temperature to 770 °C, fast cooling to the different temperature and slow cooling (SC).

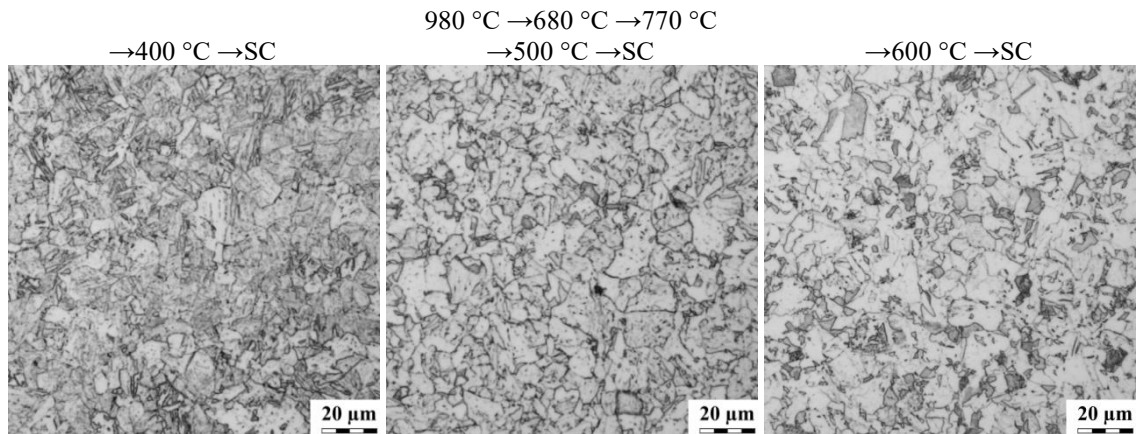


Fig. 68. LOM structure of the samples after heating to the austenitization temperature 980 °C, cooling to 680 °C with increased temperature to 770 °C, fast cooling to the different temperature and slow cooling (SC).

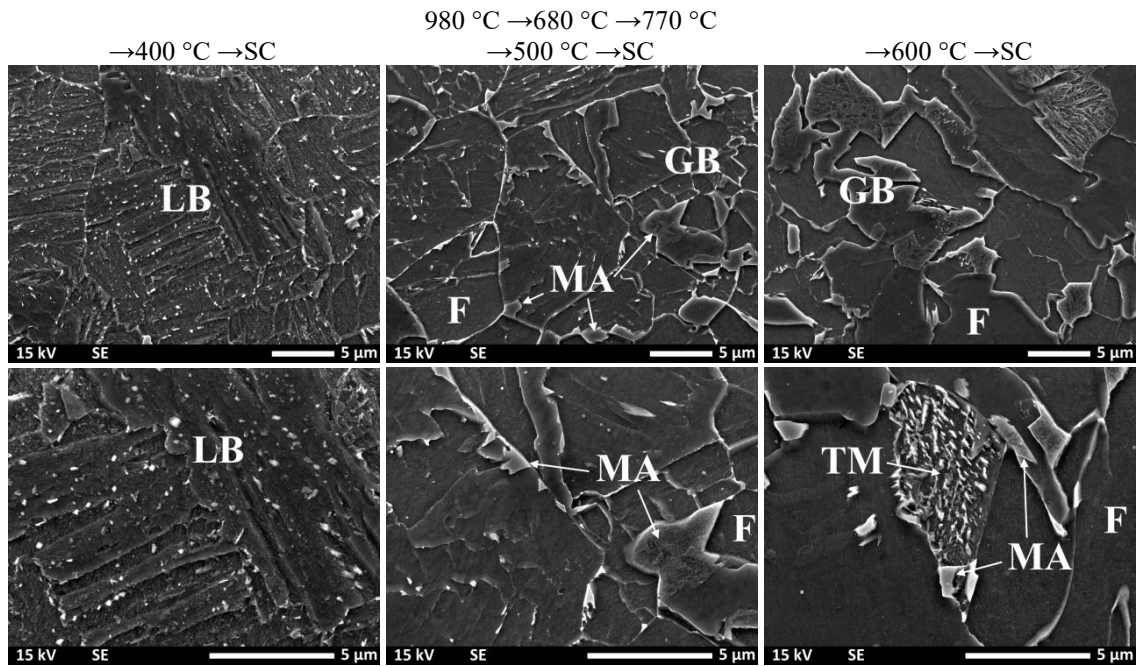


Fig. 69. SEM structure of the samples after heating to the austenitization temperature $980\text{ }^{\circ}\text{C}$, cooling to $680\text{ }^{\circ}\text{C}$ with increased temperature to $770\text{ }^{\circ}\text{C}$, fast cooling to the different temperature and slow cooling (SC).

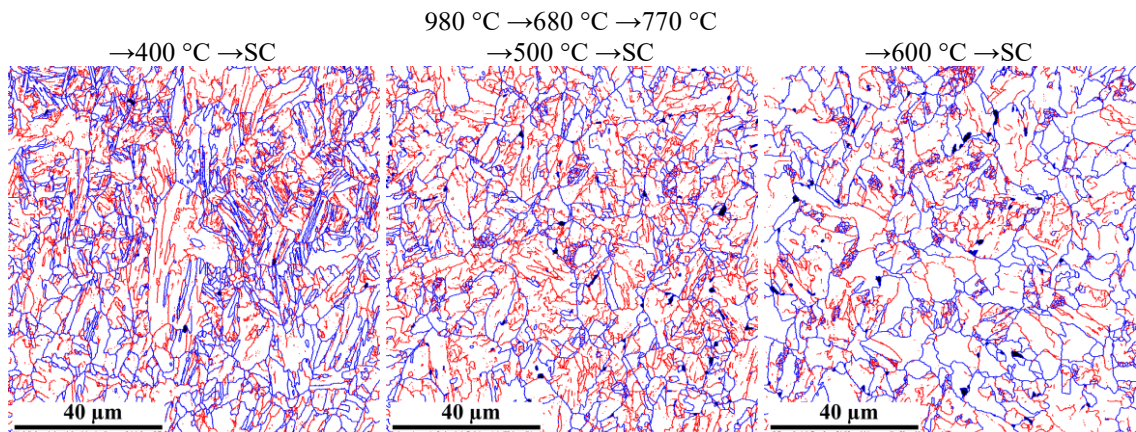


Fig. 70. Distribution of the LAGB (red) and HAGB (blue) on the phase map with A (black) for the samples after heating to the austenitization temperature $980\text{ }^{\circ}\text{C}$, cooling to $680\text{ }^{\circ}\text{C}$ with increased temperature to $770\text{ }^{\circ}\text{C}$, fast cooling to the different temperature and slow cooling (SC).

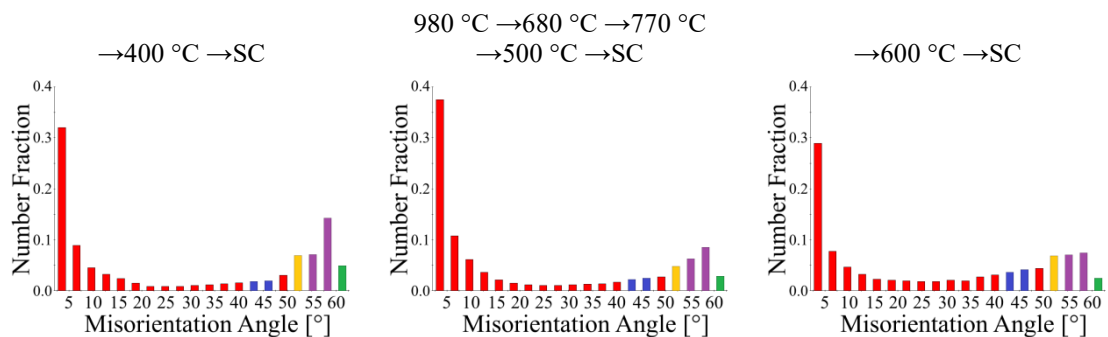


Fig. 71. Misorientation angles for the samples after heating to the austenitization temperature $980\text{ }^{\circ}\text{C}$, cooling to $680\text{ }^{\circ}\text{C}$ with increased temperature to $770\text{ }^{\circ}\text{C}$, fast cooling to the different temperature and slow cooling (SC).

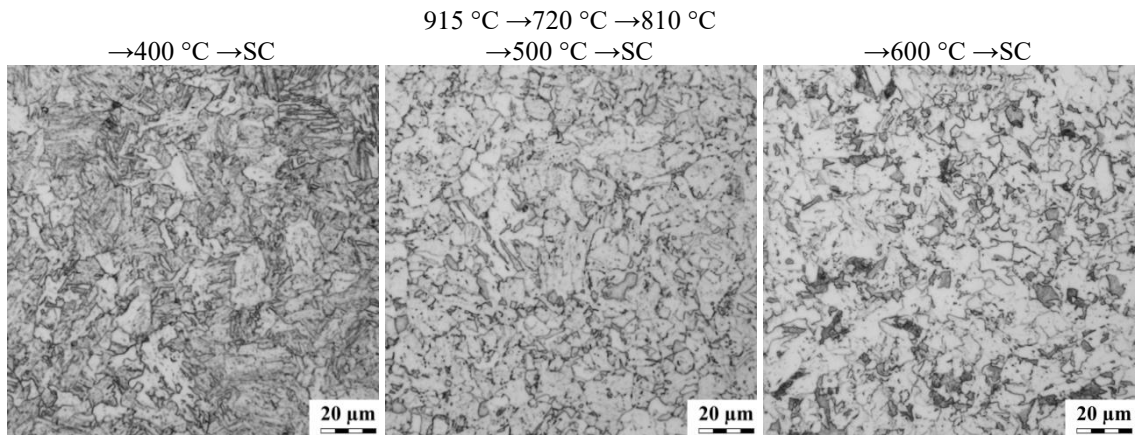


Fig. 72. LOM structure of the samples after heating to the austenitization temperature 915 °C, cooling to 720 °C with increased temperature to 810 °C, fast cooling to the different temperature and slow cooling (SC).

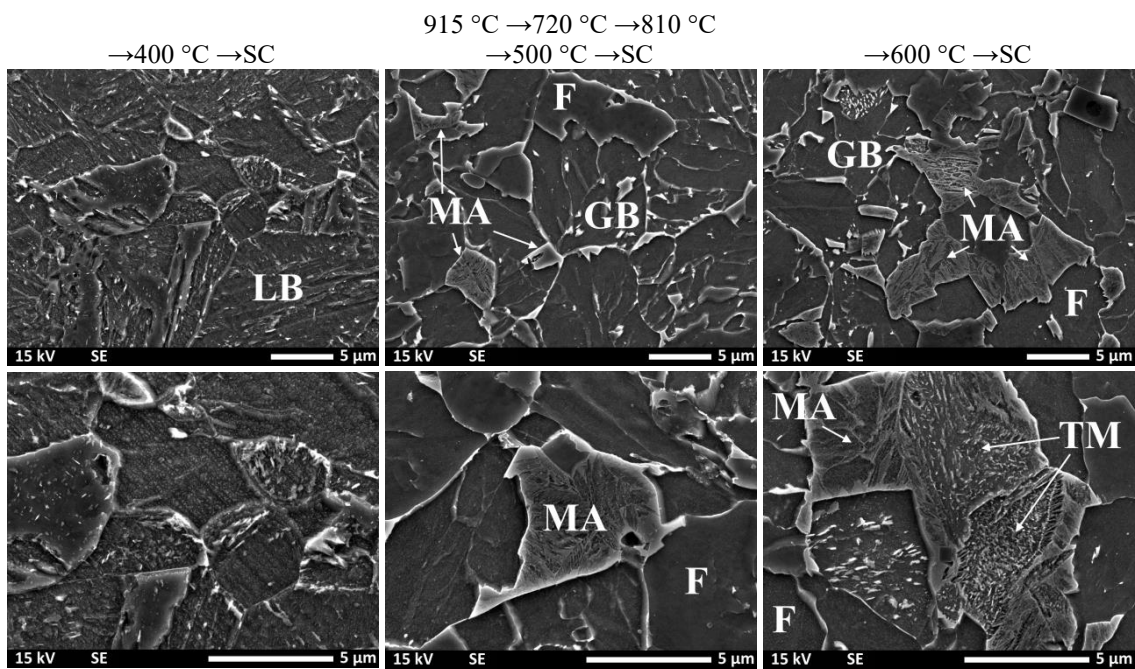


Fig. 73. SEM structure of the samples after heating to the austenitization temperature 915 °C, cooling to 720 °C with increased temperature to 810 °C, fast cooling to the different temperature and slow cooling (SC).

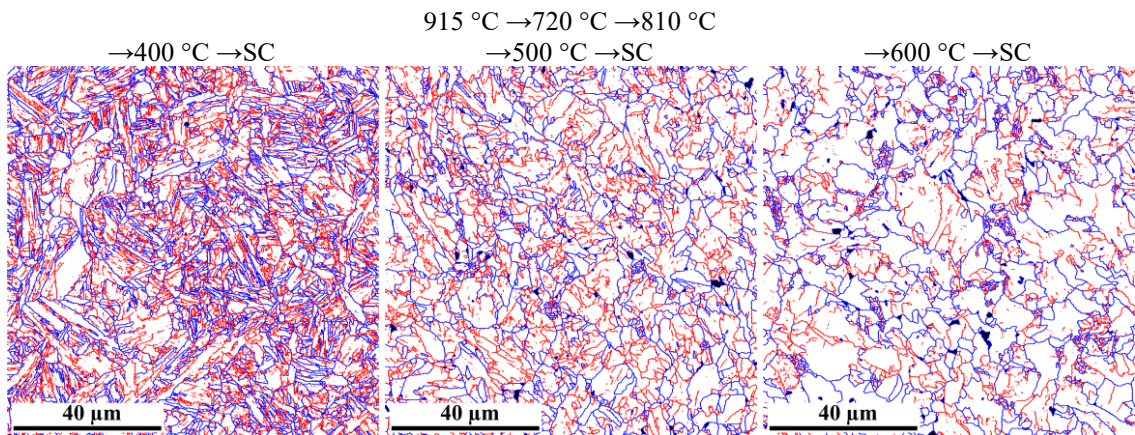


Fig. 74. Distribution of the LAGB (red) and HAGB (blue) on the phase map with A (black) for the samples after heating to the austenitization temperature 915 °C, cooling to 720 °C with increased temperature to 810 °C, fast cooling to the different temperature and slow cooling (SC).

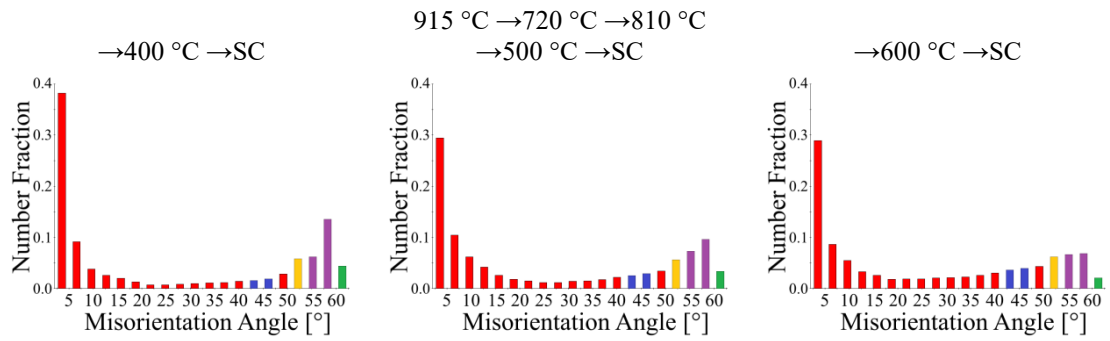


Fig. 75. Misorientation angles for the samples after heating to the austenitization temperature 915 °C, cooling to 720 °C with increased temperature to 810 °C, fast cooling to the different temperature and slow cooling (SC).

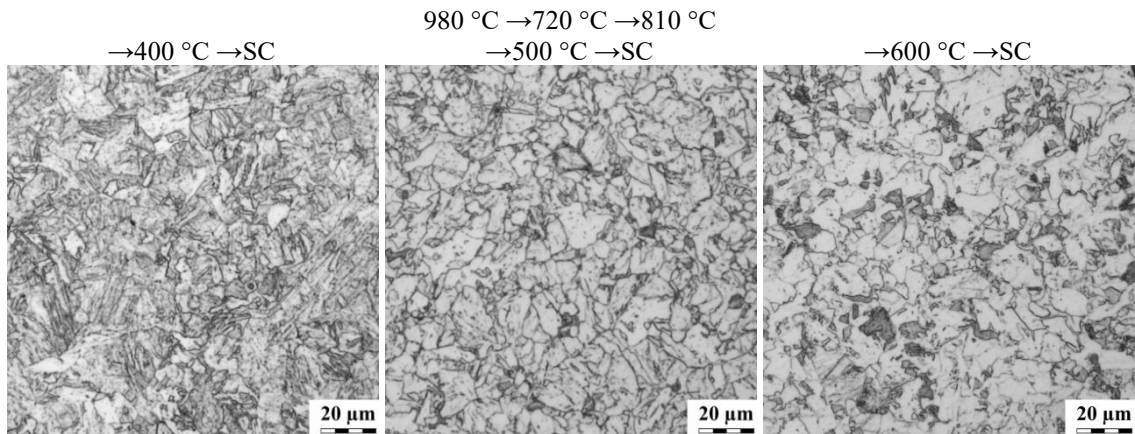


Fig. 76. LOM structure of the samples after heating to the austenitization temperature 980 °C, cooling to 720 °C with increased temperature to 810 °C, fast cooling to the different temperature and slow cooling (SC).

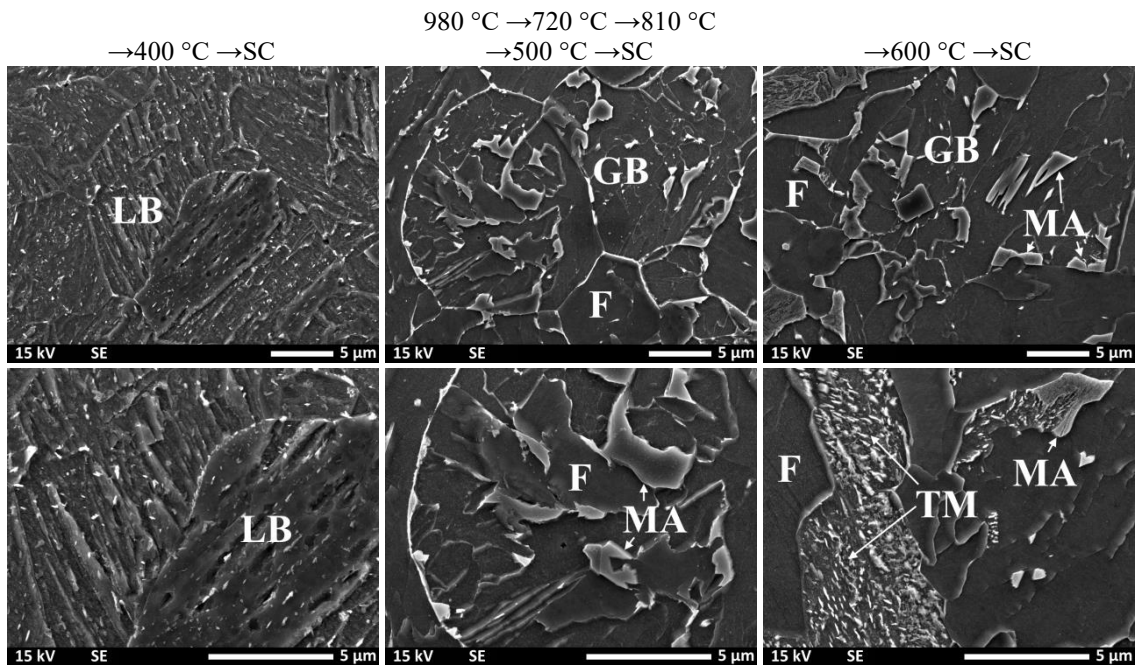


Fig. 77. SEM structure of the samples after heating to the austenitization temperature 980 °C, cooling to 720 °C with increased temperature to 810 °C, fast cooling to the different temperature and slow cooling (SC).

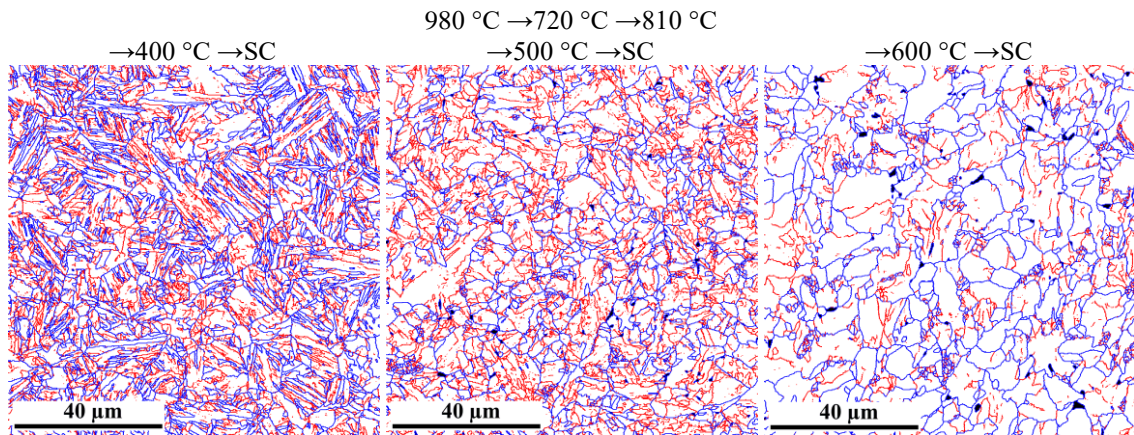


Fig. 78. Distribution of the LAGB (red) and HAGB (blue) on the phase map with A (black) for the samples after heating to the austenitization temperature 980 °C, cooling to 720 °C with increased temperature to 810 °C, fast cooling to the different temperature and slow cooling (SC).

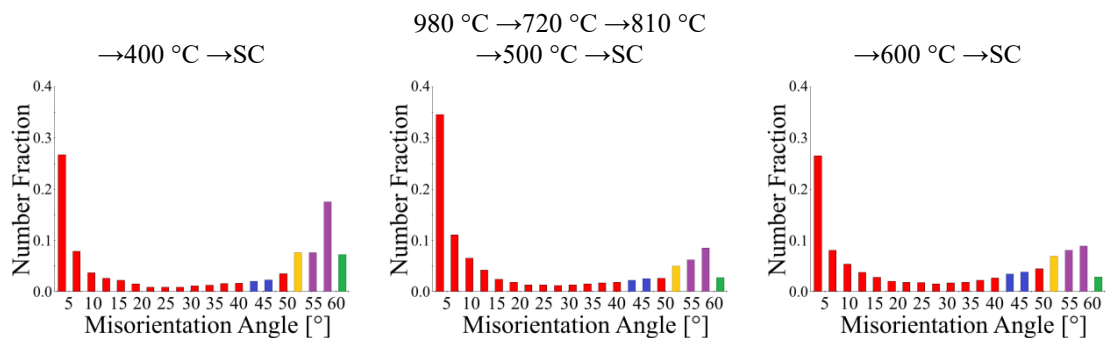


Fig. 79. Misorientation angles for the samples after heating to the austenitization temperature 980 °C, cooling to 720 °C with increased temperature to 810 °C, fast cooling to the different temperature and slow cooling (SC).

Analysis of the area fraction and grain size of RA (Fig. 80) shows no significant differences between samples only austenitized or after deformation. The differences are observed in the samples cooled to three final temperatures. The highest area fraction of RA is in the samples with GB, where carbon from the bainitic ferrite stabilizes RA, while in LB carbon is mostly consumed by cementite precipitations, thus low fraction of RA is observed in the samples cooled down to 400 °C. Furthermore, as it can be noticed, a sample (915 °C → 680 °C → 770 °C) cooled down to 500 °C has more RA than the sample with the final intermediate temperature of 600 °C. The simulations scheme shows that the cooling rate for those samples was 7.9 °C/s (Fig. 37). Because of that, a part of the A could transform to M, if the cooling rate was sufficient and for the samples cooled with 5.0 °C/s, phase transformation may occur different as with cooling rate 7.9 °C/s. However, it needs to be highlighted that the area fraction of the M was not analyzed quantitatively at this stage of the research. In the samples with the final temperature of 600 °C, areas with TM were observed (Fig. 65, 69, 73 and 77). The conclusion is that high temperature and slow cooling in air may cause auto-tempering of the M present in the structure.

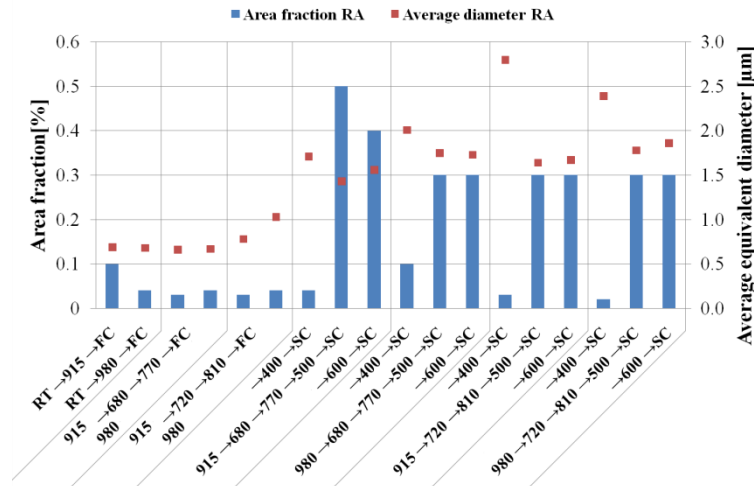


Fig. 80. Area fraction and average diameter of RA for all samples after process simulations.

Simulations of the process conducted with the use of samples from 7MnB8 steel showed slight differences in the grain size of the former austenite depending on the austenitizing temperature and the holding time at that temperature. In addition, the steel structure was found to be most affected by the final temperature after accelerated cooling. The structure of samples cooled to 400 °C was characterized by LB, while those cooled to 500 °C and 600 °C, with GB with M/A islands. The highest final temperature (600 °C) was found to result in the tempering of martensite upon further cooling in air.

5.1.3. Thermodynamic calculations

In order to prepare a proposal for the process parameters, the simulations results were supplemented with the characteristic temperature stable phases, estimated by using ThermoCalc software (Fig. 81), however the investigations were focused on precipitations in steel. The calculations were performed based on the results of chemical composition analysis for 7MnB8 steel, which are presented in Table 2. The first stable phase is Ti carbonitride, which precipitates in the first stage, during the crystallization from the liquid. Then, as it continues to cool, $Ti_4C_2S_2$ phase begins to separate in the temperature range between ~1140 °C and ~1230 °C, while the sulfur binding tendency changes. At ~1230 °C, the precipitation of MnS begins.

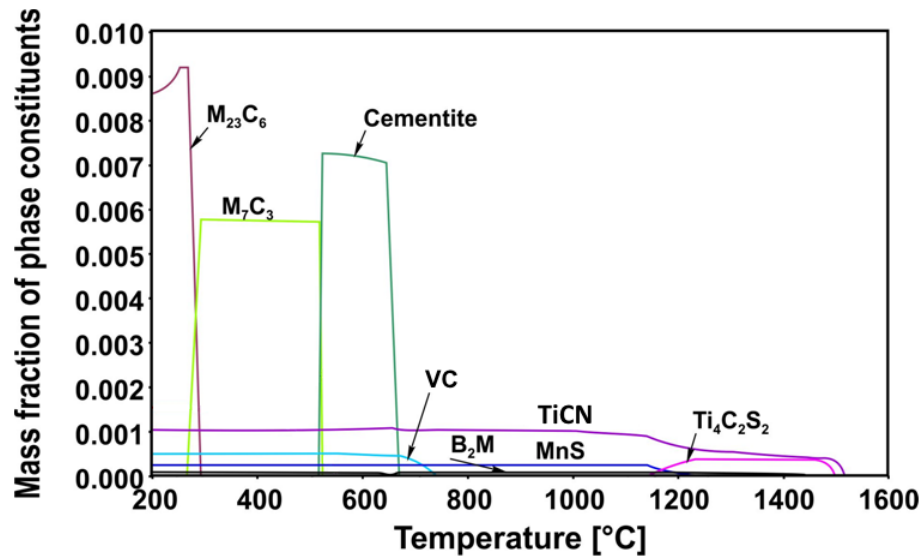


Fig. 81. Characteristic temperature stable phases for industrial 7MnB8 steel.

Earlier, at ~ 1450 °C, the B_2M phase appears. At ~ 730 °C, VC carbide formation begins, while cementite is formed at 670 °C. Unlike VC carbides, which are formed during cooling to 200 °C, cementite precipitates up to ~ 510 °C. At this temperature, M_7C_3 -type carbides begin to precipitate, and at around ~ 180 °C they cease to participate in the precipitation processes in favor of $M_{23}C_6$ -type carbides. Due to a high titanium content of the steel and a high formation temperature of TiCN and $Ti_4C_2S_2$, large precipitations of these phases in the structure can be expected. According to the literature review, these precipitations negatively affect the resistance of steel to dynamic loads [128,129]. Therefore, efforts should be made to minimize the size of these precipitations, which will improve the mechanical properties.

5.2. Industrial trials with the developed process parameters for 7MnB8 steel

In order to determine the effect of XTP process parameters on the mechanical properties, microstructure and phase composition of industrial 7MnB8 steel, a rolling process was carried out using four groups of parameters with varying austenitizing temperature, rolling temperature and post-rolling cooling intensity. Accelerated cooling carried out immediately after the guided deformation determines the final temperature of the bar, from which slow cooling in air follows. A summary of the applied temperature and cooling rates in the conducted industrial tests is presented in Table 3.

5.2.1. Tensile tests

The results of tensile tests are presented in Fig. 82. Furthermore, in Fig. 83 stress-strain curves for all samples are presented. As it can be seen in comparison to the initial state of the material, after rolling the elongation and UTS, an increase of ~10% for all rolling schedules can be observed.

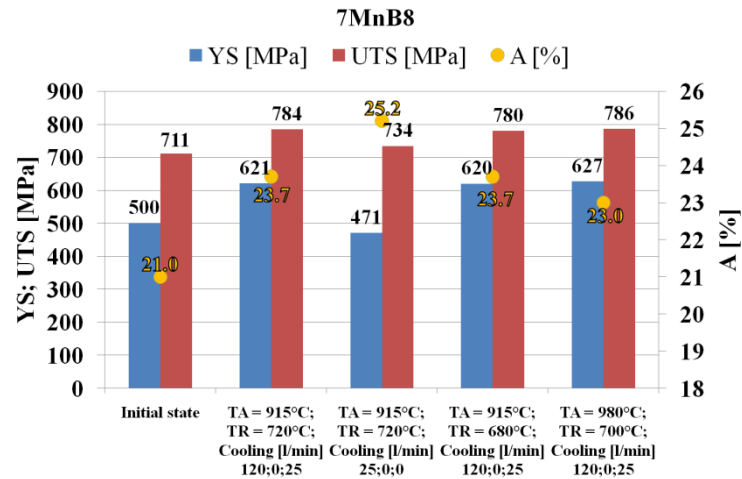


Fig. 82. Mechanical properties of industrial 7MnB8 steel in the initial state and after rolling with different process parameters.

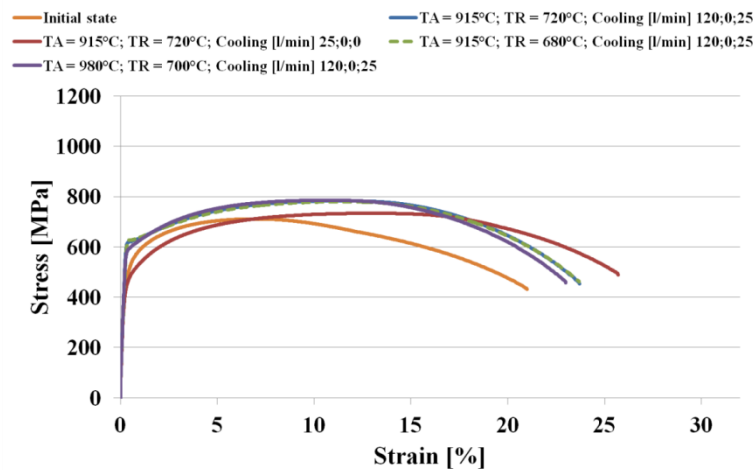


Fig. 83. Stress-strain curve for 7MnB8 steel in the initial state and after rolling.

However, the sample with the highest final temperature after the process in which the cooling rate was the lowest, the UTS, increases only by ~3%. Moreover, a drop in the YS and, simultaneously, the highest value of the elongation can be observed for this sample. For samples made from the bars with austenitization temperature 915 °C with a high cooling rate (system of boxes 120;0;25) after rolling, the stress-strain curves with pronounced YS can be observed, in contrast to the rest (Fig. 83).

5.2.2. Hardness measurements

The hardness measurements were performed for the raw material (Fig. 84) and after rolling (Fig. 85). Furthermore, average hardness was estimated in the visible zones (Table 7).

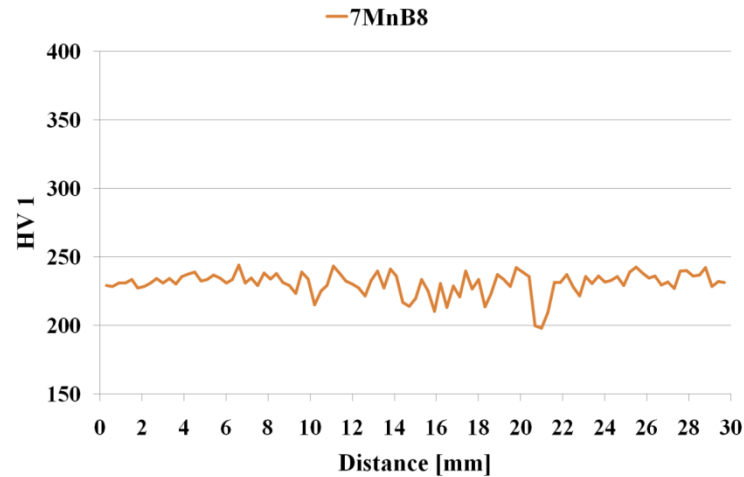


Fig. 84. Cross-section profile on the diameter of the HV₁ hardness for 7MnB8 material in the initial state.

Table 7. Average HV₁ measured in two areas for 7MnB8 steel in the initial state and after rolling.

Area	Initial state	T _A = 915 °C; T _R = 720 °C; Cooling [l/min] 120;0;25	T _A = 915 °C; T _R = 720 °C; Cooling [l/min] 25;0;0	T _A = 915 °C; T _R = 680 °C; Cooling [l/min] 120;0;25	T _A = 980 °C; T _R = 700 °C; Cooling [l/min] 120;0;25
2 mm from the surface	231 ± 9	323 ± 27	204 ± 10	323 ± 24	323 ± 28
Core		243 ± 8	209 ± 10	238 ± 9	240 ± 7

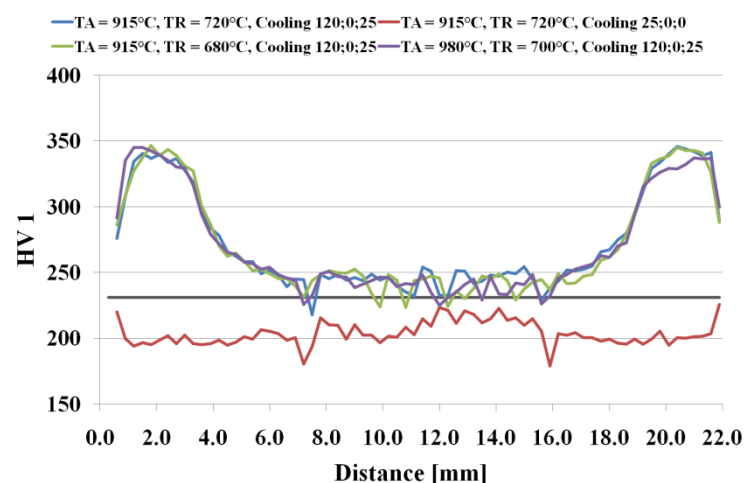


Fig. 85. Cross-section profile of the HV₁ hardness on the diameter for 7MnB8 steel after rolling. Gray line - average hardness of 7MnB8 material in the initial state.

As it can be seen, due to grain refinement in the outer layer, the hardness increased by 100 HV for all samples cooled after the deformation, with a high cooling rate. However,

the hardness of the bar with slow cooling is less than for the material in the initial state, despite the fact that a smaller grain size was obtained.

5.2.3. Charpy tests

The results of Charpy V-notch impact measurements are presented in Fig. 86. The DBTT were estimated with the use of polynomial regression (Table 8).

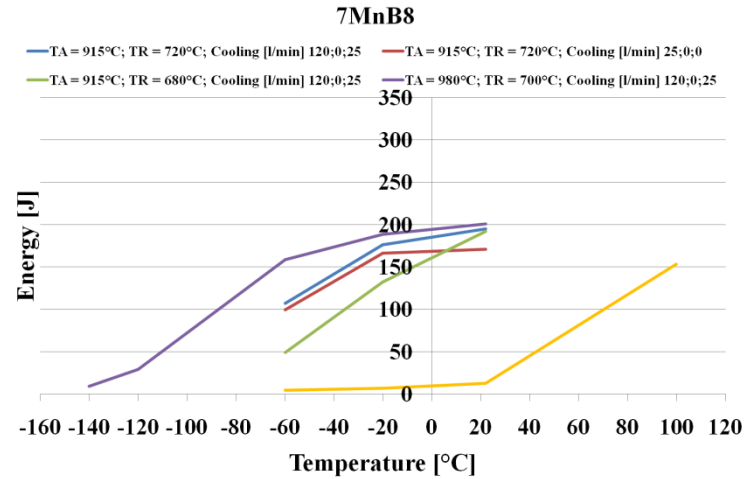


Fig. 86. Charpy V-notch impact measurements at different temperature for 7MnB8 steel in the initial state (yellow line) and after rolling.

Table 8. Estimated DBTT for 7MnB8 steel in the initial state and after rolling, in °C.

DBTT [°C]				
Initial state	T _A = 915 °C T _R = 720 °C Cooling [l/min] 120;0;25	T _A = 915 °C T _R = 720 °C Cooling [l/min] 25;0;0	T _A = 915 °C T _R = 780 °C Cooling [l/min] 120;0;25	T _A = 980 °C T _R = 700 °C Cooling [l/min] 120;0;25
45	-90	-90	-70	-120

In Fig. 86 it can be seen that with the use of all groups of rolling parameters compared to the raw material, the fracture energy was increased and the DBTT values were shifted to the left and are lower (Table 8).

5.2.4. Light optical microscopy

The LOM investigations for 7MnB8 steel in the initial state and after rolling with proposed four groups of process parameters (Table 3) are presented in Fig. 87 - 92. The bainitic structure is produced in trials with a high cooling rate, in opposition to the trial with a decreased cooling rate, where ferrite with M/A islands can be recognized (Fig. 90). As it can be seen in Fig. 87, two zones on the cross-sections of the bars can be observed

after rolling, with refined structure on the surfaces of the bars after rolling in comparison to the initial bar. The obtained gradient structure is also visible for the LOM cross-section structures of the bars in Fig. 88 - 92. Furthermore, comparing the zones observed in the bars after rolling, a finer than in the cores structure is observed on the surface (Fig. 89 - 92). However, the thickness of the outer zone of the bar is decreased after less intense cooling and after rolling (Fig. 87).

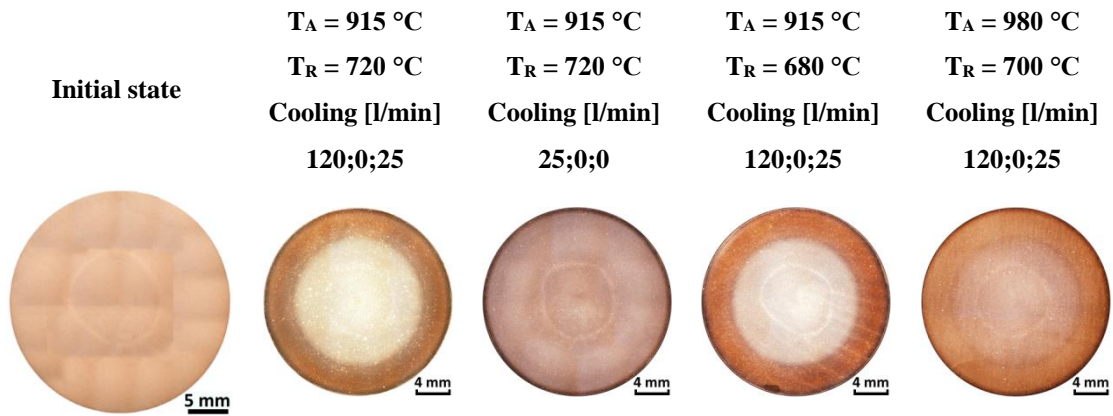


Fig. 87. Cross-section of the bars in the initial state and after rolling, 7MnB8 material.

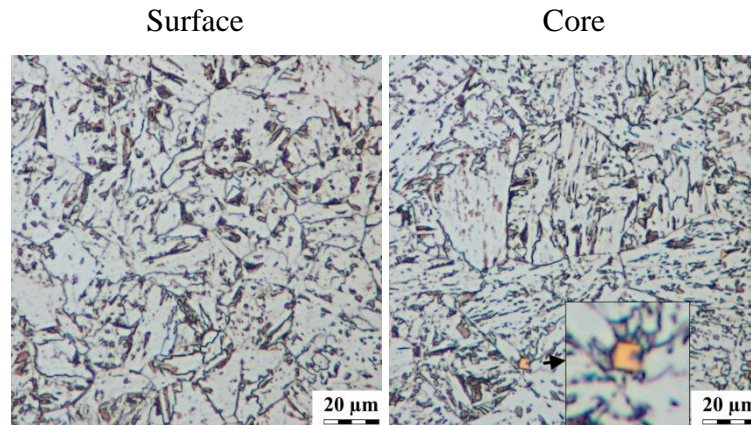


Fig. 88. LOM structure of 7MnB8 material in the initial state with coarse TiN precipitations, cross-section.

Furthermore, the larger grain size is obtained in comparison to the bars which were cooled more intensively by using cooling boxes in the 120;0;25 arrangement (Fig. 89 - 92). It is due to a higher temperature at the end of the process, which was 720 °C. The temperature leads to the recrystallization processes and grain growth after rolling so in the outer layer and in the core area the grain size increased (Fig. 90).

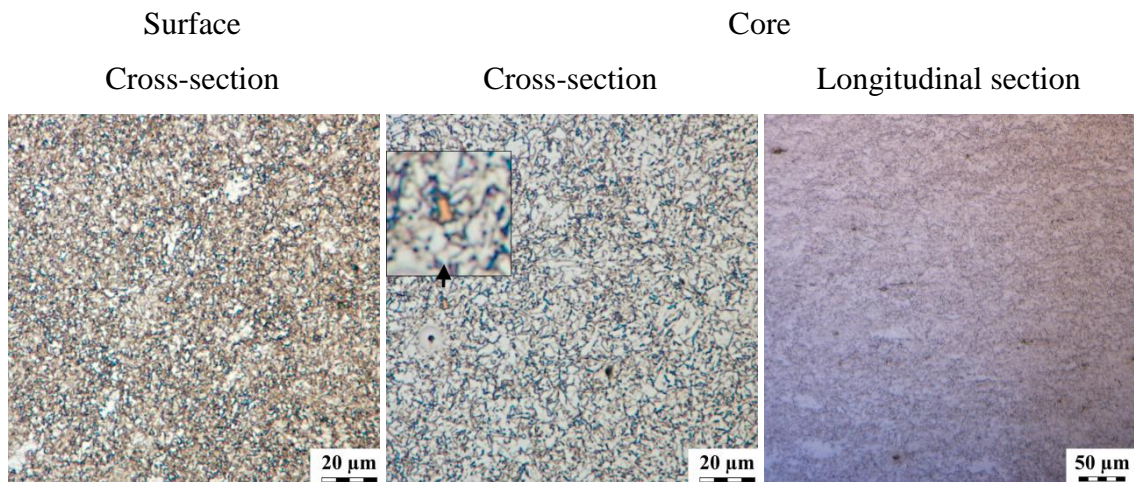


Fig. 89. LOM structure of 7MnB8 steel rolled using process parameters: $T_A = 915\text{ }^\circ\text{C}$; $T_R = 720\text{ }^\circ\text{C}$; Cooling [l/min] 120;0;25, with coarse TiN precipitations.

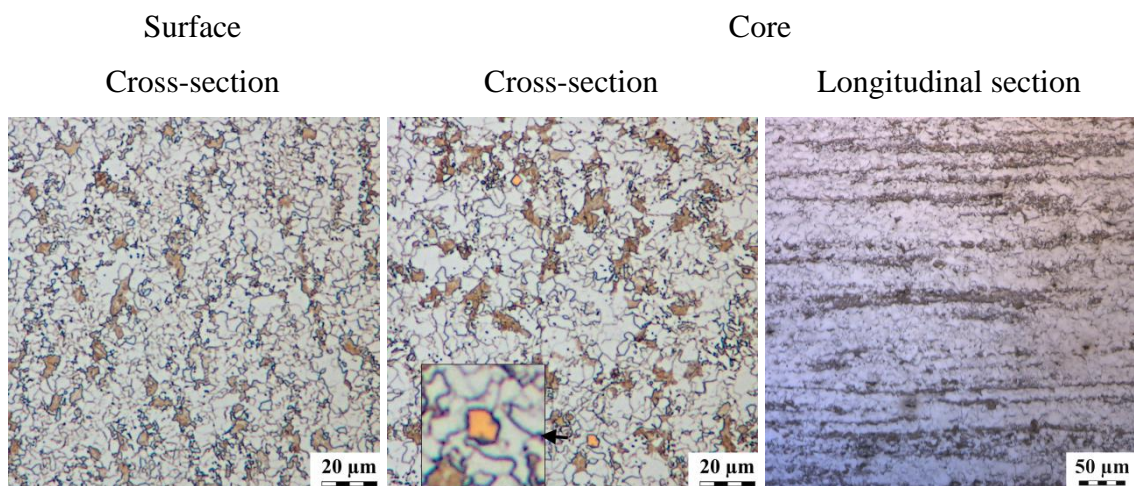


Fig. 90. LOM structure of 7MnB8 steel rolled using process parameters: $T_A = 915\text{ }^\circ\text{C}$; $T_R = 720\text{ }^\circ\text{C}$; Cooling [l/min] 25;0;0, with coarse TiN precipitations.

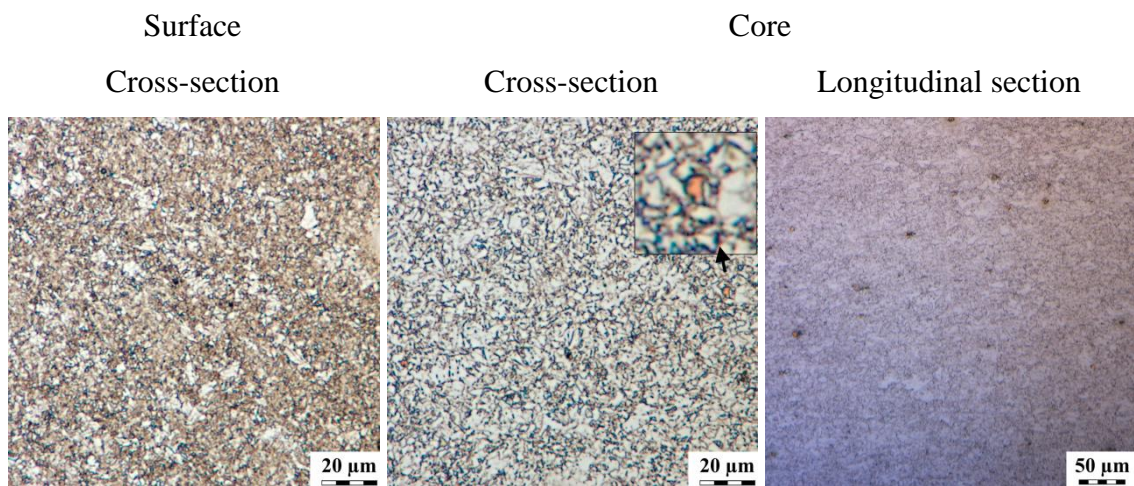


Fig. 91. LOM structure of 7MnB8 steel rolled using process parameters: $T_A = 915\text{ }^\circ\text{C}$; $T_R = 680\text{ }^\circ\text{C}$; Cooling [l/min] 120;0;25, with marked TiN precipitations.

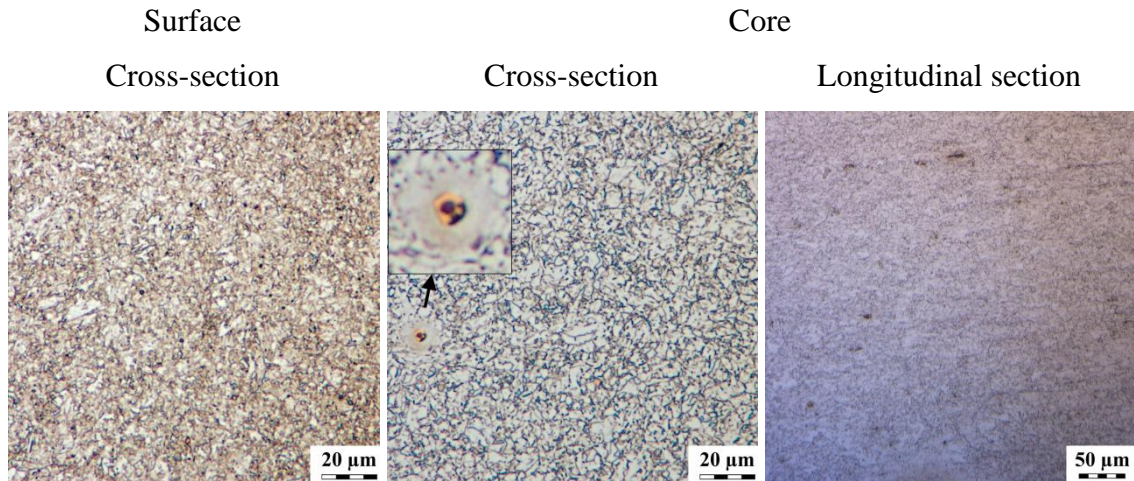


Fig. 92. LOM structure of 7MnB8 steel rolled using process parameters: $T_A = 980\text{ }^\circ\text{C}$; $T_R = 700\text{ }^\circ\text{C}$; Cooling [l/min] 120;0;25, with marked TiN precipitations.

Moreover, a banded structure occurs in the core (Fig. 90), lengthwise to the rolling direction. This also has its basis in the cooling rate and final temperature. However, as it was described in the literature review, this type of structure is expected in connection with the specific phenomena of the material flow during radial rolling. However, it is not observed in the rest of bars with more intensive cooling and lower final temperature, where fine grain size was obtained (Fig. 89, 91 and 92). As noted, higher temperature caused a recrystallization processes and grain growth, but it also facilitated the diffusion and segregation of the elements stabilizing A like carbon and Mn, therefore a banded structure was obtained.

5.2.5. Scanning electron microscopy

The SEM investigations included structure imaging by a SE detector and the EBSD method. The results are presented in Fig. 93 - 97 and Fig. 98 - 101, respectively. The SEM images and crystal orientation maps (Fig. 99) confirm the conclusions from the LOM microscopy. The structure refinement in comparison to the initial state (Fig. 93) of 7MnB8 steel is observed after all rolling variants (Fig. 94 - 97). Designated $D_{ef.}$ for steel before rolling equals $\sim 57,7 \mu\text{m}$, while after rolling the value decreases 3.5 - 7 times, depending on the rolling parameters (Table 9). GB is mainly observed in the bars, however the sample with a banded structure has the structure characteristics of Dual Phase (DP) steels due to the lower cooling rate (Fig. 95).

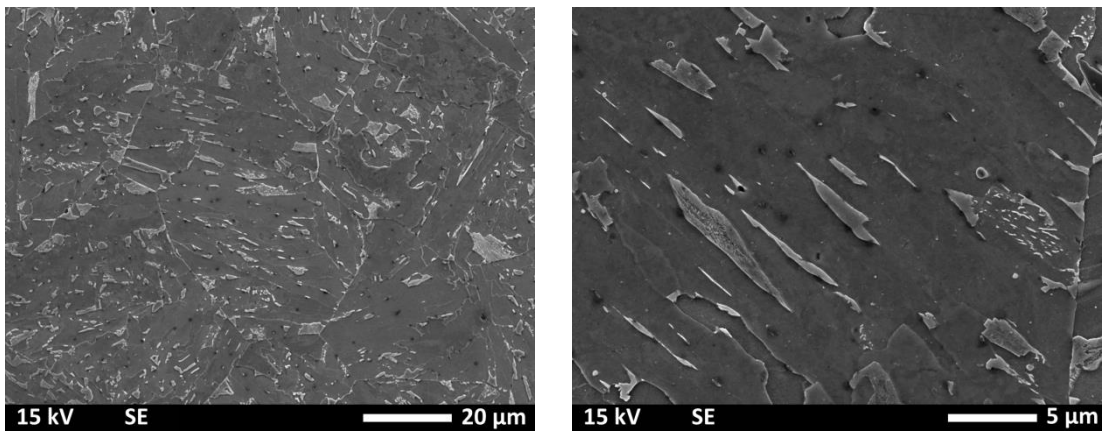


Fig. 93. SEM images of 7MnB8 material in the initial state.

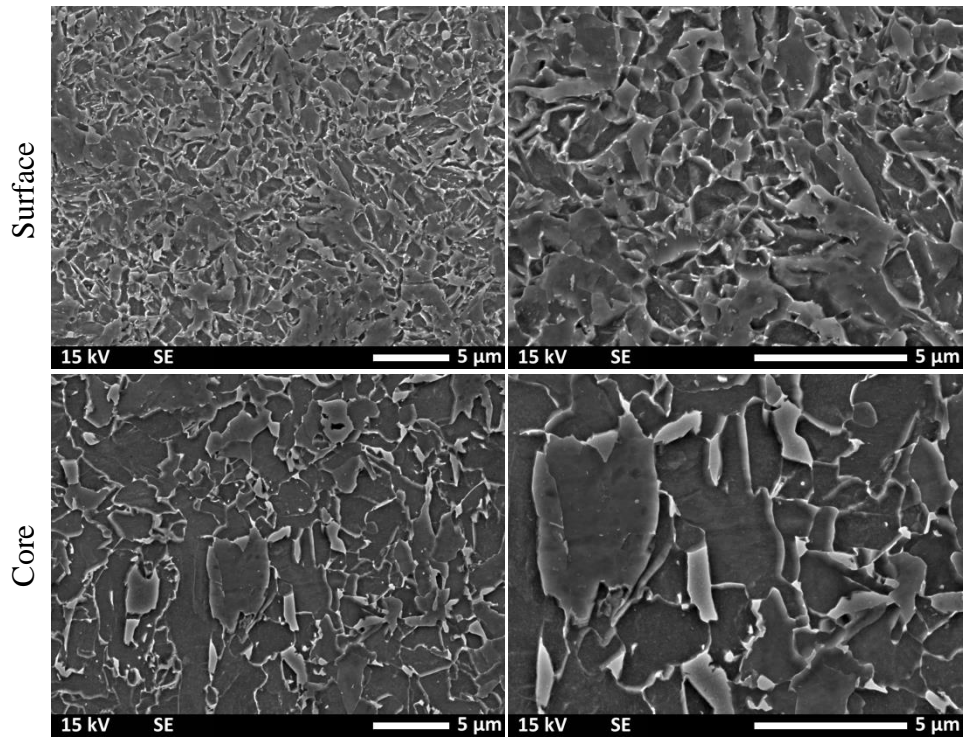


Fig. 94. GB in 7MnB8 steel rolled with use: $T_A = 915\text{ }^\circ\text{C}$; $T_R = 720\text{ }^\circ\text{C}$; Cooling [l/min] 120;0;25 process parameters.

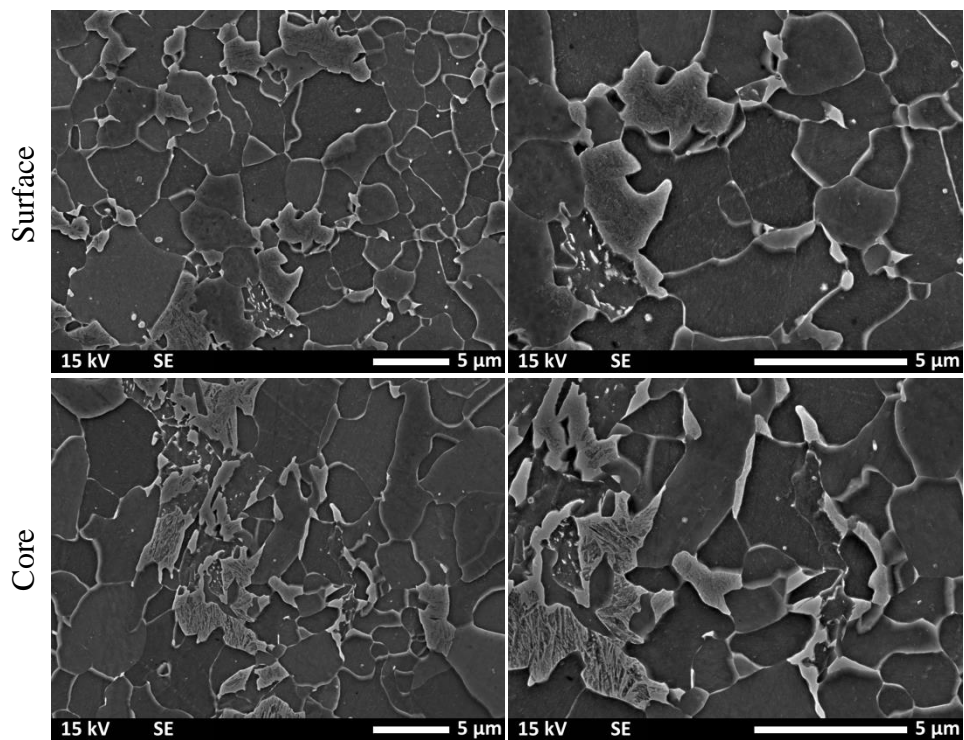


Fig. 95. Ferrite + M/A in 7MnB8 steel rolled with use: $T_A = 915\text{ }^\circ\text{C}$; $T_R = 720\text{ }^\circ\text{C}$; Cooling [l/min] 25;0;0 process parameters.

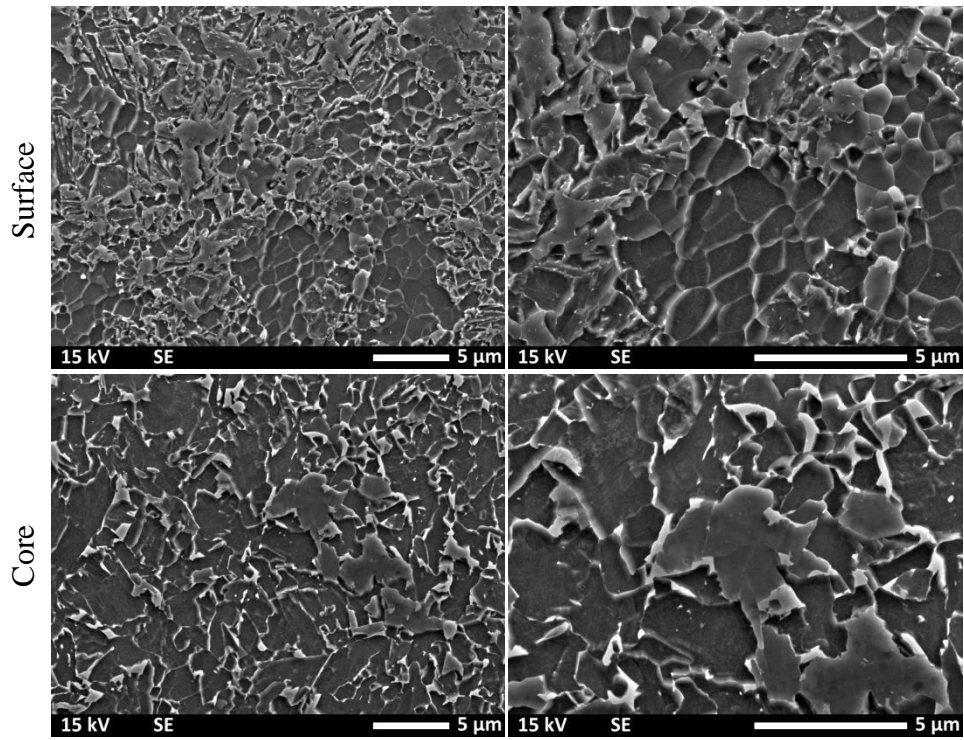


Fig. 96. GB in 7MnB8 steel rolled with use: $T_A = 915$ °C; $T_R = 680$ °C; Cooling [l/min] 120;0;25 process parameters.

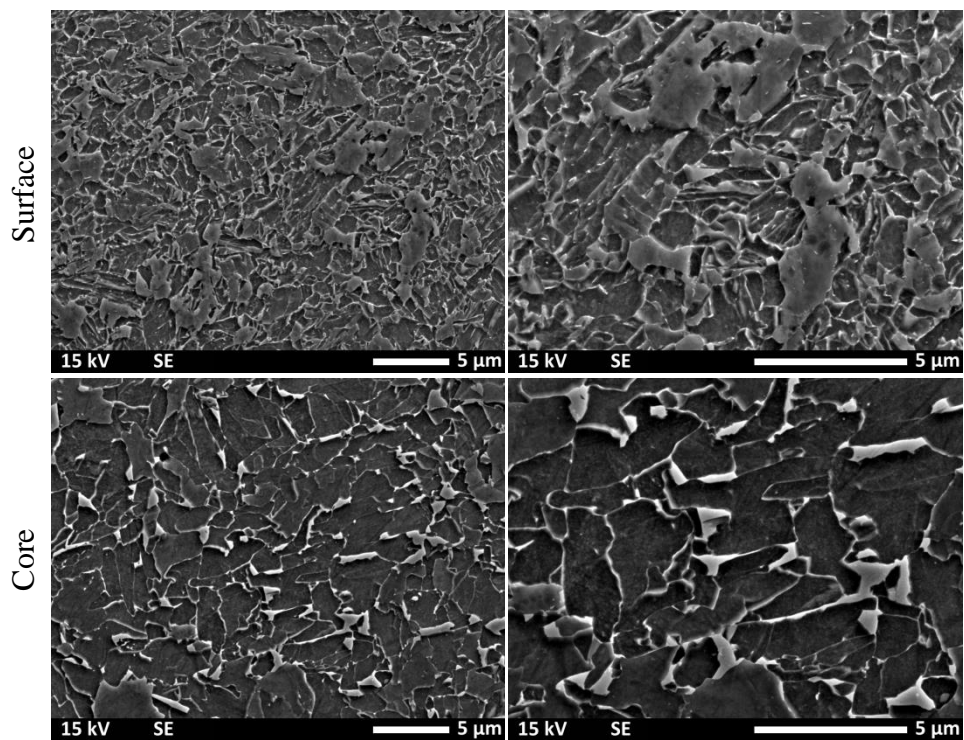


Fig. 97. GB in 7MnB8 steel rolled with use: $T_A = 980$ °C; $T_R = 700$ °C; Cooling [l/min] 120;0;25 process parameters.

Table 9. Designated D_{ef} from grain size distribution for 7MnB8 steel in the initial state and after rolling.

		D_{ef} [μm]				
Core	Initial state	$T_A = 915\text{ }^\circ\text{C}$ $T_R = 720\text{ }^\circ\text{C}$ Cooling [l/min] 120;0;25	$T_A = 915\text{ }^\circ\text{C}$ $T_R = 720\text{ }^\circ\text{C}$ Cooling [l/min] 25;0;0	$T_A = 915\text{ }^\circ\text{C}$ $T_R = 780\text{ }^\circ\text{C}$ Cooling [l/min] 120;0;25	$T_A = 980\text{ }^\circ\text{C}$ $T_R = 700\text{ }^\circ\text{C}$ Cooling [l/min] 120;0;25	
	Surface	57.7	12.3	8.2	16.6	9.8
			3.9	5.7	3.5	3.7

Furthermore, orientation of the grains on the surface is different in comparison to the core. More grains with [111] perpendicular to the sample surface can be seen on the surface, while in the core [101] is the predominant orientation (Fig. 99), whereas the leading grain orientation cannot be recognized in the initial state of the material (Fig. 98)

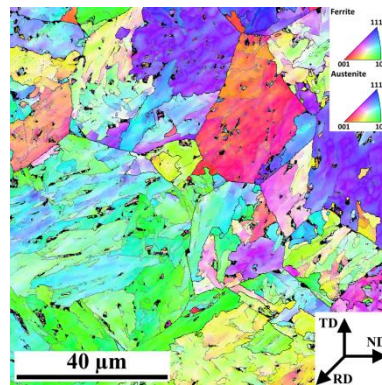
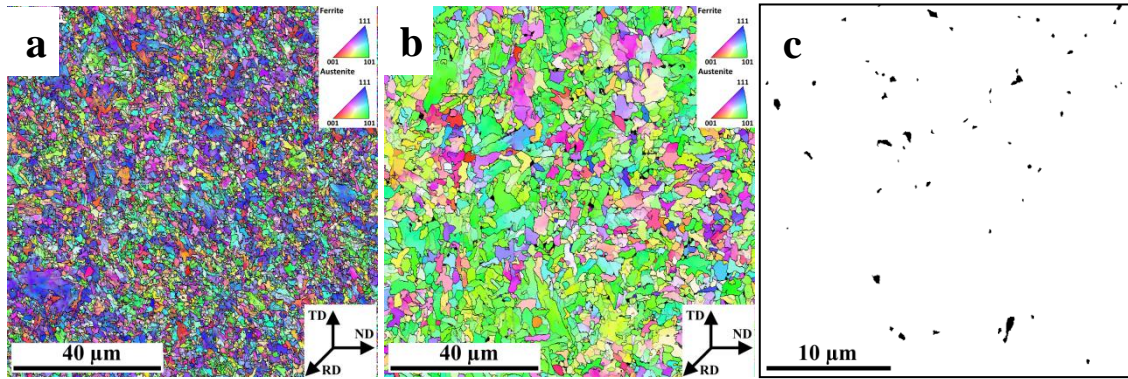
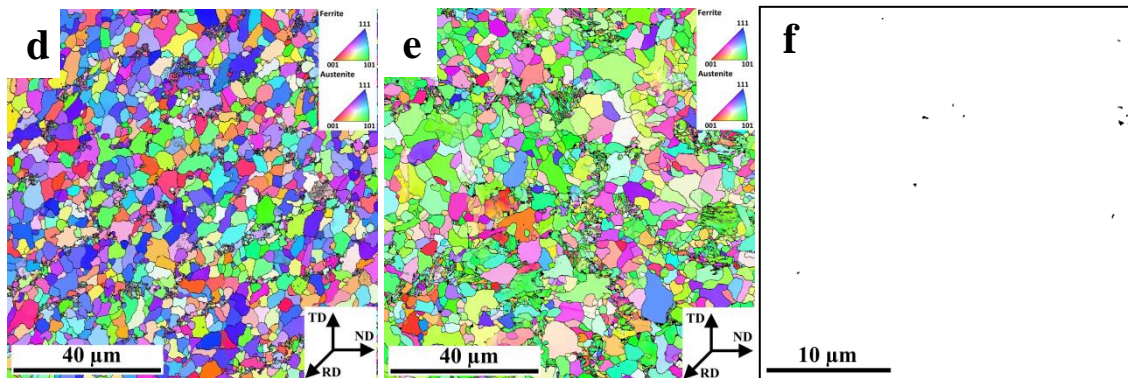


Fig. 98. IPF for raw 7MnB8 steel with grain boundaries $2^\circ - 15^\circ$ (gray) and $15^\circ - 63^\circ$ (black).

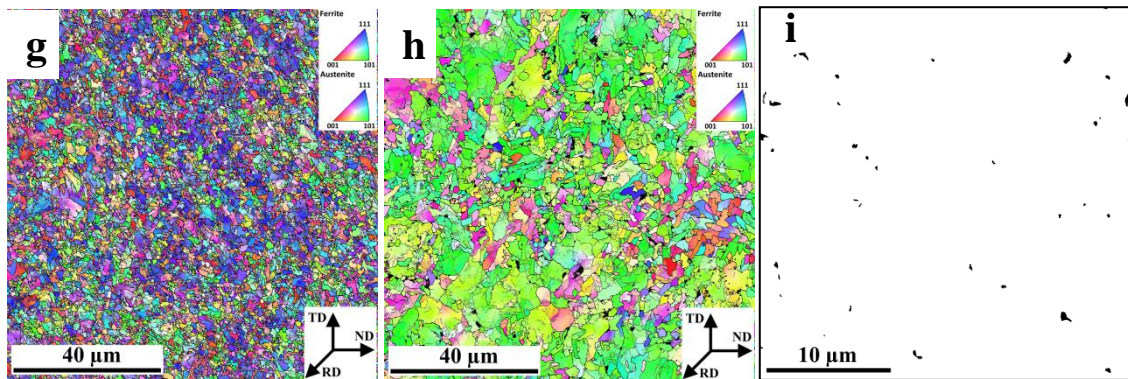
$T_A = 915\text{ }^\circ\text{C}$; $T_R = 720\text{ }^\circ\text{C}$; Cooling [l/min] 120;0;25



$T_A = 915\text{ }^\circ\text{C}$; $T_R = 720\text{ }^\circ\text{C}$; Cooling [l/min] 25;0;0



$T_A = 915\text{ }^\circ\text{C}$; $T_R = 680\text{ }^\circ\text{C}$; Cooling [l/min] 120;0;25



$T_A = 980\text{ }^\circ\text{C}$; $T_R = 700\text{ }^\circ\text{C}$; Cooling [l/min] 120;0;25

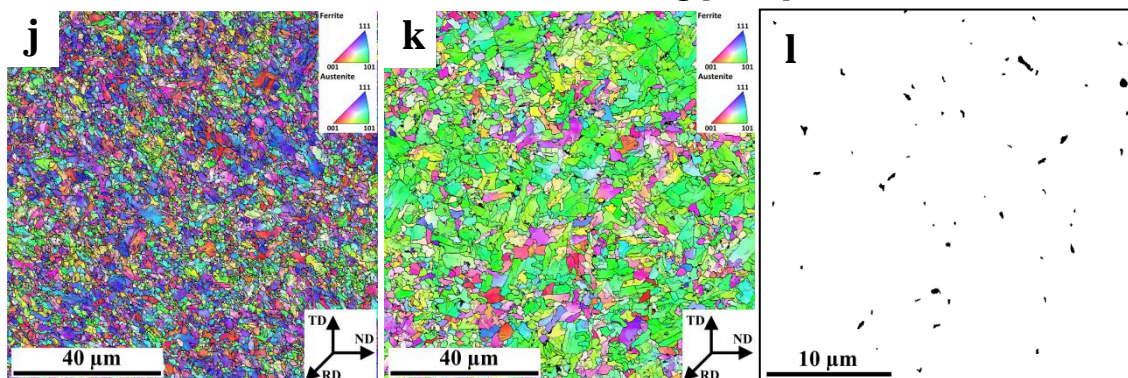


Fig. 99. EBSD results for 7MnB8 steel rolled with use different groups of the process parameters, for a, d, g, j) surface and b, c, e, f, h, i, k, l) core, present crystal orientation maps and phase maps for RA (black).

The distribution of the misorientation angles in the core indicates packets and blocks of M in the steel from the second trial, while in the others an increase within 10° corresponds to sub-blocky M (Fig. 100). Moreover, in the range of characteristic misorientation angles for RA, the samples with GB have an increased number fraction for those angles. The same can be seen in Fig. 99, on the phase maps, more RA is in the samples with the GB structure and also the distribution of RA in the investigated areas is uniform.

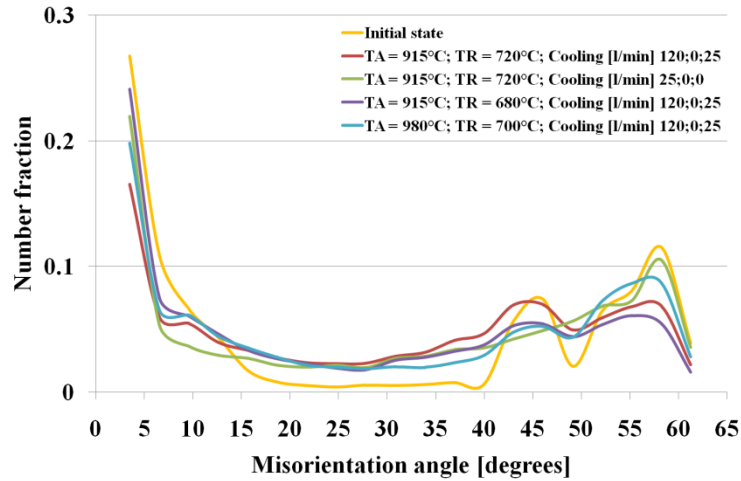


Fig. 100. Distribution of the misorientation angles in the core of 7MnB8 steel in the initial state and after rolling.

In Fig. 101 the total length of grain boundaries in division of low and high angle boundaries for the analysed areas is presented. As it can be seen, due to the recrystallization processes and grain growth in the bar with a lower cooling rate after rolling, total length of LAGB and HAGB is decreased significantly at the surface of the bar, in comparison to the bars with fast cooling (Fig. 101b).

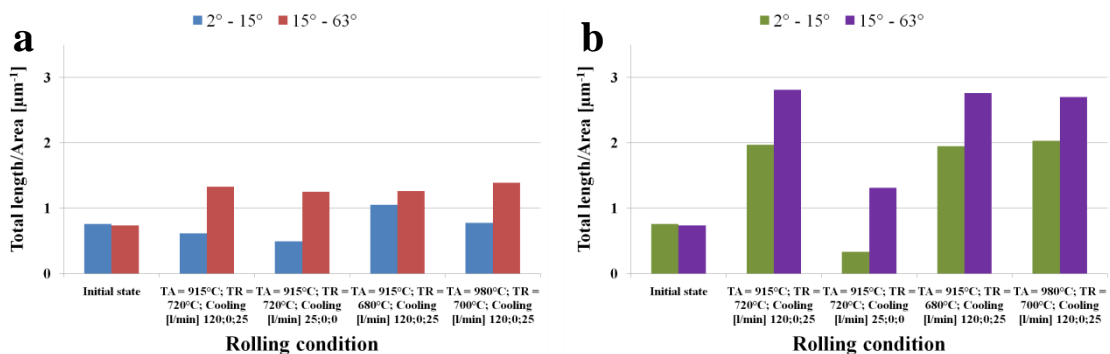


Fig. 101. Total length of grain boundaries for 7MnB8 steel in the initial state and after rolling, measured: a) in the core and b) at the surface of the bars.

However, in the core a decrease is seen only for LAGB and the total length of HAGB is on the same level for all bars. As can be seen from the relationship of the disorientation angles, the structure of the sample is dominated by packs and blocks of M, which are

characterized by HAGB, hence the length of these boundaries is comparable with the values for the other rod cores (Fig. 101a).

5.2.6. X-ray diffraction - retained austenite

The results of RA content determined by using X-ray diffraction are presented in Fig. 102. In the structure of three bars, the RA fraction is increased to about 5 % in comparison to 7MnB8 steel in the initial state. Those samples were austenitized at 915 °C and 980 °C, rolled at 680 - 720 °C and all were intensively cooled using cooling boxes in the arrangement: 120;0;25 [l/min]. Due to a high cooling rate, fine grained structures were obtained (Fig. 89, 91, 92 and Fig. 94, 96, 97). Thus, it could explain a higher amount of RA in those samples in comparison to the ones which were also austenitized and rolled at a similar temperature, but the final temperature after cooling, due to decreased cooling rate was the highest. It also confirms the EBSD results, where in the range of characteristic misorientation angles for RA, the samples with GB have an increased number fraction for those angles (Fig. 100). In the sample with decreased cooling rate, coarse grains of former A, partially transformed into M are observed (Fig. 95). Therefore, the carbon content in A was decreased, because the size of the grains is larger. Due to this A was not stabilized as much as in those three samples with fine grains, thus as the temperature decreased, the martensitic transformation occurred.

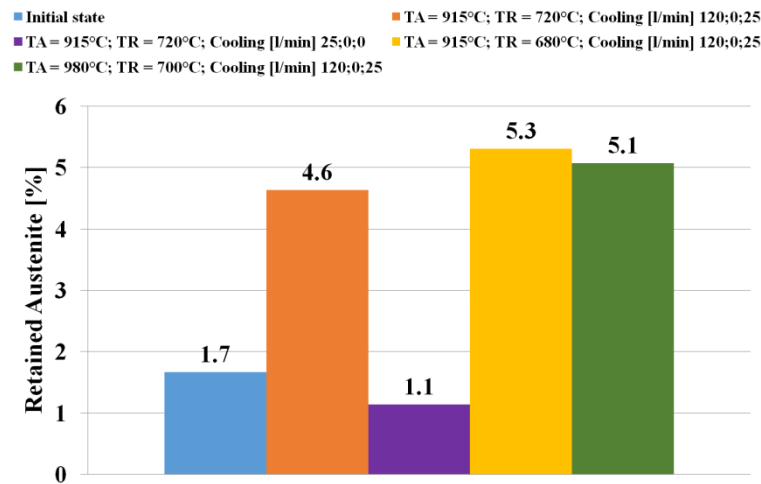


Fig. 102. XRD results of RA in the core of 7MnB8 steel in the initial state and after rolling.

5.2.7. Scanning-Transmission electron microscopy

The TEM investigations of 7MnB8 steel were performed for the material in the initial state and after rolling with the following process parameters: $T_A = 980$ °C, $T_R = 700$ °C, cooling 120;0;25. The bar for the investigations was chosen due to its lowest

DBTT temperature. The characterization included a phase identification of the precipitations observed in the structure and the EDS microanalysis of their chemical compositions. The results are presented in Fig. 104- 107 and Fig. 108 - 112 for material in the initial state and after rolling, respectively. Furthermore, in Table 10, the results of quantitative analysis of the precipitations are given. For the material in the initial state, the following phases were identified in the steel: TiN (Fig. 103), Ti₂CS (Fig. 104), MCN (Fig. 105) and MC (Fig. 106), where M = Ti. The AED of the analyzed precipitations was 72.9 nm, and the volume fraction amounted to 3 precipitations per μm^3 (Table 10).

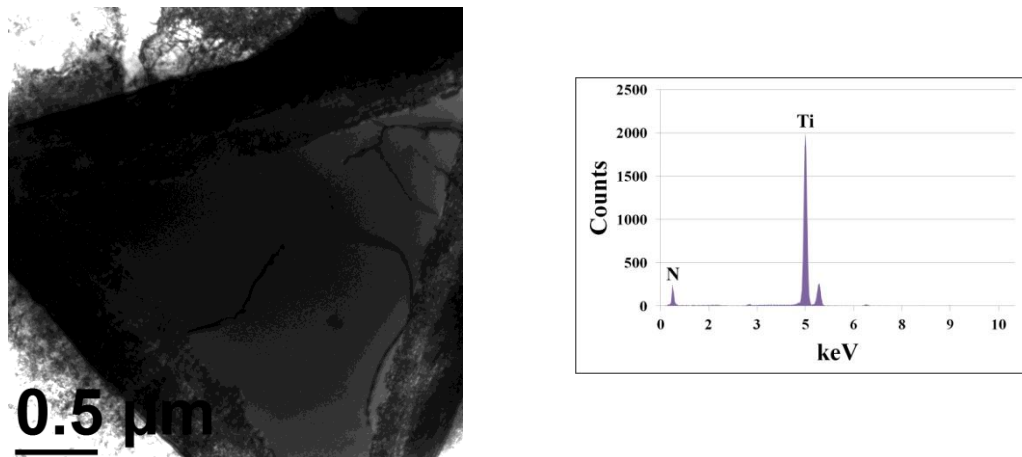


Fig. 103. Coarse TiN precipitation observed in 7MnB8 steel in the initial state.

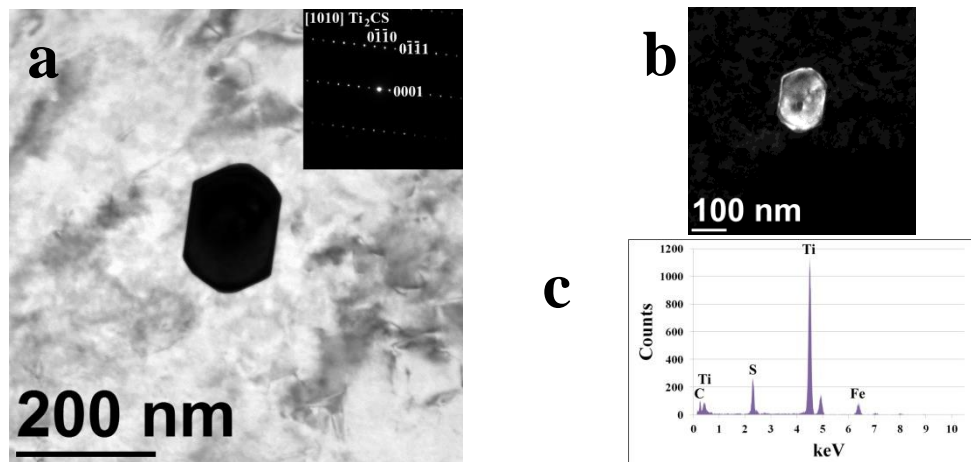


Fig. 104. Ti₂CS precipitation in 7MnB8 steel in the initial state: a) bright field with electron diffraction b) dark field, c) EDS microanalysis.

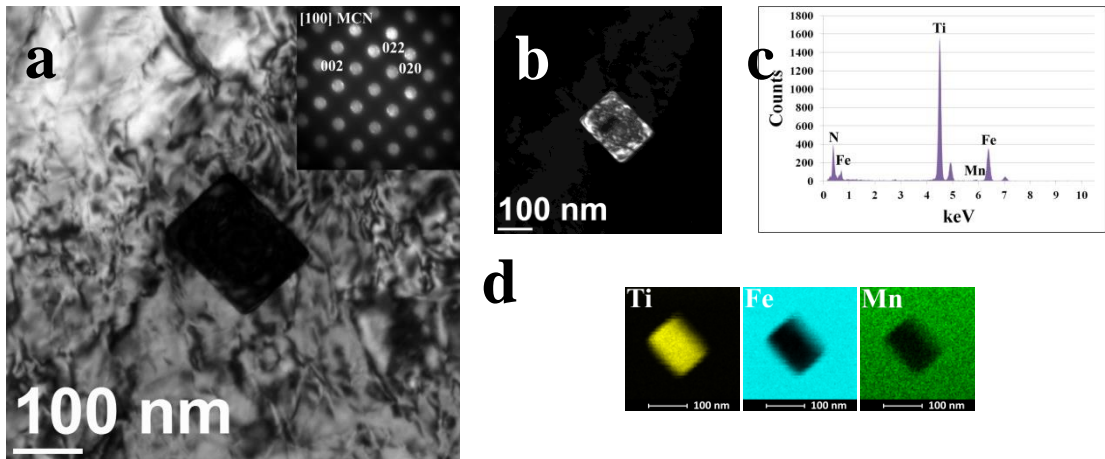


Fig. 105. MCN precipitation in 7MnB8 steel in the initial state: a) bright field with electron diffraction b) dark field, c) EDS microanalysis, d) element distribution.

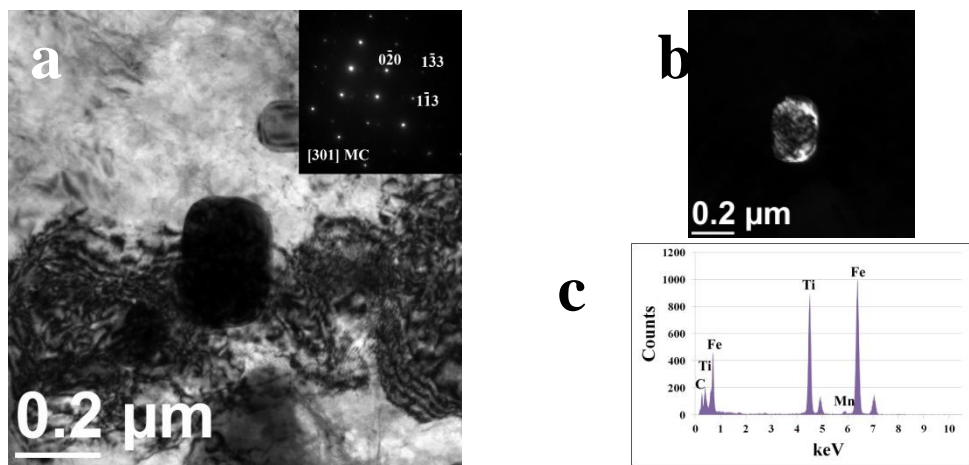


Fig. 106. MC precipitation in 7MnB8 steel in the initial state: a) bright field with electron diffraction b) dark field, c) EDS microanalysis.

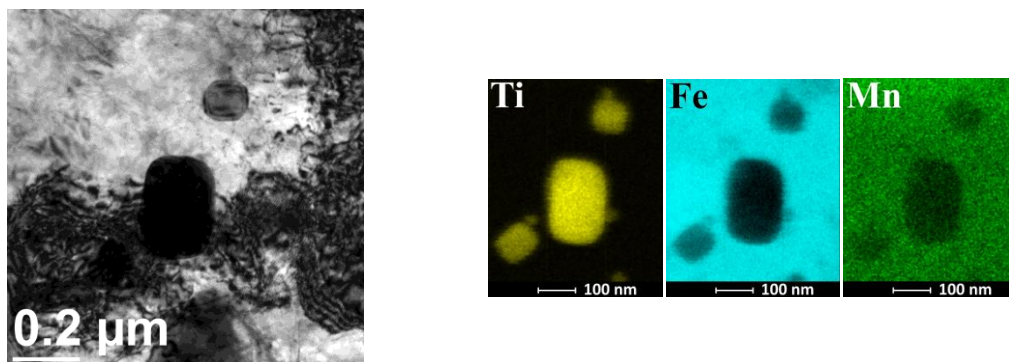


Fig. 107. Element distribution in the region of the precipitations shown in Fig. 106.

After the rolling process finer precipitations were observed in the structure. The AED decreased to 15.7 nm and the volume fraction increased to 27 precipitations per μm^3 (Table 10).

Table 10. AED, area fraction and number of the precipitations per μm^3 in 7MnB8 steel in the initial state and after rolling using fourth group of process parameters: $T_A = 980\text{ }^\circ\text{C}$; $T_R = 700\text{ }^\circ\text{C}$; Cooling [l/min] 120;0;25.

	Initial 7MnB8	After rolling 7MnB8
AED [nm]	72.9	15.7
Area fraction [%]	0.22	0.18
Precipitations/ μm^3	3	27

However, except the Ti_2CS (Fig. 113) and MC (Fig. 109) precipitations observed in the steel in the initial state, MN (Fig. 110), M_2CN (Fig. 111) and M_2S (Fig. 112) precipitations were additionally identified after the process. It has to be noticed that MC precipitations after rolling contain Mo in contrast to carbides in the material before the process (Fig. 106 and Fig. 108, 109). Furthermore, after the process, very fine MC precipitations were identified in the steel (Fig. 108), as opposed to the initial state. Simultaneously, all precipitations contain Ti and Mn in different proportions. However, it has to be mentioned, that also coarse TiN precipitates were observed in the structure, in both cases. However, they were not analyzed by TEM, due to their size (Fig. 103).

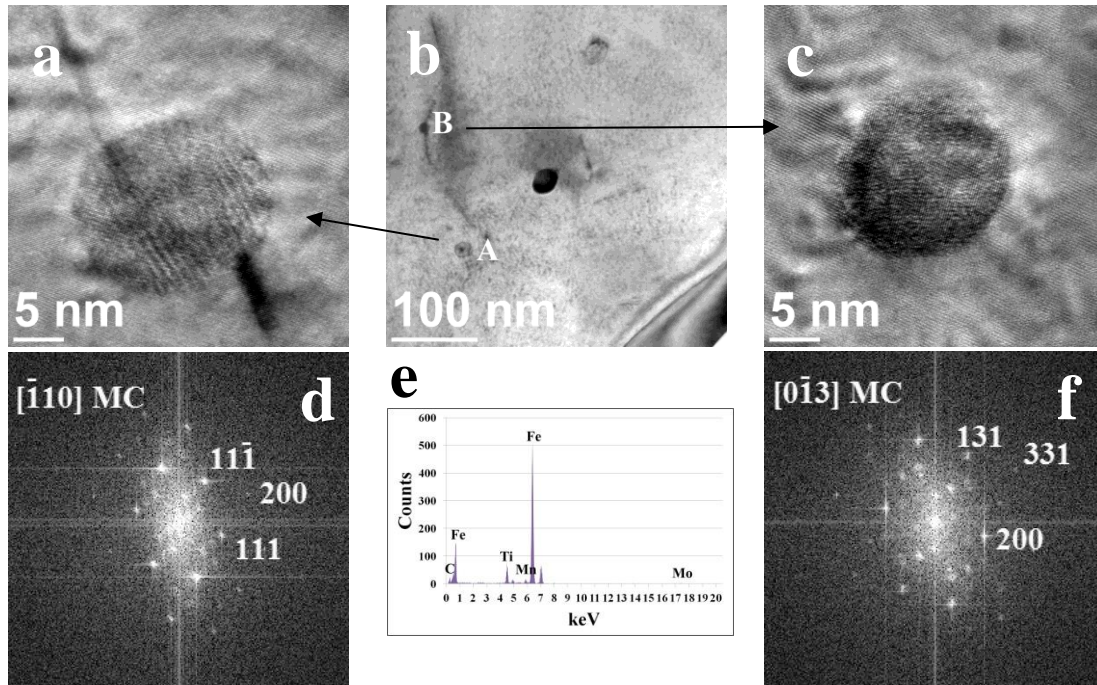


Fig. 108. Fine MC precipitations in 7MnB8 steel after rolling with $T_A = 980\text{ }^\circ\text{C}$, $T_R = 700\text{ }^\circ\text{C}$, cooling 120;0;25: a, c) HRTEM images of the precipitations A and B, b) bright field image with investigated precipitations, d, f) electron diffraction by HRTEM Fast Fourier Transform (FFT) e) EDS microanalysis results for precipitation A.

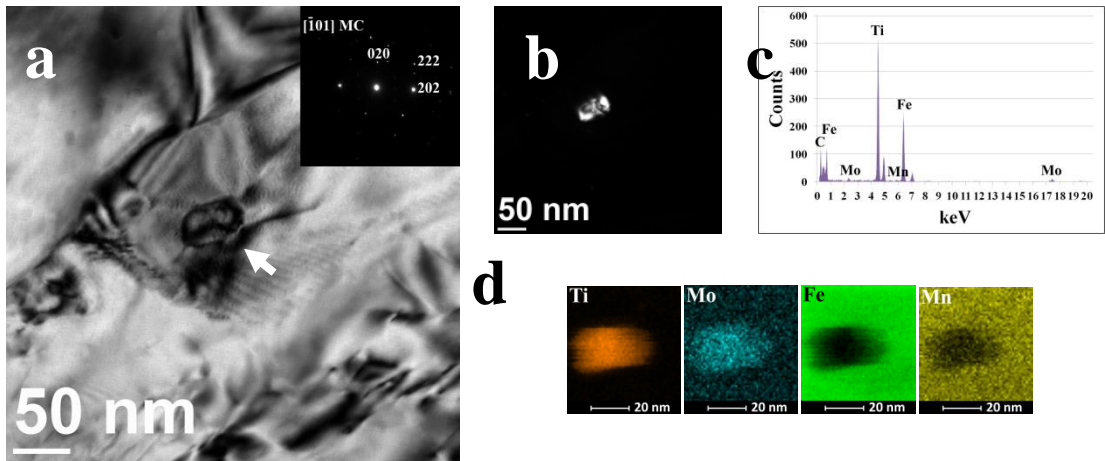


Fig. 109. MC precipitation in 7MnB8 steel after rolling with $T_A = 980\text{ }^\circ\text{C}$, $T_R = 700\text{ }^\circ\text{C}$, cooling 120;0;25: a) bright field with electron diffraction b) dark field, c) EDS microanalysis, d) element distribution.

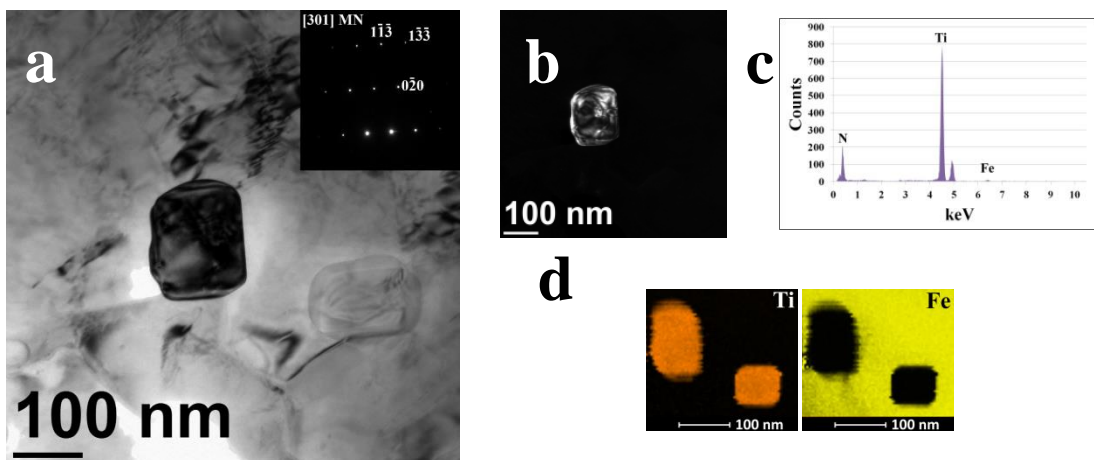


Fig. 110. MN precipitation in 7MnB8 steel after rolling with $T_A = 980\text{ }^\circ\text{C}$, $T_R = 700\text{ }^\circ\text{C}$, cooling 120;0;25: a) bright field with electron diffraction b) dark field, c) EDS microanalysis, d) element distribution.

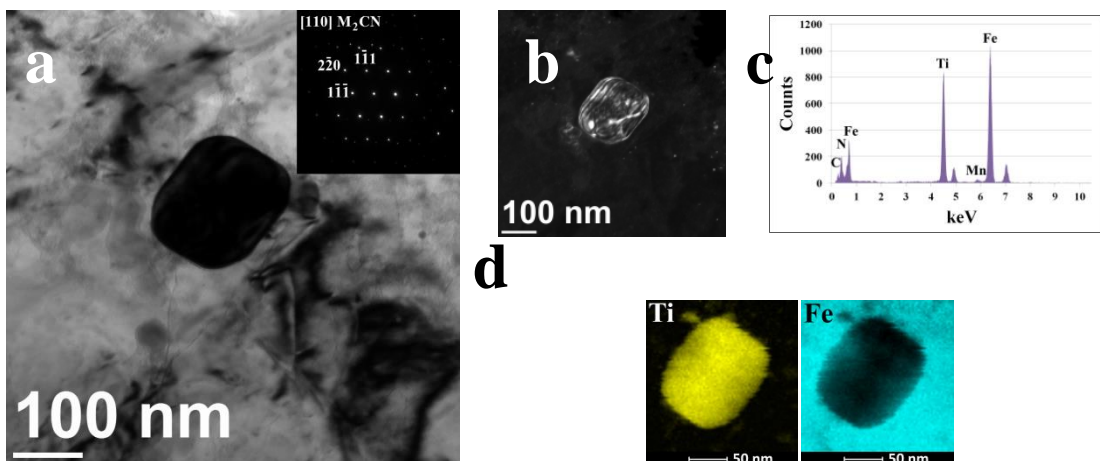


Fig. 111. M_2CN precipitation in 7MnB8 steel after rolling with $T_A = 980\text{ }^\circ\text{C}$, $T_R = 700\text{ }^\circ\text{C}$, cooling 120;0;25: a) bright field with electron diffraction b) dark field, c) EDS microanalysis, d) element distribution.

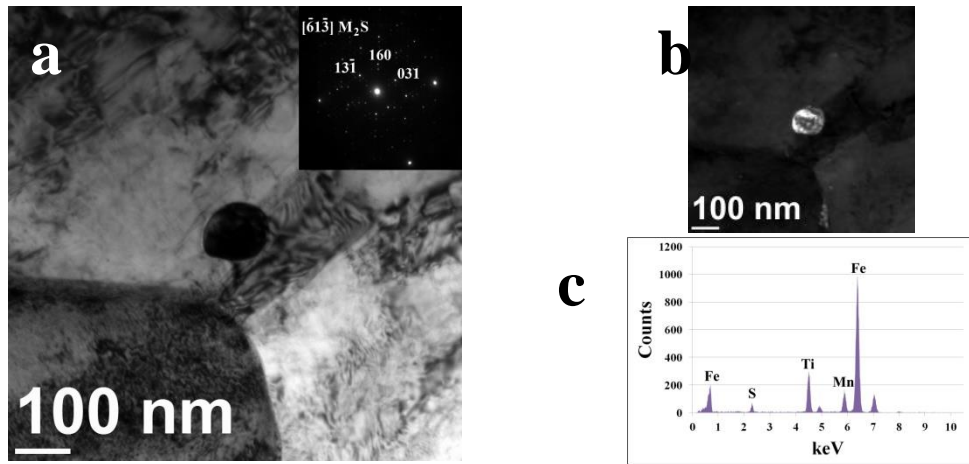


Fig. 112. M_2S precipitation in 7MnB8 steel after rolling with $T_A = 980$ °C, $T_R = 700$ °C, cooling 120;0;25: a) bright field with electron diffraction b) dark field, c) EDS microanalysis.

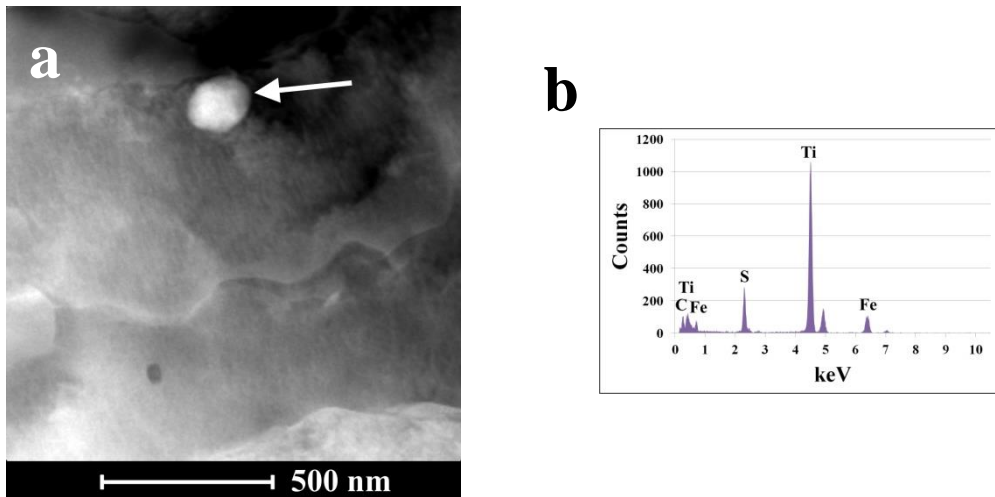


Fig. 113. Ti carbosulfide in 7MnB8 steel after rolling with $T_A = 980$ °C, $T_R = 700$ °C, cooling 120;0;25: a) HAADF STEM image, b) EDS microanalysis.

According to the literature review, the Ti content in 7MnB8 steel is sufficient to form all its phases during solidification [128,130]. On the other hand, coarse TiN particles act as initiation sites of cleavage fracture and also are difficult to dissolve during reheating, so with regard to impact toughness and grain refinements, their presence should be inconsiderable and/or steel solidification rate should be enhanced to produce finer precipitates.

5.3. New steels with selected chemical composition

During the selections, TTT and CCT diagrams were made to predict the behavior of the new materials with the use of Thermo-Calc and JMatPro supporting software. Also, temperature stable phases were designated, focused on the precipitation types, depending on the chemical composition (Table 4). Fig. 114, 115 and 116 present the CCT, TTT charts and temperature stable phases, respectively, for chosen steels from prepared variants. Austenitization temperature 915 °C and grain size 15 μm were assumed in the calculations.

5.3.1. Justification of the chemical composition of experimental steels

All steels have A3 temperature above 800 °C (Fig. 114). The addition of 0.19 wt. % Mo to the S654 steel, retard ferritic transformation on the TTT diagram (Fig. 115). The higher addition of Mo in S657 steel, 0.49 wt. %, as well as the addition of 2.9 wt. % of Mn in S658 steel, shifts the ferrite and pearlite regions to the higher timing (Fig. 115).

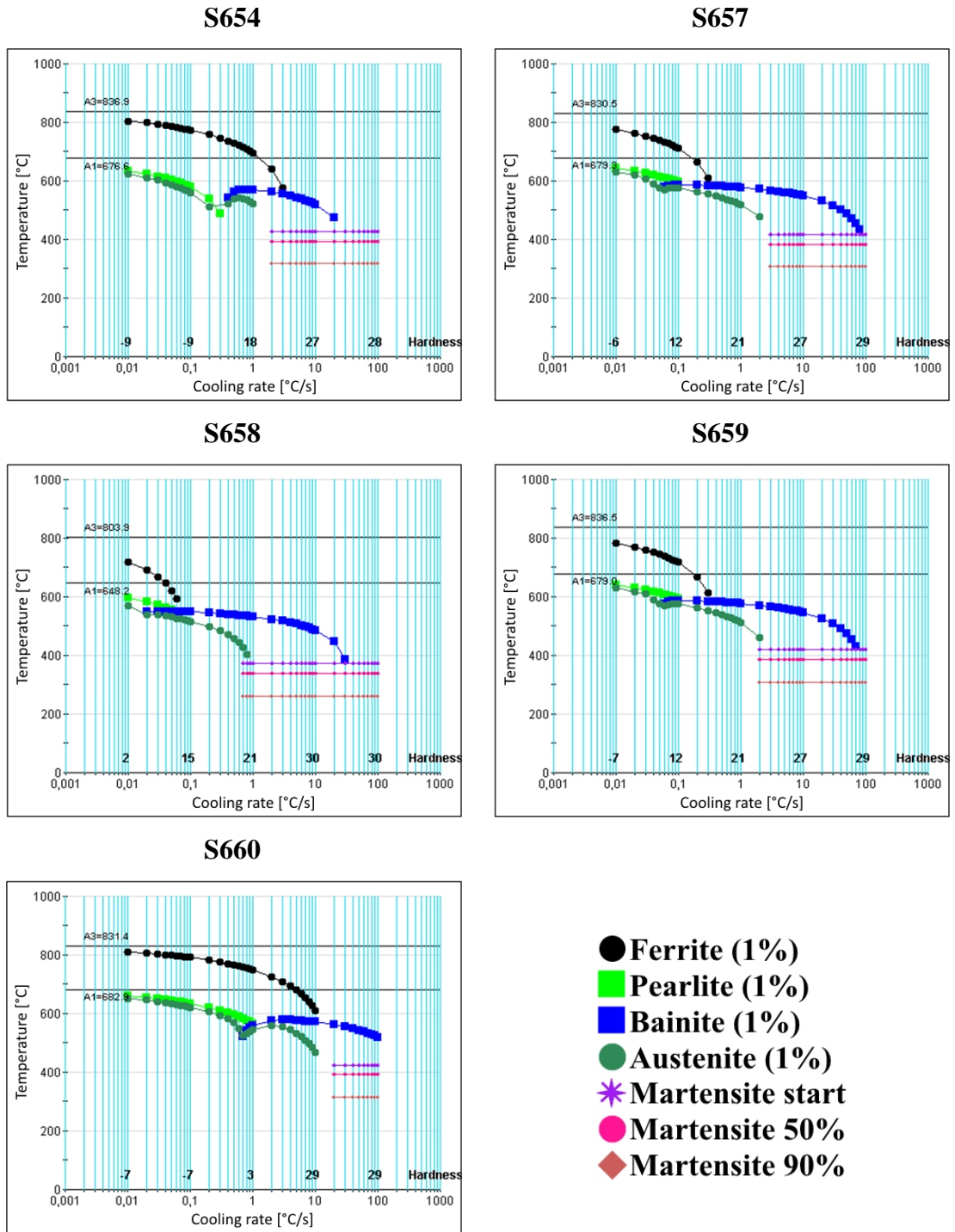


Fig. 114. Continuous cooling transformation (CCT) diagrams for the new steels, calculated with the assumption of austenitization temperature 915 °C and grain size 15 μm .

Furthermore, TTT diagrams are similar for both steels, however, M in S658 steel can be obtained with lower cooling rates, which could be seen on the CCT diagram (Fig. 114). For S659 steel, where the Ti content was decreased to 0.023 wt. %, and addition of 0.037 wt. % Nb was applied, the ferrite and pearlite regions are shifted to the shorter timing on the TTT diagram (Fig. 115). Otherwise, the CCT diagram is similar to S657 steel (Fig. 114). For S660 steel, the lowest Ti content (0.019 wt. %) and Nb, V additions (0.021 and

0.15 wt. %, respectively) are characteristic. For this steel, curves for bainite, ferrite and pearlite regions are shifted to the shorter timings on the TTT diagram (Fig. 115). Due to this, S660 steel is different from the rest of the steels. Furthermore, to obtain M in the structure, higher cooling rates have to be applied (Fig. 114).

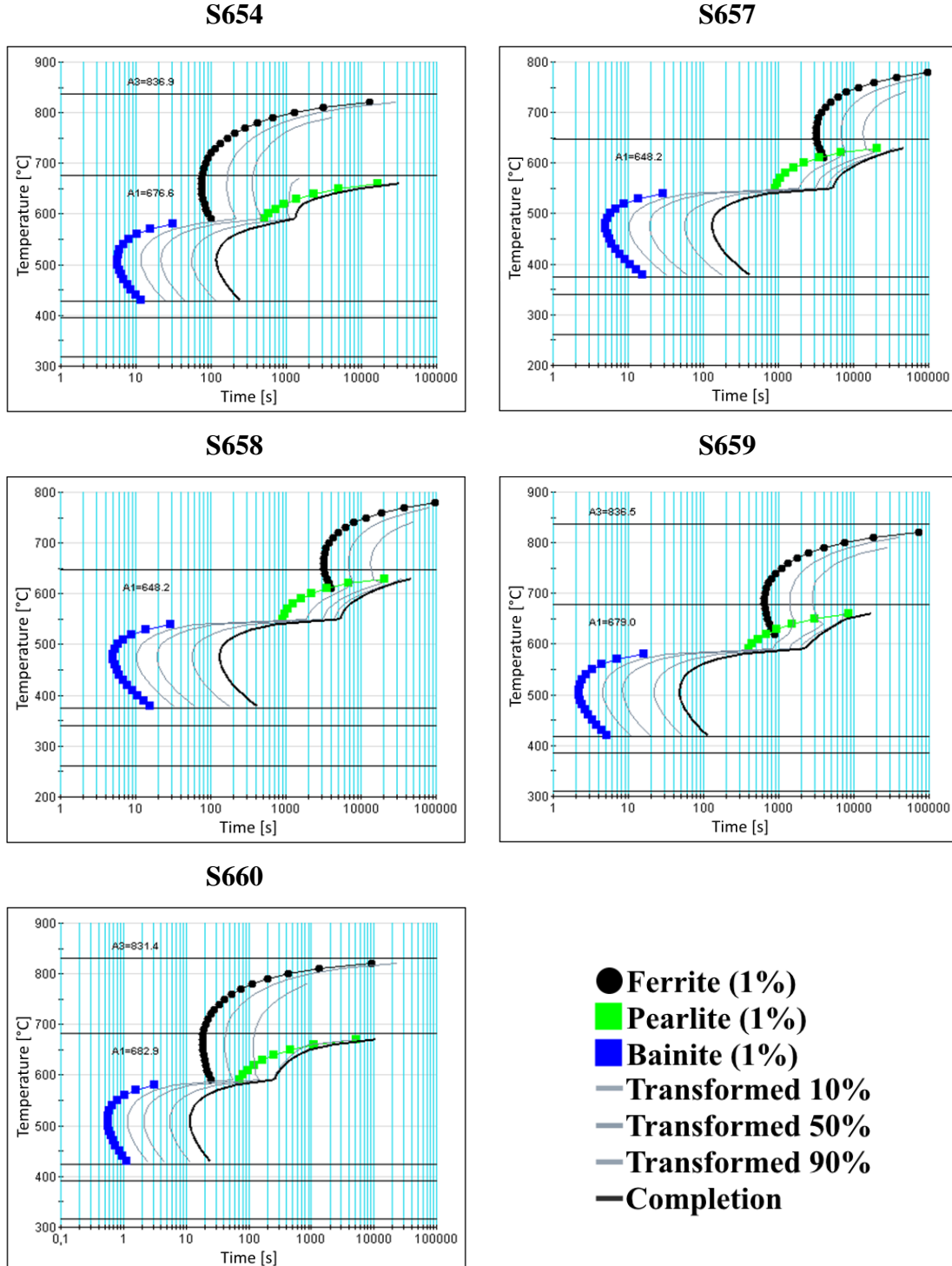


Fig. 115. Time-temperature isothermal transformation (TTT) diagrams for the new steels, calculated with the assumption of austenitization temperature 915 °C and grain size 15 μm.

The temperature stable phases for the new steels are presented in Fig. 116. All steels contain the addition of Ti. For this reason, the first phase, the precipitation of which begins in the liquid phase, is M(N, C), where M = Ti, Nb, V, depending on the steel. In steels S654 and S657, with high Ti content, an additional compound appears at ~ 1490 °C, which is Ti carbosulfide $Ti_4C_2S_2$. Below 1100 °C, this compound stops precipitates and MnS sulphide occurs. In steels S658, S659 and S659, where the Ti content was decreased, the $Ti_4C_2S_2$ phase is not observed on the diagrams. For those steels only MnS formation is expected at ~1420 °C for S658 steel with high Mn content. In steels with standard Mn level (1.85 - 1.95 wt. %), the temperature for MnS is higher by ~ 30 °C. Next, in the V-free S659 steel, at ~ 1100 °C start precipitate M(C, N) phase, where M = Nb and/or Ti. The same starts at ~ 1040 °C in S660 steel, however, for this steel M, beside Nb and/or Ti, V can be additionally present. For those two steels, S659 and S660, AlN appears during cooling, in opposition to the others. Precipitation of the phase begins at ~ 1000 °C for S659 steel and at ~ 690 °C for S660. Between those temperature ranges, for S660 steel at ~ 960 °C, another M(N, C) precipitations can be recognized. However, in this one M refers to V, Nb and/or Mo. Furthermore, in steels S654, S657 and S658, MC precipitation starts due to further cooling. For S654 and S657 steels with high Ti content, 0.11 and 0.092 wt. %, respectively, the elements forming the carbide are V, Mo and/or Ti and the characteristic temperature is ~ 760 °C. Decrease of the Ti content to 0.036 wt. % in S658 causes elimination of Ti in the carbide. Moreover, the temperature at which the precipitations can be expected decreases to ~ 720 °C. As the temperature decreases, precipitations of Fe_3C appear in all steels. It can be noticed, that the temperature of cementite forming is comparable for all new grades, approximately 660 °C. However, for the Mn-rich steel, S658, the temperature decreases to ~ 640 °C. The last phase where the change of mass fraction of phases is visible and participates in precipitation processes is MC type carbide in S660 steel, where M is V and/or Mo. The temperature of formation starts at ~ 450 °C.

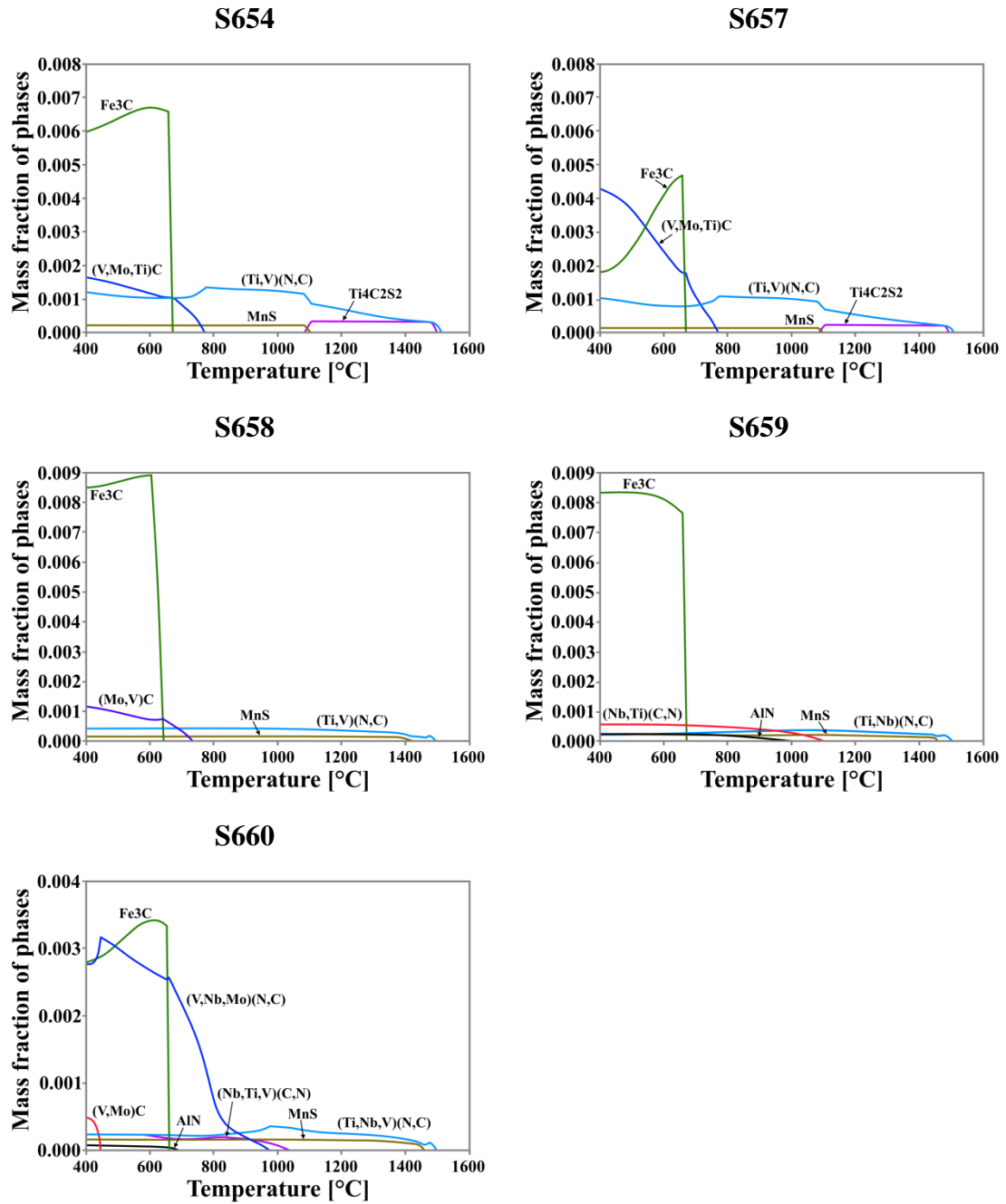


Fig. 116. Changes of mass fraction of phases with temperature at equilibrium.

Besides the precipitation order during the cooling, it can be observed that the chemical composition of M(N, C) precipitations evolves towards M(C, N), and Ti is replaced by other alloying elements (Nb, V or Mo). The precipitation process of the aforementioned carbonitride is accompanied by the precipitation of MC type carbides, in which M = V, Mo, Ti depending on the chemical composition of steel. In general, Nb-rich carbides are precipitated already in the rolling temperature range, while V and Mo-rich carbides are formed during cooling after rolling. Moreover, according to chemical composition of the steels (Table 11), it can be noticed that with a decrease of the Ti content in the steel, the

presence of $Ti_4C_2S_2$ phase can be eliminated. In steels S658, S659 and S660 with Ti contents below 0.4 wt. %, the $Ti_4C_2S_2$ phase does not precipitate during the cooling.

Furthermore, the change of length during heating/cooling of samples from the new steels (Fig. 117) was determined with the heating rate ~ 12.2 °C/s and the cooling rate ~ 171.8 °C/s to characterize the linear waveform indicating the occurrence of phase changes. After the heating to the austenitization temperature 915 °C and 980 °C with 90 s holding time, a full A structure is obtained in all new steels. The transformation starts from ~ 750 °C to ~ 810 °C, depending on the material. During the cooling, it can be noticed that for steels S654, S657 and S658 only one phase transformation occurs in both austenitization temperatures, which corresponds to the martensitic transformation (Fig. 114).

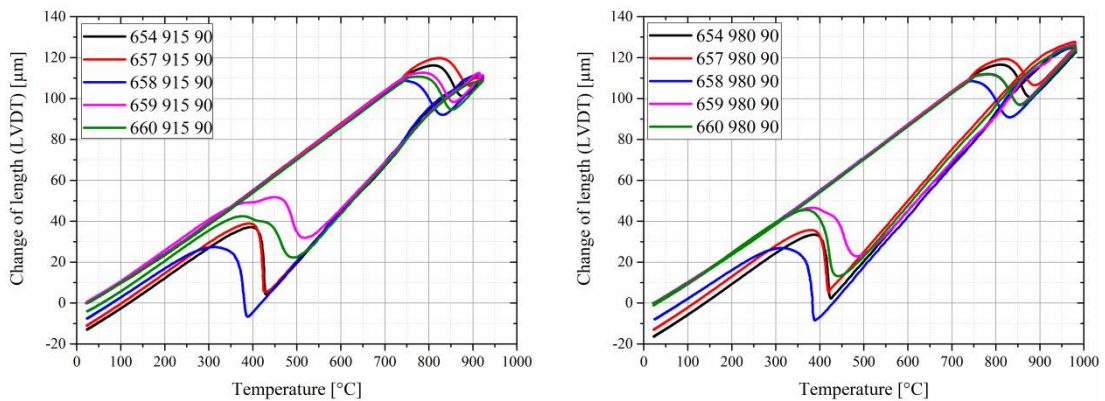


Fig. 117. Change of length during heating/cooling of the new steels.

In S660 steel, during the test with lower austenitization temperature, two transformations can be distinguished, on the other hand, with higher austenitization temperature only one transformation occurred. It can be explained by grain size, which grows with increased temperature, *ipso facto* the TTT diagram (Fig. 115) is shifted to the right, so the cooling curve does not cross the bainitic region. The same can be observed for S659 steel, however, in this case, the bainitic transformation occurred in both tests, but at different temperature, which can also be explained by different grain sizes, due to the austenitization temperature.

On the basis of thermodynamic calculations (Fig. 114 - 116), five new steels were produced, for which main changes in chemical composition are combined in Table 11.

Table 11. Main changes in chemical composition for the new steels in comparison to industrial 7MnB8 steel, in wt. %.

Steel	Elements [wt. %]											
	C	Mn	Si	P	S	Cr	Mo	V	Nb	Ti	Al	B
S654	Min.							0.04				
	Max.						0.20	0.05				
S657	Min.						0.40					
	Max.						0.50					
S658	Min.	2.80								0.03		
	Max.	3.00					0.20			0.04		
S659	Min.							-	0.03	0.02		-
	Max.						0.20	-	0.04	0.03		-
S660	Min.							-	0.02	0.01	-	-
	Max.						0.20	0.15	0.03	0.02	0.005	-
7MnB8	Min.	0.06	1.85	0.15	-	-	-	0.03	-	0.06	0.020	0.0015
	Max.	0.09	1.95	0.25	0.015	0.015	0.1	0.02	0.04	-	0.10	0.0030

Compared to 7MnB8 steel, the steels were made with the following changes in the chemical composition:

- S654 steel - addition of Mo influences hardenability and reduces temper embrittlement, V mainly increases strength by precipitation strengthening mechanisms.
- S657 steel - Mo content increased to 0.4 - 0.5 wt. %, in comparison to the rest of steels where the addition was max. 0.2 wt. %.
- S658 steel - Mn content changed to 2.8 - 3.0 wt. % range instead of 1.85 - 1.95 wt. % to increase the hardenability of the steel. Ti content decreased to 0.3 - 0.4 wt. %, to prevent formation of coarse TiN precipitations.
- S659 steel - V eliminated in the chemical composition in favor of Nb - inhibiting static recrystallization, which content was increased to 0.03 - 0.04 wt. %. Further decrease of Ti to 0.02 – 0.03 wt. %.
- S660 steel - simultaneous use of carbide formers like Ti, Nb and V. Further decrease of the amount of Ti to 0.01 - 0.02 wt. %. In comparison to S659 steel, Nb content decreased to 0.02 - 0.03 wt. %. V was increased to max 0.15 wt. %.

5.4. Investigation of the rods structure in the forged state

For comparison purposes, the structure and mechanical properties of the developed steels were characterized in the initial state, that is, after the forging process at elevated temperatures ~ 1200 °C.

5.4.1. Tensile tests

The results of tensile tests comparing the properties of the new steels in the initial state, as forged, are presented in Fig. 118 and Fig. 119. Samples taken from S659 and S660 steels have the lowest YS and UTS, however, the highest elongation (Fig. 118).

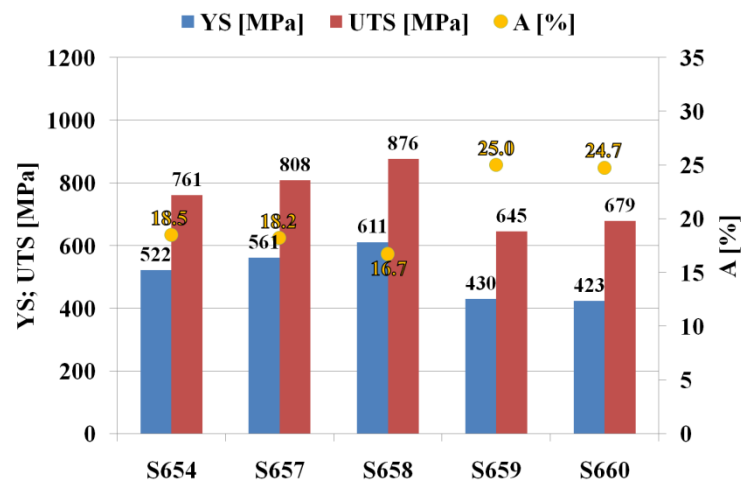


Fig. 118. Mechanical properties of the new steels.

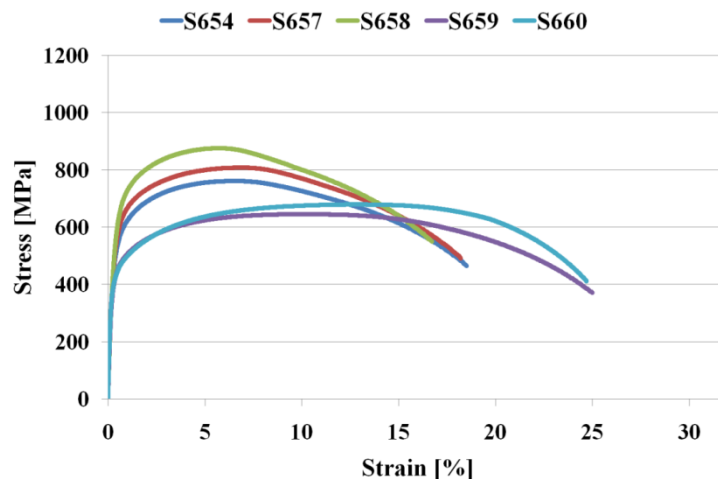


Fig. 119. Stress-strain curves for the investigated new steels.

For S654, S657 and S658 steels, an increase in YS and UTS was observed in comparison to 7MnB8 steel in the initial state (Fig. 82 and Fig. 118). The stress-strain curves for all steels are without pronounced YS (Fig. 119)

5.4.2. Hardness measurements

The cross-section profiles of hardness measurements of the bars produced with the new steels are presented in Fig. 120. Furthermore, Table 12 presents hardness averages. It can be seen that S658 steel has the highest hardness.

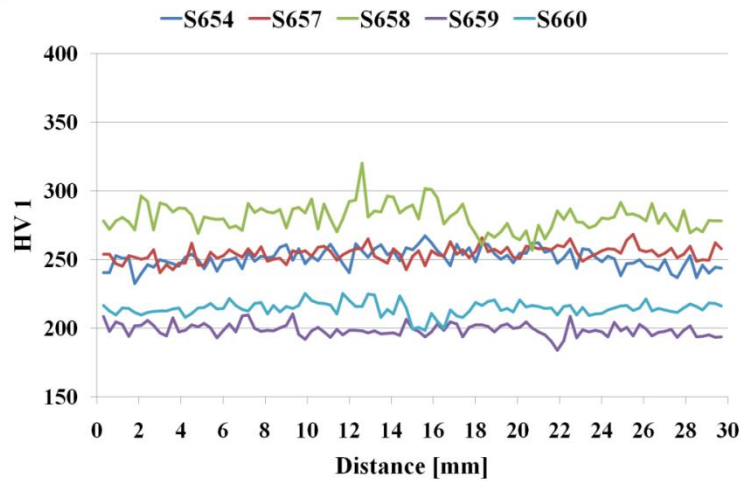


Fig. 120. Cross-section profile of the HV₁ hardness on the diameter for the new steels.

Table 12. Average HV₁ for the new steels.

Raw material				
S654	S657	S658	S659	S660
251 ± 7	254 ± 5	281 ± 10	199 ± 5	214 ± 5

On the other hand, steels S659 and S660 have the lowest hardness. The hardness of the steels S657 and S654 is comparable with the hardness of raw 7MnB8 steel.

5.4.3. Charpy tests

The Charpy V-notch tests were performed for the new materials in different temperatures and the results are presented in Fig. 121 and in Table 13. Samples taken from S659 and S660 steels have the highest fracture energy at RT and the lowest DBTT in the Charpy impact test. For S660 steel the energy is ~ 220 J and for S659, ~ 165 J. Estimated DBTTs for those two steels are below 0 °C and amount to -95 °C and -45 °C, for S660 and S659 steels, respectively.

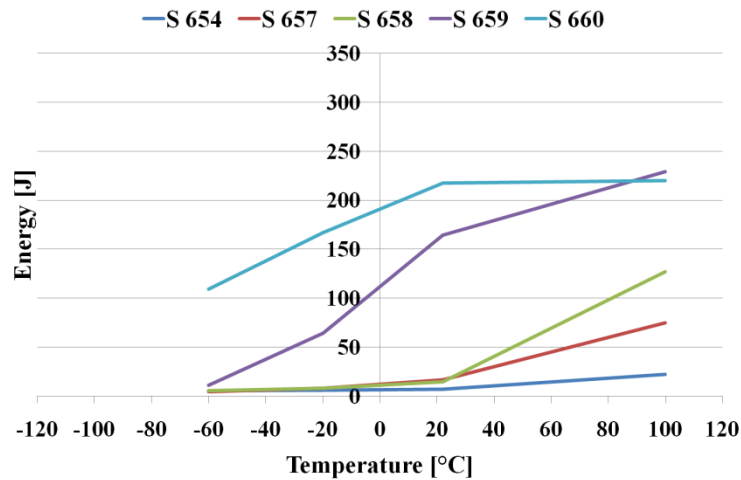


Fig. 121. Charpy V-notch impact measurements at different temperature for steels in the initial state.

Table 13. DBTT estimated for materials in the initial state, in °C.

DBTT [°C]				
S654	S657	S658	S659	S660
135	50	45	-45	-95

In contrast to the results obtained for those steels the behavior of the rest is different. The DBTT and the fracture energy in Charpy impact test at RT are in contrast to the results for S659 or S660 steels. It can be seen in Fig. 121 that the energies at RT for S654, S657 and S658 steels are very low (7, 16.5 and 14.5 J, respectively). The additional investigations at 100 °C increase the energy, but for S654 steel the value is still below 27 J. The estimated DBTT for this steel is the highest from all new steels, 135 °C. The DBTT for S657 and S658 are also at positive temperatures: 50 °C and 45 °C, respectively. Furthermore, the temperatures for S657 and S658 steels are comparable with the results obtained for 7MnB8 steel in the initial state, for which the DBTT was 45 °C.

5.4.4. Light optical microscopy

The results of LOM structure observations of the new steels rods in the initial state (after forging and turning) are presented in Fig. 123 - 127. Moreover, etching to reveal the PAG (Fig. 122) and quantitative analysis of PAGS (Table 14) were made. The structure of forged S654, S657 and S658 steels is mostly GB (Fig. 123 - 125), while the structure of S659 and S660 is ferrite with M/A islands (Fig. 126 and 127, respectively). Coarse TiN precipitations were observed in the structure of all new steels.

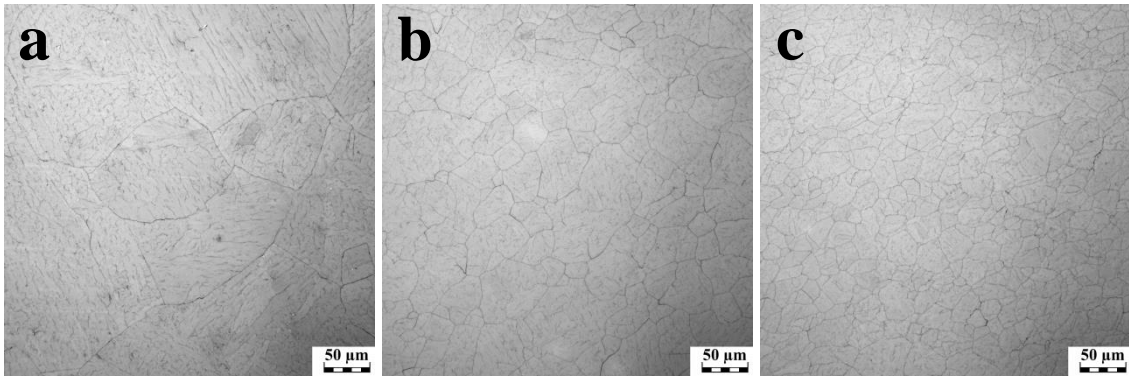


Fig. 122. Microstructure presenting former A grains in the new steels: a) S654, b) S657, c) S658, used in the grain size measurements.

Table 14. PAGS for the investigated new steels and 7MnB8 steel.

	7MnB8	S654	S657	S658
AED [μm]	40	117	34	22
Standard deviation [μm]	± 18	± 87	± 20	± 16

However, for steel S659 and S660 the etching results were unsatisfactory despite using a few different etchants. Therefore, no results for those two steels are available. For steels with satisfying results of etching, it can be seen that average grain size of former A in the S657 and S658 steels is decreased in comparison to 7MnB8 steel. On the other hand, the S654 steel has very large average grain size, 117 μm .

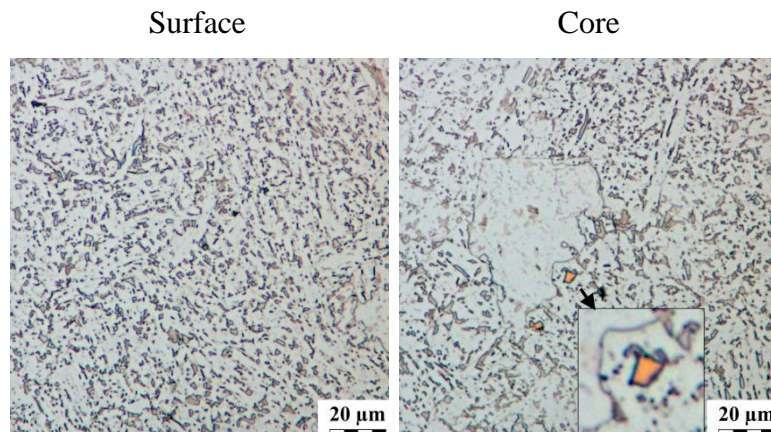


Fig. 123. Structure of S654 steel, with coarse TiN precipitation.

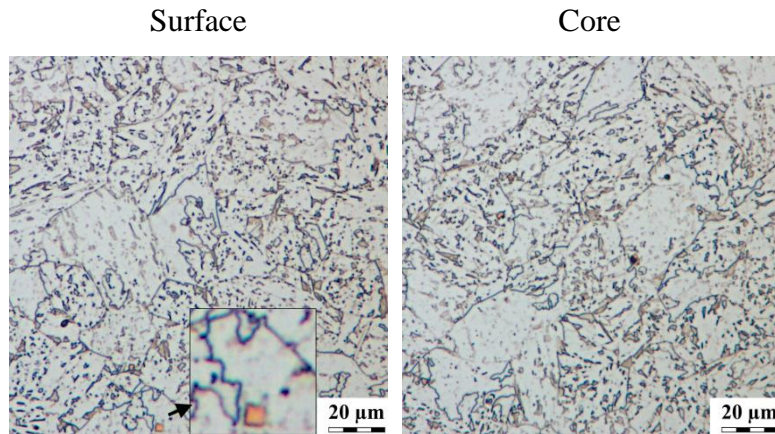


Fig. 124. Structure of S657 steel, with coarse TiN precipitation.

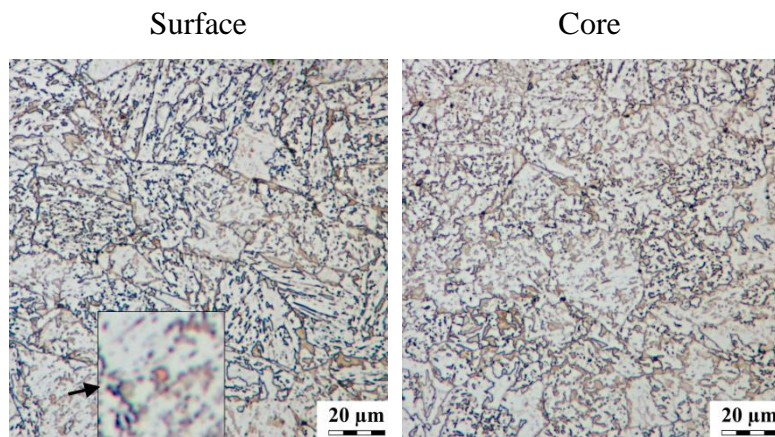


Fig. 125. Structure of S658 steel, with TiN precipitation.

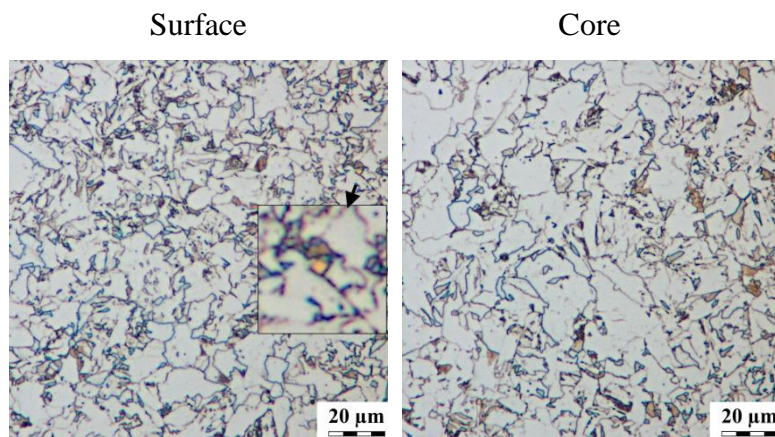


Fig. 126. Structure of S659 steel, with TiN precipitation.

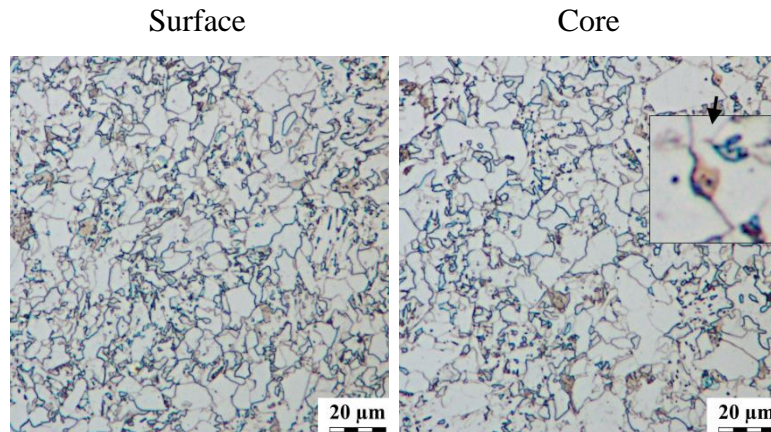


Fig. 127. Structure of S660 steel, with TiN precipitation.

5.4.5. Scanning electron microscopy

The results of the structure observations using SEM are presented in Fig. 128 - 132. Furthermore, Fig. 133 - 136 comprise the results from the EBSD investigations. As it can be seen, in the structure of S654, S657 and S658 steels, $\sim 1 - 5 \mu\text{m}$ size grains of second phases (M/A islands and RA) are present (Fig. 128 - 130). In the structure of the steels, DUB areas can be found. On the other hand, in steels S659 and S660 M/A islands and RA are also recognized, with the size of a few μm , however, coarse M/A islands ($> 5 \mu\text{m}$) are additionally observed in those steels (Fig. 131, 132). Between the GB areas, in the structure, coarse ferrite grains are observed (Fig. 131, 132).

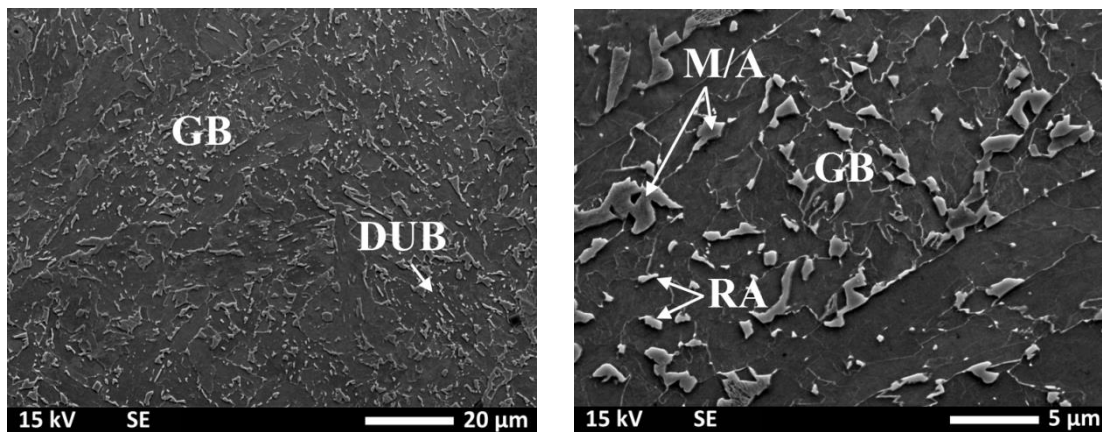


Fig. 128. Structure in the core of S654 steel in the initial state, different magnifications.

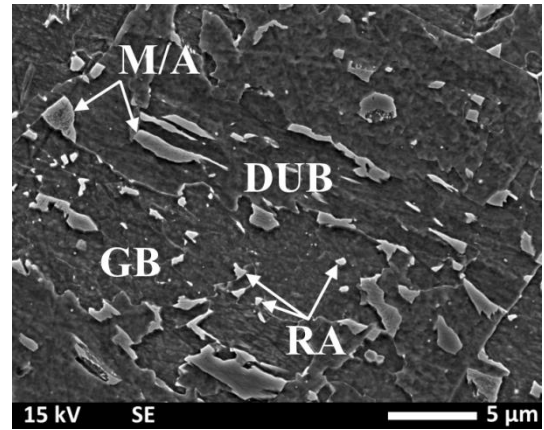
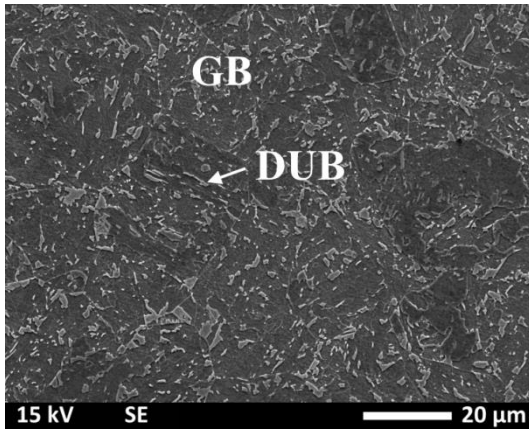


Fig. 129. Structure in the core of S657 steel in the initial state, different magnifications.

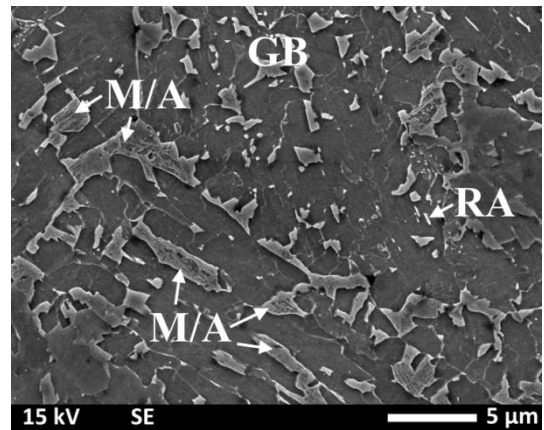
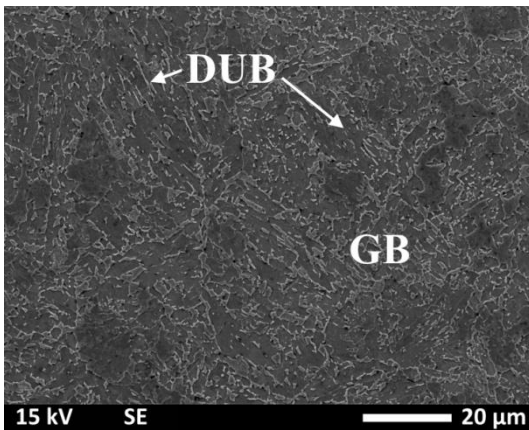


Fig. 130. Structure in the core of S658 steel in the initial state, different magnifications.

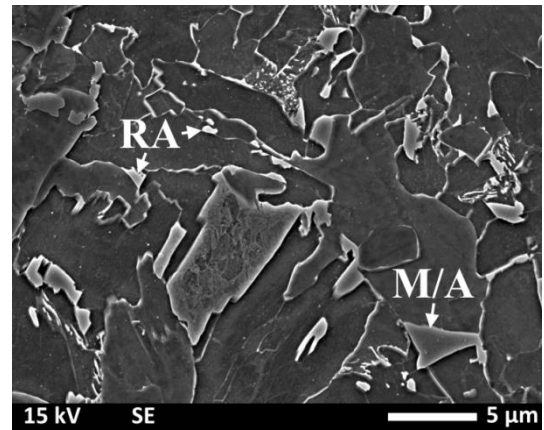
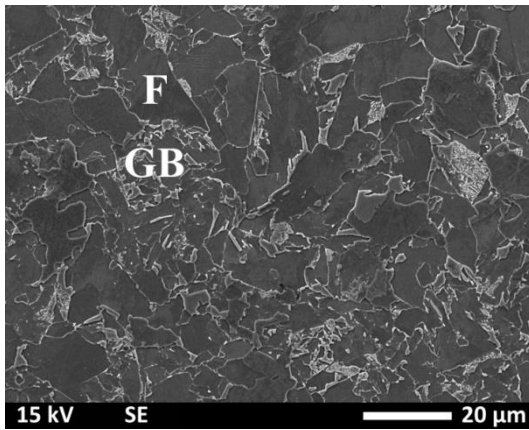


Fig. 131. Structure in the core of S659 steel in the initial state, different magnifications.

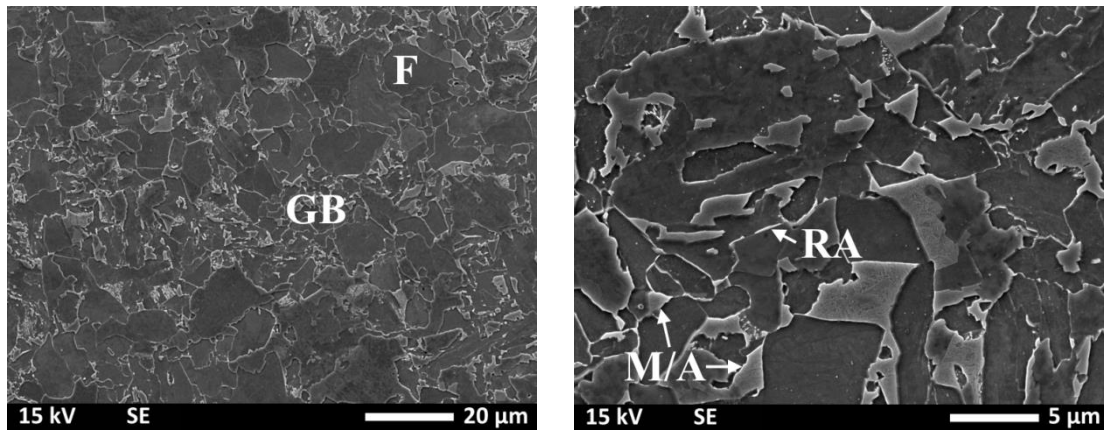


Fig. 132. Structure in the core of S660 steel in the initial state, different magnifications.

In Fig. 133, the crystal orientation maps are presented. It can be seen that, for S654, S657 and S658 steels, the PAGs can be recognized by similar orientation within one PAG and for steels S659 and S660 this is not the case. The forging process used for preparation of bars was not given any specific regime of the process temperature or cooling conditions. Therefore, the structure of those steels could be formed with conditions allowing free diffusion. Because of that, the M/A areas are coarser as carbon stabilizing A had enough time to diffuse to those grains. On the other hand, the carbon concentration was probably not sufficient, so A grains partially transformed into M during cooling.

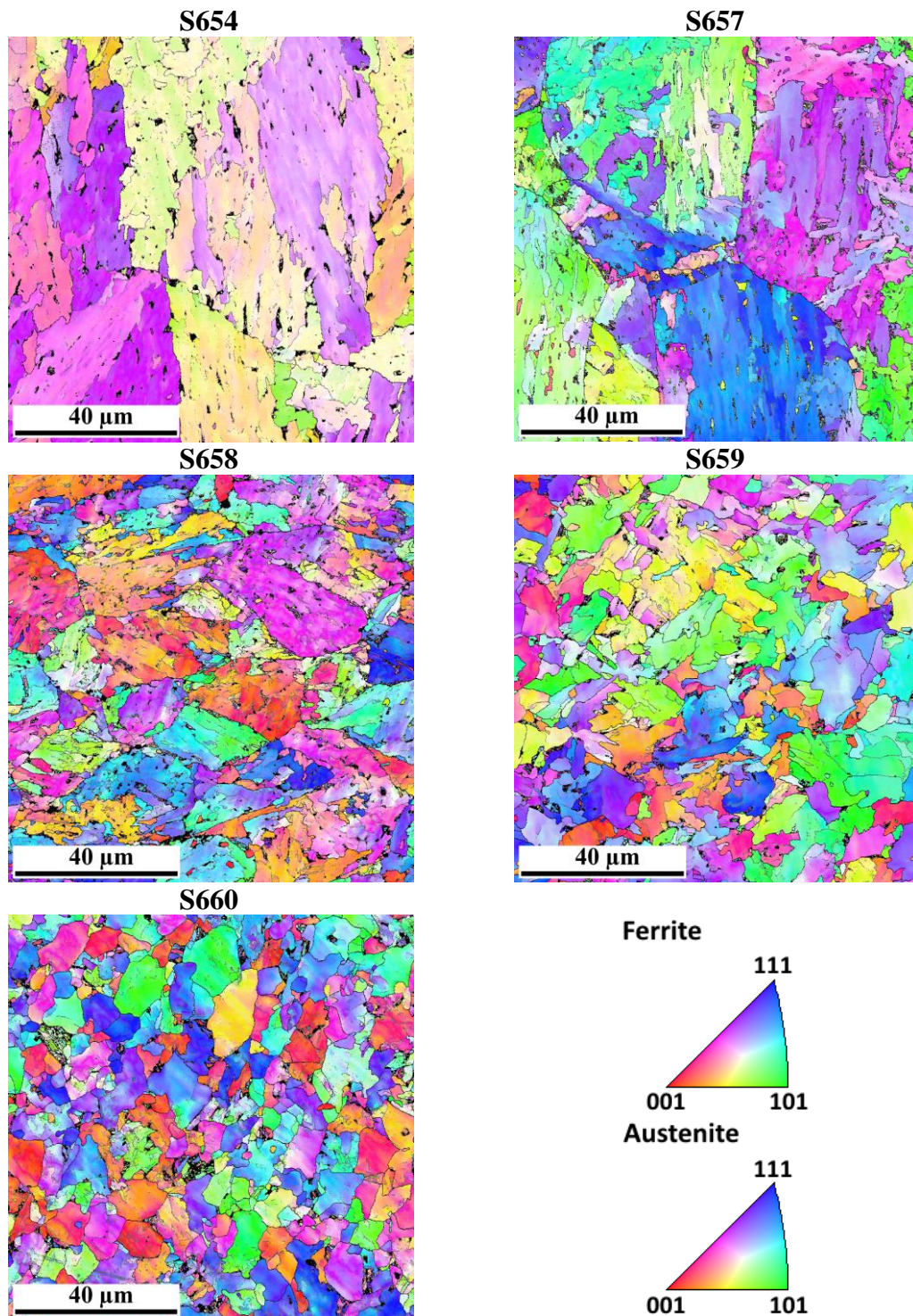


Fig. 133. Crystal orientation maps from EBSD for the new steels in the initial state.

This is also visible in Fig. 134, where the distribution of the misorientation angles is presented. The increase can be observed for all samples in the area of 10° due to M sub-blocks. Furthermore, packets and blocks of M can be found at characteristic misorientation angles 47° to 57° and 49° to 60° , respectively, for all steels. The highest number fraction at those angles is visible for S658 steel, for which the A region is the smallest one. However, RA is confirmed in the structure of the investigated steels in the

initial state, evidenced by the increased number fraction of the misorientation angles between 42° - 46° .

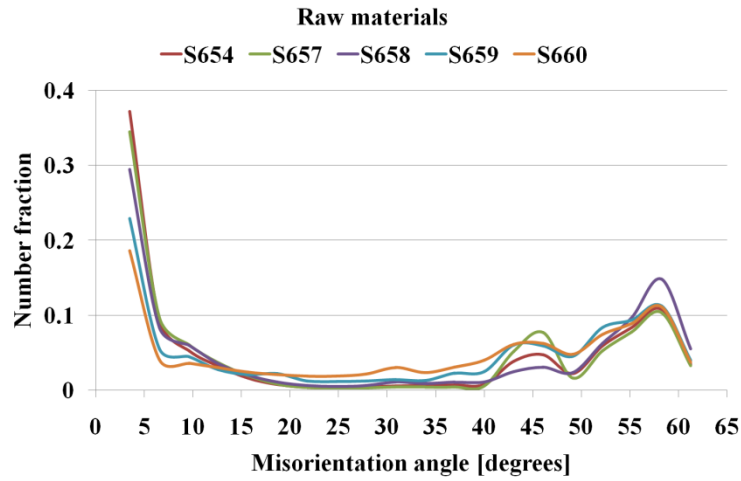


Fig. 134. Distribution of the misorientation angles in the core of the new materials.

The highest LAGB and HAGB total length (Fig. 135) is for S658 steel. It can be connected with fine second phases, which are mostly M, as can be seen in Fig. 130 and 134. Due to sub-blocky M in S657 steel and coarse M/A islands in S660 steel, the LAGB total length is higher than in the rest of steels, except for S658 steel. The highest PAGS in S654 steel results in higher sub-blocks and packets sizes, so during analysis for the same area for all samples, the total length of grain boundaries is the lowest for this steel. Furthermore, for steels with the highest HAGB, good toughness was indicated in the Charpy tests (Fig. 121). However, the best results were for S659 and S660 steels, for which higher number fraction for A characteristic angles can be seen in Fig. 134, in comparison to S658 steel.

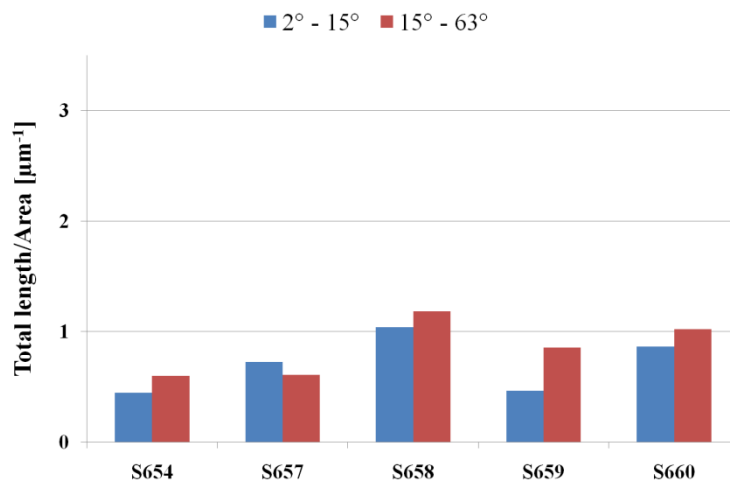


Fig. 135. LAGB and HAGB total length measured from EBSD for raw materials.

At the end, the parameter D_{ef} was determined. In Fig. 136, accumulated grain size distribution is presented. The results of D_{ef} for investigated steels are presented in Table 15.

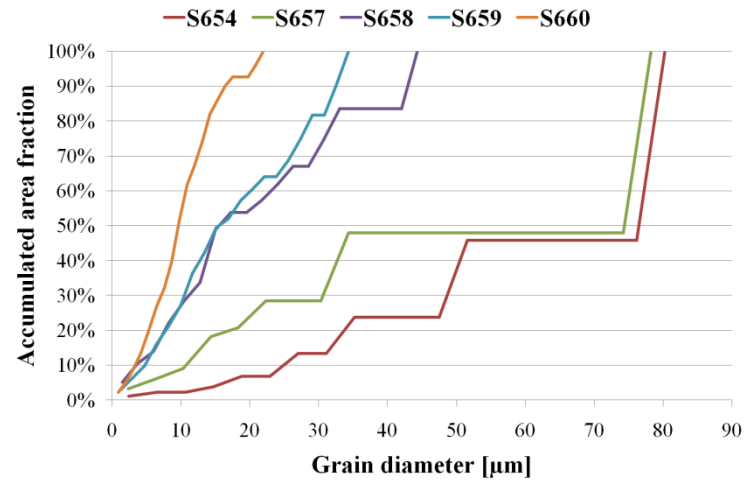


Fig. 136. Grain size distribution using 15° misorientation criterion plotted in terms of accumulated area for investigated steels in the initial state [116].

Table 15. D_{ef} determined from grain size distribution for steels in the initial state.

	7MnB8	S654	S657	S658	S659	S660
D_{ef} [μm]	57.7	78.8	66.4	31.9	28.4	13.8

S654 steel has the highest D_{ef} and the highest PAGS while the lowest D_{ef} was determined for S600 steel.

5.4.6. X-ray diffraction - retained austenite

The results of X-ray diffraction investigations of RA in the bar cores of the new steels are presented in Fig. 137. The highest amount of RA is in S654 and S658 steels.

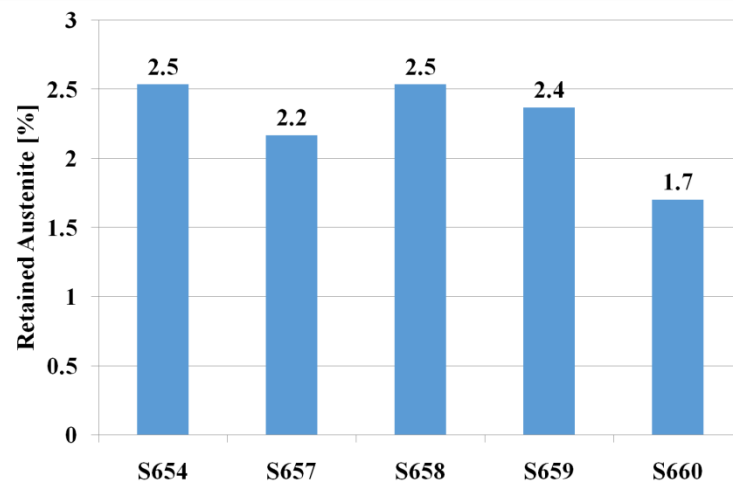


Fig. 137. XRD results of RA in the cores of the bars from new materials.

However, the difference between the steel with the highest and the lowest amount of RA is not significant and varies approximately $\pm 0.8\%$. Because the amount of RA in S659 and S660 steels is comparable with the others (Fig. 137), the difference is that most RA in S659 and S660 steels is in the coarse M/A islands observed in the structure (Fig. 131 and 132).

5.4.7. Scanning-Transmission electron microscopy

The results of TEM investigations of precipitations in the new steels are presented in Fig. 138 - Fig. 151. In steels S654 and S657 with high Ti content, the Ti_2CS phase was identified in the structure (Fig. 140 and 141, respectively).

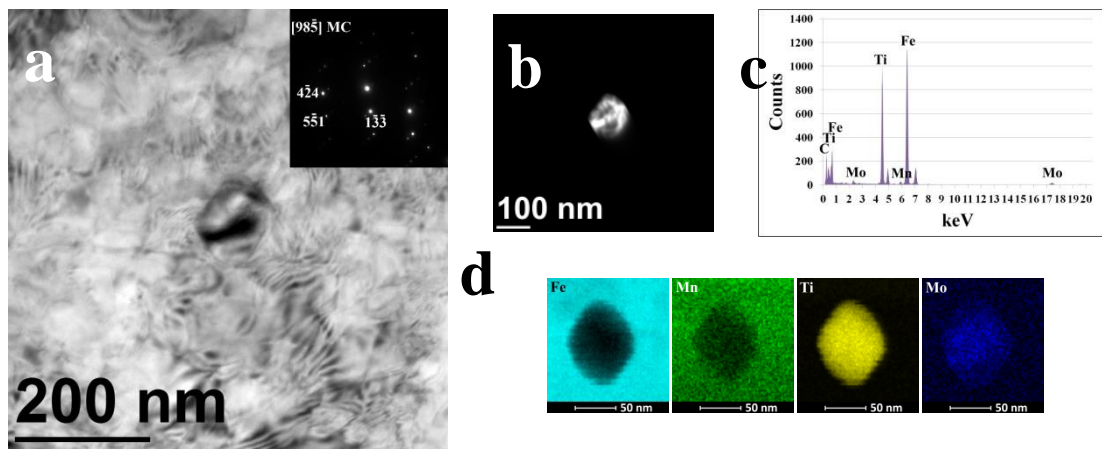


Fig. 138. MC precipitation in S654: a) bright field with electron diffraction b) dark field, c) EDS microanalysis, d) element distribution.

Additionally, MC precipitations were observed, consisting of Ti, Mo and also V in few precipitations in S654 steel (Fig. 138, 139 and Fig. 141, 142). However, due to the Mo content increased to 0.49 wt. %, the participation of this element in carbides is increased.

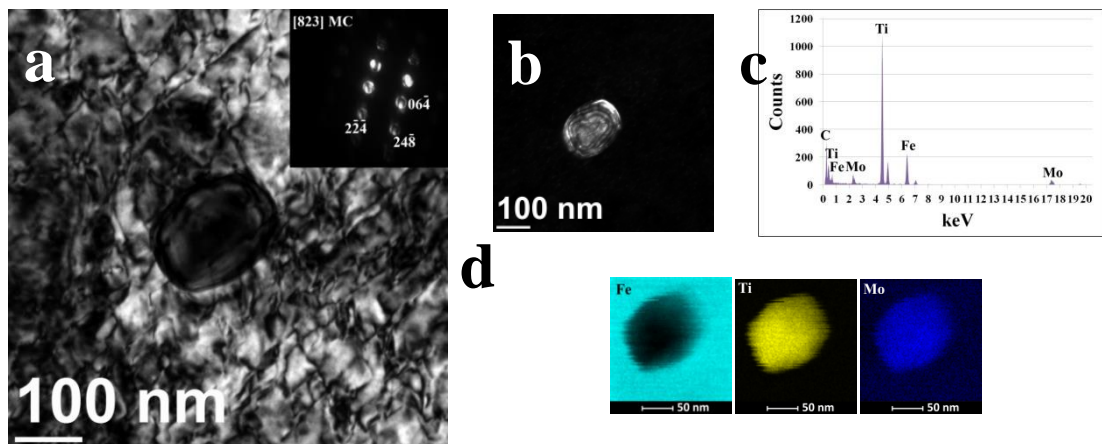


Fig. 139. MC precipitation in S654: a) bright field with electron diffraction b) dark field, c) EDS microanalysis, d) element distribution.

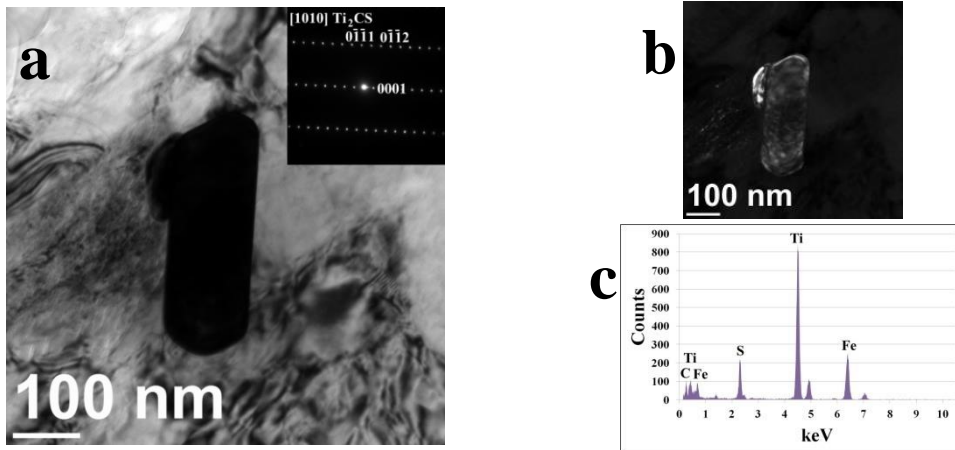


Fig. 140. Ti_2CS precipitation in S654: a) bright field with electron diffraction b) dark field, c) EDS microanalysis.

Furthermore, V was not analyzed in the particles in S657 steel in carbides. With decreasing the Ti content, the presence of Ti carbo-sulfides vanished and, for the rest of the steels, this phase was not observed in TEM tests. In S658 steel, the following precipitations were identified: MN, MCN, MC and MnS (Fig. 143 - 146), where M is mostly Ti. However, in some MN precipitations (Fig. 146) V was detected.

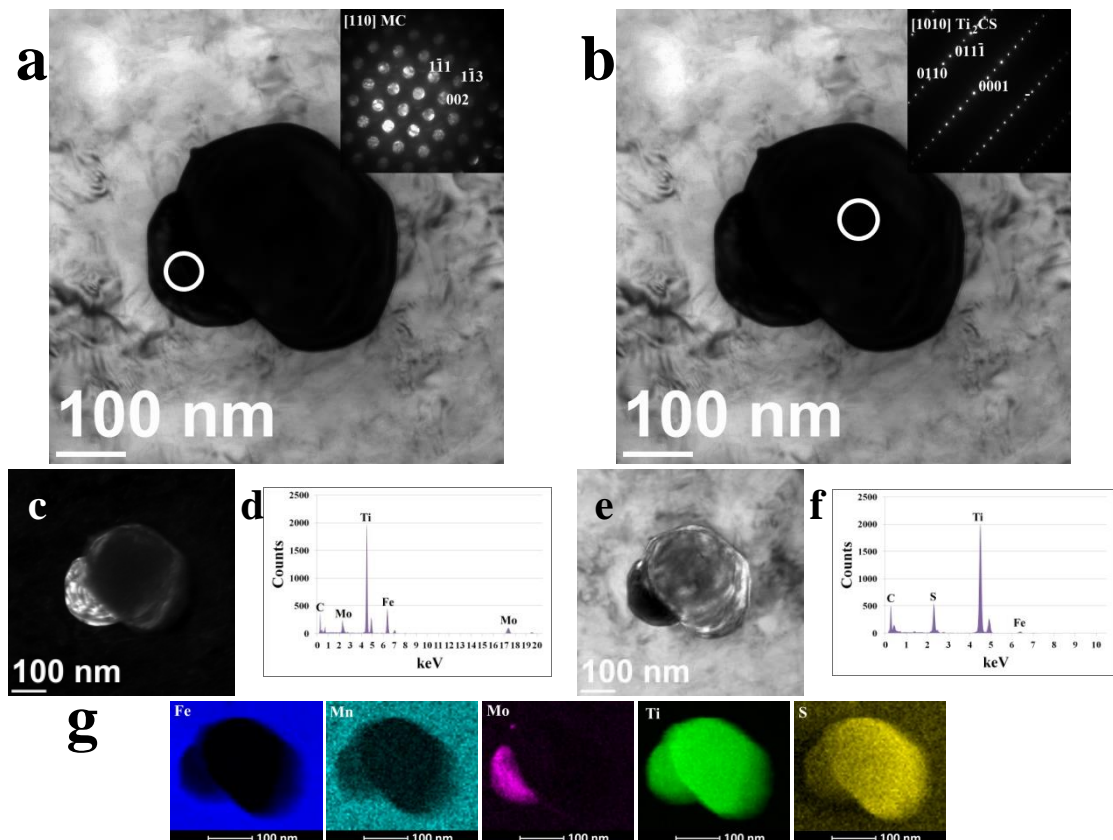


Fig. 141. MC and Ti_2CS precipitations in S657: a, b) bright field with electron diffraction, c, e) dark field, d, f) EDS microanalysis, g) element distribution.

During the microanalysis of the chemical composition of the investigated precipitations, in some cases, as for example in Fig. 144, a high Fe concentration can be noticed. It is due to the precipitation sizes and the limitation of the electron beam spot size. A precipitation is smaller than the area lighted by the beam, so the signal is also from the matrix around the precipitation. Successive lowering of the Ti content, combined with increased nitrogen in S659 steel, caused MN precipitations in the structure (Fig. 147 - 148). Moreover, as a result of the addition of Nb to the steel, the element is present in the analyzed nitrides, besides, in some cases, Nb is the main element creating the nitride (Fig. 147).

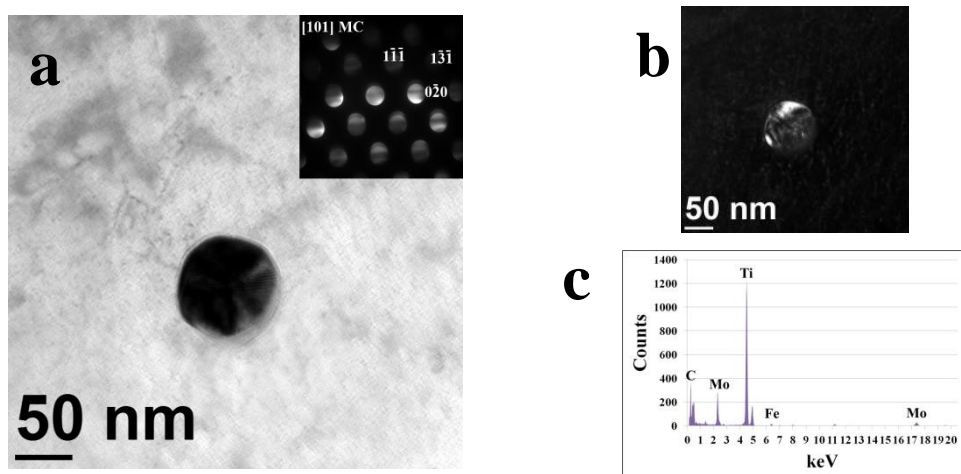


Fig. 142. MC precipitation in S657: a) bright field with electron diffraction b) dark field, c) EDS microanalysis.

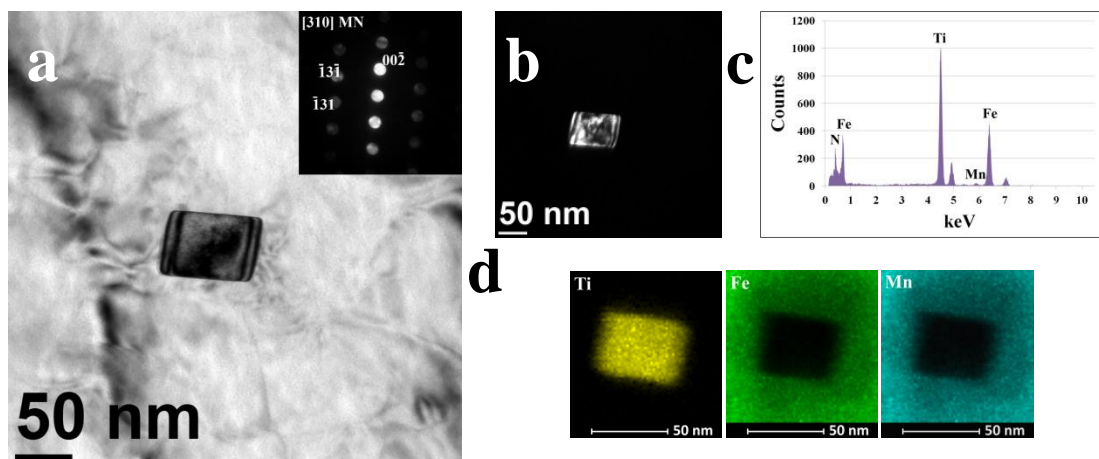


Fig. 143. MN precipitation in S658: a) bright field with electron diffraction b) dark field, c) EDS microanalysis, d) element distribution.

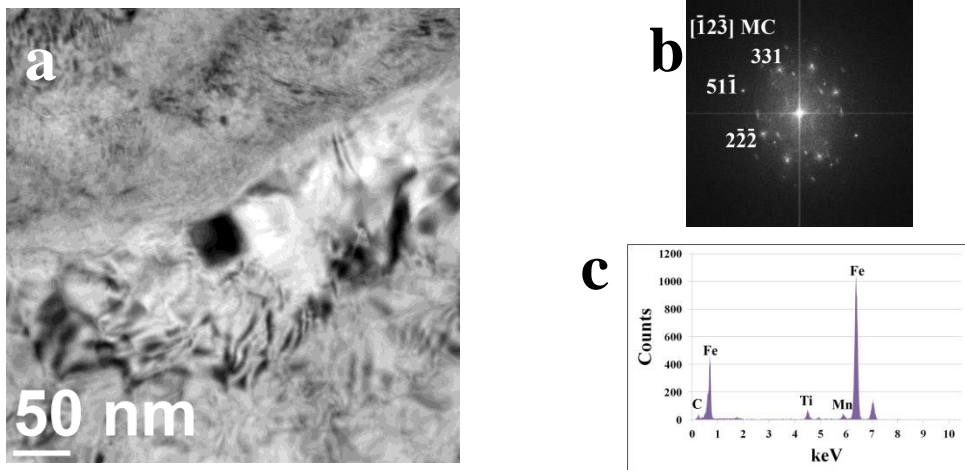


Fig. 144. MC precipitation in S658 steel: a) bright field, b) electron diffraction c) EDS microanalysis.

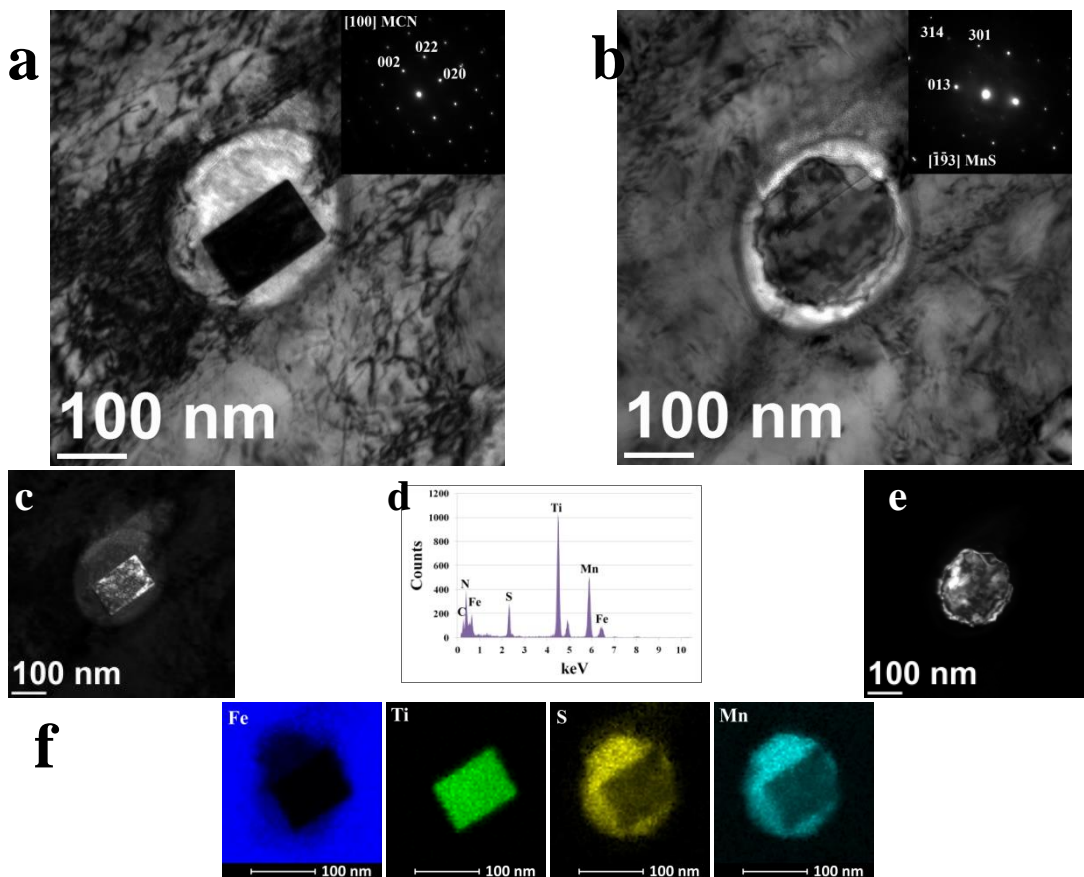


Fig. 145. MCN and MnS precipitations in S658: a, b) bright field with electron diffraction c, e) dark field, d) EDS microanalysis, f) element distribution.

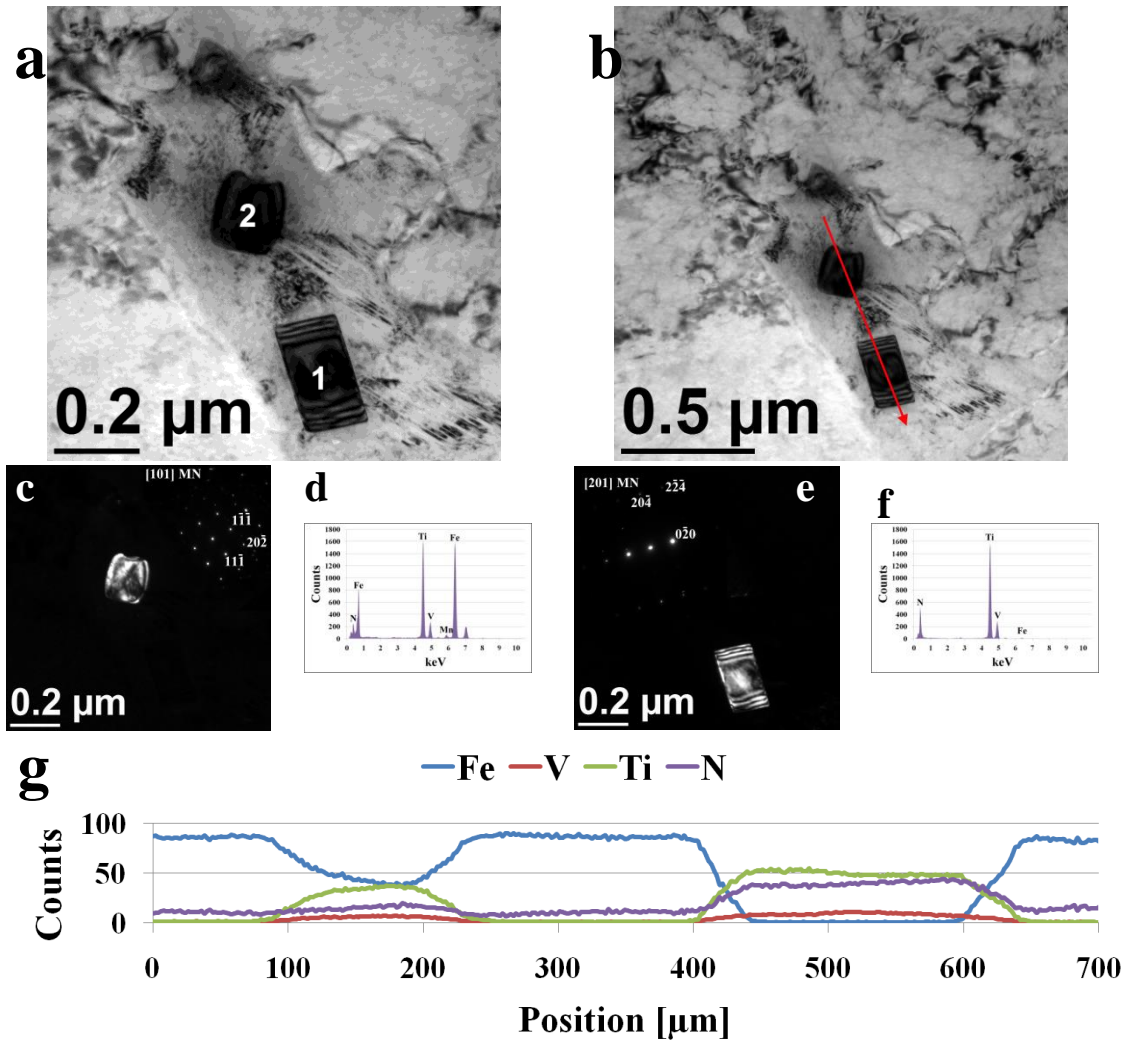


Fig. 146. MN precipitations in S658: a) bright field b) marked EDS line profile c, e) dark field with electron diffraction, d, f) EDS microanalysis, g) results of the EDS elemental line scan.

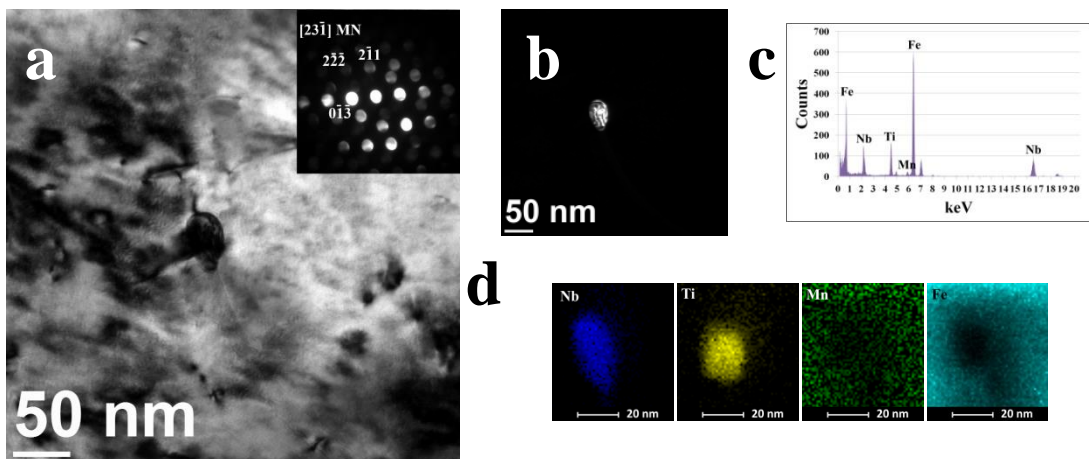


Fig. 147. MN precipitation in S659 steel: a) bright field with electron diffraction b) dark field, c) EDS microanalysis, d) element distribution.

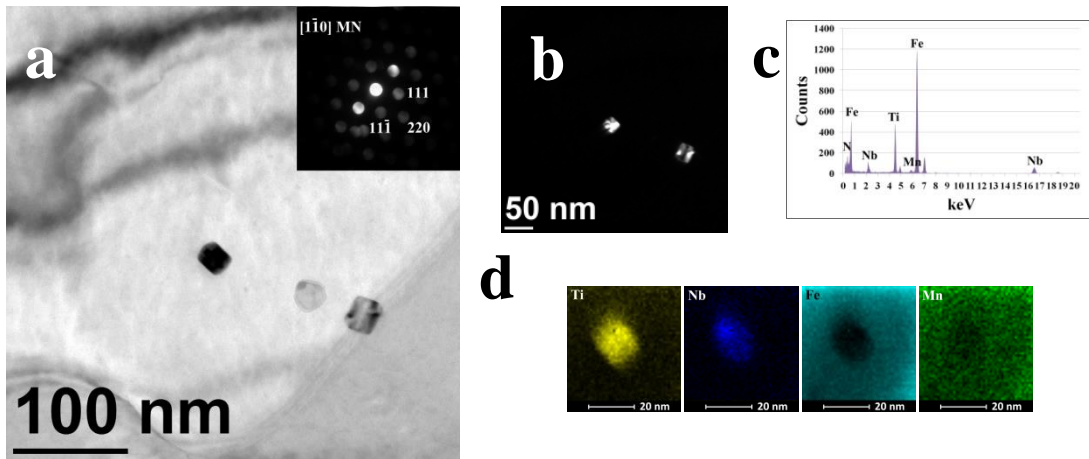


Fig. 148. MN precipitation in S659 steel: a) bright field with electron diffraction b) dark field, c) EDS microanalysis, d) element distribution.

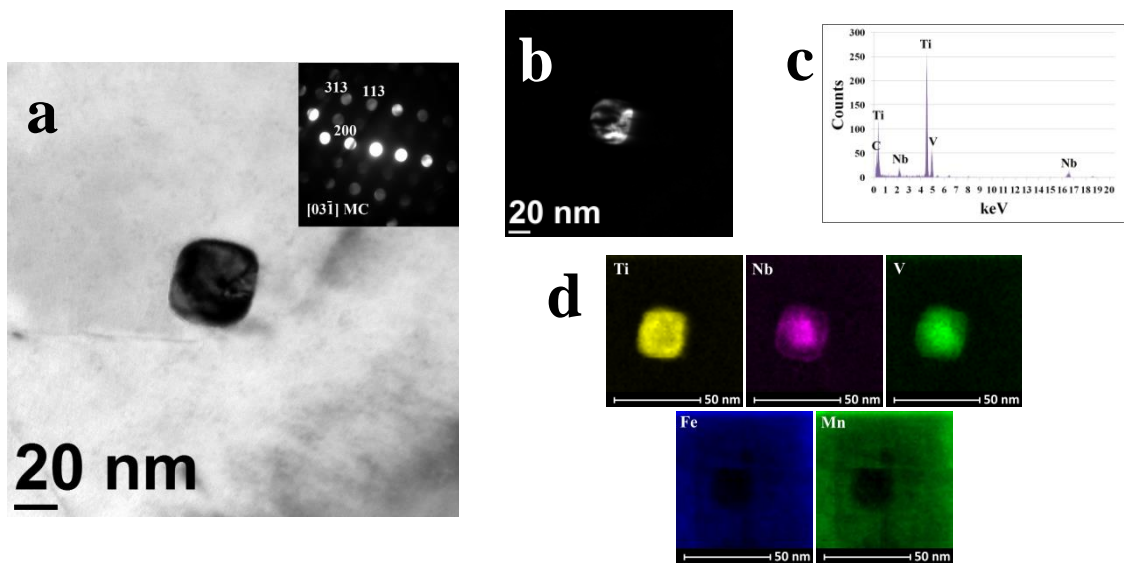


Fig. 149. MC precipitation in S660 steel: a) bright field with electron diffraction b) dark field, c) EDS microanalysis, d) element distribution.

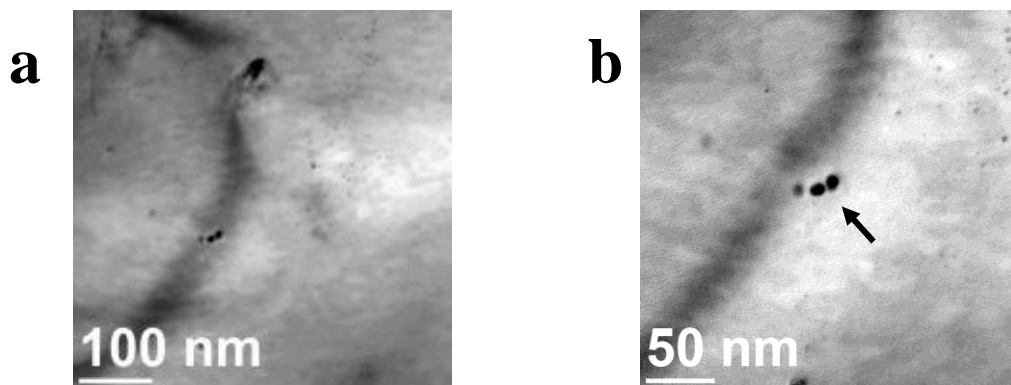


Fig. 150. Bright field with marked precipitations observed in S660 steel, investigated in Fig. 151.

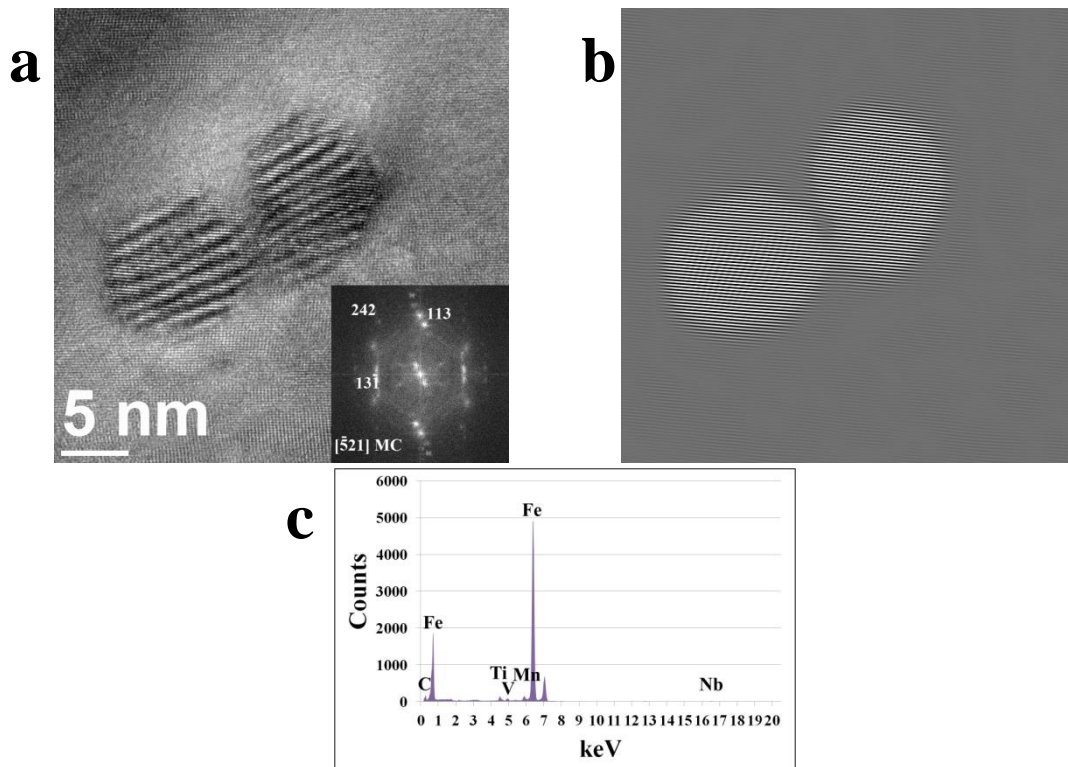


Fig. 151. MC precipitation in S660 steel: a) HRTEM with FFT b) inverse FFT, c) EDS microanalysis.

Table 16. AED, area fraction and number of precipitations per μm^3 in industrial 7MnB8 and new steels in the initial state.

	7MnB8	S654	S657	S658	S659	S660
AED [nm]	72.9	84.6	70.3	47.2	37.2	36.1
Area fraction [%]	0.22	0.31	0.51	0.19	0.60	0.44
Precipitations/μm^3	3	2	5	10	43	48

S660 steel has the lowest Ti and Nb content (from the steels which have additions of those elements) and the highest V content out of all new steels. In effect, MC carbides in S660 steel (Fig. 149 - Fig. 151) are characterized by the smallest particles in all steels, which is visible in Table 16, which contains the results of quantitative analysis of the precipitations. The microanalysis of the chemical composition of the precipitations observed in S660 steel indicates presence of Ti, Nb and V in the particles. However, Ti and Nb are the main elements, due to the temperature in which the precipitations form. Higher amount of V was analyzed in very fine precipitations (Fig. 151).

5.5. The new steels after rolling with optimized production parameters

In order to determine the effect of the proposed process parameters on the properties and structure of the new steels with modified chemical composition, rolling tests were carried out. The process parameters were developed within the second part of the study, with the use of 7MnB8 steel. The same process parameters were used for rolling of the new steels. Tests conducted on 7MnB8 steel showed that the lowest DBTT ~ -120 °C was obtained for the rolled bar material using 4 groups of process parameters: $T_A = 980$ °C, $T_R = 700$ °C and accelerated cooling 120;0;25 (Fig. 86 and Table 8). The same results were observed for most of the new steels. Therefore, the presented results of performed tests for the new steels are focused on the structure characterizations and mechanical properties of the bars rolled with the use of the fourth parameters group, $T_A = 980$ °C, $T_R = 700$ °C and accelerated cooling 120;0;25.

5.5.1. Rolling conditions

Due to different chemical composition of the new steels, it is expected that the response of the rolling material will be different during heating and/or cooling. Therefore, the temperature measurements were performed for the bars at every stage of interest. The bar used for the fourth trial was combined from S654, S657, S658 S659 and S660 steels as it was for every trial with a different parameters group. It was described in the methodology. The joined bars length in the 4th trial was 60, 60, 60, 100 and 60 cm, respectively, so the longest part of the whole bar was made from S659 steel.

Table 17. The averages temperature measured on the line at different stages of the process for new steels.

	Austenitization Temperature [°C]	Standard deviation [°C]	Rolling temperature [°C]	Standard deviation [°C]	Average temperature after rolling [°C]	Standard deviation [°C]	Cooling [l/min]	Average temperature after cooling [°C]	Standard deviation [°C]
Set	980	n.s.	700	n.s.	n.s.	n.s.	120;0;25	n.s.	n.s.
S654	983	± 1	731	± 4	818	± 6	120;0;25	499	± 9
S657	979	± 1	737	± 2	833	± 6	120;0;25	521	± 5
S658	983	± 1	741	± 1	820	± 7	120;0;25	449	± 2
S659	984	± 2	743	± 3	808	± 8	120;0;25	516	± 3
S660	994	± 1	745	± 2	810	± 5	120;0;25	505	± 2

n.s. - not specified

The average temperatures presented in Table 17, are prepared from 10 measurements in the case of smaller pieces (60 cm), and from 20 values for 100 cm. Due to the calibration of the assumed temperatures in the process, with use of 7MnB8 steel, the measured temperatures are close to the assumed.

5.5.2. Tensile test

The results of tensile tests are presented in Fig. 152 and Fig. 153. As it can be noticed, the highest increase of YS is observed for S659 and S660 steel, ~ 26 % and ~ 33 % respectively, in comparison to the materials in the initial state (Fig. 118). For the other steels, after rolling, also an increase of YS is observed. YS for S654 steel increased by ~ 16 %, and for S657 and S658 steels, by ~ 12 %. Simultaneously, for all steels, the values of UTS increased after rolling. However, the highest increase was about 12 % and was observed for S658 steel. The lowest, ~ 6 % increase was for S659 and S660 steels.

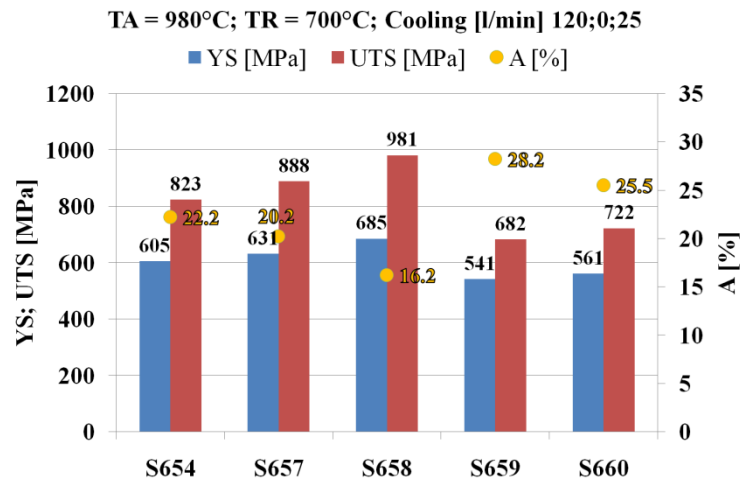


Fig. 152. Mechanical properties of the investigated new steels after rolling.

Contrary to the increment in YS and UTS for all steels, elongation did not increase for all. In the case of S658 steel, elongation is similar after rolling. Despite that, for the rest of steels elongation is improved, the highest increase was observed for S654 steel (~ 20 %) and the lowest for S660 steel (~ 3 %).

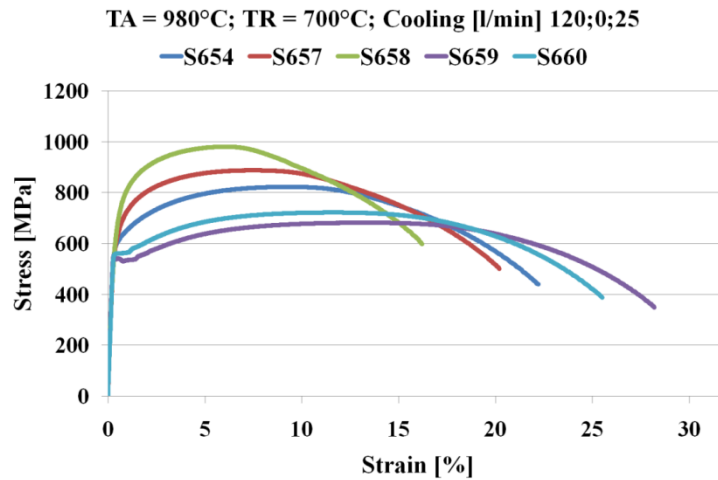


Fig. 153. Stress-strain curve for the new steels after rolling.

Comparing the stress-strain curves of the steels, Fig. 153, the stress-strain curves with pronounced YS are observed for S659 and S660 steels. To the contrary, the stress-strain curves for S654, S657 and S658 steels are without pronounced YS.

5.5.3. Hardness measurements

The cross-section hardness profiles performed on the bars after rolling revealed the increase of hardness in the outer layer of the examined bars (Fig. 154). Only S658 steel shows a gradual increase of hardness from the core to the surface. For the other steels, the highest hardness is approximately 2 mm from the surface and decreases close to the surface. The highest hardness decrease at the surface is observed for S654 steel.

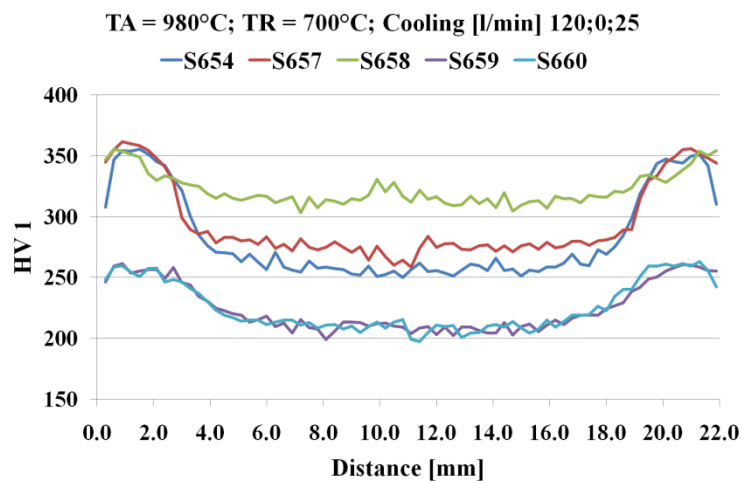


Fig. 154. Cross-section profile of the HV₁ hardness on the diameter for the new steels after rolling.

In the Table 18, the average hardness measurements for the steels after rolling, at the surfaces and in the cores of the bars, are presented. There are minor differences (30 HV) in the hardness between the surface and core of S658 steel, which can be observed in Fig. 154. The highest hardness is observed for S654, S657 and S658 steels, and the values are

comparable with the hardness of industrial 7MnB8 steel after rolling with use the same parameters group. S659 and S660 steels have hardness lower from the rest, both at the surface and in the core.

Table 18. Average HV₁ measured in two areas for the new steels after rolling.

	S654	S657	S658	S659	S660
Surface	343 ± 15	352 ± 16	345 ± 10	257 ± 6	256 ± 6
Core	255 ± 4	271 ± 6	317 ± 6	209 ± 4	208 ± 4

However, in comparison to the initial state, the hardness at the surface is increased in both cases, by ~ 50 HV. In reference to the initial state of the new materials (Table 12), the hardness in the cores after rolling is in most cases similar for the same steel grade in the initial state. The hardness in the core of S658 steel is an exception, identified with an increase by ~ 40 HV.

5.5.4. Charpy tests

The results of Charpy V-notch analyses are presented in Fig. 155. After rolling, the fracture energy in the Charpy impact test is increased at RT for all steels. As it can be noticed, steels S659 and S660 have the highest energy, even at a low temperature. Furthermore, the DBTTs for all steels were shifted to negative temperature values. In the Table 19, the estimated DBTTs are presented.

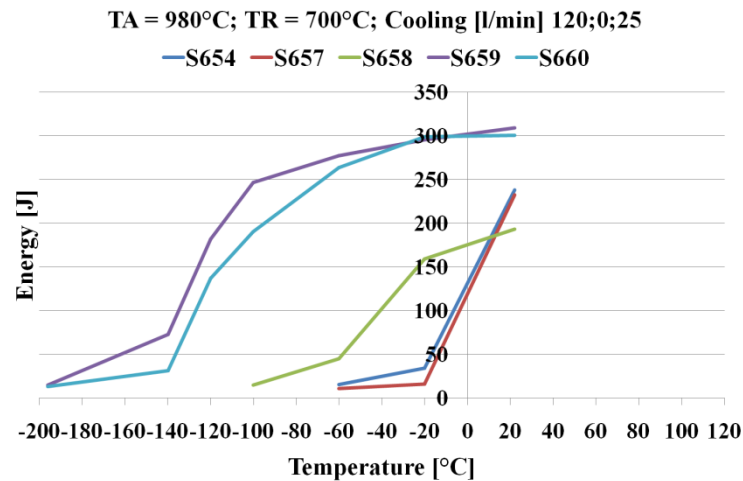


Fig. 155. Charpy V-notch impact measurements at different temperatures for the investigated steels after rolling with different process parameters.

Table 19. DBTTs estimated for the new steels after rolling with different process parameters, in °C.

Steel	DBTT [°C]				
	S654	S657	S658	S659	S660
$T_A = 980\text{ °C}$; $T_R = 700\text{ °C}$; Cooling [l/min] 120;0;25	-40	-25	-80	-180	-150

The lowest DBTT is for S659 steel (-180 °C) and the temperature is shifted by the process by 135 °C to the left, in comparison to the initial state. Next is S660 steel with the DBTT of -150 °C and the observed decrease after the process is 55 °C. For S654, S657 and S658 steels the DBTT is -40 °C, -25 °C and -80 °C, respectively. The achieved temperature shift is similar to S659 steel, for S658 steel (125 °C) and to S660 for S657 steel (75 °C). The highest difference in the DBTT before and after the process is observed for S654 steel. The DBTT is decreased by 175 °C.

5.5.5. Light optical microscopy

After rolling, the same phenomena of structure refining and gradient structure, as was observed for 7MnB8 steel, was obtained for the new steels.

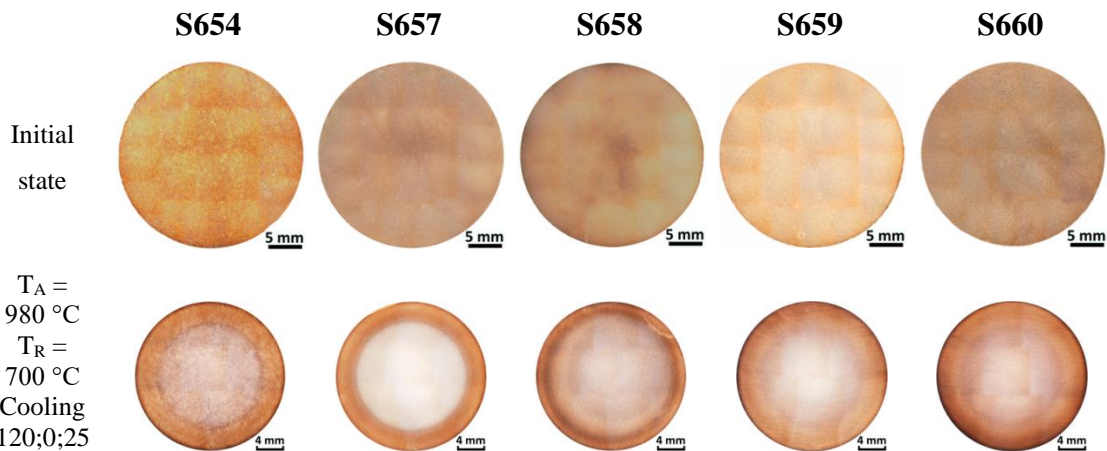


Fig. 156. Cross-section of the bars in the initial state and after rolling, made from the new steels.

As it can be seen in Fig. 156, two zones are visible in the cross section of the bars after rolling: the outer zone at the surface with finer structure and the coarser core zone (Fig. 157 - 161).

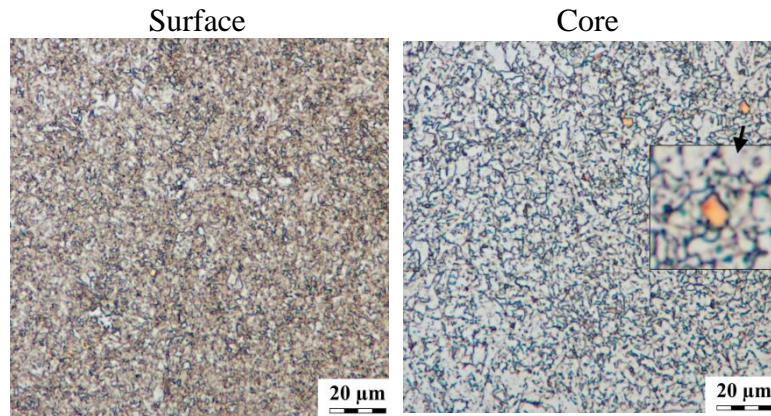


Fig. 157. GB on the surface area and in the core of the S654 bar after rolling, with coarse TiN precipitation.

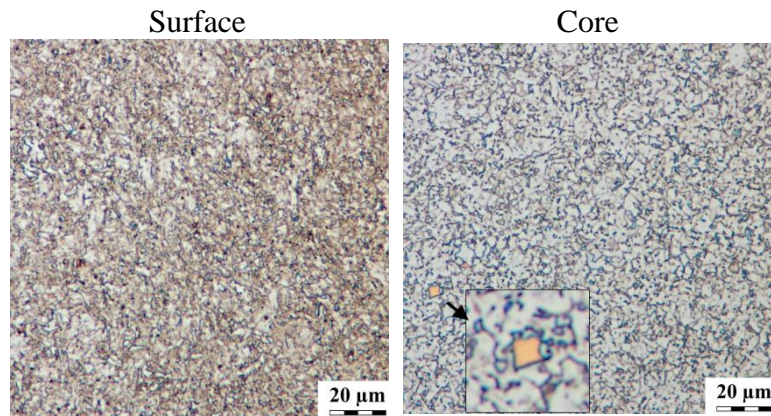


Fig. 158. GB on the surface area and in the core of the S657 bar after rolling, with coarse TiN precipitation.

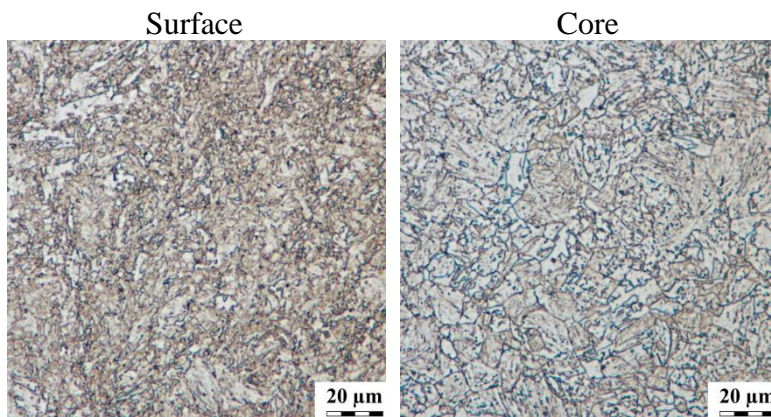


Fig. 159. UB on the surface area and in the core of the S658 bar after rolling.

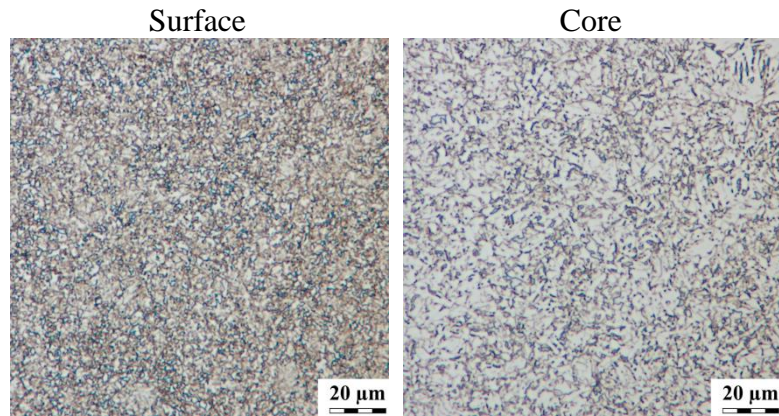


Fig. 160. GB on the surface area and in the core of the S659 bar after rolling.

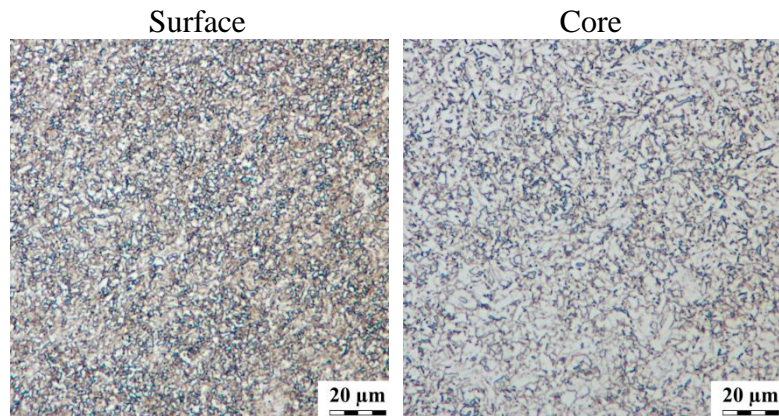


Fig. 161. GB on the surface area and in the core of the S660 bar after rolling.

The maximum thickness of the fine-grained surface is approximately 4 mm. The same was observed for 7MnB8 steel.

5.5.6. Scanning electron microscopy

The results of SEM analyses of the structure in the two areas: at the surface and in the core of the bars after rolling are presented in Fig. 162 - 166. Rolling provides refinement to the structure and its constituents on the surface of the bars in comparison to their cores. The structure of the bars is mostly GB (Fig. 162, 163 and Fig. 165, 166). However, due to the increased Mn concentration in S658 steel, the structure is different and DUB, UB and LB were obtained, Fig. 164. Moreover, in S659 and S660 steels with decreased Ti content, higher volume fraction can be observed in the structure, in comparison to the others with very fine precipitations, Fig. 165 and 166. Fig. 167 present the crystal orientation maps performed in the cores and at the surfaces of the bars.

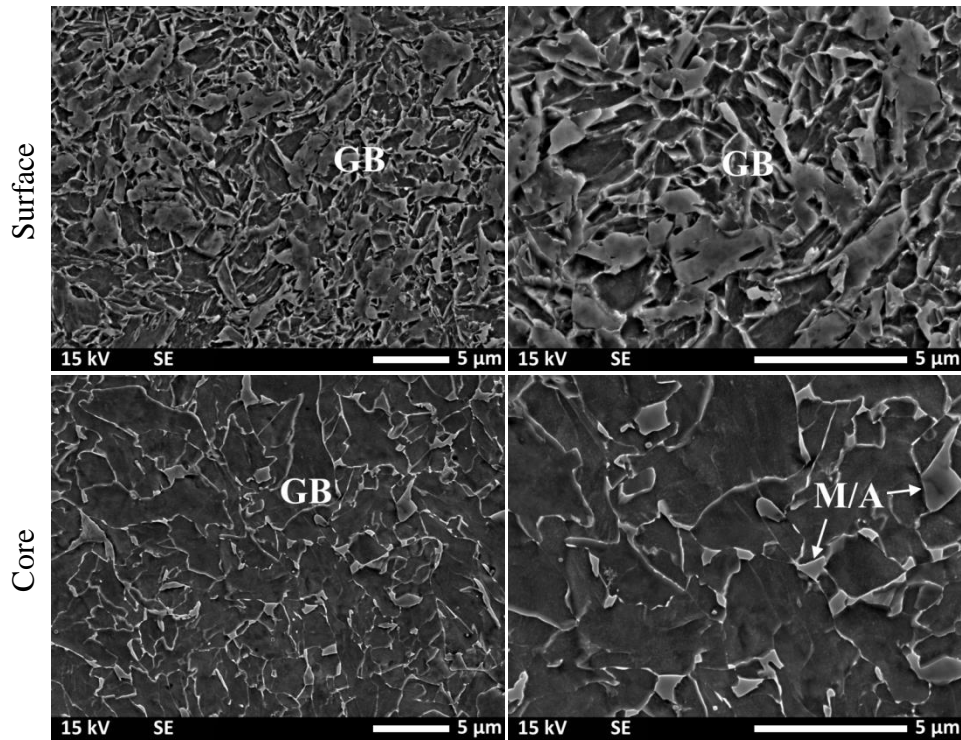


Fig. 162. Microstructure of S654 steel after rolling process with parameters: $T_A = 980\text{ }^\circ\text{C}$, $T_R = 700\text{ }^\circ\text{C}$, Cooling 120;0;25.

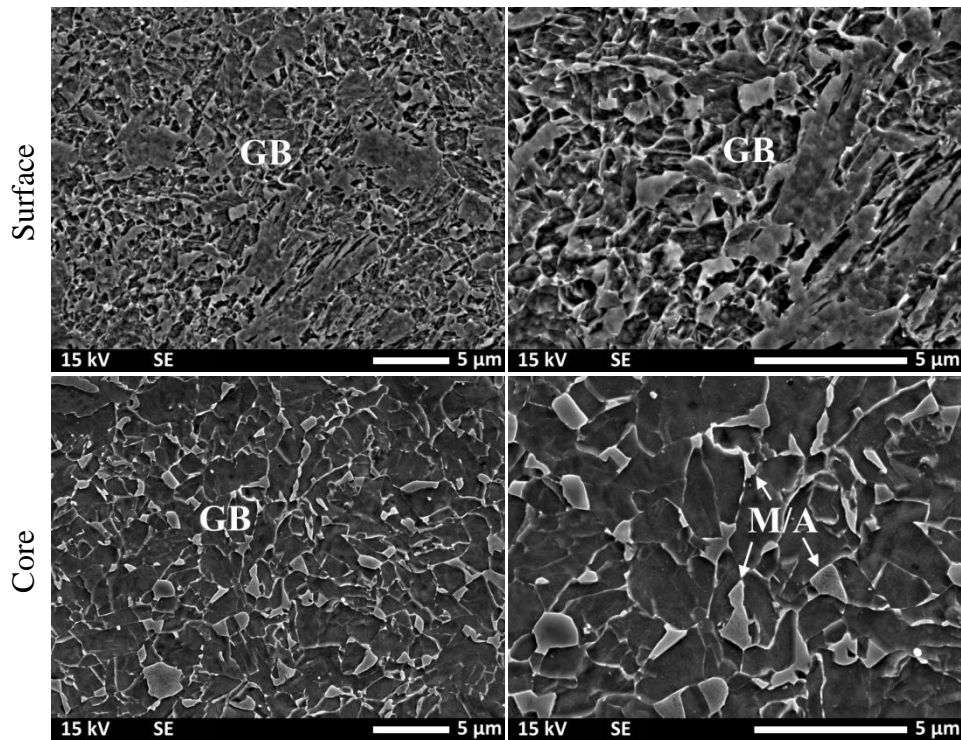


Fig. 163. Microstructure of S657 steel after rolling process with parameters: $T_A = 980\text{ }^\circ\text{C}$, $T_R = 700\text{ }^\circ\text{C}$, Cooling 120;0;25.

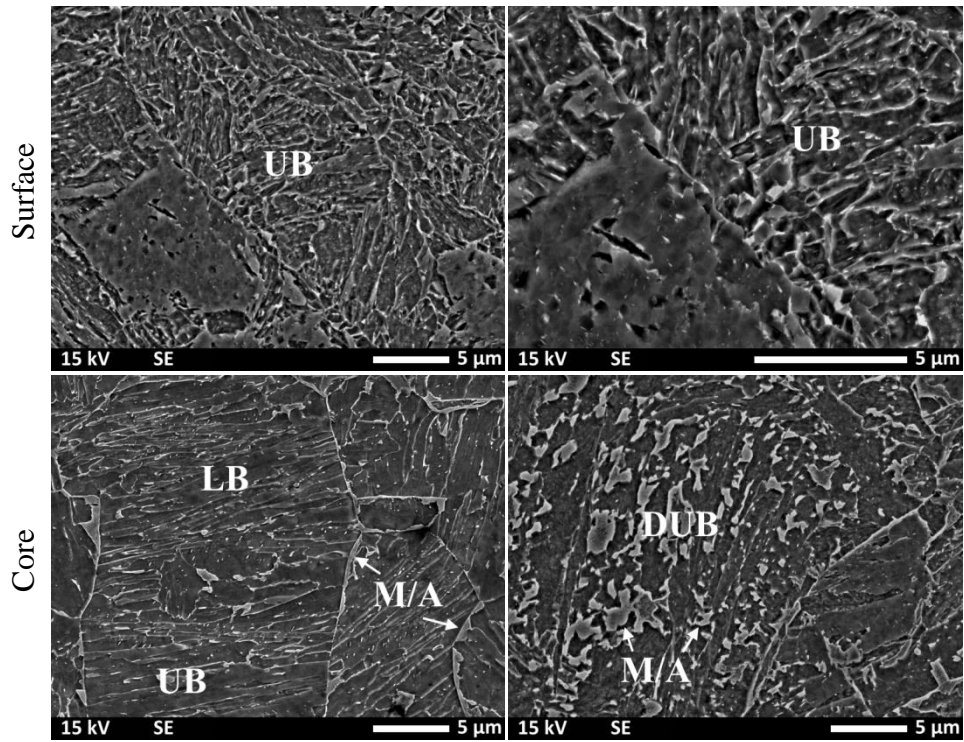


Fig. 164. Microstructure of S658 steel after rolling process with parameters: $T_A = 980\text{ }^\circ\text{C}$, $T_R = 700\text{ }^\circ\text{C}$, Cooling 120;0;25.

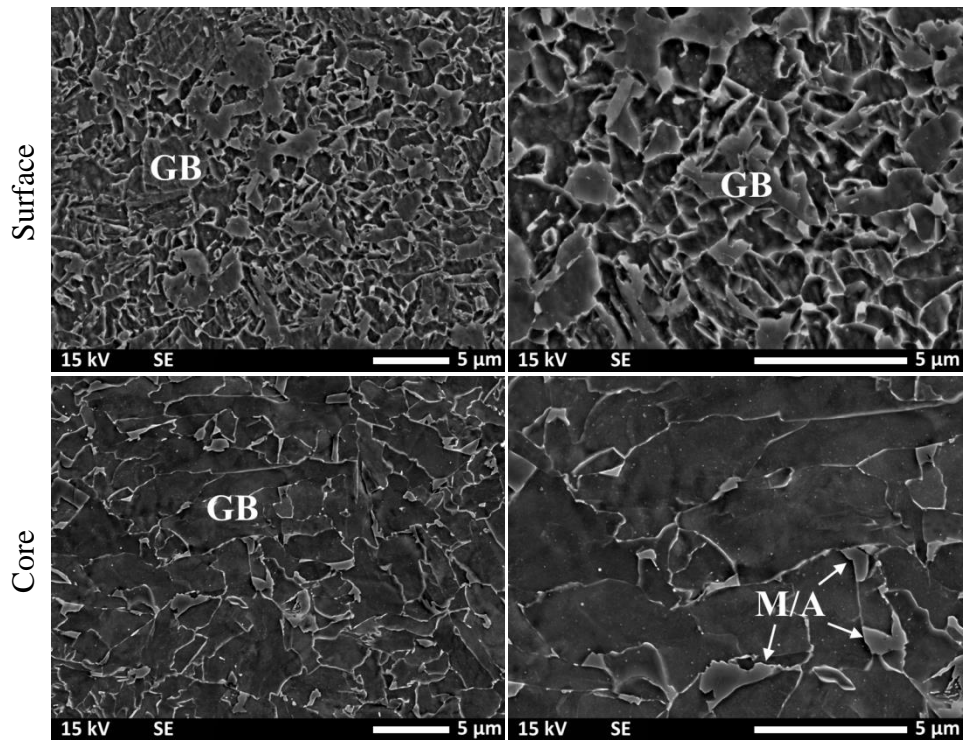


Fig. 165. Microstructure of S659 steel after rolling process with parameters: $T_A = 980\text{ }^\circ\text{C}$, $T_R = 700\text{ }^\circ\text{C}$, Cooling 120;0;25.

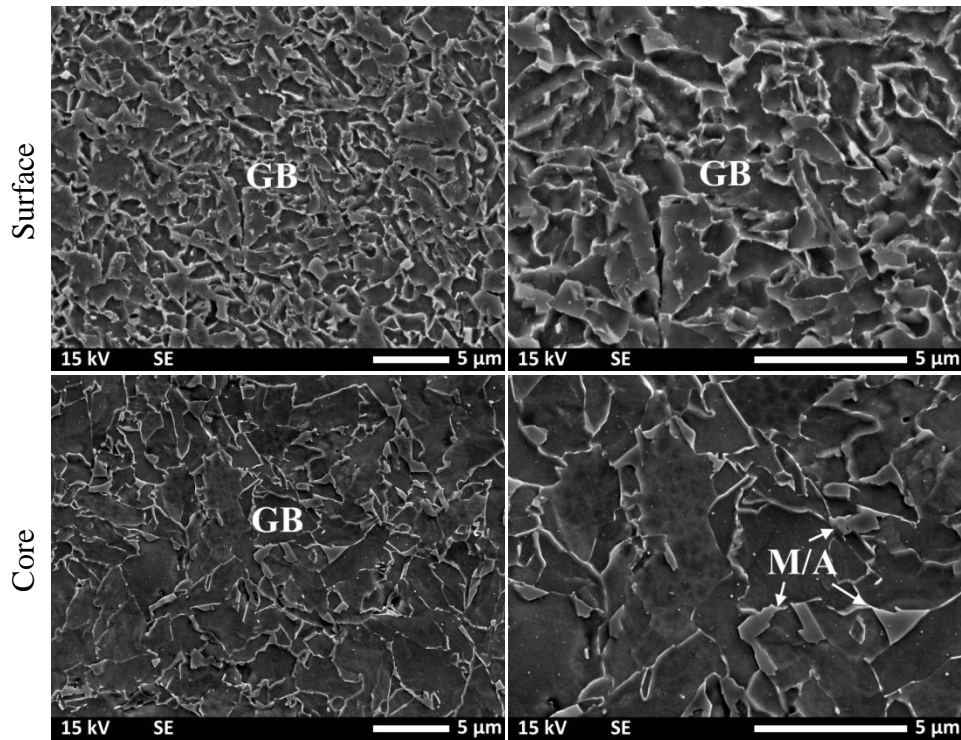


Fig. 166. Microstructure of S660 steel after rolling process with parameters: $T_A = 980\text{ }^\circ\text{C}$, $T_R = 700\text{ }^\circ\text{C}$, Cooling 120;0;25.

However, in the case of cores, during the investigations of the RA distribution, higher magnification was used during the EBSD examinations due to the RA grains size. The distribution of the misorientation angles in the cores was examined (Fig. 168) and the total length of grain boundaries in the cores and at the surfaces was measured (Fig. 169). For better understanding of the grain size influence on the mechanical properties, without simultaneous possibility of revealing the PAGs, the D_{ef} parameter for bars made of each steel was determined, based on the EBSD results from the surface and core areas. The results are shown in Fig. 170 and in Table 20.

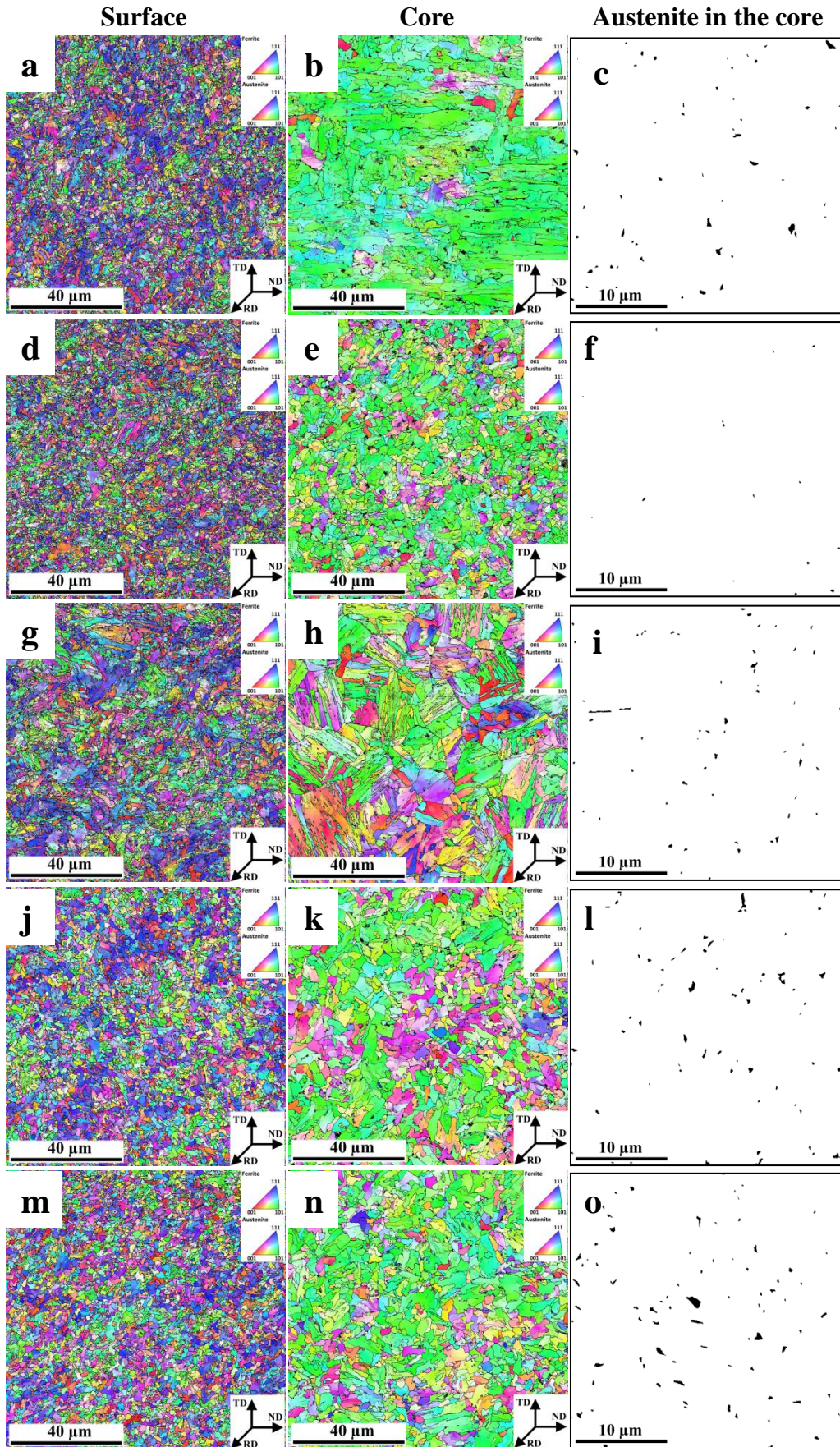


Fig. 167. Crystal orientation maps and phase maps for RA (black) for new steels rolled with use $T_A = 980$ °C; $T_R = 700$ °C; Cooling [l/min] 120;0;25 process parameters, for steel: a, b, c) S654, d, e, f) S657, g, h, i) S658, j, k, l) S659, m, n, o) S660.

The grain size in comparison to the steels in the initial state (Fig. 128 - 132) is refined by XTP rolling. Moreover, the refinement is more intensive on the surface than in the core of the bars. Furthermore, the differences between the grain orientation at the surfaces and in the cores of the bars are visible on the crystal orientation maps. The two leading variants of orientation are: [111] at the surface and [101] in the cores, perpendicular to the samples surface.

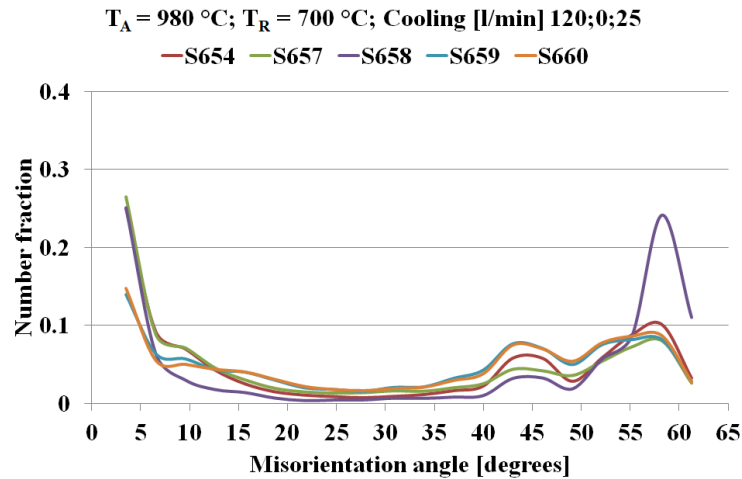


Fig. 168. Distribution of the misorientation angles in the core of the investigated steels after rolling.

The results of the distribution of the misorientation angles, presented in Fig. 168, confirm the SEM structure observations, that the GB is present in steels S654, S657, S659 and S660 after rolling. However, the increased number fraction of the low angle region proves some participation of UB. For S658, the curve is more characteristic for LB, but in the core, mostly UB was observed in the structure (Fig. 164). However, the low angle signal characteristic for UB is also visible for this steel.

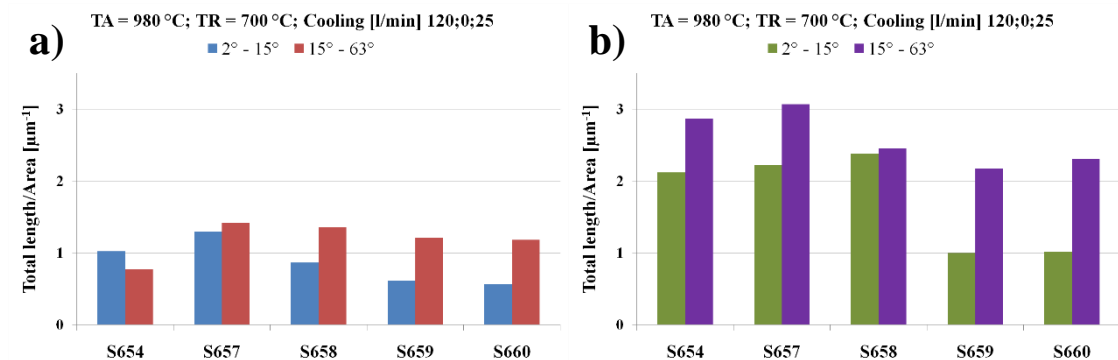


Fig. 169. Total length of grain boundaries: a) in the core, b) at the surface of the investigated steels after rolling.

The analysis of the total length of grain boundaries shows an increase of LAGB and HAGB on the surface of the bars after rolling (Fig. 169). In the cores of the bars, the total length of HAGB doubles its value in comparison to the initial state of the steels (Fig.

135). The higher participation of those grain boundaries has beneficial influence on the DBTT and fracture energies measured for the steels (Fig. 121 and Fig. 155).

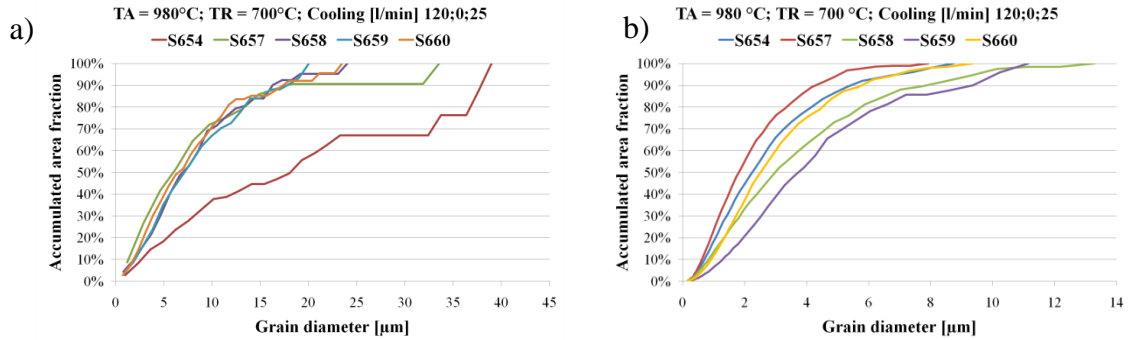


Fig. 170. Grain size distribution using 15° misorientation criterion plotted in terms of accumulated area for the investigated steels after rolling with different process parameters: a) core, b) surface.

Table 20. Determined D_{ef} from grain size distribution for the steels after rolling, core area.

		S654	S657	S658	S659	S660
Core Surface	D_{ef} [μm]	36.8	13.3	12.9	13.3	11.5
		4.2	3.3	5.9	6.1	4.4

The determined D_{ef} for the steels was decreased by the applied XTP process. The highest decrease in comparison to the values for the initial state is obtained for S657 steel, ~ 80%. For S654, S657 and S659 steels the D_{ef} is about two times lower after the rolling. The effect of refinement by rolling in S660 steel is poor in comparison to the other steels. However, this steel has the smallest D_{ef} of the new steels in the initial state. On the other hand, the highest D_{ef} is for S654 steel, for which the highest initial D_{ef} (78.8 μm) was obtained by forging.

5.5.7. X-ray diffraction - retained austenite

The results of RA are presented in Fig. 171. The smallest amount of RA can be observed in S657 steel, 2.6 %. Higher RA participation is in S658 steel, 3.8 %. S654 steel has RA at the level comparable to industrial 7MnB8 steel after rolling with the same process parameters group.

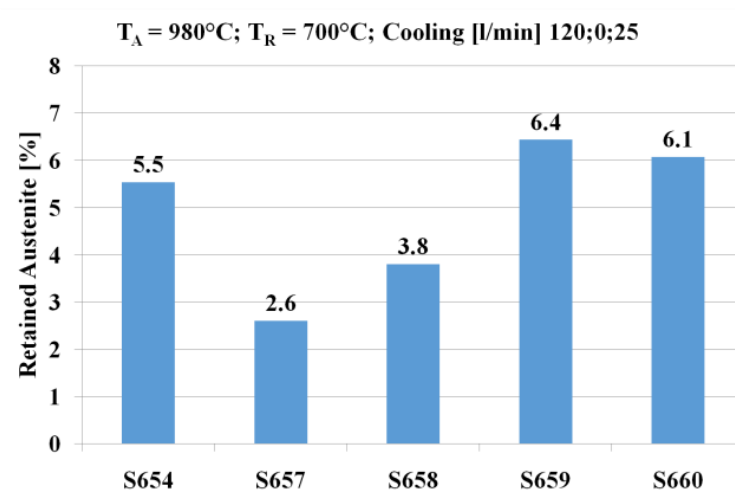


Fig. 171. XRD results of RA in the core of the investigated steels after rolling.

However, fraction of RA in S654 (5.5 %) steel is 0.4 % higher than in 7MnB8 steel (5.1 %). The highest fraction of RA is observed in S659 and S660 steels, where its participation is over 6 %. For S659 steel it is 6.4 % and for S660, 6.1 %.

5.5.8. Scanning-Transmission electron microscopy

The samples for the TEM analysis were chosen based on the best toughness properties after rolling with the optimized process parameters. The best toughness was obtained for S658, S659 and S660, by rolling with the fourth parameters group ($T_A = 980$ °C, $T_R = 700$ °C, cooling 120;0;25, therefore the examination of those three steels was performed. The research included phase identification of the precipitations and microanalysis of the chemical composition by EDS. No carbides were identified in S658 steel, only MN and M_2N nitrides were observed, formed by Ti, Mo and V (Fig. 173 and Fig. 174). However, carbon was identified in precipitations MCN as can be seen in Fig. 172. Furthermore, the cementite was present in steel along with the presence of UB and LB structures (Fig. 175 and Fig. 176). With a decreased Ti content, coarse Ti-rich precipitations were not observed in S659 and S660 steels. In S659 steel with Nb additions, this element accompanies Ti in MN and MC phases (Fig. 177 and 178, respectively). Furthermore, it forms very fine MC and $MC_{0.76}$ precipitations with Mo (Fig. 180 and 181). Fine MN with Ti and Nb were identified in the neighborhood of fine NbC precipitations (Fig. 181), yet not in all cases. In Fig. 182, the examples of dark field images of very fine precipitations are presented. The results for S660 steel are presented in Fig. 183 - 186. Very fine M_2N and MC precipitations were observed in the structure. For the most part, the elements in the particles were Ti, Nb and V. However, in some single cases also a small amount of Mo was observed (Fig. 185).

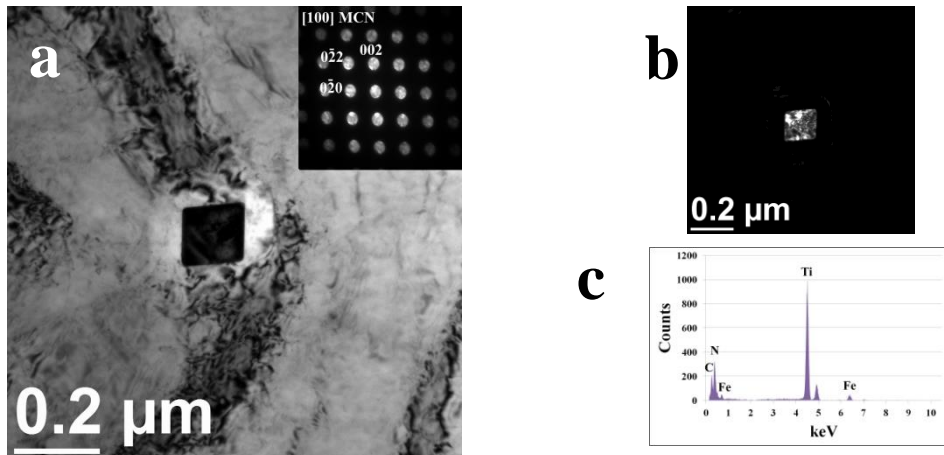


Fig. 172. MCN precipitation in S658 steel after rolling with $T_A = 980$ °C, $T_R = 700$ °C, cooling 120;0;25: a) bright field with electron diffraction b) dark field, c) EDS microanalysis.

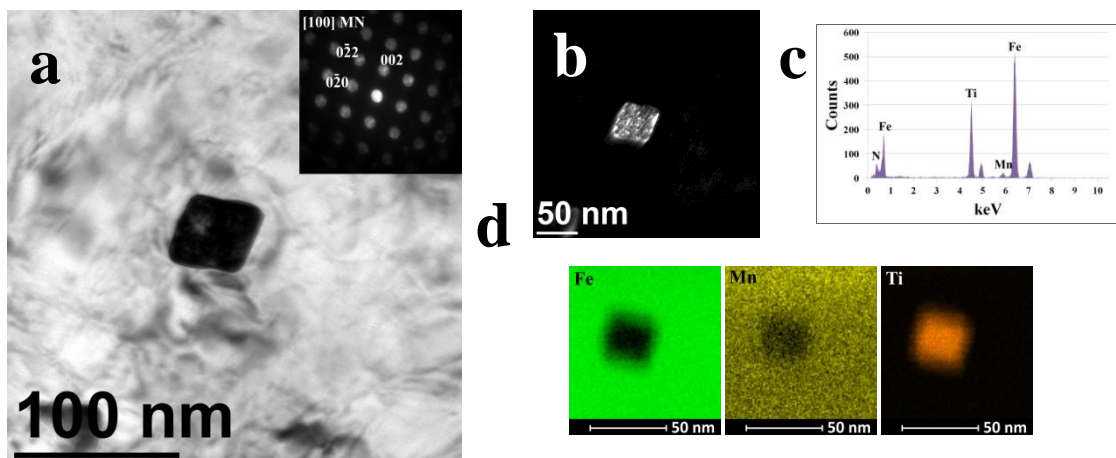


Fig. 173. MN precipitation in S658 steel after rolling with $T_A = 980$ °C, $T_R = 700$ °C, cooling 120;0;25: a) bright field with electron diffraction b) dark field, c) EDS microanalysis, d) element distribution.

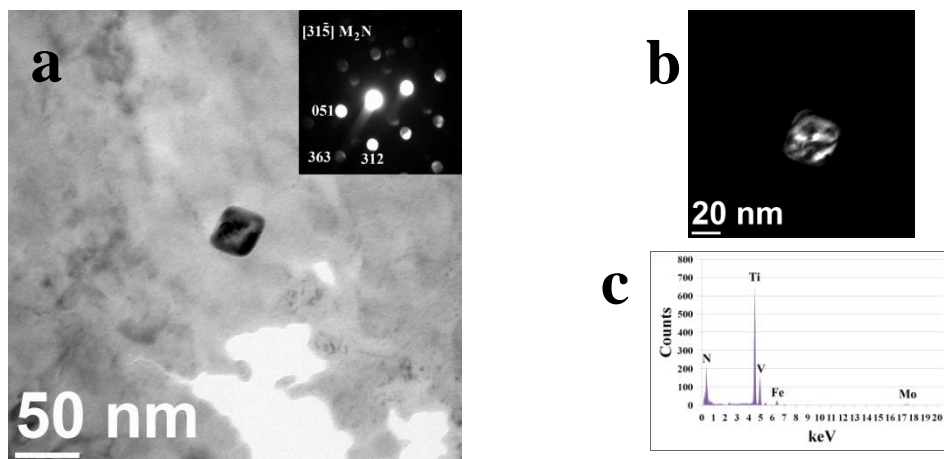


Fig. 174. M_2N precipitation in S658 steel after rolling with $T_A = 980$ °C, $T_R = 700$ °C, cooling 120;0;25: a) bright field with electron diffraction b) dark field, c) EDS microanalysis.

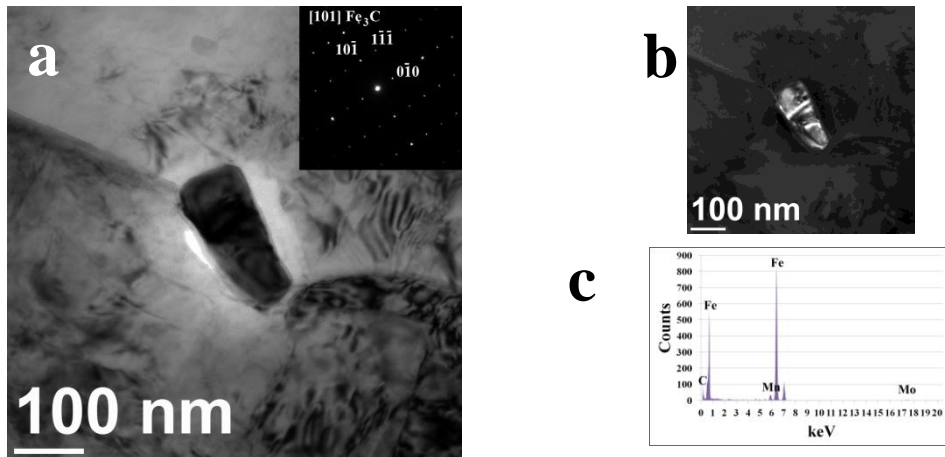


Fig. 175. Fe_3C precipitation in S658 steel after rolling with $T_A = 980^\circ\text{C}$, $T_R = 700^\circ\text{C}$, cooling 120;0;25: a) bright field with electron diffraction b) dark field, c) EDS microanalysis.

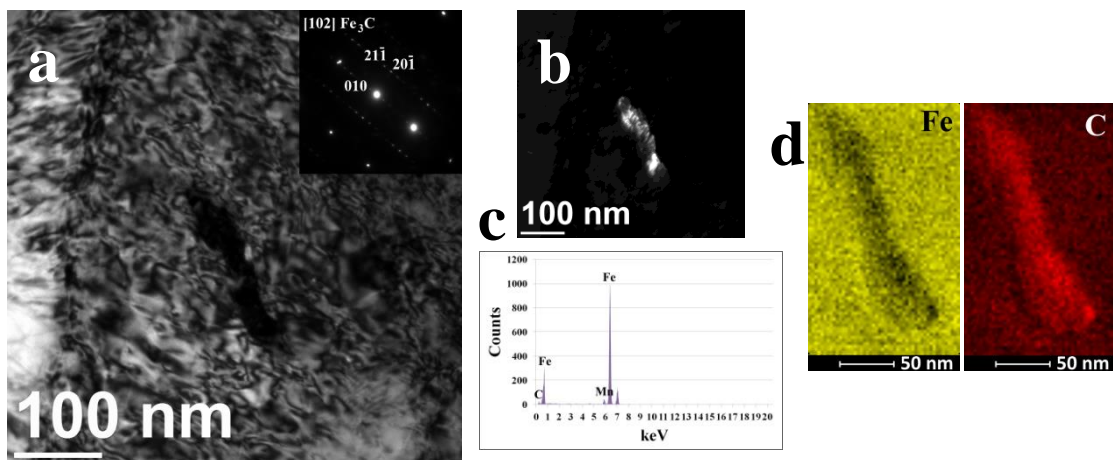


Fig. 176. Fe_3C precipitation in S658 steel after rolling with $T_A = 980^\circ\text{C}$, $T_R = 700^\circ\text{C}$, cooling 120;0;25: a) bright field with electron diffraction b) dark field, c) EDS microanalysis, d) element distribution.

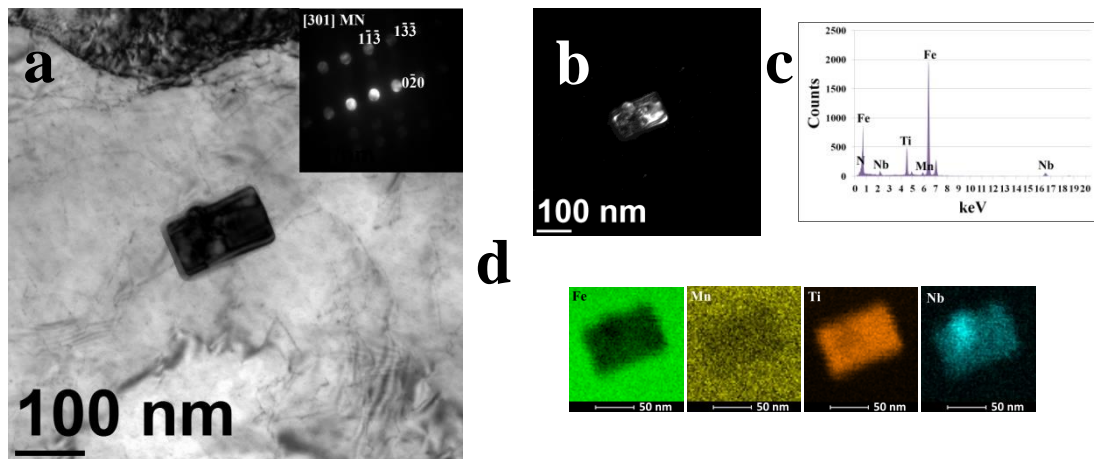


Fig. 177. MN precipitation in S659 steel after rolling with $T_A = 980^\circ\text{C}$, $T_R = 700^\circ\text{C}$, cooling 120;0;25: a) bright field with electron diffraction b) dark field, c) EDS microanalysis, d) element distribution.

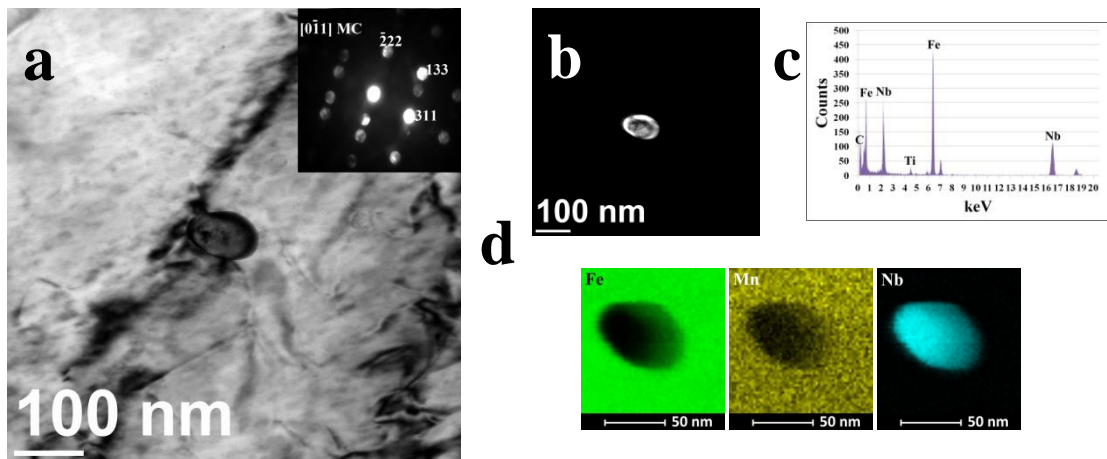


Fig. 178. MC precipitation in S659 steel after rolling with $T_A = 980\text{ }^\circ\text{C}$, $T_R = 700\text{ }^\circ\text{C}$, cooling 120;0;25: a) bright field with electron diffraction b) dark field, c) EDS microanalysis, d) element distribution.

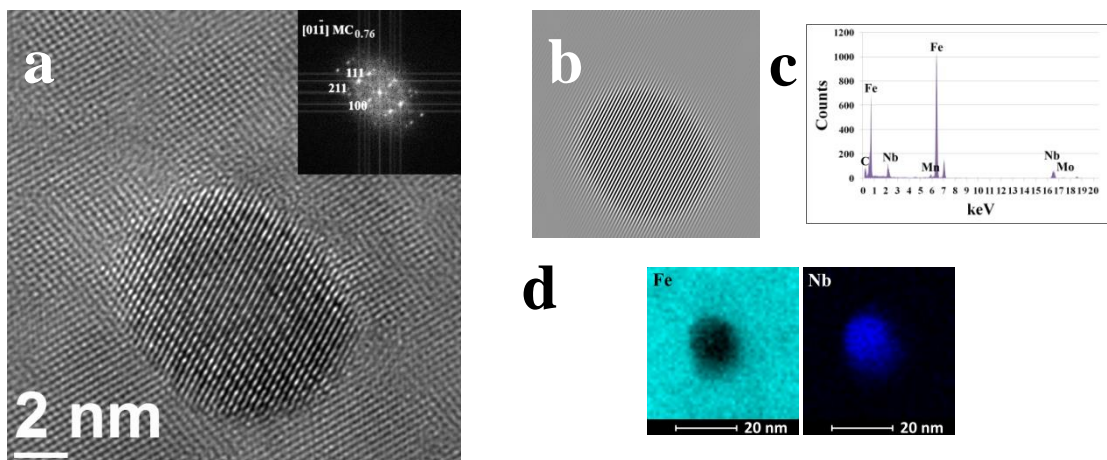


Fig. 179. $MC_{0.76}$ precipitation in S659 steel after rolling with $T_A = 980\text{ }^\circ\text{C}$, $T_R = 700\text{ }^\circ\text{C}$, cooling 120;0;25: a) bright field with electron diffraction b) dark field, c) EDS microanalysis, d) element distribution.

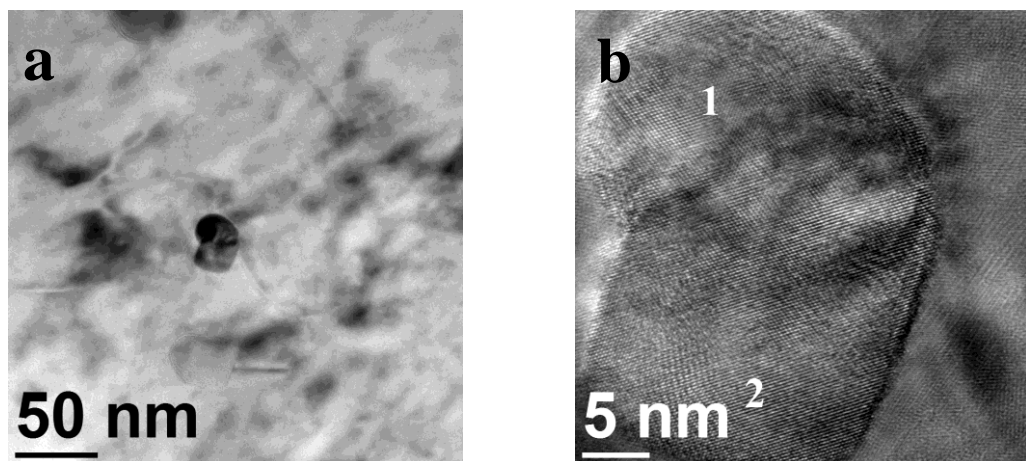


Fig. 180. Fine precipitations observed in S659 steel after rolling with $T_A = 980\text{ }^\circ\text{C}$, $T_R = 700\text{ }^\circ\text{C}$, cooling 120;0;25: a) bright field, b) HRTEM with marked areas of interest, investigated in Fig. 181.

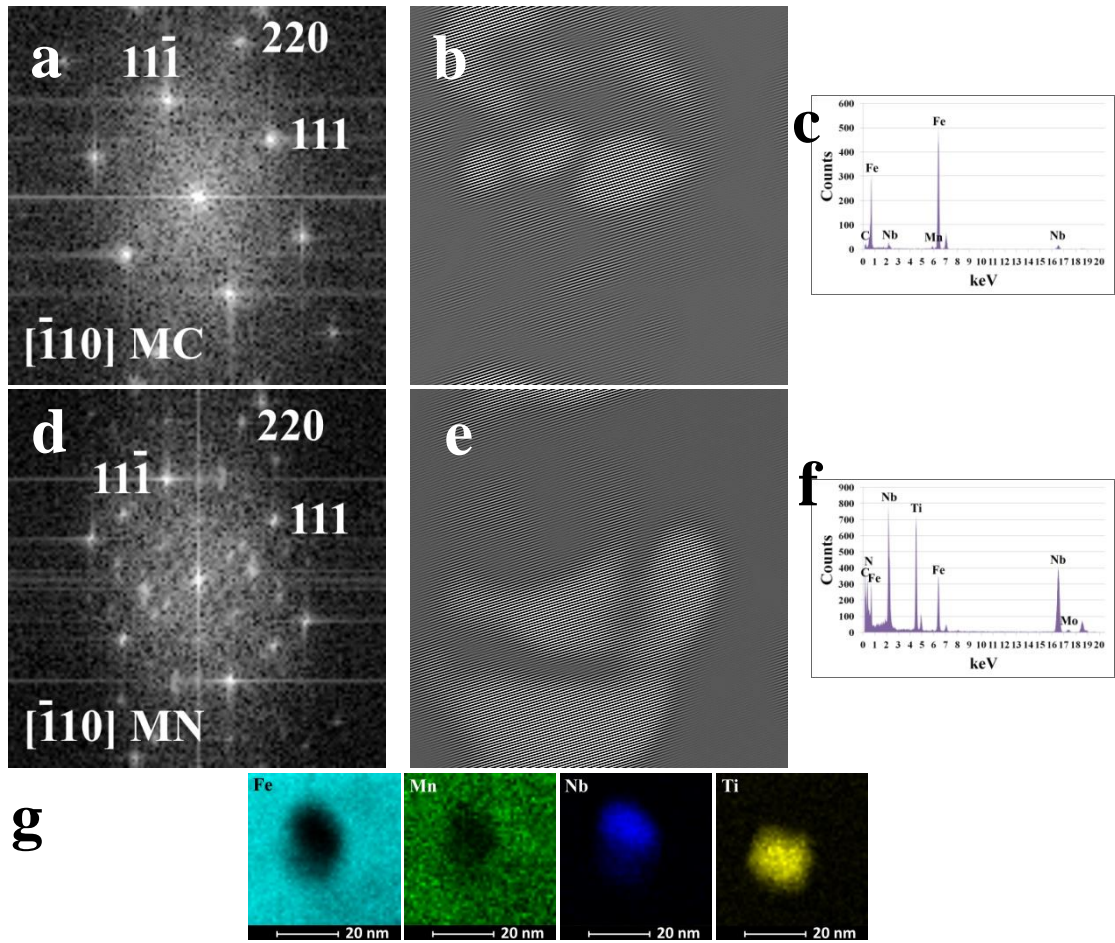


Fig. 181. MN and MC precipitations analysis from Fig. 180: a, d) FFT b, e) inverse FFT, c, f) EDS microanalysis, d) element distribution.

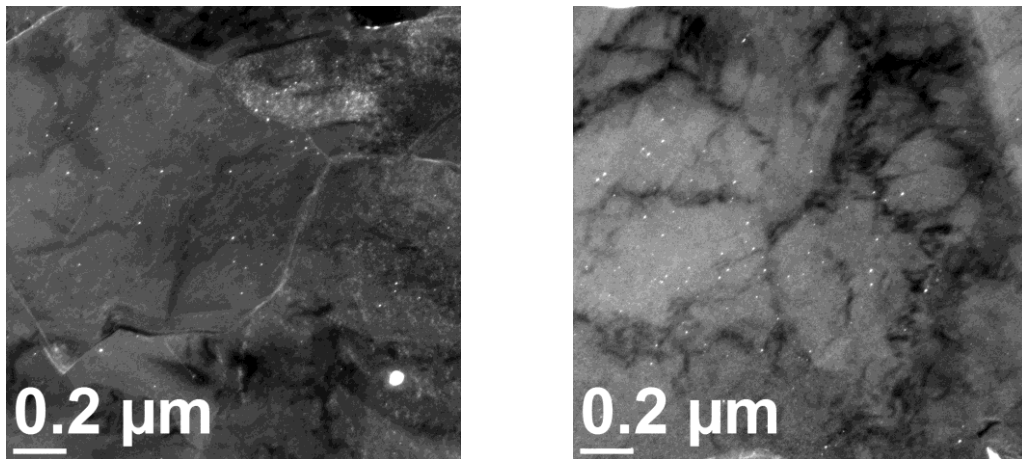


Fig. 182. Dark field images of the fine precipitations observed in S659 steel after rolling with $T_A = 980\text{ }^\circ\text{C}$, $T_R = 700\text{ }^\circ\text{C}$, cooling 120;0;25.

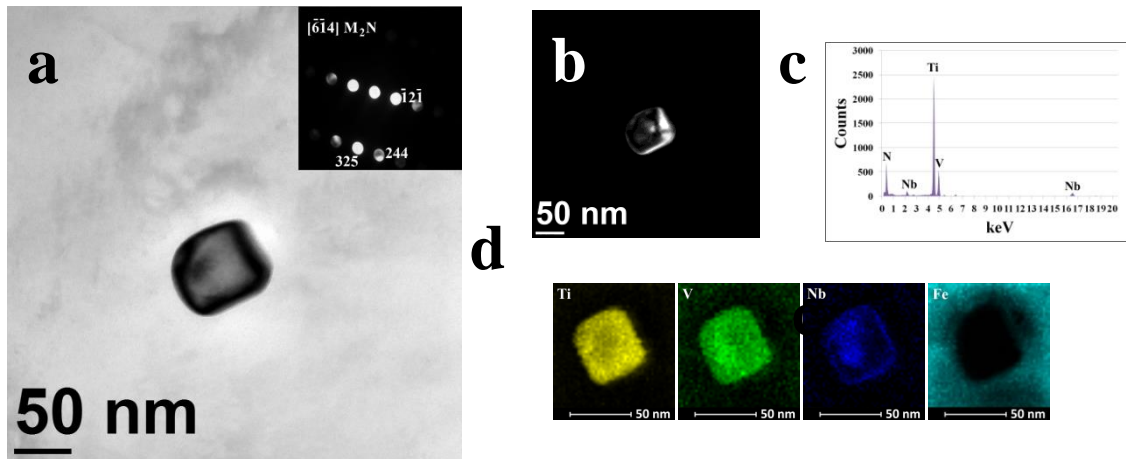


Fig. 183. M_2N precipitation in S660 steel after rolling with $T_A = 980$ °C, $T_R = 700$ °C, cooling 120;0;25: a) bright field with electron diffraction b) dark field, c) EDS microanalysis, d) element distribution.

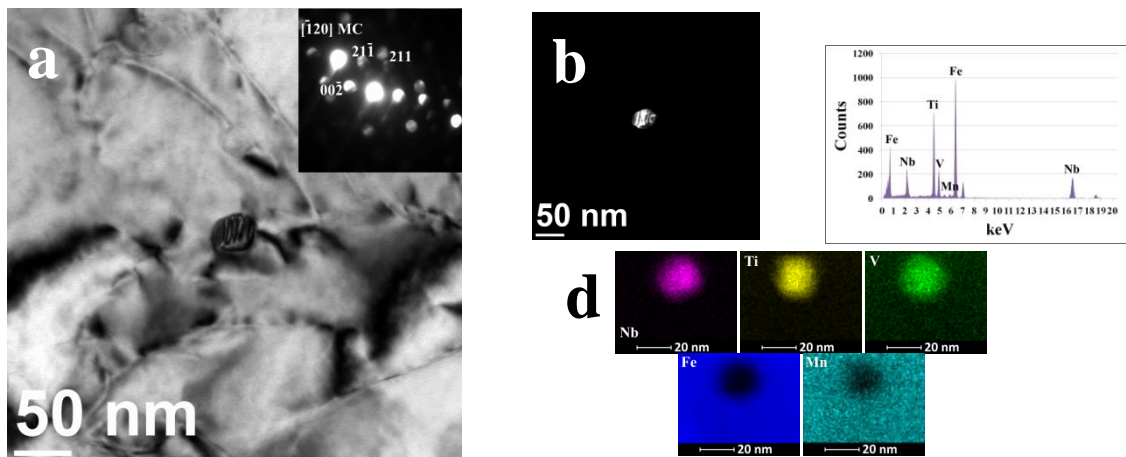


Fig. 184. MC precipitation in S660 steel after rolling with $T_A = 980$ °C, $T_R = 700$ °C, cooling 120;0;25: a) bright field with electron diffraction b) dark field, c) EDS microanalysis, d) element distribution.

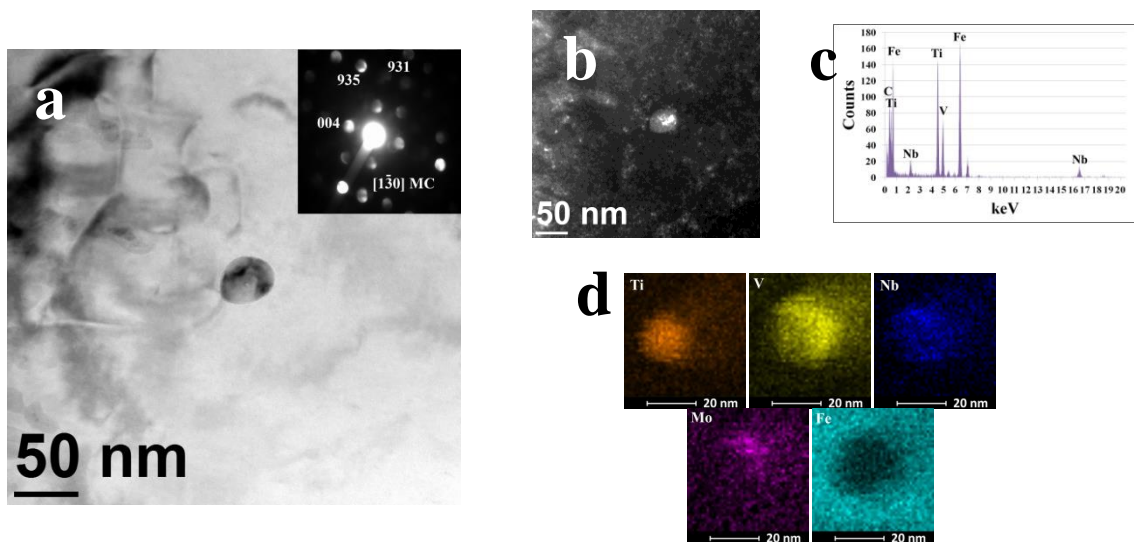


Fig. 185. MC precipitation in S660 steel after rolling with $T_A = 980$ °C, $T_R = 700$ °C, cooling 120;0;25: a) bright field with electron diffraction b) dark field, c) EDS microanalysis, d) element distribution.

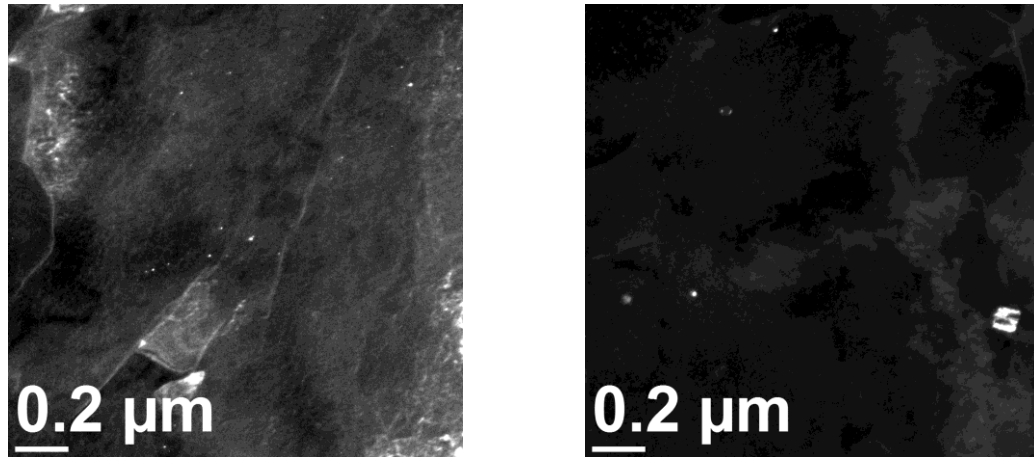


Fig. 186. Dark field images of the fine precipitations observed in the S660 steel after rolling with $T_A = 980$ °C, $T_R = 700$ °C, cooling 120;0;25.

The quantitative analysis results are collected in Table 21. After the process of cross rolling, finer precipitations are obtained in those steels in comparison to the steels in the initial state. However, in the case of steel S658 it is the opposite: AED of the precipitations increases after the process. Comparing Table 16 and Table 21, it can be noticed that after thermomechanical treatment, carbides dissolve in the steel and they are no longer observed in the structure. The nitrides are stable at the increased temperature, so their dissolving is limited. The absence of fine MC precipitations observed in the initial S658 steel caused an increase in the equivalent diameter due to the averaged result of measurements.

Table 21. AED, area fraction and number of the precipitations per μm^3 in industrial 7MnB8 and the new steels after rolling with a) blue color - $T_A = 915$ °C, $T_R = 720$ °C, cooling 25;0;0, b) orange color - $T_A = 980$ °C, $T_R = 700$ °C, cooling 120;0;25.

	S658	S659	S660	7MnB8
AED [nm]	65.8	22.9	40.5	15.7
Area fraction [%]	0.7	0.5	0.9	0.2
Precipitations/μm^3	10	54	24	27

The same but less intensive phenomena can be observed in S660 steel. AED of precipitations increased in comparison to the initial state and precipitations per μm^3 decreased, while in S659 steel it is the opposite. S660 steel has the lowest Ti content and it is decreased in comparison to the Nb content of S659 steel. After the process, the D_{ef} for S660 steel is smaller than for S659 steel, but the initial D_{ef} was also small, ~ 28 μm for S659 and ~ 14 μm for S660 steel (Table 15). Therefore, after rolling, S660 steel which

also contains Nb, has lower D_{ef} . The chemical composition of S660 steel has an increased V content to the highest value of all steels. However, it seems that the element is mainly dissolved in the matrix after the rolling process. No V precipitations were found during the TEM investigations. However, by substitution of Ti and Nb it participates in the precipitations, but no precipitations were observed where V is the main component: in S660 steels after rolling.

6. Discussion

The first of the two objectives of this study was to develop process parameters to reduce the DBTT below $-100\text{ }^{\circ}\text{C}$ for industrial 7MnB8 steel, by optimizing the process temperature at each stage of bar production by XTP rolling, in order to fragment the structure of the structure. According to the research scheme presented in Fig. 34, the PAG growth kinetics was the most important feature to be characterized at the beginning, due to the influence of the initial grain size on the refinement of the final structure. The results (Fig. 48 and 49) show that the increase of the austenitization temperature or holding time do not influence the PAGS of industrial 7MnB8 steel significantly. Tests were performed in the temperature range used in the XTP rod heating process. Depending on the temperature or holding time, the differences between AED of grains varies from 1 to 3 μm , which is not significant, because it falls within the range of the variation of measurement results. During the development of the process parameters, two austenitization temperatures were chosen: $920\text{ }^{\circ}\text{C}$ and $980\text{ }^{\circ}\text{C}$. The second factor in T_A selection was the no-recrystallization temperature to inhibit the static recrystallization of A during rolling. Both temperatures are the result of a decrease by $20\text{ }^{\circ}\text{C}$ of the temperature used in the simulations, to achieve a finer grain size. Furthermore, in one of the process parameters groups, it was decided to leave the temperature on an increased level to promote dissolution of former carbides, which, in the next steps, should have provided greater grain refinement after phase transformation and further precipitation strengthening, due to the assumed chemical composition choices. It is related to changes of the elements participating in the precipitation processes and dissolves NbC carbides to prevent A recrystallization. Additionally, thermally stable nitrides present in the treated steel would maximize the fine grain size due to the pinning effect, according to the Zener and Smith equation [23,67,131]. This should lead to an improvement of the mechanical properties [132,133] and reduce the impurities concentration at the grain boundaries. The grain boundaries free from the elements, which provide embrittlement or with reduced amount of those impurities by increased grain boundaries volume fraction, should have a beneficial effect on the toughness and counteract the steel embrittlement.

Having in mind the rest of the process parameters, which are rolling temperature (T_R) and cooling rate, dilatometric simulations of the rolling process were performed to characterize the structure after rolling. The simulations were made according to the

scheme presented in Fig. 37. It can be seen that the deformations applied at a lower temperature produce nonuniform distribution of LAGB (Fig. 58), while the increase of the temperature from 680 °C to 720 °C provides uniform distribution for both LAGB and HAGB (Fig. 62). However, this is due to different structures obtained in the simulations. In the samples deformed at 680 °C, GB can be mostly observed in the structure (Fig. 56 and 57) with low fraction of UB, while in the samples deformed at 770 °C, more UB regions were obtained (Fig. 60 and 61). These results are straightforwardly combined with the differences in the cooling and also with the cooling start temperature, which leads to shifting of the curve into the different bainite transformation regions, so two bainite morphologies are produced. Furthermore, grain refinement can be found in both simulations due to the applied deformation of the samples in comparison to the samples without deformation (e.g. Fig. 53 and 62). For complementary performance of the process simulations, the last experiments included passing through the temperature sets characteristic for all steps on the production line. Therefore, the samples were austenitized, cooled to the rolling temperature and heated up by 90 °C according to the measurements on the line, where the deformation implied the temperature increment. The end stage of the simulation included intensive cooling to the final temperature, imitating the cooling section of the line and then, cooling in air. The details are presented in Fig. 37. It can be seen from the results that, in the sample structures cooled down to 400 °C, a mixture of UB+LB was obtained (Fig. 65, 69, 73, 77) according to the lowest transformation temperature of this type of bainite. On the other hand, cooling to 500 °C and 600 °C allowed to obtain the GB structure (Fig. 64 - 79). Furthermore, it was found that a higher final temperature causes larger grain size, due to a higher transformation temperature. The investigations of RA show a higher area fraction of this constituent in the samples with GB, than in the samples with UB. It is due to the behavior of carbon. When partitioned from the bainitic ferrite, carbon stabilizes RA in GB, while, in UB, carbon is mostly consumed by cementite precipitations. Moreover, the conducted tests show that obtaining an increased proportion of HAGB that provides an obstacle to crack propagation is provided by the lowest final temperature of 400 °C, from which there is slow cooling in air (Fig. 55). However, in the studied samples, the structure was characterized by UB+LB with low RA content (Fig. 80). Samples cooled to 500 °C and 600 °C exhibit similar RA content, but, as the final temperature increases, the total length of HAGB decreases. In addition, the higher temperature (600 °C) causes M tempering, which was observed in samples after dilatometric simulations (e.g. Fig. 77).

Based on the results from the simulation section of the study, four groups of process parameters were designed (Table 3). Due to no significant grain growth in one of them, the austenitization temperature was increased to 980 °C to intensify the dissolution of former phases during the reheating. For the other three groups, the austenitization temperature was 915 °C. In two cases 720 °C rolling temperature was applied, yet with different cooling. One trial with a high cooling rate was obtained by using 2 of 3 cooling boxes and in the second trial the cooling rate was decreased. In the last one, the assumptions were to obtain different bainitic structure and, due to the high final temperature, by decreasing the cooling rate in this trial, to minimize the deformation at the surface, which was expected due to the phenomena of cross-rolling described in the literature [134–136]. Therefore, the obtained mechanical properties should have been more uniform at the cross-section of the bars, due to the recrystallization processes in this particular rolling. In the third group with austenitization temperature of 915 °C, the rolling temperature was decreased to 680 °C with fast cooling to increase the dislocation density and to produce a harder and stronger, but less plastic variant of the material [99]. The last trial, with austenitization temperature of 980 °C was focused on dissolution of thermal stable precipitations and on the influence of the precipitation processes on the microstructure and mechanical properties. Therefore, for comparable results, the rolling temperature was established at 700 °C with fast cooling after the deformation. The finalization of the second stage included industrial trials with the use of the developed groups of parameters where the initial material was 7MnB8 steel after hot rolling at 1000 °C.

The thermodynamic calculations made for 7MnB8 steel showed forming of the TiN phase in the first stage of solidification. On the other hand, at similar temperature, also Ti₄C₂S₂ precipitations occurred. Due to the high precipitation temperature, the sizes of those phases were very large. Therefore, the influence of precipitations on grain refinement is limited, according to the Zener and Smith equation (2). Coarse TiN particles have harmful influence on toughness, they act as initiation sites of cleavage fracture and also are difficult to dissolve during reheating. However, as it was found in Fig. 86, the toughness for steel improved after rolling with all groups of parameters. This was due to grain refinement of the bar structure (Fig. 85, Fig. 87 - 92, Fig. 98 and 99). The XTP rolling of the bars also shifts the DBTT temperature to a lower value (Table 8 and Fig. 86). On the other hand, hardness after rolling increased significantly only on the surface,

where the grain refinement was the most intensive (Fig. 87, 89, and Fig. 91, 92). However, it was observed for bars rolled with the parameters groups, where the water flow through the cooling boxes was the highest, the highest cooling rate was obtained. The gradient structure was obtained with the use of all rolling parameters groups. Nevertheless, with a decrease of the cooling rate in the second trial, the structure was more uniform in the cross-section of the bar (Fig. 87 and Fig. 90), in the context of thickness of the refined structure on the surface, which was 1 mm thick, 4 times less in comparison to the rest of the rolling trials. The hardness of the steel produced with a decreased cooling rate was lower in comparison to the initial state (Fig. 85 and Table 7). This was due to nonuniform distribution of M/A constituents in the cross-section, resulting from the banded structure (Fig. 90). Moreover, great areas of soft ferrite grains are predominant between the coarse M/A islands, so their influence on the hardness was insignificant and lower hardness was mainly caused by the ferrite (Fig. 90). The final temperature was measured directly after cooling on the surface of the bar. The temperature in the core was higher than the one measured on the surface, due to the temperature gradient as a result of cooling of the surface. The higher temperature in the core increased the temperature at the surface area, while the slow cooling in air occurred, following fast cooling, which provided conditions for element diffusion. Therefore, a banded structure was obtained in the longitudinal sections (Fig. 90). As it can be seen in results of the SEM structure investigations, Fig. 95, coarse M/A islands between ferrite grains were formed. On the other hand, lower final temperature obtained by intensive cooling resulted in a higher total length of LAGB on the surface of the bars (Fig. 101b) in comparison to the cores. In terms to the total length of grain boundaries in the cores of the bars and influence of the LAGB and HAGB on the mechanical properties, many researchers combine the strength of controlling and inhibiting of cleavage fracture with low and high grain boundaries, respectively [58,76,137]. As it can be noticed in the comparison to the material in the initial state, the steels after rolling had two times higher total length of HAGB in the core of the bars and an improvement in toughness was observed. However, total length of LAGB in the core after rolling was smaller or at the same level as in the raw material and UTS for samples from the cores was comparable with apparent slight increase. Although YS did not change at all, the improvement can be seen in elongation of the bars, approximately 2.5% higher than the material in the initial state. The exception was visible for the bar with slow cooling, but it was due to the obtained structure. In the bars with intensive cooling, mainly GB was obtained (Fig. 94, 96 and 97), and the sample with a slow cooling rate had DP

steels structure (Fig. 95). Furthermore, a banded structure on the longitudinal section in the bar core was observed (Fig. 90). Therefore, due to ferrite grains bands and presence of hard phase (M/A islands) bands arranged along the stretching direction, the plastic deformation was facilitated and the steel had the highest elongation. Furthermore, the distributions of the misorientation angles in the cores of the bars (Fig. 100) indicated packets and blocks of M in this sample which increased the total length of HAGB. On the other hand, in other bars, an increase within 10° characterized sub-blocky M, so the increased amount of HAGB was not caused by presence of M in the structure. Moreover, in the range of characteristic misorientation angles for RA, the samples with GB had an increased number fraction for those angles. The presence of RA in the samples was confirmed by X-ray analysis (Fig. 102). The highest fraction was observed in the bars with GB structure, which were produced according to the process with intensive cooling, where the final temperature was lower. It can be seen from EBSD results that the distribution of RA in the investigated area was uniform (Fig. 99). To the contrary, due to fast cooling and lower final temperature, fine grains were produced in all steels. As a result, the carbon content in A was sufficient to stabilize it. Decreased cooling rate caused increased final temperature and, as a result, coarse grains were produced. Therefore, A was not stabilized as much as in the samples with fine grains, thus as the temperature decreased, the martensitic transformation started. The investigations of precipitations in steel in the initial state and after selected rolling trials showed an increase of precipitation density after rolling. Furthermore, AED of precipitations decreased in comparison to the material before thermomechanical treatment (Table 10). However, coarse TiN precipitations were observed in the structure of the bars after the process with all process parameters. To reduce the volume fraction of primary TiN particles (Fig. 103), which are harmful to the toughness of the material and have a limited influence on the grain refinement, an increase of the austenitization temperature should be implemented. Unfortunately, the XTP process is complicated in achieving the assumed parameters. Moreover, due to construction solutions, the temperature 980°C was the highest one, which allows to cool down the moving bar to the rolling temperature in the next section of the production line. Also, holding time adjustment is complex and it is done by changing the process velocity. Therefore, the change of the bar speed affects the heating capacity and the assumed austenitization temperature is not achieved. The conclusion is that the Ti content has to be decreased in steel. This will allow to reduce the size of coarse TiN precipitations (Fig. 103), which will be beneficial to the grain refinement according

to the Zener and Smith equation (6) and will inhibit their harmful influence on toughness. Second advantage of decreasing Ti content is elimination of Ti_2CS phase presence in steel. For 7MnB8 steel, where the Ti content is 0.088%, in both samples, before and after rolling, Ti_2CS precipitations were observed in the structure of the bars (Fig. 104 and Fig. 113). This hard and brittle phase influences toughness like coarse TiN, so the presence of Ti_2CS is undesirable in steel, where the resistance to dynamic loads is required. As reported in the literature, increasing the Ti content leads to formation of Ti-containing Mn sulfide and then to formation of globular carbosulfides [138]. During the TEM investigation of the steel in the initial state, no Mn sulfides were observed in the structure. To the contrary, after the rolling, singular sulfides were identified (Fig. 112). However, microanalysis of the chemical composition shows participation of Ti in the lattice of the precipitations. Therefore, on the one hand, reheating releases Ti combined in precipitations, but on the other hand, the element is still consumed in sulfide formation due to its affinity to sulfur. However, some Ti precipitates as very fine carbides, with a low Mo content (Fig. 108). Thus, the precipitation density after the process is increased and AED is decreased.

The second scope of the work was modified chemical composition of 7MnB8 steel, for a decrease of the DBTT obtained for industrial steel after rolling. Five new steels were produced. The investigations of new steels at the stage of the development of the chemical composition showed that the increase of Ti content in S654 steel was adverse to the D_{ef} parameter. The results of D_{ef} calculations, which are shown in the Table 15, demonstrate that the highest content of Ti at the level of 0.11 % increased the average D_{ef} to 78,8 μm . The total length of HAGB was the lowest for this steel in comparison to the others. A comparable value was observed also for S657 steel (Fig. 135). For this steel, D_{ef} was, as in case of S654 steel, higher than for 7MnB8 steel and equaled 66,4 μm . In Fig. 133, coarse PAG can be recognized in the crystal orientation maps from EBSD. Comparing the results of RA in steel, the amount of this constituent was similar for all five steels (Fig. 137). Therefore, it can be concluded that low participation of HAGB in the structure had the main influence on the DBTT of S654 and S657 steel, due to the GB structure obtained from coarse PAG in the steels. Simultaneously, the D_{ef} parameter characterizing the effective grain size was the highest from the investigated steels. Furthermore, the analysis of changes of phases mass fraction with temperature (Fig. 116) indicated the presence of TiN and $Ti_4C_2S_2$ phases. The TEM analysis confirmed those phases in the structure of the steels. Both, in S654 steel and in S657, the coarse TiN

particles and Ti carbosulfides (Fig. 140 and Fig. 141b, respectively) were identified. Considering the harmful influence of those coarse precipitations on the DBTT, in combination with low HAGB total length and high D_{ef} , the toughness properties were unsatisfying. For the other steels, the Ti content was drastically decreased to the range of 0.019 - 0.036, depending on the steel grade (Table 4). During the LOM analysis, precipitations were observed spontaneously in those steels and the sizes were much lower than for the previous steels. Therefore, it was found that the size of TiN precipitations forming at the first stage of the solidification can be controlled by lowering of the element content participating in the precipitation of this phase. Second advantage of the maintenance of the Ti content on the low level is the elimination of Ti_2CS phase in steel. The thermodynamic calculations indicated that a decrease in the Ti content below 0.036 wt. %, allowed to eliminate this undesirable phase (Fig. 116). The STEM investigations of the steels with a low range of Ti (0.019 - 0.036 wt. %), confirmed that the steels are Ti_2CS -free. Furthermore, the Mo contents were changed in all new steels, due to its influence on the temper embrittlement by inhibiting the impurities segregations on the grain boundaries. The amount of this element was increased to 0.20 %, and because 0.21% of the steels is silicon, Mo was increased to 0.49% in one steel. According to the observations from other researchers, an improvement is obtained with Mo additions up to 0.94%, when 0.25% of silicon is added [16]. However, the property influence of Mo on the toughness takes place when the element is dissolved in the matrix. Its beneficial effect is limited when it is tied up in the precipitated phases, which can occur due to Mo participation in the precipitation processes, by partial replacing of Nb or Ti [25,38,39]. Following the structural investigations of the steels in the initial state, it can be noticed that in the steels with predominant Ti as a precipitations former, Mo is present in the crystallographic lattice of the particles (e.g. Fig. 138 and 142 for S654 and S657 steels, respectively). Furthermore, the increased Mo content in S657 steel increases its amount in precipitations. However, S657 steel demonstrates better toughness than S654 steel (Fig. 121), but there is also a $\sim 10 \mu m$ difference in D_{ef} parameter which has influence on the DBTT (Table 15). Analyzing the results for the steels with decreased Ti content with or without modifications of other elements like Nb and V shows Mo-free precipitations in those steels. This proves that Mo is completely dissolved in the matrix, so its beneficial influence of toughness should be achieved. The results of Charpy V-notch investigations (Fig. 121 and Table 13) indicate the highest fracture energy for those steels. Furthermore, the DBTT for the steels is the lowest and is $-45 \text{ }^\circ\text{C}$ and $-95 \text{ }^\circ\text{C}$ for S659 and S660 steel,

respectively. Thus, combining the dissolved Mo influence and fine effective grain size determined as D_{ef} provides the best toughness. Furthermore, in Fig. 133, where the crystal orientation maps from the EBSD for the new steels in the initial state are presented, the structure of those steels is refined in comparison to S654 and/or S657 steels. Classification from the smallest to the largest D_{ef} parameter ranks the steels in the following order: S659 and S660, S658, S657 and the steel with the largest effective grain size, S654. In the steels characterized by the smallest effective grain size (D_{ef}), the highest precipitation density and the smallest AED of the particles was observed in the structure (Table 16). Therefore, according to the Zener and Smith equation, those precipitations inhibited the grain growth due to the pinning effect, so the PAG was refined in comparison to the other steels. After the transformation, the structure refinement was higher, and the steels are characterized with the smallest D_{ef} value. For S660 steel, very fine precipitations of MC were identified (Fig. 150 and Fig. 151), which provide the strengthening mechanisms of the steel. It can be seen on the stress - strain curves (Fig. 119), that for S660 steel, after the YS point is reached, the stress increases, which proves the presence of ongoing strengthening mechanisms. In comparison to S659 steel, where those fine precipitations were not observed and the structure was similar, the stress was more constant after it crossed the YS point during the test. The decreased Ti content in S659 and S660 steels inhibited the growth of coarse TiN precipitations, which were spontaneously observed in the structure (Fig. 126 and Fig. 127). However, for S659 steel, all identified precipitations in the structure were nitrides, but due to the Ti content, their sizes were smaller in comparison to TiN precipitations observed in the steels with high Ti content (> 0.088 wt. %). In those steels, S654 and S657, coarse TiN particles were not analyzed in TEM due to their size (AED $\sim 3000 - 3500$ nm), similarly to those observed for 7MnB8 steel, AED ~ 3200 nm (Fig. 103). Furthermore, the additions of other elements: Nb (S659 and S660) and V (S660), participated in the precipitation processes. The change of alloying elements combination and a decreased Ti content supplemented with other precipitations formers allowed to obtain the precipitation density at 43 precipitations/ μm^3 and 48 precipitations/ μm^3 , in steel S659 and S660, respectively. On the other hand, in the steels with high Ti (> 0.088 wt. %, S654 and S657) the precipitations had Ti and Mo, as M. V was not included in the precipitations, however, it has stronger ability to form carbides than Mo. It is confirmed that Mo can replace Ti in MC precipitations [139]. Therefore, due to the additions of Mo to all steels (~ 0.2 wt. %) and even more in S657 (0.49 wt. %), Ti in precipitations is replaced by this element, beside

the V. TiN particles are stable at the forming temperature, while MX particles can be released during or after deformation. The steels with high Ti (> 0.088 wt. %), have approximately ten times less precipitations per μm^3 . According to the Zener and Smith equation, the better results of the pinning effect on the migrating grain boundaries, and subsequently finer grains, are provided by high density of fine precipitations, which has been confirmed in the results for the investigated steels (Table 15 and Table 16). It can be concluded that changing alloying elements combination decreases precipitation AED and increases the density of precipitations. Due to this, the PAG is refined more efficiently, which leads to a decrease in the effective grain size of the final structure. Thus, with the impurity elements (P and S) at comparable levels for the new steels (Table 4), the DBTT is shifted to the lower temperature (Table 13 and Fig. 121).

Structure characterization shows the bainitic structure in the investigated steels. GB was mostly obtained, however in S657 and S658 steels, DUB was also present. As it can be seen in the structure of S654, S657 and S658 steels, very fine second phases (M/A islands and RA) in the bainitic ferrite matrix were obtained, while in steels S659 and S660 coarse M/A islands and single RA grains were present (Fig. 128 - 132). According to the results from the XRD investigations (Fig. 137) it can be noted that RA fraction in the steels in the initial state was comparable, and the deviation was ± 1 %, approximately. However, the main difference was that most RA in S659 and S660 steels was in coarse ($> 5 \mu\text{m}$) M/A islands, while in the rest of steels RA was present separately and its size was mainly below $5 \mu\text{m}$. An increase in characteristic angles between $\sim 42^\circ$ to $\sim 45^\circ$ (Fig. 134), demonstrated the presence of RA, which was compatible with the XRD results. Moreover, the increase could be observed for all samples in the area of 10° , thus it can be concluded that M sub-blocks morphology or bainitic ferrite were present. Furthermore, for all steels, packets and blocks of M could be found at characteristic misorientation angles from 47° to 57° and from 49° to 60° , respectively. Due to the type of bainite, morphology of the second phase (M/A and/or RA) and structure refinement in the steels, different contribution of LAGB and HAGB (Fig. 135) was received. In S657 steel, similarly to 7MnB8, the bainitic structure was finer in comparison to the structure of S654 steel. Therefore, during analysis of grain boundaries for the same area, the total length of the grain boundaries was higher for the steels with finer structures (7MnB8 and S657). In S658 steel, more areas of DUB were observed in the structure and the bainitic structure was finer than in S657 steel. Observations with the use of SEM showed a higher fraction of the second phase constituents (Fig. 130), and an increased number fraction of

misorientation angles for M/A (Fig. 134) indicated its high contribution, as the range of angles characteristic for A ($\sim 42^\circ$ to $\sim 45^\circ$) was decreased. Therefore, for this steel, the total length of grain boundaries was the highest for all steels, caused by the fine structure and fine M/A islands. On the other hand, in steels S659 and S660, coarse M/A islands were observed, which correspond with the increase of LAGB and HAGB. Furthermore, the EBSD investigations indicated HAGB between observed ferrite in the structure (Fig. 133). Those two features caused a high total length of grain boundaries in S660 and S659 steels. Characterizing the mechanical properties of the new steels (Fig. 118 and 119), S659 and S660 had the lowest YS and UTS, however, the highest elongation. It was due to coarse ferritic grains facilitating plastic deformation. For S654, S657 and S658 steels, an increase in YS and UTS was observed in comparison to the 7MnB8 steel. It was due to the size and contribution of M/A islands which increased in the new steels and the islands were finer in comparison to 7MnB8 steel. This could be clearly seen comparing S654 and 7MnB8 steels. S654 steel had a larger effective grain size than 7MnB8 steel, however, the presence of finer M/A islands homogeneously distributed in S654 steel compensated for the negative influence of coarse grain size, which affected the improvement of the mechanical properties of steel. Analyzing the results from the tensile tests it could be noticed that, for all steels, the curves without pronounced yield strength could be recognized.

The final stage of the study comprised the industrial trials with the use of the new steel grades. Due to the best results of the DBTT improvement for industrial 7MnB8 steel rolled with the fourth group of parameters ($T_A=980^\circ\text{C}$, $T_R=700^\circ\text{C}$, cooling 120;0;25), the investigations of the new steels were focused on that rolling schedule. The measurements of the temperature provided on the process line showed the different behavior of the steels during inductive heating. Therefore, the temperatures of each material were different at every stage of the process. It is because different steels with different chemical composition, and therefore with different morphology and thermophysical properties were combined into one bar for the rolling process and the parameter adjustments were performed with the use of 7MnB8 steel. Thus, the assumptions obtained for 7MnB8 regarding the temperature at each stage of the process were changed depending on the part of the new steels bar. The results of the measurements are presented in the Table 17, where the average temperatures from one pass of the five steels were calculated. Due to different chemical compositions, the main differences were in the temperature directly after cooling. Steel S658 with the highest

hardenability by increased Mn content had the lowest final temperature at the end of the process, ~ 449 °C. For the rest of the steels the temperature was in range ~ 499 °C – 521 °C, depending on the steel. The average difference between the temperature for those steels was ± 10 °C (standard deviation), while including S658 steel, the average was ± 30 °C. To the contrary, the highest austenitization temperature was achieved for S660 steel, $T_A = 994$ °C. For the rest of the steels the austenitization temperature was close to the assumed 980 °C. The structure investigations using SEM (Fig. 162 – 167) and LOM (Fig. 156) indicated the gradient structure and grain refinement achieved due to the XTP process. Simultaneously, the obtained grain size on the surface area of the bars was finer than in the cores. The structure of the bars was GB (Fig. 162 – 166). However, the increased Mn concentration in 658 steel resulted in obtaining DUB and/or LB in the core of the bar (Fig. 164). Furthermore, the crystal orientation maps show the grains orientation differences between the surface, where [140] orientation dominates, and core areas of the bars with [57] orientation. Those two variants of orientation are the result of different mechanisms of material flow during rolling and were also observed in the structure of the 7MnB8 steel bars (Fig. 99). The hardness measurements indicated the highest hardness for S658 steel, 354 HV at the surface and 317 HV in the core (Table 18). It can be found that the difference in the two zones is limited. The hardness improvement by structure refinement obtained at the surface was close to the hardness provided by the obtained structure, which consisted of low temperature transformation products, lower and DUB (Fig. 164). Thus, the hardness on the cross-section of the bar was more uniform in comparison to the other steels (Fig. 154). For GB obtained for the rest of steels, due to lower hardness of this type of bainite, the greater hardness difference between surface and the core was revealed. Furthermore, for this high Mn steel, S658, the YS and UTS were the highest for the new steels, 685 Mpa and 981 Mpa, respectively (Fig. 152). Measured D_{ef} for the steel was 12.9 μm (Table 19) and the DBTT was 80 °C (Table 19). Despite that, the results for S658 steel, placed it in the middle of the new steels, in terms of the achieved DBTT. A higher DBTT value was for S654 and S657 steels, with hardness and mechanical properties comparable between them (Fig. 154 and Table 18). For both steels, the highest increase of hardness was observed at the surface area of the bars, where 343 HV and 352 HV, for S654 and S657 steel respectively, was measured, while the hardness for the cores was 255 HV and 271 HV. Thus, the average hardness increase was ~ 85 HV. For S659 and S660 steels, hardness in the cores was 209 HV and 208 HV, thus hardness at the surface increased by ~ 55 HV (Table 18). Comparing those two steels

groups, S654 and S657 with S659 and S660, it can be seen in Fig. 169b, that on the surface of S654 and S657 steels, higher total length of HAGB and LAGB was present. Due to this, it can be concluded that for those two steels, higher structure refinement was obtained. This indicates the finer structures obtained in those steels and explains the hardness differences between those two groups of steels. On the other hand, also hardness in the cores showed similar dependence. Higher hardness was measured for S654 and S657 steel, and the total lengths of LAGB and/or HAGB were also higher for those steels in comparison to S659 and S660 (Fig. 169a). Moreover, in S654 and S657 steels, higher number fraction of characteristic misorientation angles for M is visible in Fig. 168, which increases hardness as a hard phase. As it can be seen in the SEM structure of the steels (Fig. 162 – 166), the fraction of M/A was similar for those four steels. However, the XRD results of RA showed the lowest fractions for S657 steel (Fig. 171). Compared to M, RA in steel improves resistance to dynamic loads. The number fraction of characteristic misorientation angles for A was decreased for S657 steel in comparison to S660 and S659 (Fig. 168). The same can be observed in Fig. 167f, where the phase map from EBSD for S657 steel is presented. The distribution of RA is different from e.g. S660 steel. This indicates, that M was mostly present in the observed M/A islands in the structure of S657 steel. The presence of brittle M has negative influence on the DBTT for the steel, for which the temperature is $-25\text{ }^{\circ}\text{C}$ (Table 19), although D_{ef} is comparable to the sizes measured for S659 or S660 steels (Table 20). For S654 steel, the DBTT is lower, $-40\text{ }^{\circ}\text{C}$. However, in this case, the calculated D_{ef} is the highest from all steels, $36.8\text{ }\mu\text{m}$. Furthermore, the total length of HAGB, which prevents crack propagation, is the lowest (Fig. 169a). Moreover, for both steels with high Ti content, in Fig. 157 and 158, coarse TiN precipitations were observed, which have detrimental influence on toughness. Basically, the best results are for S660 and S659 steels, for which the DBTT is $-150\text{ }^{\circ}\text{C}$ and $-180\text{ }^{\circ}\text{C}$, respectively (Table 19). It can be noticed that for those steels with the GB structure, total length of HAGB is double the LAGB (Fig. 169). Furthermore D_{ef} for those steels was the smallest, $11.5\text{ }\mu\text{m}$ for S660 and $13.3\text{ }\mu\text{m}$ for S659 steel (Table 20). Moreover, in contrast to S654 or S657 steels, LOM and SEM investigations did not indicate any coarse TiN precipitations in the structure of S659 and S660 steels (Fig. 160, 161, 165 and 166). The results of RA in Fig. 171 show the highest fraction in all steels, $6.4\text{ }\%$ and $6.1\text{ }\%$, for S659 and S660, respectively. The EBSD investigations indicate uniform distribution of RA in the analyzed areas (Fig. 167l and o). RA and ferrite in the structure influence the elongations of the steels. As it can be seen when comparing all GB

steels, coarse ferrite in the structure indicates (Fig. 171) an increase in elongation (Fig. 152). Additionally, when comparing S659 and S660 steels, characterized with coarse ferrite regions, higher elongation is for S659 steel which has increased amount of RA in comparison to S660 steel. Therefore, for S659 with the highest, 6.4 %, volume fraction of RA, the highest elongation was measured, 28.2 %. To the contrary, the lowest A fraction was in S657 steel with finer ferrite, because M was mostly in M/A islands. Thus, for this steel, the elongation decreased to 20.2 %, while for S654 steel with 5.5 % of RA, the elongation was higher, 22.2 %. However, due to M in the structure of S657 steel, which has beneficial influence on the strength, the UTS for this steel was the highest, 888 MPa, as observed for the steels with the GB structure. Disregarding the obtained values in the tensile tests, stress strain curves with pronounced YS are characteristic for S659 and S660 (Fig. 153), while the curves without pronounced YS are typical for the rest of the steels. Ti content and Nb additions in S659 and S660 steels are the main differences between the steels (Table 4). Nb additions, dissolved in the matrix, retard the recrystallization processes. The grain refinement phenomena increase the volume of regions for nucleation and lead to structure refinement after the phase transformation. Therefore, the calculated D_{ef} values for the steels were the smallest ones. Furthermore, the vanadium was increased to 0.15 wt. % in S660 steel, which was due to its effect of lowering the bainitic transformation temperature, refining the bainite structure, so the effective grain size was decreased in comparison to the V-free steel, S659 (Table 20). The additions of niobium and/or vanadium with decreased titanium content eliminated the molybdenum participation in the precipitation of complex carbides (Ti, Mo) C. In S654 and S657 steels, the molybdenum was already identified in the precipitations in the initial state (e.g. Fig. 139 and 142). For S658 steel, the molybdenum was dissolved in the matrix before rolling. After the XTP process, the element was analyzed in nitrides (Fig. 174) and also in precipitations of cementite (Fig. 175). Therefore, its influence on toughness was limited. On the other hand, the analysis of the precipitations in S659 and S660 steels shows molybdenum in the particles, however, it was only present in singular, fine precipitations (Fig. 179 and 185). Inhibition of precipitation occurs due to the fact that Mo is first at the boundary, thus displacing impurities. As a result, it improves the impact strength. It can be concluded that molybdenum is mostly dissolved in the matrix of S659 and S660 steels, fulfilling the assumptions connected with its beneficial influence on toughness due to avoiding the impurities segregation on the grain boundaries. The DBTT

of those steels is the lowest, even in the initial state. The rolling process additionally shifts the temperature to $-150\text{ }^{\circ}\text{C}$ and $-180\text{ }^{\circ}\text{C}$, for S660 and S659 steels, respectively.

7. Summary

The development of bainitic steels for automotive and railroad applications is associated with improved resistance to low-temperature dynamic loads while maintaining strength. The paper deals with the development of technological parameters of a one-step XTP rolling process, and also discusses the selection of the chemical composition of 7MnB8 steel to reduce the DBTT temperature of the produced bars.

In this paper, a study was conducted that included simulations of the rolling process, which made it possible to propose technological parameters. Rolling tests were carried out using the proposed parameter groups. Detailed microstructural studies and an analysis of the effect of parameters on the mechanical properties of 7MnB8 steel showed the obtaining of a gradient structure and refinement of the microstructure in the cores of the tested bars and on their surface. A finer structure was found on the surface, compared to the core of the bars, the thickness of which was ~ 4 mm when applying intensive cooling (~ 7.6 °C/s) after deformation. It was shown that lowering the water output during cooling, and limiting the cooling rate to ~ 2.3 °C/s, reduces the thickness of the refined near-surface zone by about four times, so that the bar structure on the cross-section is characterized by greater homogeneity. In the structure of 7MnB8 steel with Ti content of 0.088 wt. %, large precipitations of TiN and Ti₂CS were revealed, the presence of which affects the reduction of impact properties. The effect of the rolling process parameters on the impact toughness of 7MnB8 steel after rolling was determined. The lowest temperature DBTT = -120 °C was shown for a bar of 7MnB8 steel rolled using the rolling parameters TA = 980 °C, TR = 700 °C and accelerated cooling in 120;0;25 configuration.

Based on the results of our own research, a comparative analysis of the microstructure and mechanical properties of steels with different contents of Mn, Mo, Nb, V and Ti subjected to processing was made, with the use of a group of technological parameters for which the lowest DBTT for industrial steel was obtained. It was shown that changing the configuration of alloying additives with a reduction in Ti content leads to elimination of Ti₂CS and coarse TiN particles in the structure. A different bar structure was found to be obtained from steel with increased Mn content up to 2.9 wt. %. In the case of this steel, a UB structure with LB and GB areas was revealed, while, for the steel with Mn content of 1.9 wt. %, mainly GB was observed. The lowest DBTT temperatures of -150 °C and -180 °C were found for S660 and S659 steels, respectively, in which Nb

additives were used and Ti content was reduced below 0.03 wt. %. Fig. 187 shows the scheme of the obtained structures of the developed steel grades after XTP rolling, highlighting the most important characteristics and mechanical properties of the produced steels.

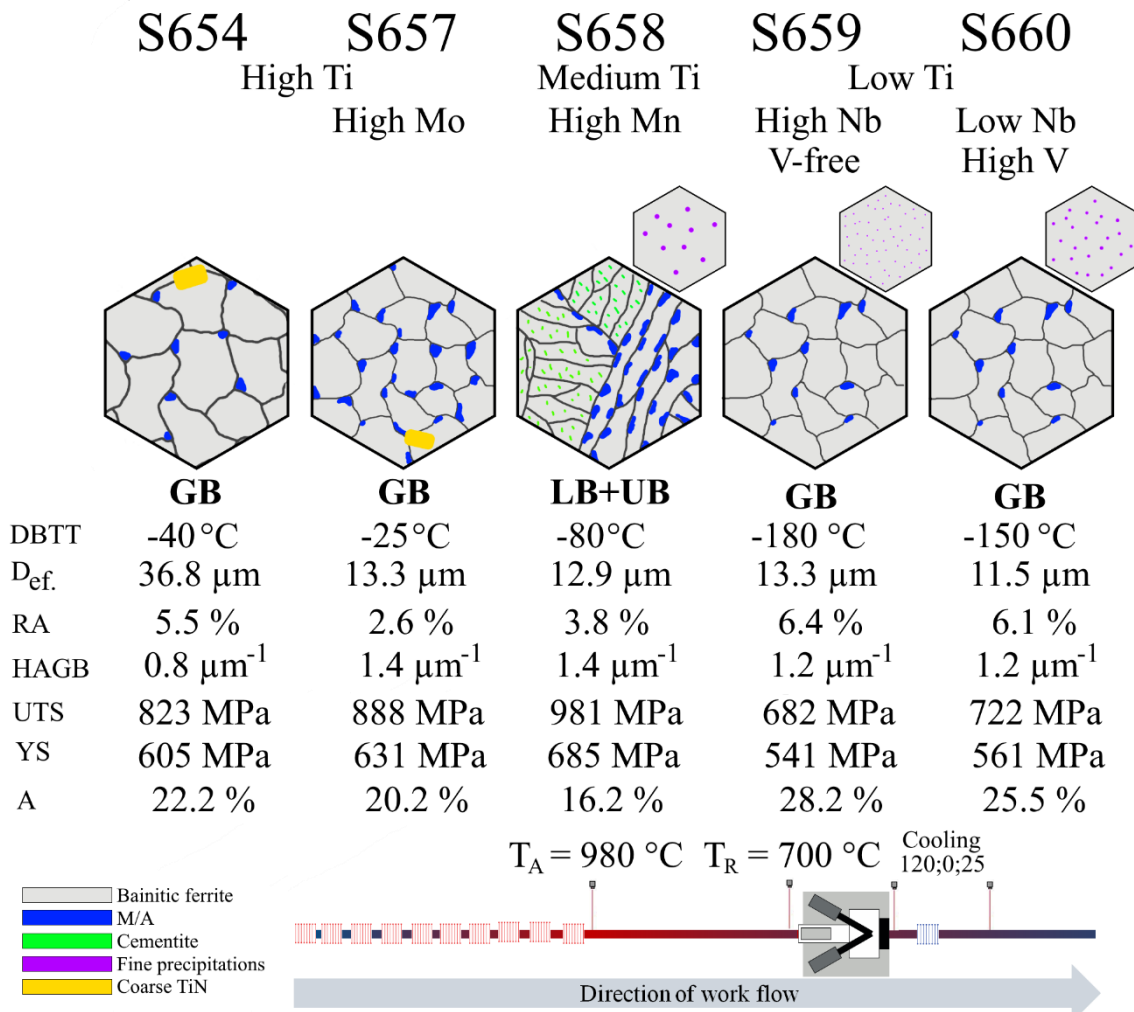


Fig. 187. A diagram of the structures obtained for the developed steel grades with the most important features and the obtained properties after XTP rolling.

Considering the above, it may be concluded that the thesis of the study stating that: “The selection of the content of alloying additives of bainitic steel, in conjunction with the development of parameters of an innovative one-step thermomechanical rolling process using the XTP method, makes it possible to obtain a gradient structure leading to a reduction in the temperature of the transition of the material into a brittle state with no significant changes in the values of the other basic mechanical properties of the bars relative to conventional steel 7MnB8”.

8. Conclusions

A comprehensive analysis of the results of the research carried out as part of the thesis has led to the following final conclusions:

- The austenitizing temperatures of 940 °C and 1000 °C used in the thermomechanical rolling process analyzed have no significant effect on the grain size of the former austenite for 7MnB8 steel, which shows the stability of the austenite grain size at the temperatures studied.
- The high grain refinement is achieved by the deformation applied during the XTP process. Rolling results in a gradient structure. Deformations mainly accumulate in the near-surface region, where the greatest grain refinement is observed.
- Final temperature of 400 °C obtained after fast cooling allows to obtain LB in the structure of 7MnB8 steel. Fast cooling to 500 °C and 600 °C and further slow cooling in still air create M/A islands in GB. Slow cooling from 600 °C, leads to tempered M in the structure during cooling in still air.
- The structure of bars after fast cooling (~ 7.6 °C/s), and after the cross-rolling process, is composed of GB and grain size decreases in comparison to the initial state, both in the core and in the subsurface zone of the bar. $D_{ef.}$ in the core decreases by ~ 2.5 times, and on the surface by 10 times in relation to the initial material. An increase in hardness by $\sim 30\%$ on average is observed mainly in the near-surface zone. In the core, an increase in hardness after rolling was observed for S657 and S658 steels.
- The grain size ($D_{ef.}$) in the cross-section of the bar after rolling is 4 times smaller in the near-surface zone compared to the core. At the same time, hardness of the near-surface zone increases by $\sim 30\%$, while an increase of $\sim 5\%$ is observed in the core, compared to the hardness of the initial state.
- More Uniform structure in the cross-section of the bar after rolling could be obtained by a decrease of the cooling rate (~ 2.3 °C/s) after deformation.
- Toughness investigated at the temperature range of - 200 °C - 100 °C is improved by rolling with the use of all four groups of process parameters. The DBTT temperature is shifted by about 150 °C to the negative temperature.

- The lowest DBTT = - 120 °C for 7MnB8 steel is obtained with the use of the following process parameters: TA = 980 °C; TR = 700 °C; cooling rate 120;0;25 (~ 7.6 °C/s).
- Increasing hardenability due to higher Mn content in S658 steel after forging creates UB morphology as the basic microstructure, with partial participation of lower and GB.
- Decreasing the Ti content from 0.088 wt. % in 7MnB8 steel to below 0.036 wt. % in S658 steel, S659 and S660 causes finer TiN particles formation and prevents the formation of Ti₂CS phase in the steels. Simultaneously, that leads to an increase in the fine precipitation density, which allows for a more efficient grain refinement applied by the pinning effect.
- A higher Mo content (0.4 wt. %) improves the toughness of S657 steel in comparison to S654 steel (0.2 wt. %) in the initial state after forging. In both steels, MC precipitations with Mo were identified.
- The structure of the new steels after the rolling is GB mostly. Increasing the hardenability by increasing Mn from ~ 1.9 to 2.9 wt. % leads to complex bainite morphology, UP, LB and GB, in S658 steel.
- The Mn addition in S658 steel, due to its influence on the hardenability provides more uniform hardness in the cross-section of the bars produced in the XTP process, due to UB morphology in the core of the bar, whose transformation temperature is lower than the temperature of GB identified for other steels in the core, thus its hardness is higher and the surface/core difference is smaller.
- Applying cross-rolling improves the mechanical properties of the new materials. After the rolling process, YS increases on average by ~20%, while UTS and A increase by ~10%.
- The V in S660 steel after the rolling process was observed as a substitution of Ti and Nb in MC and M₂N precipitations. As in the initial state, no V-based precipitations were observed in the structure.
- The lowest DBTT = -150 °C for S660 and -180 °C for S659 steels, containing Nb, whose addition delays recrystallization processes, refining the grain size, were obtained with the use of the following process parameters: TA = 980 °C; TR = 700 °C; cooling rate 120;0;25 (~ 7.6°C/s).

- The use of the XTP rolling method, combined with the choice of chemical composition, makes it possible to significantly reduce the brittleness threshold temperature while retaining other strength properties at similar levels.

9. Literature

- [1] Steel Statistical Yearbooks, <https://www.worldsteel.org/steel-by-topic/statistics/steel-statistical-yearbook.html> (accessed February 27, 2020).
- [2] Mineral Commodity Summaries, <https://www.usgs.gov/centers/nmic/mineral-commodity-summaries> (accessed February 27, 2020).
- [3] B.E.S. Davenport, E.C. Bxin, N.J. Kexrny, Transformation of Austenite at Constant Subcritical Temperatures, *Metallurgical Transactions*. 1 (1970) 3503–3530.
- [4] H.K.D.H. Bhadeshia, A personal commentary on “transformation of austenite at constant subcritical temperatures,” *Metallurgical and Materials Transactions A*. 41A (2010) 1351–1390. doi:10.1007/s11661-010-0250-2.
- [5] S. Zajac, V. Schwinnand, K.H. Tacke, Characterisation and quantification of complex bainitic microstructures in high and ultra-high strength linepipe steels, *Materials Science Forum*. 500–501 (2005) 387–394. doi:10.4028/www.scientific.net/msf.500-501.387.
- [6] Courtesy of WorldAutoSteel, www.worldautosteel.org (accessed May 25, 2022).
- [7] C. Garcia-Mateo, F.G. Caballero, Ultra-high-strength bainitic steels, *ISIJ International*. 45 (2005) 1736–1740. doi:10.2355/isijinternational.45.1736.
- [8] N. Saeidi, A. Ekrami, Impact properties of tempered bainite–ferrite dual phase steels, *Materials Science and Engineering: A*. 527 (2010) 5575–5581. doi:10.1016/J.MSEA.2010.05.015.
- [9] H.K.D.H. Bhadeshia, Nanostructured bainite, *Proceedings of the Royal Society A: Mathematical, Physical and Engineering Sciences*. 466 (2010) 3–18. doi:10.1098/rspa.2009.0407.
- [10] F.G. Caballero, H.K.D.H. Bhadeshia, Very strong bainite, *Curr Opin Solid State Mater Sci*. 8 (2004) 251–257. doi:10.1016/j.cossms.2004.09.005.
- [11] T. Sourmail, Bainite and superbainite in long products and forged applications, in: *Bainite - from Nano to Macro Symposium on Science and Application of Bainite*, 2017: pp. 32–42.
- [12] P. Pan, H. Tang, X. Chen, Z. Wang, L. Zuo, M. Yang, Y. Cao, Effects of direct-quenching and tempering on the microstructure and mechanical properties of an

- ultra-low carbon Ti containing bainite steel, *Materials Science and Engineering A*. 796 (2020). doi:10.1016/j.msea.2020.139987.
- [13] H. Wang, Y. Chen, The effect of finish rolling temperature on the microstructure and properties of non-quenched and tempered Bainite steel, *Procedia Eng.* 207 (2017) 1839–1843. doi:10.1016/J.PROENG.2017.10.948.
- [14] H. Roelofs, M. Lembke, Taming the bainite for use in bright bar applications, in: *Bainite - from Nano to Macro Symposium on Science and Application of Bainite*, 2017: pp. 43–51.
- [15] A.W.T. Arbeitsgemeinschaft, W. Werkstofftechnik, *Bainite - from nano to macro Symposium on science and application of Bainite*, (2017).
- [16] A.R. Kalantari, A. Zarei-Hanzaki, H.R. Abedi, M. Hassanpour-Esfahani, S.J. Park, J.Y. Park, Microstructure evolution and room temperature mechanical properties of a thermomechanically processed ferrite-based low density steel, *Materials Science and Engineering A*. 754 (2019) 57–67. doi:10.1016/j.msea.2019.03.048.
- [17] A.A. Krugljakow, S.A. Nikulin, S.O. Rogachev, H.X. Nguyen, N. V. Lebedeva, G.A. Panova, Hot-hardening phenomenon in die steel during thermomechanical processing, *Mater Lett.* 266 (2020). doi:10.1016/j.matlet.2020.127475.
- [18] X. Fu-Ren, C. Ya-Bin, G.-Y. Qiao, X.-B. Zhang, B. Liao, Effect of Nb Solute and NbC Precipitates on Dynamic or Static Recrystallization in Nb Steels, *Journal of Iron and Steel Research*. 19 (2012) 52–56. doi:doi.org/10.1016/S1006-706X(13)60020-5.
- [19] B. Mintz, J.R. Banerjee, K.M. Banks, Regression equation for Ar₃ temperature for coarse grained as cast steels, *Ironmaking and Steelmaking*. 38 (2011) 197–203. doi:10.1179/030192310X12827375731429.
- [20] S.F. Medina, M. Gomez, A. Quispe, L. Rancel, The role of vanadium in microalloyed steels: austenite grain refinement, intragranular nucleation of ferrite and bainite and mechanical properties, *Chemical Physics Research Journal*. 5 (2012) 1–34.
- [21] M.N. Akhtar, M. Khan, S.A. Khan, A. Afzal, R. Subbiah, S.N. Ahmad, M. Husain, M.M. Butt, A.R. Othman, E.A. Bakar, Determination of Non-Recrystallization Temperature for Niobium Microalloyed Steel, *Materials*. 14 (2021) 1–14.
- [22] B. Buchmayr, Thermomechanical Treatment of Steels – A Real Disruptive Technology Since Decades, *Steel Res Int*. 88 (2017). doi:10.1002/srin.201700182.

- [23] F. Siciliano, S.F. Rodrigues, C. Aranas, J.J. Jonas, The Dynamic Transformation of Ferrite Above A_{e3} and the Consequences on Hot Rolling of Steels, *Tecnol Metal Mater Min.* 17 (2020) 90–95. doi:10.4322/2176-1523.20202230.
- [24] V.C. Olalla, Influence of the Thermo Mechanical Control Processing Finishing Condition on Microstructure and Properties of High Strength Low Alloy Pipeline Steels, 2015.
- [25] W. Wang, R. Ma, L. Li, R. Zhai, S. Ma, H. Yan, S. Zhang, S. Gong, Constitutive analysis and dynamic recrystallization behavior of as-cast 40CrNiMo alloy steel during isothermal compression, *Journal of Materials Research and Technology.* 9 (2020) 1929–1940. doi:10.1016/j.jmrt.2019.12.025.
- [26] D. Belato Rosado, W. De Waele, D. Vanderschueren, S. Hertelé, Latest developments in mechanical properties and metallurgical features of high strength line pipe steels, *International Journal Sustainable Construction & Design.* 4 (2013). doi:10.21825/scad.v4i1.742.
- [27] K. Bhansali, A.J. Keche, C.L. Gogte, S. Chopra, Effect of grain size on Hall-Petch relationship during rolling process of reinforcement bar, *Mater Today Proc.* (2020). doi:10.1016/j.matpr.2020.02.655.
- [28] X. Wang, K. Chandrashekhara, M.F. Buchely, S. Lekakh, D.C. Van Aken, R.J. O'Malley, G.W. Ridenour, E. Scheid, Experiment and simulation of static softening behavior of alloyed steel during round bar hot rolling, *J Manuf Process.* 52 (2020) 281–288. doi:10.1016/j.jmapro.2020.02.031.
- [29] P. Andersson, J. Levén, B. Hemming, Hot rolling tests with steel bars and silicon nitride rolls, *J Mater Process Technol.* 209 (2009) 884–893. doi:10.1016/j.jmatprotec.2008.02.069.
- [30] S. Choi, Y. Lee, P.D. Hodgson, A comparative study of microstructures and mechanical properties obtained by bar and plate rolling, *J Mater Process Technol.* 124 (2002) 329–336.
- [31] S.P. Galkin, A. Romantsev, B. A. Borowikow, New inline process for thermomechanical treatment of steel bars, *CIS Iron and Steel Review.* (2012) 16–20.
- [32] M. Orłowska, K. Topolski, T. Brynk, L. Olejnik, M. Lewandowska, A novel rolling procedure to enhance ECAP processed ultrafine grained materials, *Mater Lett.* 233 (2018) 270–273. doi:10.1016/j.matlet.2018.09.047.

- [33] G. Le Roy, J.D. Embury, G. Edwards, M.F. Ashby, A model of ductile fracture based on the nucleation and growth of voids, *Acta Metallurgica*. 29 (1981) 1509–1522. doi:10.1016/0001-6160(81)90185-1.
- [34] L. Zhang, D. Cheng Guo, A General Etchant for Revealing Prior-Austenite Grain Boundaries in Steels, *Mater Charact.* 30 (1993) 299–305.
- [35] S. Zaefferer, J. Ohlert, W. Bleck, A study of microstructure, transformation mechanisms and correlation between microstructure and mechanical properties of a low alloyed TRIP steel, *Acta Mater.* 52 (2004) 2765–2778. doi:10.1016/J.ACTAMAT.2004.02.044.
- [36] Z. Pater, J. Tomczak, T. Bulzak, A Cross Wedge Rolling Process for Forming 70 mm Diameter Balls from Heads of Scrap Railway Rails, *Procedia Manuf.* 11 (2017) 466–473. doi:10.1016/j.promfg.2017.07.137.
- [37] M.I.Lembke, L. Oberli, G. Olschewski, R. Dotti, Surpassing steel performance by creating a very fine grained structure, *La Metallurgia Italiana*. 6 (2018) 31–36.
- [38] A.B. Naizaberkov, S.N. Lezhnev, H. Dyja, T. Bajor, K. Tsay, A. Arbuz, N. Gusseyinov, R. Nemkaeva, The effect of cross rolling on the microstructure of ferrous and non-ferrous metals and alloys, *Metalurgija*. 56 (2017) 199–202.
- [39] K. Tsay, A. Arbuz, N. Gusseyinov, R. Nemkaeva, N. Ospanov, I. Krupen'kin, Refinement of the microstructure of steel by cross rolling, *Journal of Chemical Technology and Metallurgy*. 51 (2016) 385–392.
- [40] S.A. Mashekov, G.A. Smailova, A.M. Alshynova, A.E. Uderbayeva, N.S. Sembaev, A. Zhauyt, Structure formation of aluminum alloy D16 while rolling bars in the radial shear mill, *Metalurgija*. 59 (2020) 195–198.
- [41] T. Bajor, A. Kulakowska, H. Dyja, Analysis of the rolling process of alloy 6005 in a three-high skew rolling mill, *Materials*. 13 (2020). doi:10.3390/ma13051114.
- [42] K. Muszka, J. Majta, Ł. Bienias, Effect of grain refinement on mechanical properties of microalloyed steels, *Metallurgy and Foundry Engineering*. 32 (2006) 87–97.
- [43] H. Halfa, Recent Trends in Producing Ultrafine Grained Steels, *Journal of Minerals and Materials Characterization and Engineering*. 2 (2014) 428–469. doi:10.4236/jmmce.2014.25047.
- [44] G. Larzabal, N. Isasti, J.M. Rodriguez-Ibabe, P. Uranga, Evaluating Strengthening and Impact Toughness Mechanisms for Ferritic and Bainitic Microstructures in

- Nb, Nb-Mo and Ti-Mo Microalloyed Steels, *Metals (Basel)*. 7 (2017) 1–18. doi:10.3390/met7020065.
- [45] A. Karmakar, P. Sahu, S. Neogy, D. Chakrabarti, R. Mitra, S. Mukherjee, S. Kundu, Effect of Cooling Rate and Chemical Composition on Microstructure and Properties of Naturally Cooled Vanadium-Microalloyed Steels, *Metallurgical and Materials Transactions A*. 48 (2017) 1581–1595. doi:10.1007/s11661-017-3964-6.
- [46] D. Kuhlmann-Wilsdorf, Theory of plastic deformation: - properties of low energy dislocation structures, *Materials Science and Engineering: A*. 113 (1989) 1–41. doi:10.1016/0921-5093(89)90290-6.
- [47] S.C. Kennett, G. Krauss, K.O. Findley, Prior austenite grain size and tempering effects on the dislocation density of low-C Nb–Ti microalloyed lath martensite, *Scr Mater*. 107 (2015) 123–126. doi:10.1016/J.SCRIPTAMAT.2015.05.036.
- [48] A. Zieliński, J. Dobrzański, H. Purzyńska, Stale nowej generacji stosowane w polskiej energetyce konwencjonalnej na element ciśnieniowe kotłów o nadkrytycznych parametrach pracy - atlas zmian struktury i właściwości mechanicznych., 2015.
- [49] J. Gazdowicz, A. Zieliński, Z. Kania, Odporność korozyjna elementów konstrukcyjnych kotłów o parametrach ultra super nadkrytycznych, 2016.
- [50] Q. Wang, Z. Li, S. Pang, X. Li, C. Dong, P.K. Liaw, Coherent precipitation and strengthening in compositionally complex alloys: A review, *Entropy*. 20 (2018). doi:10.3390/e20110878.
- [51] Y. Kobayashi, J. Takahashi, K. Kawakami, Experimental evaluation of the particle size dependence of the dislocation-particle interaction force in TiC-precipitation-strengthened steel, *Scr Mater*. 67 (2012) 854–857. doi:10.1016/j.scriptamat.2012.08.005.
- [52] L.A. Dobrzański, *Podstawy nauki o materiałach i metaloznawstwo*, WNT, Warszawa, 2002.
- [53] F. Sun, Y.F. Gu, J.B. Yan, Y.X. Xu, Z.H. Zhong, M. Yuyama, Creep deformation and rupture mechanism of an advanced wrought Ni-Fe based superalloy for 700°C class A-USC steam turbine rotor application, *J Alloys Compd*. 687 (2016) 389–401. doi:10.1016/j.jallcom.2016.06.120.
- [54] A.J. Ardell, Precipitation hardening, *Metallurgical Transactions A*. 16 (1985) 2131–2165. doi:10.1007/BF02670416.

- [55] J. Moon, S. Kim, J. il Jang, J. Lee, C. Lee, Orowan strengthening effect on the nanoindentation hardness of the ferrite matrix in microalloyed steels, *Materials Science and Engineering A*. 487 (2008) 552–557. doi:10.1016/j.msea.2007.10.046.
- [56] J. Fu, G. Li, X. Mao, K. Fang, Nanoscale cementite precipitates and comprehensive strengthening mechanism of steel, *Metall Mater Trans A Phys Metall Mater Sci*. 42 (2011) 3797–3812. doi:10.1007/s11661-011-0767-z.
- [57] Z. Zhang, J. Zhang, Y. Lian, M. Ma, C. Zhao, H. Ye, G. Li, C. Zhang, J. Huang, Effects of vanadium content on the carbides transformation and strengthening mechanism of MPS700V hot-work die steel at room and elevated temperatures, *Materials Science and Engineering: A*. (2021) 141091. doi:10.1016/j.msea.2021.141091.
- [58] K.H. Lo, C.H. Shek, J.K.L. Lai, Recent developments in stainless steels, *Materials Science and Engineering R: Reports*. 65 (2009) 39–104. doi:10.1016/j.mser.2009.03.001.
- [59] Morris, J. W., *The Influence of Grain Size on the Mechanical Properties of Steel*, Barkley, 2001. doi:10.2172/861397.
- [60] F. Hu, P.D. Hodgson, K.M. Wu, Acceleration of the super bainite transformation through a coarse austenite grain size, *Mater Lett*. 122 (2014) 240–243. doi:10.1016/J.MATLET.2014.02.051.
- [61] L. Xie, C. Wang, Y. Wang, G. Wu, X. Huang, Grain size effect on the mechanical behavior of metastable Fe-23Cr-8.5Ni alloy, *Metals (Basel)*. 9 (2019). doi:10.3390/met9070734.
- [62] T. Hanamura, F. Yin, K. Nagai, Ductile-brittle transition temperature of ultrafine ferrite/cementite microstructure in a low carbon steel controlled by effective grain size, *ISIJ International*. 44 (2004) 610–617. doi:10.2355/isijinternational.44.610.
- [63] N. Hansen, Hall-petch relation and boundary strengthening, *Scr Mater*. 51 (2004) 801–806. doi:10.1016/j.scriptamat.2004.06.002.
- [64] N. Isasti, D. Jorge-Badiola, M.L. Taheri, P. Uranga, Microstructural features controlling mechanical properties in Nb-Mo microalloyed steels. Part I: Yield strength, *Metall Mater Trans A Phys Metall Mater Sci*. 45 (2014) 4960–4971. doi:10.1007/s11661-014-2450-7.

- [65] V. Musonda, E.T. Akinlabi, T.C. Jen, Optimum Temperature of Hot Rolled Reinforced Bars at the Cooling Bed, *IOP Conf Ser Mater Sci Eng.* 225 (2017). doi:10.1088/1757-899X/225/1/012297.
- [66] Q. Guo-Zheng, Characterization for Dynamic Recrystallization Kinetics Based on Stress-Strain Curves, *Recent Developments in the Study of Recrystallization.* (2013). doi:10.5772/56031.
- [67] L. Dong, Y. Zhong, M.A. Qingxian, Y. Chaolong, M.A. Lishen, Dynamic Recrystallization and Grain Growth Behavior of 20SiMn Low Carbon Alloy Steel, *Tsinghua Sci Technol.* 13 (2008) 609–613.
- [68] J.H. Kim, M.H. Kwon, G. Gu, J.S. Lee, D.W. Suh, Quenching and partitioning (Q&P) processed medium Mn steel starting from heterogeneous microstructure, *Materialia (Oxf).* 12 (2020). doi:10.1016/j.mtla.2020.100757.
- [69] T.M. Park, H.J. Kim, H.Y. Um, N.H. Goo, J. Han, The possibility of enhanced hydrogen embrittlement resistance of medium-Mn steels by addition of micro-alloying elements, *Mater Charact.* 165 (2020). doi:10.1016/j.matchar.2020.110386.
- [70] V. Raghavan, Effect of manganese on the stability of austenite in Fe-Cr-Ni alloys., *Metallurgical and Materials Transactions A.* 26 (1995) 237–242.
- [71] L. García-Sesma, B. López, B. Pereda, Effect of coiling conditions on the strengthening mechanisms of Nb microalloyed steels with high Ti addition levels, *Materials Science and Engineering A.* 748 (2019) 386–395. doi:10.1016/j.msea.2019.01.105.
- [72] Z. Zeng, K.M. Reddy, S. Song, J. Wang, L. Wang, X. Wang, Microstructure and mechanical properties of Nb and Ti microalloyed lightweight δ -TRIP steel, *Mater Charact.* 164 (2020). doi:10.1016/j.matchar.2020.110324.
- [73] M. Gouné, P. Maugis, F. Danoix, Nucleation and growth of carbo-nitride nanoparticles in α -Fe-based alloys and associated interfacial process, *Nanotechnol Rev.* 4 (2015) 517–532. doi:10.1515/ntrev-2015-0032.
- [74] Y. Chen, D. Zhang, Y. Liu, H. Li, D. Xu, Effect of dissolution and precipitation of Nb on the formation of acicular ferrite/bainite ferrite in low-carbon HSLA steels, *Mater Charact.* 84 (2013) 232–239. doi:10.1016/j.matchar.2013.08.005.
- [75] R. Staško, H. Adrian, A. Adrian, Effect of nitrogen and vanadium on austenite grain growth kinetics of a low alloy steel, *Mater Charact.* 56 (2006) 340–347. doi:10.1016/j.matchar.2005.09.012.

- [76] E. Hornbogen, Precipitation from binary substitutional solid solutions of alpha iron, in: G.R. Speich, J.B. Clark (Eds.), *Precipitation from Iron-Base Alloys*, Gordon and Breach Science Publishers, Ohio, 1963: pp. 1–66.
- [77] K. Wesołowski, *Metaloznawstwo i obróbka cieplna*, Wydawnictwo Naukowo - Techniczne, 1972.
- [78] J. Fernández, S. Illescas, J.M. Guilemany, Effect of microalloying elements on the austenitic grain growth in a low carbon HSLA steel, *Mater Lett.* (2007). doi:10.1016/j.matlet.2006.09.021.
- [79] B. Hutchinson, Different Roles for Vanadium as a Microalloying Element in Structural Steels, *Journal of Iron and Steel Research International*. 18 (2011) 1–8.
- [80] P. Zhao, C. Cheng, G. Gao, W. Hui, R.D.K. Misra, B. Bai, Y. Weng, The potential significance of microalloying with niobium in governing very high cycle fatigue behavior of bainite/martensite multiphase steels, *Materials Science and Engineering A*. 650 (2016) 438–444. doi:10.1016/j.msea.2015.10.044.
- [81] P. Zhao, Z. Liu, F. Du, R.D.K. Misra, W. Ren, E. Yan, Multiphase bainite - martensite steels: The significant impact of niobium microalloying on structure and mechanical behavior, *Materials Science and Engineering A*. 730 (2018) 262–269. doi:10.1016/j.msea.2018.06.006.
- [82] J. Fernández, S. Illescas, J.M. Guilemany, Effect of microalloying elements on the austenitic grain growth in a low carbon HSLA steel, *Mater Lett.* 61 (2007) 2389–2392. doi:10.1016/j.matlet.2006.09.021.
- [83] J. Hannula, A. Kaijalainen, D. Porter, J. Kömi, The effect of microalloying elements on prior austenite grain growth of low-carbon slab material., *J Phys Conf Ser.* (2019). doi:10.1088/1742-6596/1270/1/012018.
- [84] A. Karmakar, S. Kandu, S. Neogy, D. Srivastava, Effect of microalloying elements on austenite grain growth in Nb – Ti and Nb – V steels, *Materials Science and Technology*. 30 (2014) 653–664. doi:10.1179/1743284713Y.0000000386.
- [85] S. Hashimoto, M. Nakamura, Effects of Microalloying Elements on Mechanical Properties of Reinforcing Bars, *ISIJ International*. 46 (2006) 1510–1515. doi:10.2355/isijinternational.46.1510.
- [86] Z. Adab, W. Hwang, Pinning Effect of Cerium Inclusions during Austenite Grains Growth in SS400 Steel at 1300 °C: A Combined Phase Field and Experimental Study, *Crystals (Basel)*. 7 (2017) 308. doi:10.3390/cryst7100308.

- [87] Z. Wang, W. Hui, Z. Chen, Y. Zhang, X. Zhao, Effect of vanadium on microstructure and mechanical properties of bainitic forging steel, *Materials Science and Engineering: A*. 771 (2020) 138653. doi:10.1016/J.MSEA.2019.138653.
- [88] G. Miyamoto, R. Hori, B. Poorganji, T. Furuhashi, Interphase precipitation of VC and resultant hardening in V-added medium carbon steels, *ISIJ International*. 51 (2011) 1733–1739. doi:10.2355/isijinternational.51.1733.
- [89] T. Kvackaj, L. Nemethova, R. Misicko, P. Imrich, M. Maria, Influence of Reheating Conditions on Austenite Grain Growth, *High Temperature Materials and Processes*. 30 (2011) 1–4. doi:10.1515/htmp.2011.110.
- [90] I. Dey, S. Chandra, R. Saha, S.K. Ghosh, Effect of Nb micro-alloying on microstructure and properties of thermo-mechanically processed high carbon pearlitic steel, *Mater Charact.* 140 (2018) 45–54. doi:10.1016/j.matchar.2018.03.038.
- [91] H. Huang, G. Yang, G. Zhao, X. Mao, X. Gan, Q. Yin, H. Yi, Effect of Nb on the microstructure and properties of Ti-Mo microalloyed high-strength ferritic steel, *Materials Science and Engineering A*. 736 (2018) 148–155. doi:10.1016/j.msea.2018.08.092.
- [92] M.S. Mohebbi, M. Rezayat, M.H. Parsa, Š. Nagy, M. Nosko, The impact of Nb on dynamic microstructure evolution of an Nb-Ti microalloyed steel, *Materials Science and Engineering A*. 723 (2018) 194–203. doi:10.1016/j.msea.2018.03.054.
- [93] K. Radwański, Structural characterization of low-carbon multiphase steels merging advanced research methods with light optical microscopy, *Archives of Civil and Mechanical Engineering*. 16 (2016) 282–293. doi:10.1016/J.ACME.2015.12.001.
- [94] L.J. Habraken, M. Economopoulos, Bainitic Microstructures in Low-Carbon Allo Steels and Their Mechanical Properties, in: *Transformation and Hardenability in Steels*, Climax Molybdenum company of Michigan, Ann Arbor, 1967: pp. 69–109.
- [95] S. Hasler, H. Roelofs, U. Urlau, New Bainitic Steel for Cold Heading Applications, in: *3rd International Conference on Steels in Cars and Trucks2*, Salzburg, 2011.
- [96] F.G. Caballero, H. Roelofs, S. Hasler, C. Capdevila, J. Chao, J. Cornide, C. Garcia-Mateo, Influence of bainite morphology on impact toughness of continuously

- cooled cementite free bainitic steels, *Materials Science and Technology*. 28 (2012) 95–102. doi:10.1179/1743284710Y.0000000047.
- [97] M. Perez, E. Courtois, D. Acevedo, T. Epicier, P. Maugis, Precipitation of niobium carbonitrides in ferrite: Chemical composition measurements and thermodynamic modelling, *Philos Mag Lett.* 87 (2007) 645–656. doi:10.1080/09500830701427003.
- [98] T.N. Baker, Microalloyed steels, *Ironmaking and Steelmaking*. 43 (2016) 264–307. doi:10.1179/1743281215Y.0000000063.
- [99] H. Adrian, R. Staško, The effect of nitrogen and vanadium on hardenability of medium carbon 0.4 %C and 1.8 %Cr steel, *Archives of Materials Science and Engineering*. 33 (2008) 69–74.
- [100] F. Fazeli, B.S. Amirkhiz, C. Scott, M. Arafin, L. Collins, Kinetics and microstructural change of low-carbon bainite due to vanadium microalloying, *Materials Science and Engineering A*. 720 (2018) 248–256. doi:10.1016/j.msea.2018.02.042.
- [101] J. Klemm-Toole, J. Benz, S.W. Thompson, K.O. Findley, A quantitative evaluation of microalloy precipitation strengthening in martensite and bainite, *Materials Science and Engineering: A*. 763 (2019) 138145. doi:10.1016/J.MSEA.2019.138145.
- [102] <https://en.wikipedia.org/wiki/Austenite#/media/File:IronAlfa&IronGamma.svg> (accessed September 8, 2023).
- [103] T. Gladman, *The physical metallurgy of microalloyed steels*, Intitute of Materials, London, 1997.
- [104] R. Lagneborg, B. Hutchinson, T. Siwiecki, S. Zajac, *The Role of Vanadium in Microalloyed Steels*, 2014. <https://www.researchgate.net/publication/326069877> (accessed September 8, 2023).
- [105] K.A. Taylor, Solubility products for Titanium-, Vanadium-, and Niobium-Carbide in Ferrite, *Scripta Metallurgica et Materialia*. 32 (1995) 7–12.
- [106] T. Obara, G.J. Shiflet, H.I. Aaronson, Influence of interfacial structure upon carbide precipitation at austenite:ferrite boundaries in an Fe-C-Mo alloy, *Metallurgical Transactions A*. 14A (1983) 1159–1167.
- [107] Y. Funakawa, Interphase precipitation and application to practical steels, *Mater Trans*. 60 (2019) 2086–2095. doi:10.2320/matertrans.M2018197.

- [108] A. Nayzabekov, S. Lezhnev, O. Maksimkin, K. Tsai, E. Panin, A. Arbuz, Microstructure and mechanical properties of austenitic stainless steel AISI-321 after radial shear rolling, *Journal of Chemical Technology and Metallurgy*. 53 (2018) 606–611.
- [109] A. Naizabekov, S. Lezhnev, A. Arbuz, E. Panin, The effect of radial-shear rolling on microstructure and mechanical properties of stainless austenitic steel AISI-321, in: *MATEC Web of Conferences* 190 (ICNFT), 2018: pp. 1–6. doi:10.1051/mateconf/201819011003.
- [110] XTP process, <https://www.xtp-technology.com/en/> (accessed March 17, 2020).
- [111] C. Keul, V. Wirths, W. Bleck, New bainitic steels for forgings, *Archives of Civil and Mechanical Engineering*. 12 (2012) 119–125. doi:10.1016/j.acme.2012.04.012.
- [112] B.X. Liu, K.Y. Fan, F.X. Yin, J.H. Feng, P.G. Ji, Effect of caliber rolling reduction ratios on the microstructure and mechanical properties of 45 medium carbon steel, *Materials Science and Engineering A*. 774 (2020). doi:10.1016/j.msea.2020.138954.
- [113] XTP Technology, <https://www.xtp-technology.com/en/technical-details/> (accessed September 21, 2020).
- [114] Technical Datasheet: Micro-alloyed Steel 7MnB8 XTP (Xtreme Performance Technology), https://www.xtp-technology.com/media/ste_ds_7mnb8_xtp_en.pdf (accessed September 8, 2023).
- [115] M. Olasolo, P. Uranga, J.M. Rodriguez-Ibabe, B. López, Effect of austenite microstructure and cooling rate on transformation characteristics in a low carbon Nb-V microalloyed steel, *Materials Science and Engineering A*. 528 (2011) 2559–2569. doi:10.1016/j.msea.2010.11.078.
- [116] N. Isasti, D. Jorge-Badiola, M.L. Taheri, P. Uranga, Microstructural features controlling mechanical properties in Nb-Mo microalloyed steels. Part II: Impact toughness, *Metall Mater Trans A Phys Metall Mater Sci*. 45 (2014) 4972–4982. doi:10.1007/s11661-014-2451-6.
- [117] H. Beladi, Y. Adachi, I. Timokhina, P.D. Hodgson, Crystallographic analysis of nanobainitic steels, *Scr Mater*. 60 (2009) 455–458. doi:10.1142/s2010194512001778.
- [118] S. Zaefferer, J. Ohlert, W. Bleck, A study of microstructure, transformation mechanisms and correlation between microstructure and mechanical properties of

- a low alloyed TRIP steel, *Acta Mater.* 52 (2004) 2765–2778. doi:10.1016/j.actamat.2004.02.044.
- [119] V. Tari, A.D. Rollett, H. Beladi, Back calculation of parent austenite orientation using a clustering approach, *J Appl Crystallogr.* 46 (2013) 210–215. doi:10.1107/S002188981204914X.
- [120] R. Petrov, L. Kestens, A. Wasilkowska, Y. Houbaert, Microstructure and texture of a lightly deformed TRIP-assisted steel characterized by means of the EBSD technique, *Materials Science and Engineering A.* 447 (2007) 285–297. doi:10.1016/j.msea.2006.10.023.
- [121] Y.-W. Chen, B.-M. Huang, Y.-T. Tsai, S.-P. Tsai, C.-Y. Chen, J.-R. Yang, Microstructural evolutions of low carbon Nb/Mo-containing bainitic steels during high-temperature tempering, *Mater Charact.* 131 (2017) 298–305. doi:10.1016/J.MATCHAR.2017.07.022.
- [122] V. Sinha, M. Gonzales, R.A. Abrahams, B.S. Song, E.J. Payton, Correlative microscopy for quantification of prior austenite grain size in AF9628 steel, *Mater Charact.* 159 (2020) 109835. doi:10.1016/J.MATCHAR.2019.109835.
- [123] J. Hidalgo, M.J. Santofimia, Effect of Prior Austenite Grain Size Refinement by Thermal Cycling on the Microstructural Features of As-Quenched Lath Martensite, *Metall Mater Trans A Phys Metall Mater Sci.* 47 (2016) 5288–5301. doi:10.1007/s11661-016-3525-4.
- [124] S. Morito, H. Tanaka, R. Konishi, T. Furuhashi, T. Maki, The morphology and crystallography of lath martensite in Fe-C alloys, *Acta Mater.* 51 (2003) 1789–1799. doi:10.1016/S1359-6454(02)00577-3.
- [125] S. Pallaspuuro, On the factors affecting the ductile-brittle transition in as-quenched fully and partially martensitic low-carbon steels, 2018. doi:10.13140/RG.2.2.32092.90245.
- [126] L. Morsdorf, O. Jeannin, D. Barbier, M. Mitsuhashi, D. Raabe, C.C. Tasan, Multiple mechanisms of lath martensite plasticity, *Acta Mater.* 121 (2016) 202–214. doi:10.1016/j.actamat.2016.09.006.
- [127] K. Radwański, Zastosowanie mikroskopii skaningowej i dyfrakcji elektronów wstecznie rozproszonych w badaniach struktury blach ze stali wielofazowych na różnych etapach procesu ciągłego wyżarzania., *Prace Instytutu Metalurgii Żelaza*, Gliwice, 2016.

- [128] D. Zhao, Y. Zhou, J. Fan, T. Liu, Y. Nie, W. Fu, Z. Lv, Structural properties and phase stability of primary Y phase (Ti₂SC) in Ti-stabilized stainless steel from experiments and first principles, *Materials*. 12 (2019) 1–15. doi:10.3390/ma12071118.
- [129] L. Gui, M. Long, H. Zhang, D. Chen, S. Liu, Q. Wang, H. Duan, Study on the precipitation and coarsening of TiN inclusions in Ti-microalloyed steel by a modified coupling model, *Journal of Materials Research and Technology*. 9 (2020) 5499–5514. doi:10.1016/j.jmrt.2020.03.075.
- [130] L. Gui, M. Long, H. Zhang, D. Chen, S. Liu, Q. Wang, H. Duan, Study on the precipitation and coarsening of TiN inclusions in Ti-microalloyed steel by a modified coupling model, *Journal of Materials Research and Technology*. 9 (2020) 5499–514. doi:10.1016/j.jmrt.2020.03.075.
- [131] Quan Guo-Zheng, Characterization for Dynamic Recrystallization Kinetics Based on Stress-Strain Curves, in: P. Wilson (Ed.), *Recent Developments in the Study of Recrystallization*, InTech, 2013: pp. 61–88.
- [132] S. V. Radcliffe, E.B. Kula, Deformation, transformation, and strength., in: W.A. Backofen, J.J. Burke, L.F. Coffin Jr., N.L. Reed, V. Weiss (Eds.), *Fundamentals of Deformation Processing*, Syracuse University Press, 1964: pp. 321–363.
- [133] A. Kundu, P.C. Chakraborti, Effect of Austenite Grain Size and Composition on Matrix Microstructure and Properties of Steel, *Procedia Materials Science*. (2014). doi:10.1016/j.mspro.2014.07.409.
- [134] R.D.K. Misra, H. Nathani, J.E. Hartmann, F. Siciliano, Microstructural evolution in a new 770 MPa hot rolled Nb-Ti microalloyed steel, *Materials Science and Engineering A*. (2005). doi:10.1016/j.msea.2004.11.041.
- [135] M. Korchynsky, H. Stuart, The role of strong carbide and sulfide forming elements in the manufacture of formable high strength low alloy steels., Jones and Laughlin Steel Corporation. (1978) 17–27.
- [136] G.L. Hu, Z.T. Liu, P. Wang, W.J. Hwa, M.K. Kang, Mechanism of tempered bainite embrittlement in some structural steels, *Materials Science and Engineering: A*. 141 (1991) 221–227. doi:10.1016/0921-5093(91)90772-F.
- [137] H. Yang, J. Shen, Y. Matsukawa, Y. Satoh, S. Kano, Z. Zhao, Y. Li, F. Li, H. Abe, Effects of alloying elements (Sn , Nb , Cr , and Mo) on the microstructure and mechanical properties of zirconium alloys, *J Nucl Sci Technol*. 52 (2015) 1162–1173. doi:10.1080/00223131.2014.996622.

- [138] Z. Yanushkevich, A. Lugovskaya, A. Belyakov, R. Kaibyshev, Deformation microstructures and tensile properties of an austenitic stainless steel subjected to multiple warm rolling, *Materials Science and Engineering A*. 667 (2016) 279–285. doi:10.1016/j.msea.2016.05.008.
- [139] C.Y. Chen, M.H. Liao, Synergistic effects of carbon content and Ti/Mo ratio on precipitation behavior of HSLA steel: Insights from experiment and critical patent analysis, *Mater Des*. 186 (2020). doi:10.1016/j.matdes.2019.108361.
- [140] R.W. Hertzberg, R.P. Vinci, J.L. Hertzberg, *Deformation and fracture mechanics of engineering materials*, 5th ed., John Wiley and Sons, Inc., New Jersey, 2012.

STRESZCZENIE PRACY

Rozwój stali bainitycznych do zastosowań w motoryzacji oraz transporcie kolejowym związany jest z poprawą odporności na obciążenia dynamiczne w niskiej temperaturze przy jednoczesnym zachowaniu wytrzymałości. W pracy podjęto tematykę związaną z opracowaniem parametrów technologicznych jednoetapowego procesu walcowania XTP, a także przeprowadzono dobór składu chemicznego stali 7MnB8 w celu obniżenia temperatury DBTT wytwarzanych prętów.

W ramach badań własnych przeprowadzono symulacje procesu walcowania, co pozwoliło na zaproponowanie parametrów technologicznych. Przeprowadzono próby przemysłowe walcowania z wykorzystaniem zaproponowanych grup parametrów. Szczegółowe badania mikrostrukturalne oraz analiza wpływu parametrów na właściwości mechaniczne stali 7MnB8 wykazały otrzymanie struktury gradientowej oraz rozdrobnienie mikrostruktury w rdzeniach badanych prętów oraz na ich powierzchni. Stwierdzono drobniejszą strukturę na powierzchni, w porównaniu do rdzenia prętów, której grubość wynosi ~ 4 mm w przypadku zastosowania intensywnego chłodzenia (~ 7.6 °C/s) po odkształceniu. Wykazano, iż obniżenie wydatku wodnego podczas chłodzenia, zmniejsza grubość rozdrobnionej strefy przypowierzchniowej, przez co struktura pręta na przekroju charakteryzuje się większą jednorodnością. W strukturze stali 7MnB8 o zawartości Ti w ilości 0.088 % mas., ujawniono duże wydzielenia TiN oraz Ti₂CS, których obecność wpływa na obniżenie właściwości udarnościowych. Określono wpływ parametrów procesu walcowania na udarność stali 7MnB8 po walcowaniu. Wykazano najniższą temperaturę DBTT = -120 °C dla pręta ze stali 7MnB8 walcowanej z wykorzystaniem parametrów walcowania: $T_A = 980^\circ\text{C}$, $T_R = 700^\circ\text{C}$ oraz przyspieszonym chłodzeniem w konfiguracji 120;0;25. Na podstawie uzyskanych wyników badań własnych przeprowadzono analizę porównawczą mikrostruktury oraz właściwości mechanicznych stali o różnej zawartości Mn, Mo, Nb, V i Ti poddawanych przeróbce z wykorzystaniem grupy parametrów technologicznych, dla których otrzymano najniższą DBTT dla stali przemysłowej. Wykazano, że zmiana konfiguracji dodatków stopowych z obniżeniem zawartości Ti prowadzi do eliminacji cząstek Ti₂CS oraz TiN w strukturze. Stwierdzono otrzymanie odmiennej struktury pręta ze stali o podwyższonej zawartości Mn do 2.9 % mas. W przypadku tej stali ujawniono strukturę UB z obszarami LB oraz GB, podczas gdy, dla stali o zawartości Mn na poziomie 1.9 % mas obserwowano głównie GB. Stwierdzono najniższe temperatury DBTT, wynoszące -150 °C oraz -180 °C odpowiednio dla stali S660 i S659, w których zastosowano dodatki Nb oraz obniżono zawartość Ti poniżej 0.03 % mas.

ABSTRACT

The development of bainitic steels for automotive and railroad applications is associated with improved resistance to low-temperature dynamic loads while maintaining strength. The paper deals with the development of technological parameters of a one-step XTP rolling process, and also discusses the selection of the chemical composition of 7MnB8 steel to reduce the DBTT temperature of the produced bars.

In this paper, a study was conducted that included simulations of the rolling process, which made it possible to propose technological parameters. Rolling tests were carried out using the proposed parameter groups. Detailed microstructural studies and an analysis of the effect of parameters on the mechanical properties of 7MnB8 steel showed the obtaining of a gradient structure and refinement of the microstructure in the cores of the tested bars and on their surface. A finer structure was found on the surface, compared to the core of the bars, the thickness of which was ~ 4 mm when applying intensive cooling (~ 7.6 °C/s) after deformation. It was shown that lowering the water output during cooling, so that the bar structure on the cross-section is characterized by greater homogeneity. In the structure of 7MnB8 steel with Ti content of 0.088 wt. %, large precipitations of TiN and Ti₂CS were revealed, the presence of which affects the reduction of impact properties. The effect of the rolling process parameters on the impact toughness of 7MnB8 steel after rolling was determined. The lowest temperature DBTT = -120 °C was shown for a bar of 7MnB8 steel rolled using the rolling parameters TA = 980 °C, TR = 700 °C and accelerated cooling in 120;0;25 configuration. Based on the results of our own research, a comparative analysis of the microstructure and mechanical properties of steels with different contents of Mn, Mo, Nb, V and Ti subjected to processing was made, with the use of a group of technological parameters for which the lowest DBTT for industrial steel was obtained. It was shown that changing the configuration of alloying additives with a reduction in Ti content leads to elimination of Ti₂CS and coarse TiN particles in the structure. A different bar structure was found to be obtained from steel with increased Mn content up to 2.9 wt. %. In the case of this steel, a UB structure with LB and GB areas was revealed, while, for the steel with Mn content of 1.9 wt. %, mainly GB was observed. The lowest DBTT temperatures of -150 °C and -180 °C were found for S660 and S659 steels, respectively, in which Nb additives were used and Ti content was reduced below 0.03 wt. %.